BEILSTEIN JOURNAL OF NANOTECHNOLOGY

Advances in nanomaterials

Edited by Herbert Gleiter and Thomas Schimmel

Imprint

Beilstein Journal of Nanotechnology
www.bjnano.org
ISSN 2190-4286
Email: journals-support@beilstein-institut.de

The *Beilstein Journal of Nanotechnology* is published by the Beilstein-Institut zur Förderung der Chemischen Wissenschaften.

Beilstein-Institut zur Förderung der Chemischen Wissenschaften
Trakehner Straße 7–9
60487 Frankfurt am Main
Germany
www.beilstein-institut.de

Beilstein Journal of Nanotechnology

Advances in nanomaterials

Herbert Gleiter*, Horst Hahn* and Thomas Schimmel*

Editorial

Open Access

Address:
Institute of Nanotechnology, Karlsruhe Institute of Technology, 76021 Karlsruhe, Germany

Email:
Herbert Gleiter* - herbert.gleiter@kit.edu; Horst Hahn* - horst.hahn@kit.edu; Thomas Schimmel* - thomas.schimmel@kit.edu

* Corresponding author

Beilstein J. Nanotechnol. **2013,** *4,* 805–806.
doi:10.3762/bjnano.4.91

Received: 21 November 2013
Accepted: 22 November 2013
Published: 27 November 2013

Guest Editors: H. D. Gleiter and T. Schimmel

In many cases new technologies are driven by the development of novel materials providing properties or combinations of properties that were not available before. The use of polymers and silicon-based semiconductor technologies are just two examples of how the availability of certain materials revolutionized existing technologies and products, giving rise to completely new technologies and having an enormous impact on our everyday life.

During the past three decades, the field of nanomaterials experienced a tremendous rise from the early beginnings to modern-day technologies, and still, new ideas and breakthroughs keep opening new perspectives for future technologies, from cars to aircraft, from semiconductors and electronics to novel displays, from energy harvesting to energy storage technologies and from biomimetic structures to medical technologies, to mention just a few examples.

One recent development in the field of nanomaterials is the ability not only to tailor the properties of nanomaterials (to achieve custom-designed, "tailor-made" values of certain properties) but to *tune* these properties. Tunable materials allow to change the properties of these materials *reversibly and in a controlled manner* after fabrication, e.g., by applying an electric field. Another remarkable development is the discovery of *"nanoglasses",* based on the idea of introducing internal interfaces on the nanometer scale not between crystalline structures (leading to nanocrystalline materials) but between non-crystalline, amorphous or glassy structures. These glasses differ structurally from present-day glasses and thus are expected to open the way to an age of glass-based technologies comparable to the contemporary, primarily crystalline-based, technologies.

This Thematic Series does not attempt to give a comprehensive overview over the vast and thriving field of nanomaterials. It rather gives a sequence of contributions on recent developments within this field.

The volume is dedicated to Horst Hahn on the occasion of his 60th birthday. Horst Hahn is Executive Director of the Institute for Nanotechnology at the Karlsruhe Institute of Technology (KIT) and Full Professor at the Technische Universität Darmstadt. In addition, he is Founding Director of the Helmholtz Institute Ulm for Electrochemical Energy Storage (HIU). He is Distinguished Professor at the Indian Institute of Technology Madras, India, and Honorary Professor at the University of Hyderabad, India, and at the Lanzhou University, China. Moreover, he is Elected Member of the German Academy of Sciences Leopoldina and the European Academy of Science. As a Fellow of the Materials Research Society (MRS), his

sustained and distinguished contributions to the advancement of international materials research were recognized. In the past two years, Horst Hahn was recipient of the highest award of the Deutsche Gesellschaft für Materialkunde (DGM), the Heyn Denkmünze, and of the renowned Robert Franklin Mehl Award of the Minerals, Metals & Materials Society (TMS). Horst Hahn has published more than 300 peer-reviewed articles in various fields of materials science. His main research interests are related to the synthesis and processing of nanocrystalline materials and nanostructures with tailored and tunable properties, with a focus on applications in printed electronics and energy materials.

The nucleation point for this Thematic Series was an international symposium held in August 2012 at the Karlsruhe Institute of Technology on the occasion of the 60th birthday of Horst Hahn – the "Nanomaterials Days" – which brought together renowned experts in the field of nanomaterials, each of them giving a short contribution on one recent research highlight in this field. A selection of these contributions is found in this Thematic Series in the form of original research articles reflecting recent advances in nanomaterials.

The articles in this Thematic Series highlight recent developments, from nanoporous polymers to graphene quantum dots, from concepts for designing magnetic properties to nanoplasticity and to the remarkable mechanical properties of a novel type of nanowires, just to mention some of the developments described.

We would like to thank all the authors for contributing their excellent work to this Thematic Series. Moreover, we would like to thank all referees for their promptly provided reports keeping the publication times short and attractive for contributors. Finally, we thank the team at the Beilstein Institut for their excellent support, and we acknowledge to the open access policy of the Beilstein Journal of Nanotechnology, which provides the basis for unrestricted discussions on "Advances in Nanomaterials".

Herbert Gleiter, Horst Hahn and Thomas Schimmel

Karlsruhe, November 2013

Beilstein Journal of Nanotechnology

Structural and electronic properties of oligo- and polythiophenes modified by substituents

Simon P. Rittmeyer and Axel Groß*

Full Research Paper

Open Access

Address:
Institute of Theoretical Chemistry, Ulm University, Albert-Einstein-Allee 11, D-89069 Ulm, Germany

Email:
Axel Groß* - axel.gross@uni-ulm.de

* Corresponding author

Keywords:
band gaps; conducting polymers; density functional theory calculations; molecular electronics; oligothiophenes

Beilstein J. Nanotechnol. **2012,** *3,* 909–919.
doi:10.3762/bjnano.3.101

Received: 23 September 2012
Accepted: 13 December 2012
Published: 27 December 2012

This article is part of the Thematic Series "Advances in nanomaterials".

Associate Editor: P. Ziemann

Abstract

The electronic and structural properties of oligo- and polythiophenes that can be used as building blocks for molecular electronic devices have been studied by using periodic density functional theory calculations. We have in particular focused on the effect of substituents on the electronic structure of thiophenes. Whereas singly bonded substituents, such as methyl, amino or nitro groups, change the electronic properties of thiophene monomers and dimers, they hardly influence the band gap of polythiophene. In contrast, phenyl-substituted polythiophenes as well as vinyl-bridged polythiophene derivatives exhibit drastically modified band gaps. These effects cannot be explained by simple electron removal or addition, as calculations for charged polythiophenes demonstrate.

Introduction

Since the first report about the electrical conductivity of doped polyacetylene (PA) in 1977 [1], significant efforts have been spent in studying organic polymers as an alternative to common inorganic semiconducting materials [2], as they can, e.g., form supramolecular architectures on surfaces [3,4] that can serve as building blocks in molecular electronics or can be used in the future solar-energy technology [5]. Although the electrical conductivity of well-prepared PA is nearly the same as for copper [6], its technical applications are very rare due to its instability towards air and humidity [7]. Searching for more stable compounds, thiophene-based materials turned out to be promising candidates, and thus, they have gained considerable attention during the past 20 years [6,8].

Like PA, nanosized polythiophene (PTp) shows a diffuse widespread conjugated π-system [8]. Consequently, removing an electron from the highest occupied polymer orbital or adding an electron to the lowest unoccupied orbital is relatively easy [9]. In a chemist's terminology one might call these processes redox reactions, whereas from a physicist's point of view one would

more likely call them n- and p-doping, respectively, to stress the analogy to the doping processes in traditional semiconducting materials such as silicon. Hence, neutral polymers, which usually show semiconducting or insulating properties, can transform into highly conductive compounds with a metal-like behavior.

The advantages of these *synthetic metals* are obvious. On the one hand they are nearly as conductive as metals but on the other hand they are as light and durable as plastics [10]. Furthermore, especially in the case of PTp, the doping processes causing the high conductivity of polymers are highly reversible [9]. This offers the opportunity to switch between conducting and insulating properties very easily and opens a broad field of application in the area of micro- and optoelectronics, e.g., as organic transistors, photoresistances or polymer light-emitting diodes (LEDs) [11]. In particular, thiophene-based organic solar cells have shown remarkable efficiency [5,8]. Nevertheless they are still relatively cheap in production [12].

For all these applications, the particular electronic structure of polymers is crucial. In this regard, a directed manipulation of the band gap to tailor the electronic properties is very desirable. Considering the significant potential of organic chemistry at synthesizing and manipulating compounds, there is definitely a demand for a better understanding of how the electronic structure of compounds such as PTp can be manipulated by using these tools. There have been already several studies addressing the electronic structure of thiophenes with electronic structure methods [13-20]. In these computational studies, typically oligothiophenes of varying size have been considered based on density functional theory (DFT), and the properties of polythiophenes have been derived by using scaling relations [21].

Here, we focus on the modification of the electronic properties of oligo- and polythiophenes by substituents based on periodic DFT calculations. Hence, we are able to address oligo- and polythiophenes within the same computational method so that no scaling relations have to be invoked. Our aim was in particular to determine the influence of different substituents on the electronic structure and especially on the band gap of thiophene-based polymers, as it is known that there is a close relationship between the geometrical structure and the physical properties of conductive polymers [22].

As a starting point, we first considered thiophene monomers and dimers and then compared their properties to those of infinite chains of thiophene, which can also act as a model for macrocyclic systems, namely cyclothiophenes [23]. As substituents we considered both singly bonded substituents, such as methyl, amino or nitro groups, as well as phenyl-like substituents. In addition, we studied vinyl-bridged polythiophene derivatives. Finally, we also addressed charged polythiophenes in order to model doped systems and to check whether the modified electronic properties can simply be regarded as effects resulting from band filling or band emptying.

Methods

Our calculations are based on the periodic DFT code implemented in the Vienna Ab initio Simulation Package (VASP) [24,25]. Exchange and correlation effects were treated in the generalized gradient approximation (GGA) by using the Perdew–Becke–Ernzerhof (PBE) functional [26], which gives a reliable description of intramolecular properties [27,28]. Dispersion corrections [29] are not necessary since we are not concerned with intermolecular interaction or adsorption of the aromatic molecules [30,31]. The ionic cores were represented by projector augmented wave (PAW) potentials [32] as constructed by Kresse and Joubert [33]. The electronic one-particle wave functions were expanded in a plane-wave basis set up to a cutoff energy of 400 eV, which was checked for convergence.

All geometrical optimizations were carried out by using the conjugated gradient algorithm implemented in VASP. Molecules were geometrically optimized by using a sufficiently large unit cell in the supercell approach and one *k*-point. In contrast, the polymers were described as one-dimensional infinite chains with a $7 \times 1 \times 1$ *k*-point sampling to replace the integration over the one-dimensional first Brillouin zone. *k*-Point convergence was carefully checked. When optimizing the polymer structure, both the geometric structure within the unit cell as well as the width of the unit cell were optimized as the latter correlates directly with the intercellular bond length.

For molecules, calculations concerning the density of states (DOS) were carried out at the Γ point with a Gaussian smearing ($\sigma = 0.01$ eV). For polymers, in contrast, a grid of $29 \times 1 \times 1$ Γ-centered *k*-points and linear tetrahedron smearing with Blöchl corrections [34] were used. Geometrically optimized structures were taken as a basis for all of these calculations. Polymers of different oxidation states were modeled by changing the number of electrons per unit cell. In order to preserve the electric neutrality of the cell, a compensating background charge is generated by default.

As we are interested in the HOMO–LUMO gap of oligothiophenes and the band gaps of polythiophenes, we have to be concerned with the well-known deficiency of DFT using current-day GGA exchange–correlation functionals to reproduce the correct magnitude of band gaps. The calculated band

structure can be improved by including self-energy corrections. However, including such corrections basically just affects the distance between valence and correction band, the shape and *k*-point dependence of valence and conduction bands remain more or less unchanged [35]. Furthermore, the more costly time-dependent DFT methods also do not necessarily yield better results [21]. In addition, hybrid functionals, which apparently work well for thiophenes [16], still require a significant computational effort in plane-wave codes such as VASP. As we are mainly interested in trends in the local density of states depending on the choice of the substituent, GGA-DFT calculations should be sufficient to reproduce these trends. However, one has to be aware that all absolute values of HOMO–LUMO and band gaps reported in this work are severely underestimated. As for the Fermi energy, it is throughout this work defined as the top of the valence band for polythiophenes with a band gap, and as the energy of the highest occupied state for periodic systems without a band gap.

Results and Discussion

Unsubstituted oligo- and polythiophenes

As a first step and as a reference, we determined the properties of unsubstituted oligo- and polythiophenes. All oligomers were modeled by using a sufficiently large box in three dimensions to avoid intermolecular interaction due to the use of a periodic DFT code. Note that in any polymer material the molecules are not isolated. However, there is no true chemical interaction between the molecules such that it is very likely that the electronic and structural properties of the oligo- and polythiophenes are not substantially modified by the presence of weakly interacting neighboring thiophenes.

For the unsubstituted monomer (thiophene, Tp), experimental geometric parameters obtained by Bak et al. [36] were reproduced quite well. Small deviations from experimental values concerning the dihedral angle were observed on modeling the dimer (2,2'-bithiophene, BTp): Calculations predicted a dihedral angle of 17.5° with a very flat rotational potential for angles from 0° to 30° whereas Almenningen et al. obtained an angle of about 34° using gas-phase electron diffraction [37]. There are known problems when using GGA-DFT to compute rotational barriers especially for conjugated systems [38], but there is definitely a flattening effect of a growing chain length as the trimer (2,5-bis(thiophen-2-yl)thiophene, TTp) was predicted to show a totally flat structure. This should be due to the extended π-system and, hence, definitely agrees with expectations. Regarding HOMO–LUMO gaps for the unsubstituted oligomers listed in Table 1, the previously mentioned problem of GGA-DFT when it comes to bandgaps is obvious. The calculated values are about 1 eV smaller than those measured by Diaz et al. [39]. Yet, the trend that the width of the HOMO–LUMO gap decreases with increasing size of the oligomer is reproduced by the calculations.

Table 1: Calculated HOMO–LUMO gaps for thiophene oligomers (in eV) compared with experimental values obtained by Diaz et al. [39].

	calculations	experiment
monomer (Tp)	4.49	5.37
dimer (BTp)	2.93	4.12
trimer (TTp)	2.21	3.52

The polymer PTp was modeled as a one-dimensional chain, which was separated by sufficiently large distances from its periodic images perpendicular to the chain as to avoid any sizable interaction between them. As shown in Figure 1 the unit cell contained two thiophene rings. We also modeled a unit cell that contained four rings, but neither structural nor electronic parameters differed from the results for the two-ring cell.

Our calculations predict PTp to form a totally planar structure as was already calculated for the trimer. This confirms the already mentioned flattening effect of a growing chain length also found in DFT calculations for other large oligomers [27,31]. It also agrees with the results of Azumi et al. [40], who found a planar structure for the crystalline penta- and heptamer by X-ray diffraction. The calculated bond lengths are the same as in the middle ring of TTp and fit quite well to the experimental values for the heptamer [40]. This definitely justifies our ansatz to approach the polymer through smaller molecules.

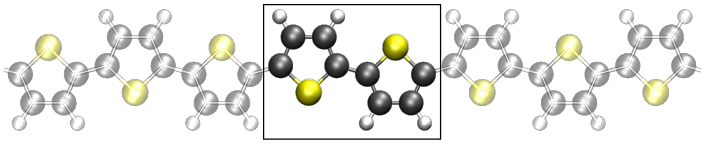

Figure 1: Considered structure of polythiophene (PTp). The frame indicates the unit cell used in the calculations, which contained two thiophene rings connected at their respective *α*-positions.

Regarding the electronic structure of PTp (see Figure 2a), we obtained a band gap of 1.2 eV. Again, the tendency of DFT to underestimate band gaps is obvious as the calculated value is about 60% of the experimental value of 2.0 eV [41]. One might ask whether modeling linear polymers as a planar chain of infinite length could be an additional source of error in comparison with experimental values that were obtained for large, but finite and, most likely, twisted polymers. But as there are known saturation effects for electronic properties in PTp when it comes to chains consisting of 10–12 rings [42,43], this should not be a source of additional errors.

In principle, there is a second possibility to build up a polymer from thiophene monomers. Instead of connecting the individual rings at their respective α-positions (2,5-connection) they can be coupled in an alternating 2,5/3,4-connection. We also modeled such an α,β-PTp system; the corresponding structure is illustrated in the inset of Figure 2b. Note that modeling a polymer consisting of exclusively 3,4-connected thiophene monomers with a two-ring unit cell is not possible because of steric hindrance. Figure 2 compares the density of states for PTp and α,β-PTp. Obviously, there is a considerable difference in the band gap of both isomers. As already mentioned, for PTp we obtained a value of 1.2 eV, whereas for α,β-PTp the calculated band gap of 2.5 eV is twice as large. This difference is most probably due to a less effective conjugation between the single-ring systems in α,β-PTp compared to PTp. As shown in Figure 3, for PTp the highest occupied crystal orbital (HOCO) as well as the lowest unoccupied crystal orbital (LUCO) are delocalized over the whole polymer chain, whereas for α,β-PTp the corresponding orbitals look rather localized. Especially in the area of the 2,5-bonds there is nearly no probability density of the orbitals, which suggests that this compound consists of basically conjugatively isolated dimeric units. This explanation is supported by the DOS plots in Figure 2. On the one hand, for PTp there are several broad populated areas, which indicate a relatively widespread conjugation over the polymer. But on the other hand, for α,β-PTp some small sharp areas of occupied states are visible, especially close to the Fermi edge. This implies flat energy bands in this area and is indicative of a relatively weak interaction between the unit cells [44]. In contrast, the DOS plot of PTp shows rather broad energy bands and, thus, a relatively strong intercellular interaction. The large band gap of α,β-PTp is not very favorable for most technical applications, hence we focus on PTp derivatives in the following.

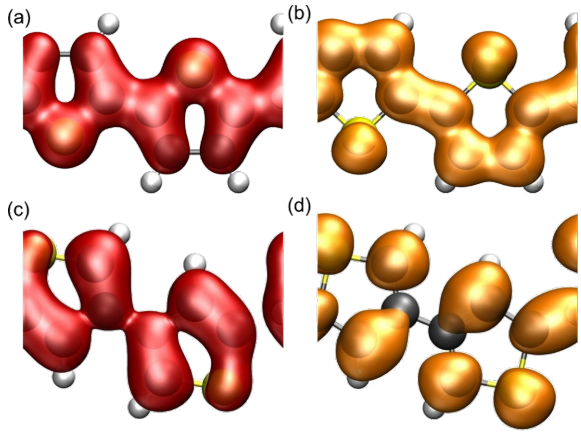

Figure 3: Electronic density isosurfaces (ρ(*r*) = 0.01 *e*/Å^3) of the highest occupied crystal orbital (HOCO, red) and the lowest unoccupied crystal orbital (LUCO, orange) for PTp (a,b) and α,β-PTp (c,d).

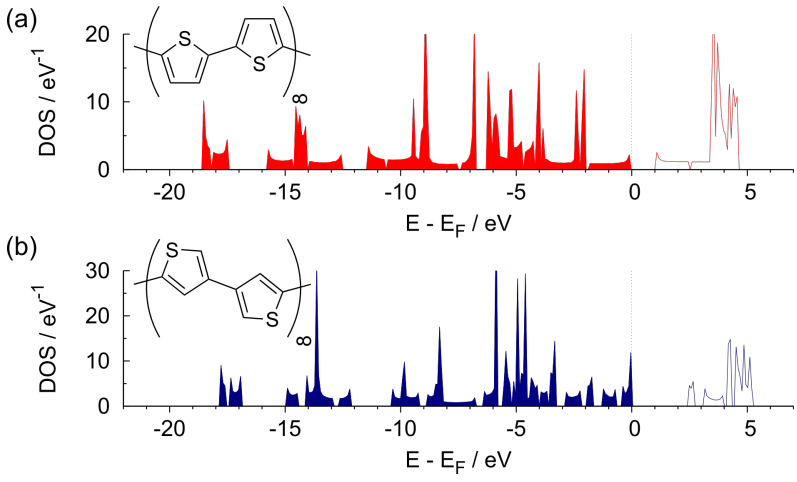

Figure 2: Structure and density of states for (a) PTp and (b) α,β-PTp.

Influence of substituents

The main goal of this study is to determine how substituents affect the electronic properties of oligothiophenes and whether the underlying effects can be transferred to the respective polymers. First, we took into account *classical* substituents, namely methyl (CH_3), amino (NH_2) and nitro groups (NO_2) and the chlorine atom (Cl). We chose these substituents, because they exemplify the basic electronic effects on the electronic charge distribution of conjugated systems known from organic chemistry. The considered substitution patterns for singly bonded substituents are illustrated in Figure 4. Furthermore, we have considered an annulated phenyl ring as a kind of special substituent to see how an explicitly extended π-system influences the respective systems.

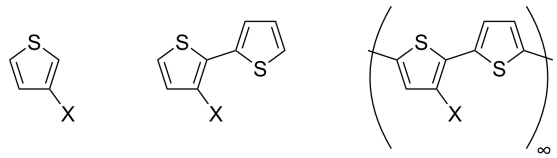

Figure 4: Illustration of the substitution patterns for singly bonded substituents of oligo- and polythiophenes considered in this study.

Structural effects concerning bond lengths in the monomers and dimers compared to the unsubstituted Tp and BTp turned out to be negligibly small. Nevertheless, the dihedral angle between the two aromatic ring-systems in the substituted dimers differs from BTp. Except for the chlorine-substituted dimer (ClBTp), all BTp derivatives show dihedral angles of about 22° to 24°. ClBTp itself is predicted to appear in a totally flat structure, probably caused by the intramolecular dipole–dipole interaction. The already mentioned flattening effect of a growing chain length again becomes observable as the dihedral angles of the substituted polymers are about 12° for NO_2PTp and NH_2PTp, and the methyl- and chlorine-substituted polymers, such as PTp, turn out to be both completely flat.

The substituents lead to recognizable effects in the electronic structure of the oligothiophenes. As shown in Table 2, except for the methyl-substituted dimer, all substituted molecules reveal a lowered HOMO–LUMO gap. The nitro group definitely causes the largest effect among the considered substituents, lowering the gap by about 1.3 eV for the monomer and by about 0.7 eV for the dimer, which we tentatively assign to the strong negative mesomeric effect of the nitro group. The influence of all other considered substituents on the electronic structure is rather minor. Regarding the chlorine-substituted bithiophene, one should take its planar structure into account. Hence, the gap-lowering effect cannot solely be accredited to the direct electronic influence of chlorine. In addition, the steric effect has to be considered, as flat structures generally tend to form more stable conjugated systems and therefore smaller HOMO–LUMO gaps. Still, the fact that, with the exception of the nitro group, all considered constituents have a rather similar effect on the HOMO– LUMO gap in spite of the fact that they influence the dihedral angle in opposite ways, suggests that the geometry may not play such an important role in the electronic structure.

Table 2: Calculated HOMO–LUMO gaps E_g (in eV) for substituted oligothiophenes compared to the unsubstituted ones.

substituent	monomer	dimer
H	4.49	2.93
CH_3	4.44	2.97
Cl	4.22	2.87
NH_2	4.46	2.75
NO_2	3.21	2.22

In Figure 5, the resulting DOS of the substituted polymers is compared with the DOS of the unsubstituted PTp. Interestingly enough, although there are some changes in the band structure, there is only a minor effect of the substituents on the band gap. The band gap of 1.19 eV for the unsubstituted polythiophene is changed to 1.19 eV (CH_3PTp), 1.22 eV (ClPTp), 1.14 eV (NH_2PTp), and 1.27 eV (NO_2PTp). The nitro group, which caused the largest reduction in the HOMO–LUMO gap for the monomer and dimer, now even leads to an increase of the band gap.

Hence, the influence of the substituents on the electronic structure is significantly reduced upon the transition from oligo- to polymer. This agrees with the results obtained by Salzner who reported similarly small effects of hydroxy and cyano substituents [15]. These groups lower the band gap of polymers only by about 0.1 eV, whereas they reduce the HOMO–LUMO gap of monomers by more than 1 eV.

In order to analyze the reason for the rather similar band gaps, we compare in Figure 6 the band structures of the unsubstituted polymer PTp (Figure 6a) with the substituted polymers NH_2PTp (Figure 6b) and NO_2PTp (Figure 6c). The amino group does not change the band structure significantly. The substituted polymer is still a direct-band-gap semiconductor with the band gap located at the Γ-point. Apparently, the delocalized states at the band gap are only weakly disturbed by the presence of the amino group. Only far below the Fermi energy are some additional almost dispersionless bands visible, reflecting the existence of localized substituent states. These

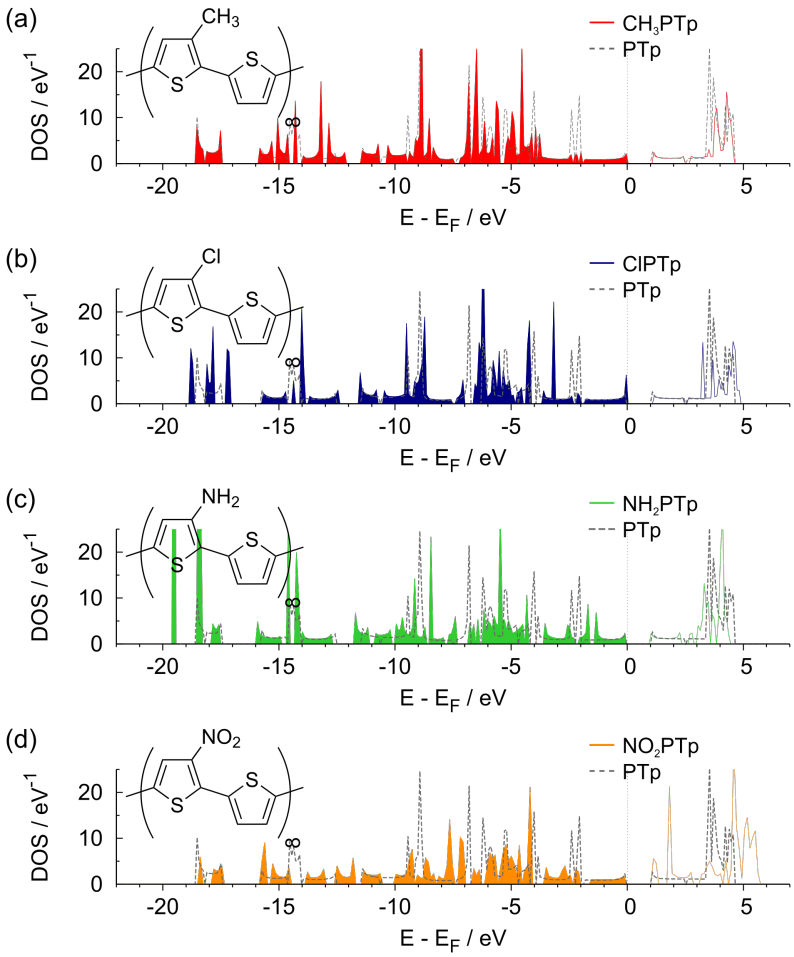

Figure 5: Density of states of substituted polymers: (a) CH_3PTp, (b) ClPTp, (c) NH_2PTp and (d) NO_2PTp. As a comparison, in each panel the DOS of the unsubstituted PTp is indicated by the dashed lines.

features are in fact present for all considered substituents, which lead to band structures that resemble the one of NH_2PTp.

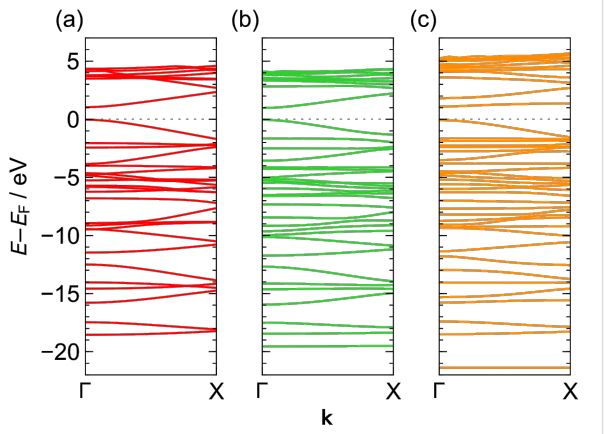

Figure 6: Calculated band structure of (a) unsubstituted PTp and of the substituted polymers (b) NH_2PTp and (c) NO_2PTp.

The only exception is NO_2PTp whose band structure is shown in Figure 6c. A rather flat band related to the addition of the nitro group appears at about 1 eV above the valence band. This flat, almost dispersionless band indicates the presence of localized electronic states caused by the presence of the strongly interacting nitro group. The former conduction band of the unsubstituted polymer is shifted up by about another 1 eV. This demonstrates that the apparently only weak modification of the band gap upon substitution with the nitro group is only coincidence, since the substitution significantly modifies the band structure of the polymer.

One might assume that the small changes in the band gaps are a consequence of the fact that the substituents hardly affect the HOCO and LUCO. But this assumption can be rejected regarding Figure 7. There, the electronic density isosurfaces of the HOCO and the LUCO for the substituted polymers are shown, which should be compared to the corresponding plot of unsubstituted polymer in Figure 3. Also the amino group leads

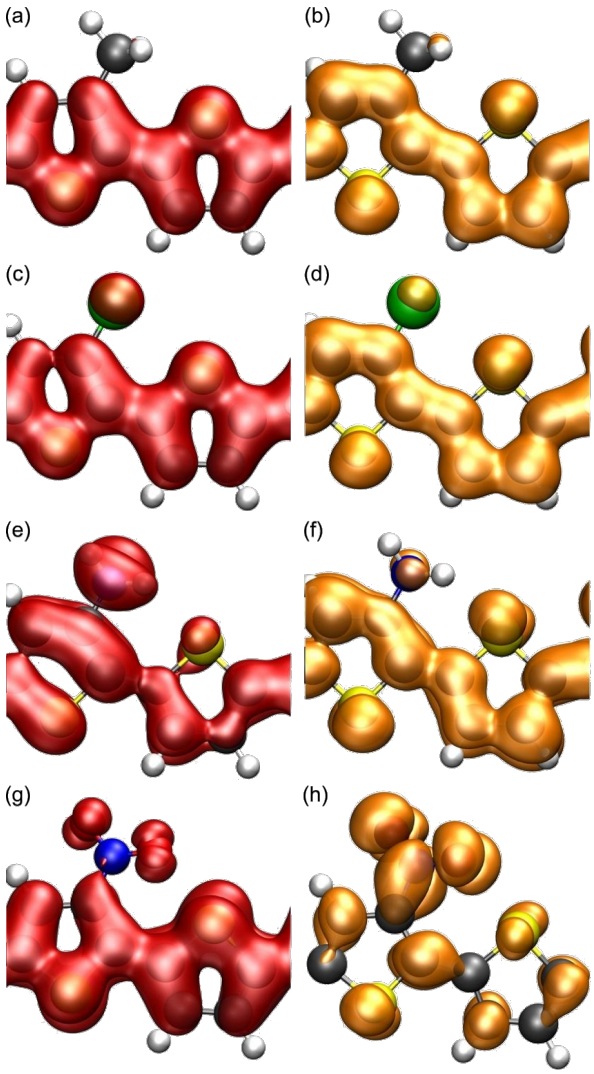

Figure 7: Electronic density isosurfaces (ρ(*r*) = 0.01 *e*/Å^3) of the HOCO (red) and LUCO (orange) for (a), (b) CH_3PTp; (c), (d) ClPTp; (e), (f) NH_2PTp; (g), (h) NO_2PTp.

to significant changes in both the HOCO and the LUCO although it only caused minor changes of the band structure. It has been suggested that one assumes a similar energetic shift of both orbitals for π-donating/accepting substituents resulting in nearly unaltered values for the respective band gaps [45]. However, energetic shifts with respect to the vacuum level can be caused both by changes in the band structure as well as by the presence of modified dipole fields that arise due to the presence of the constituents. It is rather hard to disentangle these two contributions. Still it can be concluded that although the singly bonded substituents have some effect on the electronic structure of both oligomers and polymers, they hardly affect the band gap of the corresponding polymers. Only if the substituents are strongly interacting, such as the nitro group, do significant changes in the band structure and the orbitals result (see Figure 3g and 3h).

Until now we focused our investigation on classic substituents, which are all basically singly bonded to the aromatic ring system of the thiophene backbone. In order to extend our study, we considered a phenyl ring as a substituent, thus obtaining benzo[*c*]thiophen (PhTp), 1-(thiophen-3-yl)-benzo[*c*]thiophen (PhBTp) and the corresponding polymer (PhPTp, see below inset of Figure 8 for an illustration). Since this π-extending substituent differs significantly from those previously regarded in that it is bonded to two different carbon atoms of the thiophene backbone, we discuss it here separately.

Our calculations yielded a dihedral angle of about 34° for PhBTp and 21° for the corresponding polymer, respectively. Note that this is about twice the dihedral angle of NH_2PTp and NO_2PTp due to the steric demand of the annulated phenyl ring. Still, the previously observed flattening effect upon growing chain lengths also holds for this system. The HOMO–LUMO gap for PhTp is predicted to be 2.71 eV, which is far below the other substituted monomers discussed so far. This is reasonable because the annulated phenyl ring extends the conjugated π-system quite considerably. For the dimer, the calculated HOMO–LUMO gap is further reduced to 2.19 eV, which is rather close to the corresponding nitro-substituted analogue. However, in contrast to the polymers with singly bonded substituents, the PhPTp polymer exhibits a direct band gap of 0.7 eV that is also significantly reduced with respect to the unsubstituted polymer PTp, as Figure 8 shows. Apparently, the

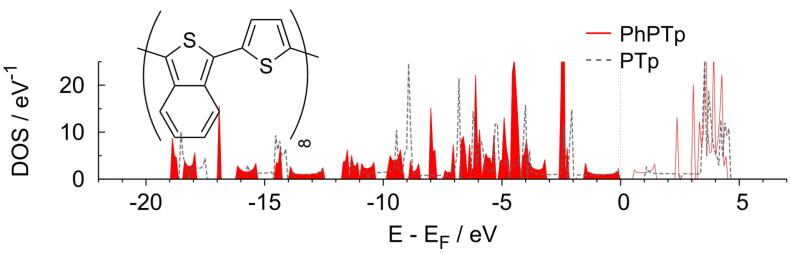

Figure 8: Calculated DOS of PhPTp compared to PTp. The inset illustrates the structure of PhPTp.

larger π-system of the phenyl-substituted polythiophene affects the electronic structure of polythiophene to a larger extent and leads to a smaller band gap. However, the valence band below the gap and the conduction band above the gap become narrower compared to the unsubstituted polymer (compare Figure 8 with Figure 2a) indicating more localized states. Note that Hong and Marynick found an increased direct band gap for an annulated cyclobutene ring [46], but also significantly reduced direct band gaps for other cyclic substituents. This suggests that it is possible to both increase and decrease the band gap with the choice of a suitable annulated substituent. Hence, annulated systems may be promising candidates for the manipulation of the band gap of polythiophene.

Vinyl-bridged polythiophene derivatives

In the discussion about the singly bonded substituents, we mentioned that the steric repulsion between the substituents also influences the geometric and electronic structure of the polythiophenes. In order to minimize this steric repulsion between the substituents, we considered polymers in which the thiophene rings in the backbone of the polymers are separated by a vinyl bridge (see Figure 9a). This results in entirely flat structures, independent of the respective substituent. Thus, geometric effects, such as deviations in the dihedral angle of the polymer, should not influence the band structure.

As Figure 9b demonstrates, the inclusion of a vinyl bridge also reduces the band gaps significantly from 1.2 eV for PTp to about 0.7 eV for the vinyl-bridged polymers. Apparently, the vinyl bridges reduce the aromaticity of the polymers by modifying the structure toward a quinoid form, leading to reduced band gaps, as the band gap of conjugated polymers depends (among other factors) on the degree of the quinoid or aromatic character of the backbone [20,46].

The trends among the substituents are similar to those for the substituted polythiophenes. Again, the nitro-substituted polymer reveals the largest band gap among the polymers. A closer look at the band structure and the density of states reveals that the widths of the bands are hardly modified, it is just the band gap between the valence and the conduction band that is reduced. Note that the band gap of the vinyl-bridged polymer with an annulated phenyl ring is even further decreased to 0.25 eV. Obviously, the effects of adding π-extending substituents and including vinyl bridges are roughly additive and can be combined in order to tailor the band gap.

Influence of doping on the electronic structure

The electrical conductivity of a large class of polymers, in particular of polythiophene, can be highly increased when they are doped. The doping process itself corresponds basically to a manipulation of the number of valence electrons of the polymers, often in an electrochemical environment induced by adding counter ions. In order to model these doped compounds we varied the number of valence electrons per unit cell. Counter ions were not explicitly considered but modeled through a homogeneous charge background. Because polythiophene is known to be a good conductor in the p-doped state [11], we limited our study to oxidized states. Note that the exact nature of the charge carriers in doped polythiophenes is still debated, i.e., it is discussed whether the conductivity is caused by bipolarons or polaron pairs [18,19]. Since our unit cell only contains two aromatic rings, we cannot address polarons, which are supposed to extend over five thiophene rings [18]. Still, our results may be helpful to understand trends in the band gap engineering. Furthermore, we note that it has been shown that changing the oxidation state through electrochemical potential control can have a decisive influence on the conductivity of molecular junctions [47].

Table 3 lists calculated bond lengths for PTp in different oxidized states. When the polymer is neutral, a unit cell consisting of two thiophene rings contains 48 valence electrons. Obviously there are some bonds that lengthen and some bonds that contract when PTp is oxidized. A closer inspection reveals that the formerly short bonds lengthen and vice versa. All in all this results in a change into a quinoid-like structure that becomes more distinct the more the polymer is oxidized. This quasi-shift of the double bond goes along with a loss of

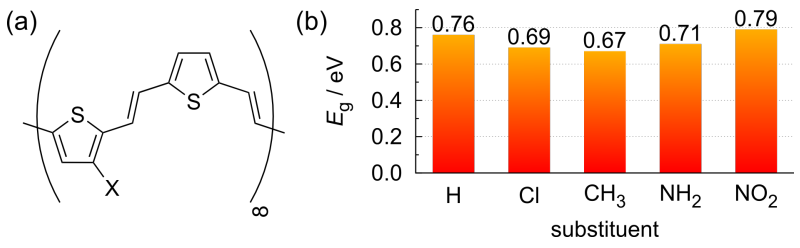

Figure 9: Considered vinyl-bridged polythiophene derivatives. (a) Structural formula, (b) band gaps E_g of the corresponding polymers.

aromaticity and thus should be energetically unfavorable at first glance. Of course the aromatic structure is more stable in the ground state, which is confirmed computationally [48], but the quinoid-like structure has a smaller ionization potential and a bigger electron affinity, and thus, the structural change caused by oxidation can be explained with the overall higher affinity of the quinoid-like structure towards charges [13].

Table 3: Calculated bond lengths for PTp (in Å) as a function of the charge state per unit cell in units of the elementary charge |*e*|.

	charge state/unit cell[a]					
	2.0	1.0	0.8	0.5	0.3	0.0
C^1–C^2	1.45	1.43	1.42	1.41	1.40.	1.39
C^2–C^3	1.37	1.38	1.38	1.39	1.39	1.41
C^4–C^6	1.42	1.41	1.42	1.42	1.42	1.44
C^1–S	1.75	1.73	1.74	1.74	1.74	1.74

a 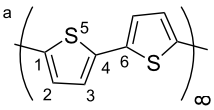

Concerning substituted polymers, we have limited our investigation in this case to NO_2PTp and NH_2PTp as these two substituents are considered to have mesomeric effects, which are of special importance when it comes to (de)stabilization of excess charges. Regarding these polymer, the effects of doping are basically the same. Both reveal a tendency to form a quinoid-like structure in the oxidized state. However, as a consequence of the broken symmetry that comes along with the addition of a substituent, these quinoid-like structures are distorted to a certain extent. Figure 10 illustrates the color-coded change of the respective bond lengths in oxidized polymers.

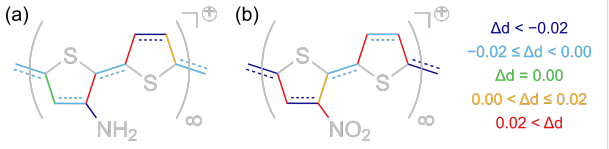

Figure 10: Color-coded change of bond lengths in (a) NH_2PTp and (b) NO_2PTp for positively charged polymers with the number of electrons per unit cell lowered by one.

Note that in the case of the amino-substituted polymer there is a contraction of the carbon-substituent bond by about 0.05 Å. In contrast, the corresponding bond length in NO_2PTp increases by about 0.03 Å. This may be due to mesomeric effects. The nitro group is known to destabilize positive excess charges whereas the amino group usually stabilizes them through its +M-effect of organic chemistry, i.e., by its capacity to increase the electron density of the rest of the molecule. Hence, on the one hand, the NH_2-group may shift electron density into the formerly aromatic electron-lacking ring system. On the other hand, it may be energetically favorable for an electron-lacking system to quit the conjugation to the nitro group and therefore to lengthen the respective bond. This could be a reason for the observed distortions of the polymer structure.

Regarding the density of states of the oxidized polymers plotted in Figure 11, it is obvious that positively charging the polymers leads to a partially occupied valence band, whereas the band structure is hardly changed compared to the neutral polymers. This indicates that charging the polymers basically corresponds to a shift of the Fermi energy without significant changes in the band structure and leads to metallic behavior. The substituted polymers, in contrast, still exhibit band gaps, cf. Figure 7. This means that the modification of the electronic structure upon substitution cannot be explained by simple electron removal or addition.

The resulting metallic state of the considered polymers seems to be at variance with the well-known fact that for π-conjugated organic polymers electrical conductivity cannot be understood with the mobility of unpaired electrons [48]. In fact, one-dimensional metals tend to distort spontaneously such that the spacing between adjacent unit cells becomes modulated [49]. In the case of polymers, conduction is associated with the formation of polarons or bipolarons. Quite often this leads to the formation of modulated quinoid-like structures [18,19] that extend over about five thiophene rings. In fact, as illustrated in Figure 10, we also find indications of a quinoid-like modification upon oxidizing the polymers. Yet, since our unit cell only contains at most two thiophene rings, such polarons, which would probably lead to the existence of a band gap, cannot be formed in our periodic DFT calculations. In order to address this issue, larger unit cells are required. Such calculations, which are more time-consuming, are planned for the future.

Conclusion

The structural and electronic properties of oligo- and polythiophenes and their modifications through substituents have been studied by periodic density functional theory calculations. Whereas the considered oligothiophenes still exhibit nonvanishing dihedral angles, the corresponding polythiophenes turn out to be basically planar. Among the considered singly bonded substituents, methyl, amino or nitro groups, or a chlorine atom, the nitro group in particular leads to a significant modification of the HOMO–LUMO gap of thiophene monomers and dimers. In contrast, the corresponding polythiophenes exhibit a hardly modified band gap compared to the unsubstituted polythiophene.

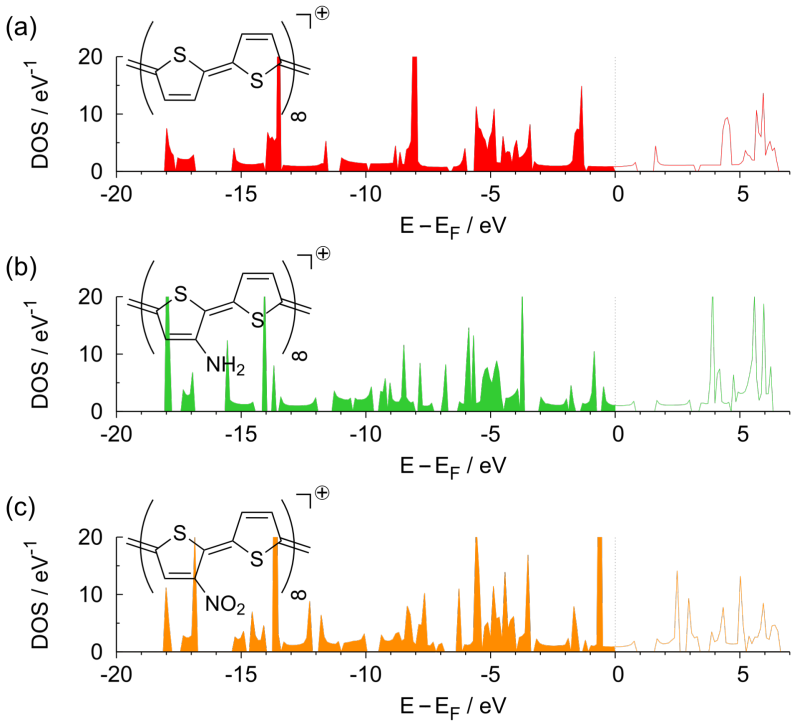

Figure 11: Density of states for positively charge polymers corresponding to a charge of 1|e| per unit cell: (a) PTp, (b) NH_2PTp and (c) NO_2PTp.

Phenyl-substituted polythiophenes as well as vinyl-bridged polythiophene-derivatives, on the other hand, have drastically modified band gaps. In addition, positively charged polythiophenes were considered as a model for doped polythiophenes. All considered charged polythiophenes become metallic, which shows that the modified band gaps cannot be explained by simple electron removal or addition. However, the unit cell in the periodic DFT calculations was still too small to allow for the formation of polarons.

Acknowledgements

Useful discussions with Elena Mena-Osteritz are gratefully acknowledged.

References

1. Chiang, C. K.; Fincher, C. R., Jr.; Park, Y. W.; Heeger, A. J.; Shirakawa, H.; Louis, E. J.; Gau, S. C.; MacDiarmid, A. G. *Phys. Rev. Lett.* **1977,** *39,* 1098–1101. doi:10.1103/PhysRevLett.39.1098
2. Heath, J. R.; Ratner, M. A. *Phys. Today* **2003,** *56,* 43–49. doi:10.1063/1.1583533
3. Koslowski, B.; Tschetschetkin, A.; Maurer, N.; Mena-Osteritz, E.; Bäuerle, P.; Ziemann, P. *Beilstein J. Nanotechnol.* **2011,** *2,* 561–568. doi:10.3762/bjnano.2.60
4. Caterbow, D.; Künzel, D.; Mavros, M. G.; Groß, A.; Landfester, K.; Ziener, U. *Beilstein J. Nanotechnol.* **2011,** *2,* 405–415. doi:10.3762/bjnano.2.46
5. Mishra, A.; Bäuerle, P. *Angew. Chem., Int. Ed.* **2012,** *51,* 2020–2067. doi:10.1002/anie.201102326
6. Bäuerle, P. *Adv. Mater.* **1993,** *5,* 879–886. doi:10.1002/adma.19930051202
7. Stevens, M. P. *Polymer Chemistry: An Introduction,* 3rd ed.; Oxford University Press: London, 1998.
8. Ma, C.-Q.; Mena-Osteritz, E.; Debaerdemaeker, T.; Wienk, M. M.; Janssen, R. A. J.; Bäuerle, P. *Angew. Chem., Int. Ed.* **2007,** *46,* 1679–1683. doi:10.1002/anie.200602653
9. Reddinger, J.; Reynolds, J. Molecular Engineering of π-Conjugated Polymers. In *Radical Polymerisation Polyelectrolytes;* Capek, I.; Hernández-Barajas, J.; Hunkeler, D.; Reddinger, J.; Reynolds, J.; Wandrey, C., Eds.; Advances in Polymer Science, Vol. 145; Springer: Berlin, 1999; pp 57–122. doi:10.1007/3-540-70733-6_2
10. Roncali, J. *Chem. Rev.* **1992,** *92,* 711–738. doi:10.1021/cr00012a009
11. McCullough, R. D.; Tristram-Nagle, S.; Williams, S. P.; Lowe, R. D.; Jayaraman, M. *J. Am. Chem. Soc.* **1993,** *115,* 4910–4911. doi:10.1021/ja00064a070
12. Die Aktuelle Wochenschau der GDCh. http://www.aktuelle-wochenschau.de/2010/w11/woche11.html (accessed Sept 22, 2012).
13. Brédas, J. L.; Thémans, B.; Fripiat, J. G.; André, J. M.; Chance, R. R. *Phys. Rev. B* **1984,** *29,* 6761–6773. doi:10.1103/PhysRevB.29.6761
14. Salzner, U.; Pickup, P. G.; Poirier, R. A.; Lagowski, J. B. *J. Phys. Chem. A* **1998,** *102,* 2572–2578. doi:10.1021/jp971652l
15. Salzner, U. *J. Phys. Chem. B* **2002,** *106,* 9214–9220. doi:10.1021/jp020141i
16. Radhakrishnan, S.; Parthasarathi, R.; Subramanian, V.; Somanathan, N. *J. Chem. Phys.* **2005,** *123,* 164905. doi:10.1063/1.2072947

17. Radhakrishnan, S.; Ananthakrishnan, S. J.; Somanathan, N. *Bull. Mater. Sci.* **2011,** *34,* 713–726. doi:10.1007/s12034-011-0186-1
18. Zade, S. S.; Bendikov, M. *J. Phys. Chem. C* **2007,** *111,* 10662–10672. doi:10.1021/jp071277p
19. Zamoshchik, N.; Salzner, U.; Bendikov, M. *J. Phys. Chem. C* **2008,** *112,* 8408–8418. doi:10.1021/jp7111582
20. Patra, A.; Wijsboom, Y. H.; Leitus, G.; Bendikov, M. *Chem. Mater.* **2011,** *23,* 896–906. doi:10.1021/cm102395v
21. Gierschner, J.; Cornil, J.; Egelhaaf, H.-J. *Adv. Mater.* **2007,** *19,* 173–191. doi:10.1002/adma.200600277
22. McCullough, R. D. *Adv. Mater.* **1998,** *10,* 93–116. doi:10.1002/(SICI)1521-4095(199801)10:2<93::AID-ADMA93>3.0.CO;2-F
23. Mena-Osteritz, E.; Zhang, F.; Götz, G.; Reineker, P.; Bäuerle, P. *Beilstein J. Nanotechnol.* **2011,** *2,* 720–726. doi:10.3762/bjnano.2.78
24. Kresse, G.; Furthmüller, J. *Comput. Mater. Sci.* **1996,** *6,* 15. doi:10.1016/0927-0256(96)00008-0
25. Kresse, G.; Furthmüller, J. *Phys. Rev. B* **1996,** *54,* 11169–11186. doi:10.1103/PhysRevB.54.11169
26. Perdew, J. P.; Burke, K.; Ernzerhof, M. *Phys. Rev. Lett.* **1996,** *77,* 3865–3868. doi:10.1103/PhysRevLett.77.3865
27. Künzel, D.; Markert, T.; Groß, A.; Benoit, D. M. *Phys. Chem. Chem. Phys.* **2009,** *11,* 8867–8878. doi:10.1039/b907443k
28. Meier, C.; Roos, M.; Künzel, D.; Breitruck, A.; Hoster, H. E.; Landfester, K.; Gross, A.; Behm, R. J.; Ziener, U. *J. Phys. Chem. C* **2010,** *114,* 1268–1277. doi:10.1021/jp910029z
29. Grimme, S.; Antony, J.; Ehrlich, S.; Krieg, H. *J. Chem. Phys.* **2010,** *132,* 154104. doi:10.1063/1.3382344
30. Tonigold, K.; Groß, A. *J. Chem. Phys.* **2010,** *132,* 224701. doi:10.1063/1.3439691
31. Künzel, D.; Tonigold, K.; Kučera, J.; Roos, M.; Hoster, H. E.; Behm, R. J.; Groß, A. *ChemPhysChem* **2011,** *12,* 2242–2245. doi:10.1002/cphc.201100240
32. Blöchl, P. E. *Phys. Rev. B* **1994,** *50,* 17953–17979. doi:10.1103/PhysRevB.50.17953
33. Kresse, G.; Joubert, D. *Phys. Rev. B* **1999,** *59,* 1758–1775. doi:10.1103/PhysRevB.59.1758
34. Blöchl, P. E.; Jepsen, O.; Andersen, O. K. *Phys. Rev. B* **1994,** *49,* 16223–16233. doi:10.1103/PhysRevB.49.16223
35. Rohlfing, M.; Krüger, P.; Pollmann, J. *Phys. Rev. B* **1995,** *52,* 1905–1917. doi:10.1103/PhysRevB.52.1905
36. Bak, B.; Christensen, D.; Hansen-Nygaard, L.; Rastrup-Andersen, J. *J. Mol. Spectrosc.* **1961,** *7,* 58–63. doi:10.1016/0022-2852(61)90341-1
37. Almenningen, A.; Bastiansen, O.; Svendsås, P. *Acta Chem. Scand.* **1958,** *12,* 1671–1674. doi:10.3891/acta.chem.scand.12-1671
38. Karpfen, A.; Choi, C. H.; Kertesz, M. *J. Phys. Chem. A* **1997,** *101,* 7426–7433. doi:10.1021/jp971606l
39. Diaz, A.; Crowley, J.; Bargon, J.; Gardini, G. P.; Torrance, J. B. *J. Electroanal. Chem.* **1981,** *121,* 355–361. doi:10.1016/S0022-0728(81)80592-X
40. Azumi, R.; Goto, M.; Honda, K.; Matsumoto, M. *Bull. Chem. Soc. Jpn.* **2003,** *76,* 1561–1567. doi:10.1246/bcsj.76.1561
41. Kobayashi, M.; Chen, J.; Chung, T.-C.; Moraes, F.; Heeger, A. J.; Wudl, F. *Synth. Met.* **1984,** *9,* 77–86. doi:10.1016/0379-6779(84)90044-4
42. Zade, S. S.; Benedikov, M. *Org. Lett.* **2006,** *8,* 5243–5246. doi:10.1021/ol062030y
43. Bednarz, M.; Reineker, P.; Mena-Osteritz, E.; Bäuerle, P. *Chem. Phys.* **2007,** *342,* 191–200. doi:10.1016/j.chemphys.2007.09.052
44. Piela, L. *Ideas of Quantum Chemistry;* Elsevier: Amsterdam, Boston, 2007.
45. Perepichka, I. F.; Perepichka, D. F. *Handbook of Thiophene-Based Materials: Applications in Organic Electronics and Photonics;* Synthesis and Theory, Vol. 1; Wiley: Chichester, U.K., 2009.
46. Hong, S. Y.; Marynick, D. S. *Macromolecules* **1992,** *25,* 4652–4657. doi:10.1021/ma00044a029
47. Leary, E.; Higgins, S. J.; van Zalinge, H.; Haiss, W.; Nichols, R. J.; Nygaard, S.; Jeppesen, J. O.; Ulstrup, J. *J. Am. Chem. Soc.* **2008,** *130,* 12204–12205. doi:10.1021/ja8014605
48. Brédas, J. L.; Street, G. B. *Acc. Chem. Res.* **1985,** *18,* 309–315. doi:10.1021/ar00118a005
49. Heeger, A. J.; Kivelson, S.; Schrieffer, J. R.; Su, W.-P. *Rev. Mod. Phys.* **1988,** *60,* 781–850. doi:10.1103/RevModPhys.60.781

License and Terms

Beilstein Journal of Nanotechnology

Hydrogen-plasma-induced magnetocrystalline anisotropy ordering in self-assembled magnetic nanoparticle monolayers

Alexander Weddemann[1], Judith Meyer[*2], Anna Regtmeier[2], Irina Janzen[2], Dieter Akemeier[2] and Andreas Hütten[2]

Full Research Paper

Open Access

Address:
[1]Research Laboratory of Electronics, Massachusetts Institute of Technology, 77 Massachusetts Ave, Cambridge, MA 02139, USA and [2]Department of Physics, Thin Films and Physics of Nanostructures, Bielefeld University, PB 100131, 33501 Bielefeld, Germany

Email:
Judith Meyer[*] - jmeyer@physik.uni-bielefeld.de

* Corresponding author

Keywords:
dipolar particle coupling; magnetic nanoparticles; magnetocrystalline anisotropy; monolayers

Beilstein J. Nanotechnol. **2013,** *4,* 164–172.
doi:10.3762/bjnano.4.16

Received: 10 October 2012
Accepted: 08 February 2013
Published: 04 March 2013

This article is part of the Thematic Series "Advances in nanomaterials".

Guest Editors: H. D. Gleiter and T. Schimmel

Abstract

Self-assembled two-dimensional arrays of either 14 nm hcp-Co or 6 nm ε-Co particle components were treated by hydrogen plasma for various exposure times. A change of hysteretic sample behavior depending on the treatment duration is reported, which can be divided in two time scales: oxygen reduction increases the particle magnetization during the first 20 min, which is followed by an alteration of the magnetic response shape. The latter depends on the respective particle species. Based on the Landau–Lifshitz equations for a discrete set of magnetic moments, we propose a model that relates the change of the hysteresis loops to a dipole-driven ordering of the magnetocrystalline easy axes within the particle plane due to the high spatial aspect ratio of the system.

Introduction

Due to their wide range of applications in physical, biological and medical fields, magnetic nanoparticles have been thoroughly studied during the past few decades [1,2]. In this regard, various manufacturing techniques to synthesize particles with distinct magnetic properties [3,4] or specific biological surface coatings [5,6] have been established. Such nanocrystals have a nonzero magnetization at zero field because of finite-size effects. Nevertheless, due to their superparamagnetic nature, the effective magnetic moment of an ensemble of noninteracting magnetic nanoparticles is zero if there is no external field applied.

The situation changes if various types of interaction become important. A common example is given by ligand- or polymer-

stabilized magnetic nanoparticles that tend to assemble in self-ordered two-dimensional arrays of high spatial symmetry [7-9] or various superstructures such as lines or rings [10,11]. In these systems, the magnetic coupling between individual particles increases the geometrical order of the assembly, which makes such patterns promising candidates for the design of novel data-storage devices [12]. A basic prerequisite for such an application is the high thermal stability of a magnetic state in order to maintain the magnetic configuration and not to lose the stored information.

In the case of a single particle, materials with a strong uniaxial magnetocrystalline anisotropy, such as face-centered tetragonal $L1_0$ FePt alloyed particles, meet this requirement [12,13]. The magnetic-moment vector aligns with the easy axis due to energy minimization. In the transition from a single free particle to a closed monolayer, stray-field contributions of contiguous particles need to be taken into account. For such ensembles of interacting magnetic nanocrystals, not only the magnetocrystalline contribution, but also the magnetic coupling determines the stability of a given magnetic state. In particular, the most stable magnetic configuration is achieved whenever the magnetocrystalline axes of individual particle components are aligned parallel to the magnetization directions of the magnetic equilibrium state of the system itself.

If particles with low magnetocrystalline anisotropy are considered, the magnetic equilibrium state is mainly dominated by dipolar coupling. In this case, the magnetic-moment vectors do not tend to align with the easy axes. Instead, as long as the crystallographic orientation of the particles can rotate freely by some mechanism, the easy axes align with the magnetic-moment vectors in order to minimize the total energy. Thus, the stability of the initial equilibrium configuration is increased. We investigate the two-dimensional assemblies of Co nanoparticles of different crystallographic phases and sizes under the influence of a hydrogen plasma. We will show evidence for such an ordering of the magnetocrystalline easy axes and consequent stabilization of the corresponding magnetic equilibrium states. The experimental results will be compared to numerical calculations based on the idea that the plasma induces a process comparable to the time-dependent creep under tension in which the plasma acts as thermal activation.

Experimental

Measurements were carried out with two different species of monodisperse Co particles, which will be referred to as sample I and sample II in the following. Sample I consists of particles with an average diameter d_I = 13.80 nm and a standard deviation of σ_I = 2.60 nm, while nanoparticles in sample II have a size of d_{II} = 6.09 nm at a standard deviation of σ_{II} = 1.14 nm. According to Hütten et al. [3], the smaller species are superparamagnetic while the larger contain a certain degree of ferromagnetic components.

Sample preparation

Both samples were prepared in a procedure introduced by Puntes et al. [14] under airless conditions. For the synthesis of sample I, 65 µL (0.2 mmol) oleylamine was dissolved in 4 mL 1,2-dichlorobenzene. The solution was subsequently heated under reflux. Separately, 150 mg (0.44 mmol) dicobaltoctacarbonyl $Co_2(CO)_8$ was dissolved in 2 mL of 1,2-dichlorobenzene.

During vigorous stirring, the second solution was rapidly injected into the refluxing bath. After a reaction time of 1 h, the mixture was cooled to room temperature. For the synthesis of particle species II, 265 µL of a mixture of equal parts of oleylamine and oleic acid were dissolved in 4 mL 1,2-dichlorobenzene and heated to 180 °C. Similar to sample I, 180 mg (0.53 mmol) dicobaltoctacarbonyl $Co_2(CO)_8$ was dissolved in 2 mL of 1,2-dichlorobenzene and rapidly injected into the refluxing bath. After a reaction time of 15 min, the mixture was cooled to room temperature. Due to the different surfactants present during the particle formation, particles in sample I are stabilized by oleylamine, while species II present a composition of oleylamine and oleic acid on the surface.

In order to realize closed nanoparticle monolayers, a silicon wafer with a SiO_2 layer of 500 nm thickness was dipped into the particle solution at an angle of 45°. The angle is experimentally chosen to provide the optimal deposition of closed particle monolayers onto the substrate. Upon evaporation of the liquid, particles remain immobile on the substrate surface. An example of a scanning electron microscopy image (SEM) taken from the resulting assemblies is shown in Figure 1a.

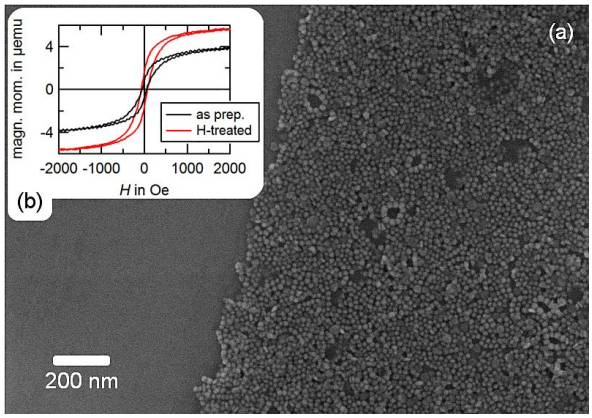

Figure 1: Monolayer of magnetic Co nanoparticles, species I. (a) SEM image of a two-dimensional particle assembly of 13.8 nm oleylamine-stabilized Co particles. (b) AGM measurements before and after hydrogen treatment.

Hydrogen plasma treatment

The self-assembled two-dimensional particle arrays were exposed to a soft hydrogen plasma (100 W) at room temperature under a pressure of 1.7×10^{-3} mbar for different exposure times. In order to analyze the influence of the plasma on the magnetic properties of the nanoparticles, alternating gradient magnetometer (AGM) measurements were performed before and after plasma treatment. Since a significant degree of oxidation can occur on very short time scales [15,16], the samples were covered in situ with a thin protective layer. These layers were deposited employing magnetron sputtering. For sample I and II, Ir and Pt were chosen as the respective layer materials; the layer thickness was set to 10 nm in both cases. Different materials were employed to ease the evaluation of the X-ray diffraction (XRD) measurements (see below).

On short time scales of approximately 20 min, an oxygen reduction of the particle material is expected, which entails an increase of the saturation magnetization of the sample [17-19]. For a sample prepared with species I, an example of such an increase is shown in Figure 1b. After a time period longer than 20 min, no further increase of the magnetic moment can be observed. However, as shown in Figure 2, the shape of the measured hysteresis loops is altered with respect to the exposure time. With M_S being the saturation magnetization of the sample material, the normalized magnetization M/M_S is shown with respect to the applied magnetic field. Subplots (a) and (b) represent the behavior of sample I for in-plane and out-of-plane measurements, respectively, and (c) and (d) the corresponding results for species II. All measurements were carried out at room temperature.

As a measure of the magnetic properties, we evaluate the remanent magnetization M_R, the coercive field H_C, and the change of the normalized magnetization M/M_S at the magnetic field strength $H = H_C$

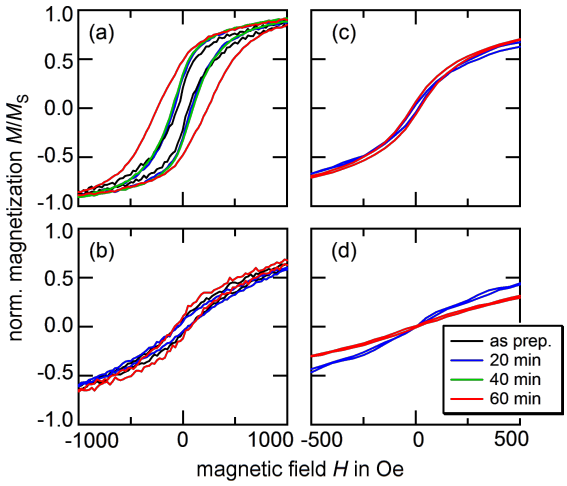

Figure 2: AGM measurements of nanoparticles assembled in monolayers after different exposure times to a hydrogen plasma. The results were obtained at room temperature. (a) and (b) show the behavior of particle species I for in-plane and out-of-plane external fields; (c) and (d) are the respective results for species II.

$$\chi_N = \frac{1}{M_S}\left(\frac{\partial M}{\partial H}\right)_{H=H_C}. \quad (1)$$

The evaluation of these parameters for in- and out-of-plane measurements are given in Table 1, with the respective indices $\parallel$ and $\perp$.

For in- and out-of-plane measurements of samples prepared with particle species I, we find increasing values for the remanent magnetization M_R and the coercive field H_C with longer treatment times. In contrast to these observations, the experiments carried out on species II show no clear tendency for these particular values. Instead, we find an increasing in-plane and a decreasing out-of-plane value for χ_N, which cannot be reported for species I.

Table 1: Characteristic magnetic data obtained from AGM measurements for sample I and II for different plasma treatment times. Measurements were taken at room temperature.

	$M_{R,\parallel}$ [M_S]	$M_{R,\perp}$ [M_S]	$H_{C,\parallel}$ [Oe]	$H_{C,\perp}$ [Oe]	$\chi_{N,\parallel}$ [mOe^{-1}]	$\chi_{N,\perp}$ [mOe^{-1}]
I, as prep.	0.200	0.059	56.72	44.40	2.95	1.43
I, 20 min	0.297	0.039	84.63	56.60	3.30	0.80
I, 40 min	0.333	0.067	100.51	63.17	3.38	0.82
I, 60 min	0.478	0.096	242.60	73.99	2.17	1.38
II, as prep.	0.028	0.010	10.69	10.02	2.65	1.01
II, 20 min	−0.018	0.007	−6.27	5.76	2.84	1.23
II, 40 min	0.004	0.021	1.27	20.64	3.01	1.02
II, 60 min	0.060	0.010	18.40	11.70	3.23	0.85

In order to ensure that the observed changes in the hysteretic behavior cannot be attributed to changes of the particle morphology due to the impact of the plasma, the particle shape was analyzed. The sample used for this analysis was prepared in a dropping procedure with species I and, consequently, exposed to the hydrogen plasma for three hours. The sample was covered by a thin Pt layer of 15 nm thickness to prevent oxidation of the Co particles. A scanning microscopy image taken along the particle plane reveals a situation similar to Figure 1. However, this observation does not exclude a deformation along the out-of-plane direction such as the flattening of the spheres towards ellipsoidal colloids.

For the imaging of a particle cross section along the out-of-plane axis, a thin sample lamella was prepared with a FEI Helios Dual Beam FIB by cutting through a suitable particle agglomeration. The lamella was subsequently thinned down to a thickness of 20 nm. In order to protect the particles from contamination and possible ablation by gallium ions, an additional thin protective layer of platinum was deposited with the electron beam before the preparation process. A scanning transition electron microscopy (STEM) image of the cross section is shown in Figure 3a, and the different material regimes are highlighted in Figure 3b to aid understanding. The area on the bottom of the figure (red) shows the Si wafer. Particles on top of the substrate (blue) are covered by a thin layer of Pt of approximately 15 nm thickness (green), to prevent oxidation, and an additional 15 nm Pt layer (bright green) deposited before cutting the lamella, to protect the sample from ablation by gallium ions. During the deposition, carbon inclusions are created, which can be seen as dark spots along the corresponding area. As highlighted in Figure 3b, Co particles maintain their spherical shape. Therefore, the observations described above cannot be related to topological changes.

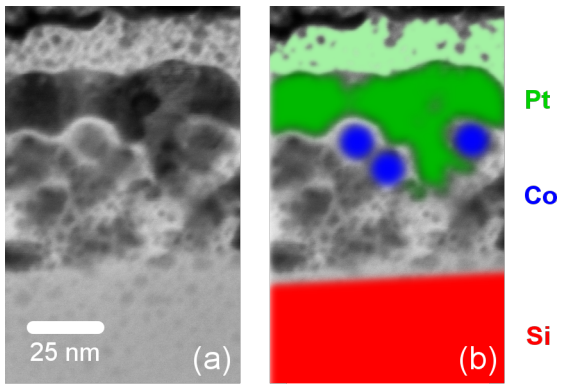

Figure 3: (a) STEM image of the cross section of a plasma-treated sample. (b) As highlighted, the Co particles maintain their spherical shape. The spots in the top Pt layer refer to carbon inclusions due to the preparation process.

XRD measurements

By annealing wet-chemically synthesized FePt nanoparticles at a temperature of 600 °C, Antoniak et al. [20] found evidence for the partial formation of the chemically ordered $L1_0$ state, which entailed a significant increase of the coercive field by a factor of 6 after thermal treatment. With the pure Co particles studied in this work, local composition variations within individual particles may not be at hand; however, Co particles can be found in the hcp-, fcc or ε-crystallographic phases [21]. In order to understand the different behaviors of sample I and II, the crystallographic structures were analyzed by XRD measurements before and after plasma treatment.

The measurements reveal that species II can be found in an ε-phase, while sample I is ordered on an hcp-lattice (Figure 4). The arrows indicate the expected peak positions of the fcc-phase (44.22° (111), 51.52° (200), 75.86° (220), 92.23° (311), 97.66° (222)), which are not present in either sample. According to the XRD data, no phase transition during plasma exposure is observed. This is in accordance with the findings by Sun and Murray [22] who reported the transitions between the different crystallographic phases ε-Co → hcp-Co and hcp-Co → fcc-Co to have activation temperatures of about 300 and 500 °C, respectively.

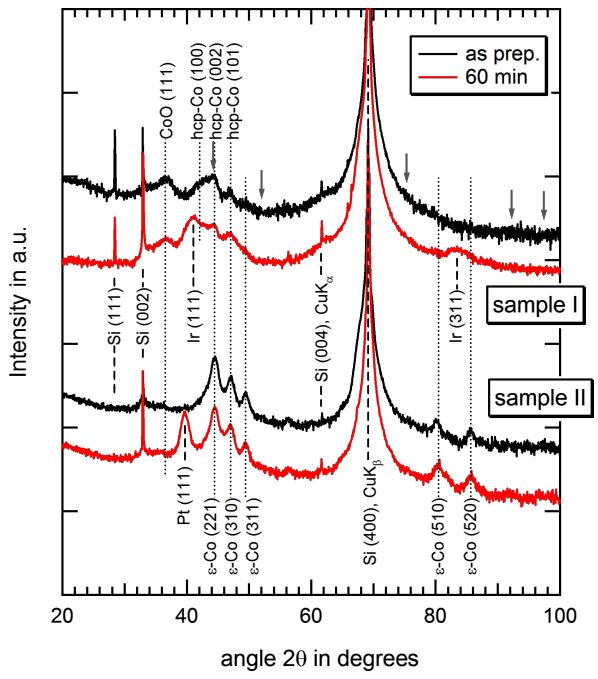

Figure 4: XRD measurements of sample I (top) and sample II (bottom) before (red) and after (blue) hydrogen-plasma treatment. Particle species I shows an hcp order while sample II is crystallized in the ε-phase. No evidence of an fcc-Co phase can be found; the gray arrows in the top plot indicate the expected peak positions. Further, each phase maintains its stability during plasma treatment.

Numerical model

In order to obtain a qualitative understanding of the microscopic origin of the experimental findings, simulations of two-dimensional particle arrays are carried out. Since particles of the given size are superparamagnetic, they are homogeneously magnetized along their volume. Therefore, each individual particle may be approached by its magnetic moment $\boldsymbol{m}_i = M_S V_P \hat{\boldsymbol{m}}_i$, with M_S being the saturation magnetization of the material, V_P the particle volume and $\hat{\boldsymbol{m}}_i$ the angular components. The equilibrium state of a system of ferromagnetic components is a solution of [23]

$$\hat{\boldsymbol{m}} \times \boldsymbol{H}_{\text{eff}} = \boldsymbol{0} \tag{2}$$

$$\boldsymbol{H}_{\text{eff}} = \frac{2A}{\mu_0 M_S}\Delta\hat{\boldsymbol{m}} - \frac{1}{\mu_0 M_S}\frac{\delta f_{\text{ani}}(\hat{\boldsymbol{m}})}{\delta\hat{\boldsymbol{m}}} + \boldsymbol{H}_{\text{demag}} + \boldsymbol{H}_{\text{ext}}. \tag{3}$$

The first term of Equation 3 corresponds to the magnetic exchange energy with the exchange constant A. Since single-domain particles are considered, no variations of the magnetization can be found along the magnetic volume, and therefore, this contribution equals 0. The second term refers to magnetocrystalline anisotropy with f_{ani} being the anisotropy energy functional. In order to study the influence of anisotropy effects, we will assume two different types of anisotropy: (a) uniaxial anisotropy, in which the crystal structure has an energetically favorable direction, the easy axis $\boldsymbol{k}$; and (b) cubic anisotropy. The respective energy functionals are given by

$$f_{\text{ani}}^{\text{uni}} = K_{\text{u}}\langle\hat{\boldsymbol{m}}, \boldsymbol{k}\rangle^2 \tag{4}$$

$$f_{\text{ani}}^{\text{cub}} = K_{\text{c}}(m_x^2 m_y^2 + m_y^2 m_z^2 + m_z^2 m_x^2) \tag{5}$$

with the anisotropy constants K_{u}, K_{c} and the Euclidean inner product $\langle\cdot,\cdot\rangle$. The corresponding energy surfaces in dependency on the solid angle are shown at the top of Figure 5 (see below).

A particle at position $\boldsymbol{R}_i$ creates a magnetic stray field at every space point $\boldsymbol{r}$. Due to its magnetic single-domain structure, the magnetic field is described by a dipolar approximation. Therefore, the j-th particle at position $\boldsymbol{R}_j$ feels a field given by the superposition of all other field contributions

$$H_{\text{ext,p}}^{j} = \frac{M_{\text{S}} V_{\text{P}}}{4\pi}\sum_{i\neq j}\left(\frac{3\langle\hat{\boldsymbol{m}}_i, \boldsymbol{r}_{ij}\rangle\boldsymbol{r}_{ij}}{r_{ij}^5} - \frac{\hat{\boldsymbol{m}}}{r_{ij}^3}\right) \tag{6}$$

with $\boldsymbol{r}_{ij} = \boldsymbol{R}_j - \boldsymbol{R}_i$ being the distance vector and $r_{ij} = |\boldsymbol{r}_{ij}|$ its absolute value. Due to a rapid decrease with distance, not all particles need to be taken into account, but it is sufficient to restrict the analysis to contributions from particles at a distance smaller than 7.5 times the average particle radius of the system. This threshold value is in accordance with the findings of Schaller et al. [24]. The total external-field contribution acting on a particle is given by the sum of Equation 6 and an additional homogeneous-field contribution applied to bring particles to magnetic saturation. Finally, the third term of Equation 3 can be omitted since the demagnetization field $\boldsymbol{H}_{\text{demag}}$ of a homogeneously magnetized sphere is antiparallel to the magnetization vector $\hat{\boldsymbol{m}}$ and, consequently, we always have $\hat{\boldsymbol{m}} \times \boldsymbol{H}_{\text{demag}} = 0$.

Assumptions

With $\hat{\boldsymbol{m}}$ constant on each individual particle, Equation 3 is transformed from a set of partial differential equations to a set of ordinary ones. A solution is obtained by consideration of its time-dependent extension [25]

$$\hat{\boldsymbol{m}} \times \boldsymbol{H}_{\text{eff}} = -\frac{1}{\gamma}\left(\frac{\partial\hat{\boldsymbol{m}}}{\partial t} - \alpha\hat{\boldsymbol{m}} \times \frac{\partial\hat{\boldsymbol{m}}}{\partial t}\right) \tag{7}$$

with γ the gyromagnetic ratio and α a dimensionless damping constant. The microscopic relaxation occurs on time scales significantly shorter than the time scales on which external fields change. Therefore, the microscopic dynamics are not in the scope of this work and the value of the damping parameter may be adjusted to provide a high numerical convergence rate. We chose α = 1 [26]. For the integration with respect to time, a backward differential formula of fifth order is applied. As a model system, we consider a two-dimensional, 10 × 10 particle lattice of hexagonal symmetry with a lattice constant of 18 nm, which was taken from the experiments. Furthermore, the particle diameter and magnetization are set to d = 13 nm and M_{S} = 900 kA/m [27], respectively. In order to analyze the influence of the magnetocrystalline anisotropy, uniaxial and cubic scenarios according to Equation 4 and Equation 5 with the respective choices of anisotropy constants K_{u} = 50, 100 and 150 kJ/m^3 and K_{c} = 30 and 50 kJ/m^3 are studied. The bulk values of fcc and hcp Co cubic anisotropy constants lie in the range of 27 to 45 kJ/m^3 [28]. For particles at the edges of the lattice, periodic boundary conditions are employed.

Examples of the equilibrium states of such systems are shown in Figure 5, for different cases: (a) amorphous particles, (b) particles with a randomly oriented uniaxial anisotropy, K_{u} = 50 kJ/m^3, and (c) particles with a randomly oriented cubic

anisotropy, K_c = 30 kJ/m^3. For each subplot, the upper part shows the in-plane magnetic component (color-code: disc) and the lower the out-of plane component (color-code: cone). The surfaces in the upper right corner of subplots (b) and (c) represent the angular energy distribution of uniaxial and cubic anisotropy, where blue areas correspond to the energy minima (easy axes) and red ones to maxima (hard axes).

For magnetically amorphous particles (Figure 5a), the spatial confinement in two dimensions entails the alignment of the magnetic moments parallel to the particle plane. Contiguous magnetic moments are likely to align parallel or antiparallel to each other. Such a configuration minimizes the stray-field energy of the system. For uniaxial anisotropy (Figure 5b), the magnetic moments partially follow the easy axis and, therefore, show a significantly higher z-component whenever the easy axis $\hat{\boldsymbol{k}}$ is perpendicular to the particle assembly. In comparison, with an increased number of such axes, the probability of an energetically favorable direction parallel to the particle plane is higher in the case of cubic magnetocrystalline anisotropy. Consequently, the z-component of individual magnetic moments lies between the amorphous and the uniaxial case (Figure 5c).

For the uniaxial settings, the distribution of the anisotropy vectors $\hat{\boldsymbol{k}}$ is chosen in three different ways:

1. equally random on the unit sphere in three dimensions,
2. equally random on the section of the three-dimensional unit sphere that includes an angle α with the xy-plane between $-45° < \alpha < 45°$,
3. and equally random on the two-dimensional unit sphere in the xy-plane.

For the systems with cubic anisotropy, two different distributions are studied:

1. easy axes are randomly distributed,
2. one easy direction coincides with the axis perpendicular to the particle plane.

Both cases are schematically shown in the insets of Figure 6. These choices are motivated by the equilibrium state for amorphous particles aligning their magnetic moment parallel to the

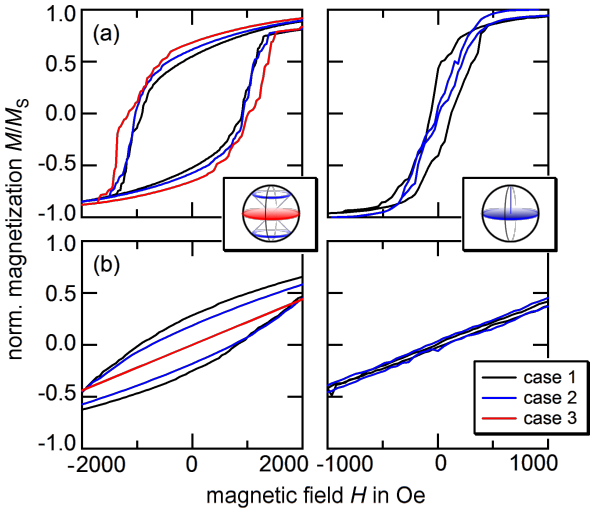

Figure 6: Hysteresis loops of the 10 × 10 hexagonal lattices shown in Figure 5 for different anisotropy cases obtained from numerical calculations. (a) and (b) show the behavior of particles with a uniaxial anisotropy and K_u = 10^5 J/m^3 for in-plane and out-of-plane external fields; (c) and (d) show the respective results for cubic anisotropy with K_c = 3 × 10^4 J/m^3. The insets visualize the different choices for the distribution of easy axes.

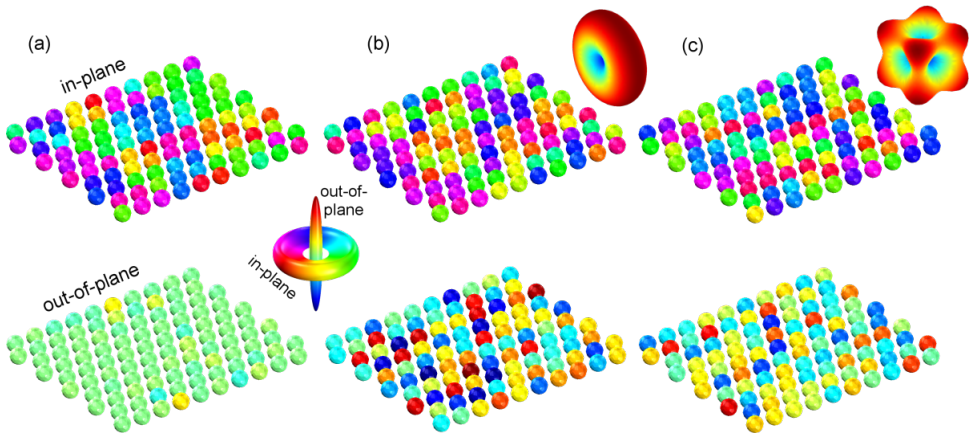

Figure 5: Equilibrium state of the model system. Particles of 13 nm size assembled in a hexagonal lattice with a grid constant of 18 nm and a saturation magnetization of M_S = 900 kA/m. Subplots show different anisotropy scenarios: (a) amorphous, (b) uniaxial and (c) cubic magnetocrystalline anisotropy. The surfaces in the upper-right corner of (b) and (c) represent the angular energy distribution of the respective anisotropy scenario where blue areas correspond to energy minima (easy axes) and red to maxima (hard axes). The upper plots present the in-plane component of the magnetic moments (color-code: disc), the lower ones the out-of-plane component (color-code: cone).

particle plane (Figure 5). After preparation of the samples, the magnetocrystalline orientations are randomly distributed along the sample. Similar to the microscopic ordering during annealing, see e.g. [29], the crystallographic orientation may change under plasma treatment following the magnetic stress induced by the stray fields of contiguous particles. The mechanism is comparable to mechanical creep under tension with the hydrogen plasma acting as the thermal actuator. With the stray-field energy minimum obtained for an in-plane magnetic configuration, the easy magnetocrystalline axes of individual particles should migrate into the particle plane, resembling the respective choices made above. In order to analyze the hysteretic behavior, an alternating external field $\boldsymbol{H}_{\mathrm{eff}}$ in the x- and z-direction is considered.

Results and Discussion

Typical hysteresis loops, which result from the numerical analysis are shown in Figure 6; remanent magnetization M_{R}, coercive field H_{C}, and magnetization change at $H = H_{\mathrm{C}}$ are given in Table 2 for various magnetocrystalline anisotropy assumptions. We begin our discussion with the case of uniaxial anisotropy: For in-plane measurements, remanent magnetization and coercive field increase with decreasing average $\langle k_z \rangle$. This is in agreement with the experimental findings. The increasing in-plane alignment of the magnetocrystalline easy axes results in a higher stability of the magnetic states and the particle assembly exhibits an increasingly harder magnetic behavior. For perpendicular external fields, the opposite tendency can be observed. The corresponding values drop down to zero and the system behaves similarly to a paramagnet. The effective anisotropy of geometrical and magnetocrystalline contributions has no longer an out-of-plane contribution, and therefore, the z-component of individual magnetic moments resembles a behavior similar to the amorphous state shown in Figure 5a, bottom. The derivative $\chi_{\mathrm{N},\parallel}$ does not show a clear tendency for the in-plane evaluation, which is due to a step-like decrease/increase of the magnetization with respect to the applied field; the appearance of hard shoulders will be discussed below. For the out-of-plane case, a decreasing $\chi_{\mathrm{N},\perp}$ with decreasing $\langle k_z \rangle$ may be reported. These results are independent of the value of the anisotropy constant. However, with higher anisotropy constants, in-plane and out-of-plane data obtain similar values, i.e., the anisotropy energy becomes the dominant contribution and overcomes the dipolar coupling.

For cubic systems, the components of remanent magnetization and coercive field are significantly lower. The higher number of easy axes provides a less restrictive energy landscape in the sense that distinct energy minima are separated by lower energy barriers, which entails a softer switching behavior. Depending on the choice of the anisotropy constant K_{c}, the in-plane magnetization may increase or decrease with a higher order of the magnetocrystalline easy axes. For low values, switching between different magnetic configurations is enhanced, which coincides with the case of the ε-Co phase employed in species II [8].

In general, the obtained values for the remanent magnetization and coercive field are much higher than the experimental observations. Further, the hysteresis loops do not exhibit smooth characteristics but show multiple step-like jumps. These effects may be attributed to various simplifications of the simulations: (a) Temperature was not taken into account, which entails a higher stability (higher obtained values [30]). (b) In compari-

Table 2: Characteristic magnetic data obtained from numerical calculations for different anisotropy cases. The remnant magnetization of particle species II is close to 0, which indicates the superparamagnetic behavior as mentioned before. Sign inversions may be attributed to noise effects such as thermal contributions.

		$M_{\mathrm{R},\parallel}$ [M_{S}]	$M_{\mathrm{R},\perp}$ [M_{S}]	$H_{\mathrm{C},\parallel}$ [Oe]	$H_{\mathrm{C},\perp}$ [Oe]	$\chi_{\mathrm{N},\parallel}$ [mOe^{-1}]	$\chi_{\mathrm{N},\perp}$ [mOe^{-1}]
uniaxial 1	50	0.6485	0.1403	408.56	370.65	6.26	0.47
uniaxial 2	50	0.7084	0.1155	427.98	348.27	6.88	0.35
uniaxial 3	50	0.7095	≈0	473.42	≈0	3.41	0.34
uniaxial 1	100	0.5356	0.2673	906.03	884.72	2.97	0.34
uniaxial 2	100	0.5952	0.1841	976.00	746.60	3.67	0.30
uniaxial 3	100	0.6682	≈0	1087.49	≈0	1.04	0.22
uniaxial 1	150	0.5400	0.3366	1527.03	1534.88	3.48	0.40
uniaxial 2	150	0.6048	0.2429	1480.74	1210.44	2.60	0.23
uniaxial 3	150	0.6198	≈0	1661.77	≈0	1.36	0.17
cubic 1	30	0.4205	0.0151	92.95	36.35	4.67	0.49
cubic 2	30	0.4216	0.0573	225.26	169.82	4.84	0.47
cubic 1	50	0.0457	0.0467	9.93	80.34	9.93	0.46
cubic 2	50	0.0470	0.1266	20.13	404.84	2.26	0.45

son to the experimental system, only a small number of particles was modeled. The appearance of small domains (compare Figure 5) that switch as a whole entails hard shoulders in the hysteresis curves. (c) The assumption of a perfect grid entails anisotropic response functions [31]. In the experimental realization, the data resemble the average taken over all measuring directions due to arbitrarily oriented particle grains. Finally, (d) a small degree of the sample area is not covered by a monolayer, but multilayers/particle clusters can be found instead. Even though they are only present on a very low area ratio, they may still contain a high number of particles. This particularity diminishes the observed effects and results in an increased $\langle k_z \rangle$ in these areas.

Conclusion

The exposure of magnetic Co nanoparticles to hydrogen plasma entails an alteration of the magnetic sample response. From XRD analysis, we were able to conclude that the plasma has no impact on the crystallographic phase, and STEM images of the particle cross sections revealed an unaffected particle shape. By comparison to numerical data obtained by solving the stationary micromagnetic equations, we proposed a model for the influence of the plasma treatment on the microscopic structure. The magnetocrystalline easy axes of individual particles align with the stray field of contiguous nanocrystals. The process is comparable to the time-dependent creep under tension with the plasma acting as the thermal activation.

For uniaxial magnetocrystalline anisotropy, the migration of the magnetocrystalline easy axes results in an increase of the effective sample anisotropy, which entails a hard switching behavior for in-plane measurements and a soft paramagnetic one for out-of-plane measurements. For cubic symmetry, the in-plane hysteresis decreases over time due to a higher number of energy minima within the particle plane.

Acknowledgements

The authors would like to thank N. Mill and C. Waltenberg for the preparation of magnetic nanoparticles and the FOR 945 for financial support in the framework of project K3. Furthermore, Alexander Weddemann gratefully acknowledges the scholarship from the Alexander von Humboldt foundation.

References

1. Hütten, A.; Sudfeld, D.; Ennen, I.; Reiss, G.; Hachmann, W.; Heinzmann, U.; Wojczykowski, K.; Jutzi, P.; Saikaly, W.; Thomas, G. *J. Biotechnol.* **2004,** *112,* 47–63. doi:10.1016/j.jbiotec.2004.04.019
2. Reiss, G.; Hütten, A. *Nat. Mater.* **2005,** *4,* 725–726. doi:10.1038/nmat1494
3. Hütten, A.; Sudfeld, D.; Ennen, I.; Reiss, G.; Wojczykowski, K.; Jutzi, P. *J. Magn. Magn. Mater.* **2005,** *293,* 93–101. doi:10.1016/j.jmmm.2005.01.048
4. Ambashta, R. D.; Yusuf, S. M.; Mukradam, M. D.; Singh, S.; Wattal, P. K.; Bahadur, D. *J. Magn. Magn. Mater.* **2005,** *293,* 8–14. doi:10.1016/j.jmmm.2005.01.036
5. Vadala, M. L.; Zalich, M. A.; Fulks, D. B.; St. Pierre, T. G.; Dailey, J. P.; Riffle, J. S. *J. Magn. Magn. Mater.* **2005,** *293,* 162–170. doi:10.1016/j.jmmm.2005.01.056
6. Woo, K.; Hong, J.; Ahn, J.-P. *J. Magn. Magn. Mater.* **2005,** *293,* 177–181. doi:10.1016/j.jmmm.2005.01.058
7. Theis-Bröhl, K.; Wolff, M.; Ennen, I.; Dewhurst, C. D.; Hütten, A.; Toperverg, B. P. *Phys. Rev. B* **2008,** *78,* 134426. doi:10.1103/PhysRevB.78.134426
8. Sun, S.; Murray, C. B.; Weller, D.; Folks, L.; Moser, A. *Science* **2000,** *287,* 1989–1992. doi:10.1126/science.287.5460.1989
9. Sohn, B.-H.; Choi, J.-M.; Yoo, S. I.; Yun, S.-H.; Zin, W.-C.; Jung, J. C.; Kanehara, M.; Hirata, T.; Teranishi, T. *J. Am. Chem. Soc.* **2003,** *124,* 6368–6369. doi:10.1021/ja035069w
10. Ghazali, A.; Lévy, J.-C. *Phys. Rev. B* **2003,** *67,* 064409. doi:10.1103/PhysRevB.67.064409
11. Levesque, D.; Weis, J. J. *Phys. Rev. E* **1994,** *49,* 5131–5140. doi:10.1103/PhysRevE.49.5131
12. Moser, A.; Takano, K.; Margulies, D. T.; Albrecht, M.; Sonobe, Y.; Ikeda, Y.; Sun, S.; Fullerton, E. E. *J. Phys. D: Appl. Phys.* **2002,** *35,* R157–R167. doi:10.1088/0022-3727/35/19/201
13. Sun, S. *Adv. Mater.* **2006,** *18,* 393–403. doi:10.1002/adma.200501464
14. Puntes, V. F.; Krishnan, K. M.; Alivisatos, A. P. *Science* **2001,** *291,* 2115–2117. doi:10.1126/science.1058495
15. Kanninen, P.; Johans, C.; Merta, J.; Kontturi, K. *J. Colloid Interface Sci.* **2008,** *318,* 88–95. doi:10.1016/j.jcis.2007.09.069
16. Auge, A.; Weddemann, A.; Vogel, B.; Wittbracht, F.; Hütten, A. *Appl. Phys. Lett.* **2010,** *96,* 093111. doi:10.1063/1.3353957
17. Ethirajan, A.; Wiedwald, U.; Boyen, H.-G.; Kern, B.; Han, L.; Klimmer, A.; Weigl, F.; Kästle, G.; Ziemann, P.; Fauth, K.; Cai, J.; Behm, J.; Romanyuk, A.; Oelhafen, P.; Walther, P.; Biskupek, J.; Kaiser, U. *Adv. Mater.* **2007,** *19,* 406–410. doi:10.1002/adma.200601759
18. Wiedwald, U.; Fauth, K.; Heßler, M.; Boyen, H.-G.; Weigl, F.; Hilgendorff, M.; Giersig, M.; Schütz, G.; Ziemann, P.; Farle, M. *ChemPhysChem* **2005,** *6,* 2522–2526. doi:10.1002/cphc.200500148
19. Spasova, M.; Wiedwald, U.; Farle, M.; Radetic, T.; Dahmen, U.; Hilgendorff, M.; Giersig, M. *J. Magn. Magn. Mater.* **2004,** *272–276,* 1508–1509. doi:10.1016/j.jmmm.2003.12.237
20. Antoniak, C.; Lindner, J.; Spasova, M.; Sudfeld, D.; Acet, M.; Farle, M.; Fauth, K.; Wiedwald, U.; Boyen, H.-G.; Ziemann, P.; Wilhelm, F.; Rogalev, A.; Sun, S. *Phys. Rev. Lett.* **2006,** *97,* 117201. doi:10.1103/PhysRevLett.97.117201
21. Dinega, D. P.; Bawendi, M. G. *Angew. Chem., Int. Ed.* **1999,** *38,* 1788–1791. doi:10.1002/(SICI)1521-3773(19990614)38:12<1788::AID-ANIE1788>3.0.CO;2-2
22. Sun, S.; Murray, C. B. *J. Appl. Phys.* **1999,** *85,* 4325–4330. doi:10.1063/1.370357
23. Landau, L. D.; Lifshitz, E. *Phys. Z. Sowjetunion* **1935,** *8,* 153–169.
24. Schaller, V.; Wahnström, G.; Sanz-Velasco, A.; Gustafsson, S.; Olsson, E.; Enoksson, P.; Johansson, C. *Phys. Rev. B* **2009,** *80,* 092406. doi:10.1103/PhysRevB.80.092406
25. Laroze, D.; Vargas, P.; Cortes, C.; Gutierrez, G. *J. Magn. Magn. Mater.* **2008,** *320,* 1440–1448. doi:10.1016/j.jmmm.2007.12.010
26. Weddemann, A.; Auge, A.; Kappe, D.; Wittbracht, F.; Hütten, A. *J. Magn. Magn. Mater.* **2010,** *322,* 643–646. doi:10.1016/j.jmmm.2009.10.031

27. Ennen, I. Magnetische Nanopartikel als Bausteine für granulare Systeme : Mikrostruktur, Magnetismus und Transporteigenschaften. Ph.D. Thesis, Bielefeld University, Germany, 2008.
28. Jamet, M.; Dupuis, V.; Mélinon, P.; Guiraud, G.; Pérez, A.; Wernsdorfer, W.; Traverse, A.; Baguenard, B. *Phys. Rev. B* **2000,** *62,* 493–499. doi:10.1103/PhysRevB.62.493
29. Müller, M.; Albe, K. *Beilstein J. Nanotechnol.* **2011,** *2,* 40–46. doi:10.3762/bjnano.2.5
30. Wiedwald, U.; Han, L.; Biskupek, J.; Kaiser, U.; Ziemann, P. *Beilstein J. Nanotechnol.* **2010,** *1,* 24–47. doi:10.3762/bjnano.1.5
31. Weddemann, A.; Ennen, I.; Regtmeier, A.; Albon, C.; Wolff, A.; Eckstädt, K.; Mill, N.; Peter, M. K.-H.; Mattay, J.; Plattner, C.; Sewald, N.; Hütten, A. *Beilstein J. Nanotechnol.* **2010,** *1,* 75–93. doi:10.3762/bjnano.1.10

License and Terms

Beilstein Journal of Nanotechnology

Plasticity of Cu nanoparticles: Dislocation-dendrite-induced strain hardening and a limit for displacive plasticity

Antti Tolvanen*[1,2] and Karsten Albe[1]

Full Research Paper

Open Access

Address:
[1]Technische Universität Darmstadt, Institut für Materialwissenschaft, Fachgebiet Materialmodellierung, Petersenstr. 32, 64287 Darmstadt, Germany and [2]Department of Physics, FIN-0014 University of Helsinki, PO Box 43, Helsinki, Finland

Email:
Antti Tolvanen* - tolvanen@mm.tu-darmstadt.de

* Corresponding author

Keywords:
dislocation interactions; mechanical properties; molecular dynamics; nanoparticle; simulation

Beilstein J. Nanotechnol. **2013,** *4,* 173–179.
doi:10.3762/bjnano.4.17

Received: 10 October 2012
Accepted: 12 February 2013
Published: 07 March 2013

This article is part of the Thematic Series "Advances in nanomaterials".

Guest Editors: H. D. Gleiter and T. Schimmel

Abstract

The plastic behaviour of individual Cu crystallites under nanoextrusion is studied by molecular dynamics simulations. Single-crystal Cu fcc nanoparticles are embedded in a spherical force field mimicking the effect of a contracting carbon shell, inducing pressure on the system in the range of gigapascals. The material is extruded from a hole of 1.1–1.6 nm radius under athermal conditions. Simultaneous nucleation of partial dislocations at the extrusion orifice leads to the formation of dislocation dendrites in the particle causing strain hardening and high flow stress of the material. As the extrusion orifice radius is reduced below 1.3 Å we observe a transition from displacive plasticity to solid-state amorphisation.

Introduction

In macroscopic metals, the plastic flow is carried by the continuous movement, multiplication, and entanglement of mobile dislocations. As system size decreases, the relative surface (nanoparticle) or interface area (nanograined material) increases, and nucleation or annihilation of dislocations at surfaces or interfaces becomes a dominant factor since conventional dislocation sources, such as Frank–Read sources, are suppressed. This is commonly cited as the reason for the high mechanical strength of nanoscale materials [1].

Nanoscale systems also exhibit modes of plasticity not encountered in their macroscopic counterparts. Nanowires, for example, tend to respond to high tensile strain rates by amorphisation [2] attributed to the kinetic energy of atoms exceeding the enthalpy of fusion [3]. Also, a near-surface nanodisturbance path, where, instead of conventional displacive plasticity, nanoscopic areas of plastic shear accommodate the stress, was reported for Ag nanowires at high stresses and zero temperatures [4]. Non-close-packed nanostructures have been reported to deform by phase-transitions to a higher density phase. A limit of displacive plasticity leading to a phase-transition path was reported for Si nanospheres [5] concluding that in ultrasmall structures, where dislocation activity is suppressed, this path should dominate. Also in the tensile testing of twinned fcc Fe

nanowires, a phase-transition path was reported as the dislocation activity is suppressed by the dense twin boundaries [6]. These findings raise a question: could there also be a size limit for the displacive plasticity of fcc metals?

Even though individual metal nanocrystallites would seem the simplest possible system in which to study nanoscale plasticity, they have not been well studied. One reason for this has been the complicated methods required to experimentally probe these systems. In a recent development, Sun et al. [7] reported a method in which individual nanocrystals are embedded inside nano-onions and pressurised by the contraction of the graphitic shells under electron irradiation. The contraction stems from the remarkable self-healing of the hexagonal network of carbon atoms as in fullerenes, carbon nanotubes, and graphene [8,9].

These nano-onions contract by electron-irradiation-induced defect formation and can exert forces in the gigapascal range on the encapsulated system. A hole punctured during the pressurisation allows the material to flow out after a threshold pressure, depending on the material properties, is reached. In their pioneering work, Sun et al. [7] studied the extrusion of Ag nanoparticles experimentally and attributed the plastic flow to dislocation activity, based on a combination of simulation results on Pt showing traces of dislocation activity (stacking faults within the encapsulated material even though the extruded material was not crystalline) and thermodynamical arguments stating the insufficient speed of diffusion for vacancy-assisted creep in the experimental system. Yet, neither dislocation nucleation nor dislocation interactions were observed in the computational study.

In this paper, we study the plasticity of Cu nanocrystallites in nanoextrusion. We show that dislocation pileup leading to the formation of dislocation dendrites inside the particle leads to strain hardening and limits the plastic flow. This supports the observed dislocation accumulation in nanograined materials [10,11]. We report novel dislocation interactions activated by the high pressure and dislocation density, and low dislocation length in the nanoparticle. We also show that the dislocation activity becomes suppressed as the extrusion hole radius is reduced to 12 Å and the mode of plasticity is changed from displacive to surface amorphisation.

Results and Discussion

Depending on the orifice radius, the mode of plasticity is either displacive or driven by surface amorphisation (see Figure 1 and Supporting Information File 1, and Supporting Information File 2). We start our analysis by presenting the details of the displacive case.

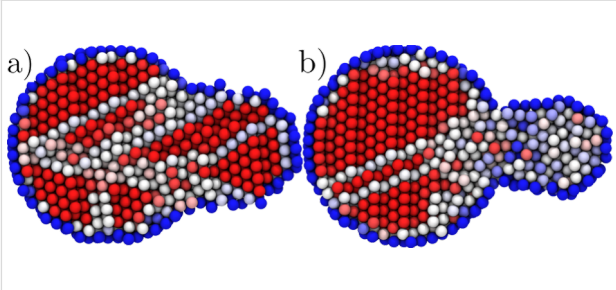

Figure 1: Two observed modes of plasticity. (a) Snapshot of the extrusion from a 15.6 Å orifice showing the displacive plasticity (b) The same from a 11.6 Å orifice showing the amorphous region about the orifice. Atoms coloured by the centrosymmetry parameter, from red (= 0, fcc) to blue (>25, surface).

The maximum shear component (the maximum eigenvalue of the atomic stress tensor) in the initial system and at the onset of plasticity for different orientations for a 15.6 Å orifice is illustrated in Figure 2a–Figure 2c. For all the orientations, larger than average values of maximum shear are roughly localised on inverted spherical caps joining the edge of the circular orifice.

The most extreme values of the atomic shear (parallel 2.4 MPa, orthogonal 2.3 MPa, and tilted 2.3 MPa) are almost the same and are located at the intersection of the orifice and the surface where the dislocations are nucleated. Before the onset of plasti-

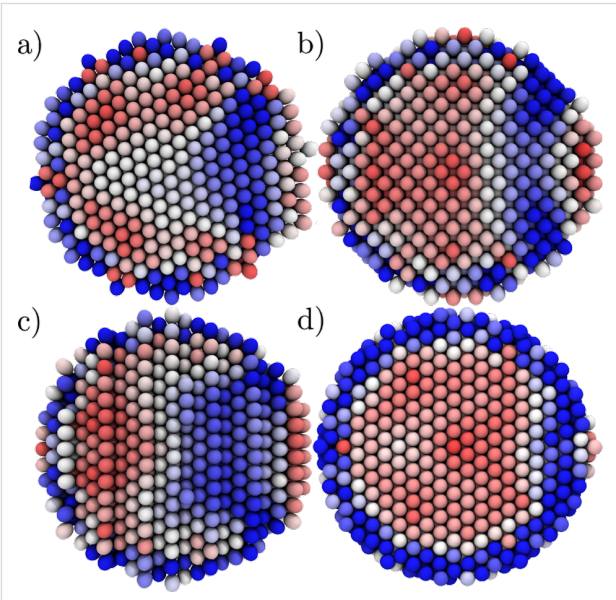

Figure 2: The maximum shear component of the atomic stress tensor expressed by the colouring of the atoms (colouring from red (= 0) to blue (>1 GPa)). (a–c) 15.6 Å orifice (displacive mode). (d) 11.6 Å orifice (surface amorphisation). (a) {111} planes oriented parallel to the extrusion direction. (b) {111} planes tilted with respect to the extrusion direction. (c) {111} planes oriented perpendicular to the extrusion direction. (d) {111} planes parallel (as in (a)) at the inset of surface amorphisation. To relieve the stress the systems have slightly rotated inside the force field.

city, the system goes through small rotations to accommodate the stresses changing slightly the initial lattice orientation.

Qualitatively, in the displacive regime, the deformation follows the same route in all our simulations. At the onset of plasticity, multiple dislocations nucleate simultaneously at the surface of the particle near the borders of the extrusion orifice (see Figure S1 in Supporting Information File 3 for illustration of this in different orientations of the system). These dislocations form complicated lock structures, named here dislocation dendrites, inside the particle that have to be broken for the plastic flow to continue. As the qualitative behaviour of the system is almost independent of the orientation, we concentrate on the case where the {111} planes are parallel with the extrusion direction (Figure 2a) remarking where the behaviour differentiates depending on the direction.

The stress–strain behaviour of this system during the extrusion process through an orifice of 15.6 Å radius is presented in Figure 3. Before the elastic regime, the system goes through a short plastic phase in which the faceted surface of the particle accommodates the spherical force field. The system yields at 11.9 GPa (2.9% strain, marked as 1 in Figure 3) when two Shockley partials are nucleated 2.5 ps apart (see Figure 4 and Figure 5). The first partial is soon met with a third partial nucleated at the opposite side of the orifice forming a $\frac{1}{6}$<011> stair-rod dislocation ((c) in Figure 4 and Figure 5). Such interactions of partial dislocations in Cu have been reported before as the obstacle for dislocation motion [12]. In the case of the nanoparticle under extreme stress, the stair-rod dislocations do not block the plastic flow, because the continuous nucleation–interaction–unzipping cycles make the Shockley partial-stair-rod systems unstable.

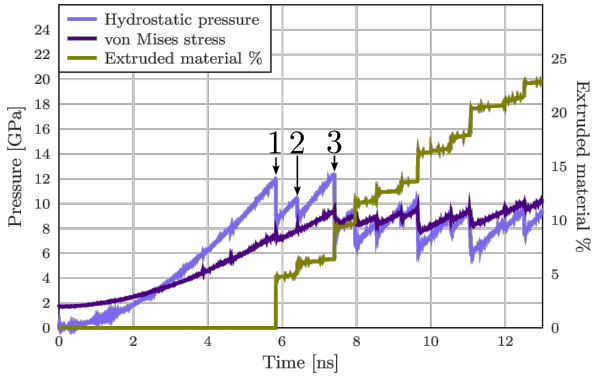

Figure 3: Extrusion from a 15 Å orifice. Hydrostatic pressure, von Mises stress and the amount of extruded material as a function of the simulation time. The nonzero initial value of the von Mises stress is due to the initial shear stresses at the faceted surface of the nanoparticle.

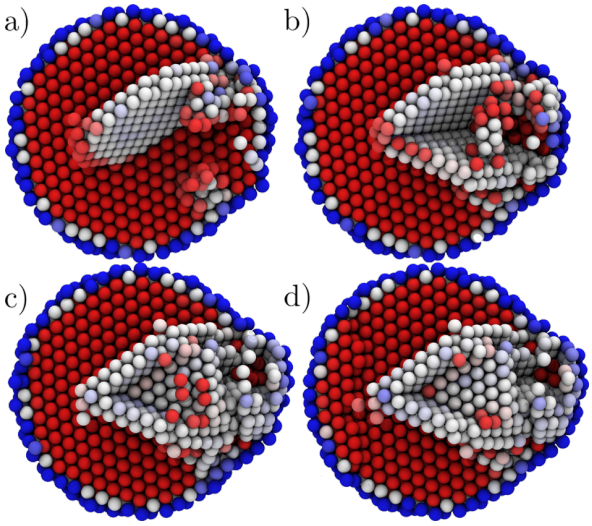

Figure 4: Extrusion from 15 Å orifice. (a) The nucleation of the first Shockley partial. (b) Two nonlocking sessile Shockley partials. (c) A stair rod is formed. (d) The dislocations are pinned to the particle surface through a <312> dislocation.

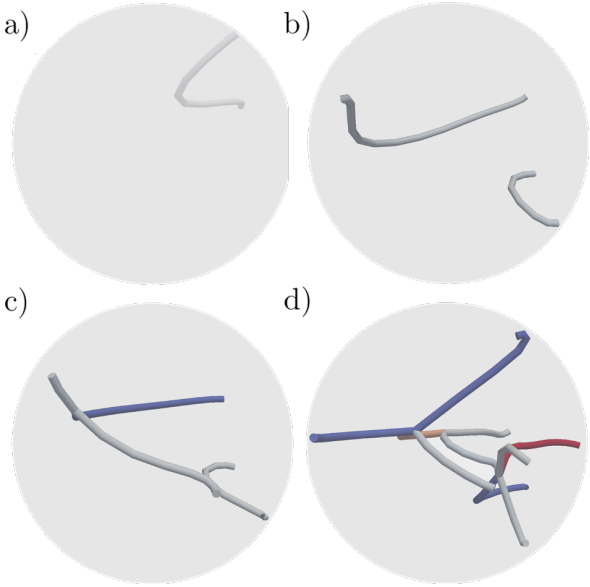

Figure 5: Dislocations interacting at the onset of plasticity. Colouring by the length of the Burgers vectors, red |$\frac{1}{6}$<312>|, grey |$\frac{1}{6}$<112>|, and blue |$\frac{1}{6}$<110>|. (a–b) Shockley partials are nucleated 2.5 ps apart at the onset of plasticity. (c) Nucleation of a third dislocation leads to the formation of a stair-rod dislocation. (d) Nucleation of multiple dislocations leads to the formation of dislocation dendrite inside the particle blocking the dislocation nucleation and motion.

Contrary to the common view of dislocation nucleation and annihilation at the surface of the grain, the dislocations can be stopped inside the particle also independently of any dislocation interaction, as shown in Figure 5b and Figure 5c, in which the second Shockley partial becomes sessile promptly after the nucleation. As the opposing surfaces of the particle are under extreme stress it would be unfavourable to accommodate the strain field associated with the partial approaching the constricted surface. This leads to accumulation of dislocations near the extrusion orifice and to dislocation interactions typically not found in bulk materials. An example of such a situation is presented in Figure 5d in which two stair-rod dislocations and a Shockley partial interact to form an unstable $\frac{1}{6}$<130> dislocation (coloured coral in Figure 5d) ($\frac{1}{6}$<0$\bar{1}\bar{1}$> + $\frac{1}{6}$<0$\bar{1}\bar{1}$> + $\frac{1}{6}$<2$\bar{1}$1> = $\frac{1}{6}$<1$\bar{3}$0>) linking to another pair of partials ($\frac{1}{6}$<2$\bar{1}\bar{1}$> + $\frac{1}{6}$<$\bar{1}$2$\bar{1}$> = $\frac{1}{6}$<1$\bar{3}$0>). A typical feature is the locking of a dislocation multijunction to the particle surface through a $\frac{1}{6}$<312> dislocation (red in Figure 5d) here by a Shockley triple junction and a stair rod ($\frac{1}{6}$<0$\bar{1}\bar{1}$> + $\frac{1}{6}$<12$\bar{1}$> + $\frac{1}{6}$<1$\bar{1}$2> + $\frac{1}{6}$<1$\bar{1}$2> = $\frac{1}{6}$<3$\bar{1}$2>). The system reaches a steady state 35 ps after the onset of plasticity, and the dislocation nucleation and movement becomes locked by a clawlike multijunction reaching the surface at the extrusion orifice (see Figure 6). Also in macroscopic materials, simpler dislocation multijunctions have been reported as a contribution to strain hardening [13].

After locking the dislocations into dislocation dendrites, they have to be broken in order to continue the plastic flow. We observe two distinct breaking mechanisms: Disassociation of dislocations or interaction with new partials nucleated at the surface. Examples of these processes are presented in Figure 7 and Figure 8 (marked as points 2 and 3 in Figure 3). The disassociation mechanism we observe is not an unzipping process as

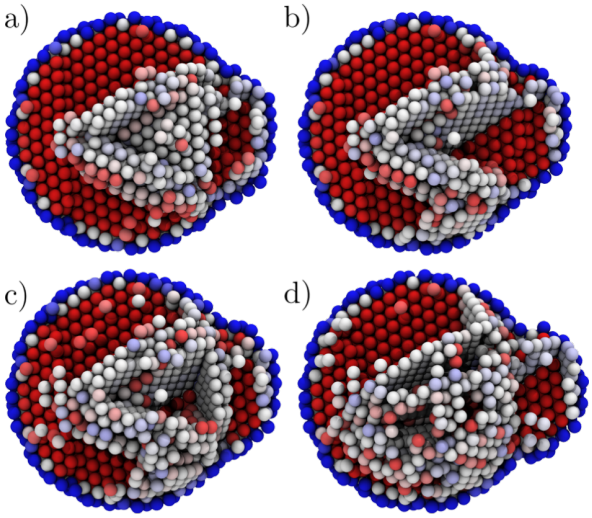

Figure 7: Atomic arrangement during the breaking of the dendrite. (a–b) The locking multijunction (see Figure 6) is broken as the $\frac{1}{6}$<112> partial is disassociated from the junction. (c–d) A partial nucleated at the particle surface (here lower right about the orifice) interacts with the partials in the dendrite pinned to the surface, resulting in a slip.

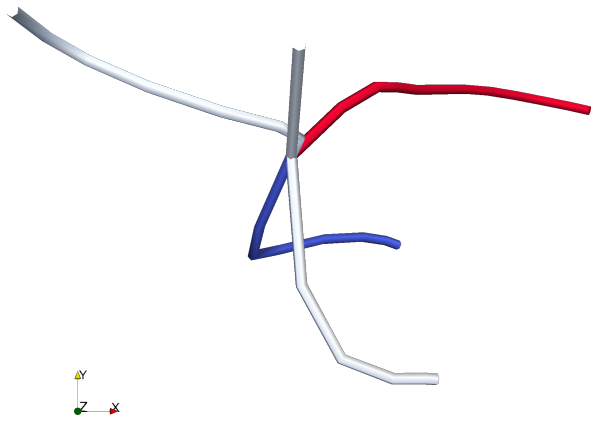

Figure 6: A dislocation multijunction blocking the dislocation mobility and nucleation in the system. Dislocations end at the right side of the figure on the particle surface, and the Shockley partial on the left connects to the other dislocations in the particle. Colouring by the length of the Burgers vectors, red |$\frac{1}{6}$<312>|, grey |$\frac{1}{6}$<112>|, and blue |$\frac{1}{6}$<110>|

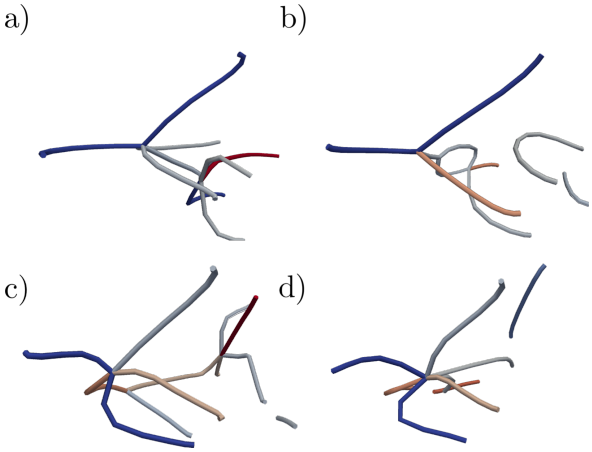

Figure 8: Dislocation interacting to break the dendrite. (a–b) The locking multijunction (see Figure 6) is broken as the $\frac{1}{6}$<112> partial is disassociated from the junction. (c–d) Partial nucleated at the particle surface (here lower right about the orifice) interacts with the partials in the dendrite pinned to the surface, resulting in a slip.

discussed above in the case of the stair-rod dislocations. Here, a partial breaks of from the clawlike structure (Figure 7a and Figure 7b and Figure 8a and Figure 8b) and the remaining $\frac{1}{6}[\bar{1}01]$, $\frac{1}{6}[\bar{1}1\bar{1}]$, $\frac{1}{6}[121]$ and $\frac{1}{6}[312]$ are broken into two partials. Note that the system is on average constantly at the limit of the lattice instability of bulk Cu (≈10 GPa), allowing such violent processes. The nucleation–interaction mechanism is initiated, if in spite of the back stresses of the dislocations locked in the dendrites inside the particle, partials are nucleated at the surface. As an example, in Figure 7c and Figure 7d and Figure 8c and Figure 8d a partial from the surface immediately meets the sessile partials in the dendrite about the orifice, resulting in a slip and a residual stair rod.

When the orifice size is reduced the maximum stress at the onset of plasticity is increased (see Figure 9) but the qualitative behaviour of the system remains the same down to an orifice radius of 12.6 Å. At this point, we observe that the displacive mode of plasticity becomes unfavourable in favour of a surface-amorphisation-induced plastic flow. As an example, we present the results for a parallel system with 11.6 Å orifice radius, see Figure 10 and Figure 1. Here at the onset of plasticity the surface of the particle breaks down leading to a burst of material out of the orifice. Von Mises stress at the onset of plasticity exceeds 1/5 $G \approx 10$ GPa, where $G = 46$ GPa is the shear strength of Cu, suggesting a stress regime above the ideal shear strength, even locally at the orifice.

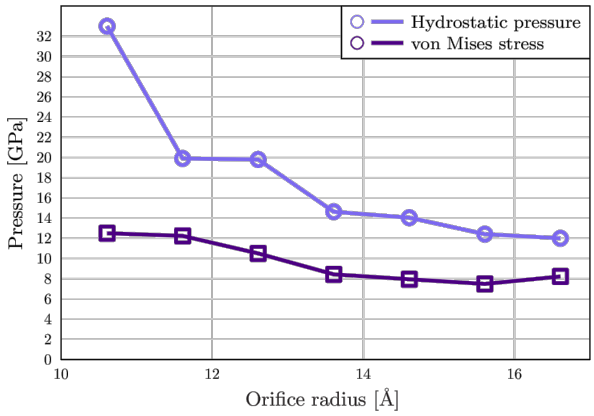

Figure 9: Hydrostatic pressure and von Mises stress at the onset of plasticity versus extrusion orifice radius. Lines are guides for the eye.

An amorphous region is observed at the orifice throughout the whole simulation, and dislocations carry the plasticity only further inside the particle (see Supporting Information File 2). Such behaviour is observed at all radii below 12.6 Å. Why is the surface amorphisation favoured over displacive plasticity? In the fcc phase, the material is at the maximum possible

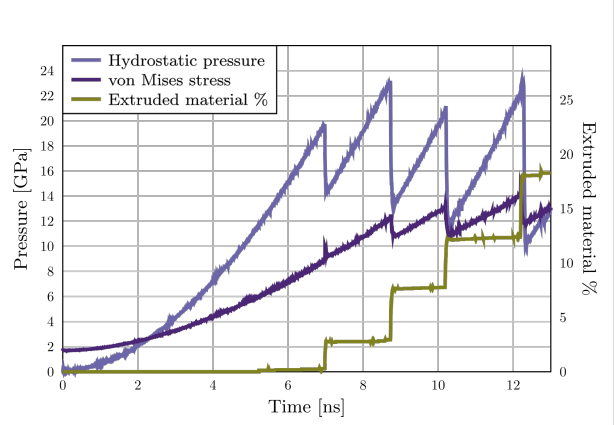

Figure 10: Extrusion from a 11 Å orifice. Hydrostatic pressure, von Mises stress and the amount of extruded material as a function of the simulation time. The nonzero initial value of the von Mises stress is due to the initial shear stresses at the faceted surface of the nanoparticle.

density and amorphisation cannot release the pressure by contraction of the atomic volume. However, in the observed surface phase transition the amorphous phase is effectively at zero pressure, and beyond the pressure limit of ca. 20 GPa the energies of the pressurised fcc phase and the zero-pressure amorphous phase coincide and the system does not lose energy when transforming to the higher-energy phase, see Figure 11.

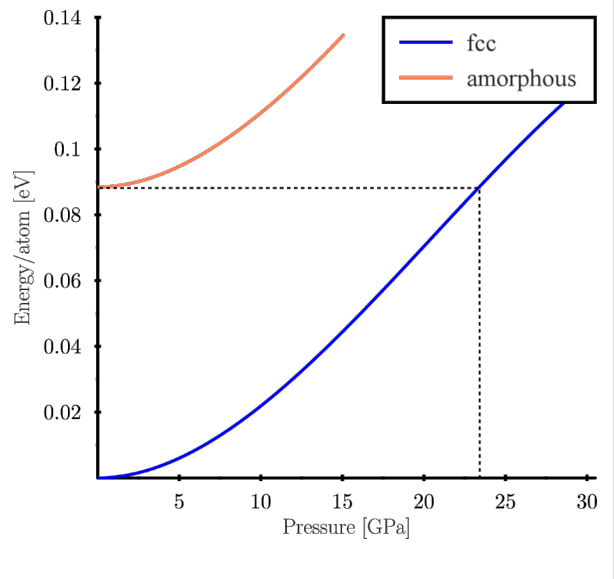

Figure 11: Energy per atom with respect to the fcc phase at zero pressure for fcc and amorphous Cu. Energy of the fcc phase coincides with the amorphous phase at 23.5 GPa.

It is important to note, that even though the amorphous region shows liquid-like flow, the system temperature stays at about

0 K and the atoms in the amorphous region stay static between the bursts of the material. Thus this process is distinct from the high-strain-rate/high-momentum driven amorphisation observed in nanowires [2], where the threshold strain rates for amorphisation are more than three orders of magnitude higher than in this study. Still, it has to be noted, that the atomic pressures as such are not well-defined locally and can give only qualitative reasons.

Regarding the suppression of the dislocation activity, the most obvious limit would be the stress required to bend the dislocation pinned at the extrusion orifice, as this stress

$$\tau_{bend} \propto \frac{Gb}{R}, \quad (1)$$

where R is the radius of curvature of the dislocation bending. However, as for Cu, G = 46 GPa, b = 1.48 Å and R = 10–16 Å. This leads to stresses in the range of 6.8–4.3 GPa, which the von Mises stress of the system exceeds in all the cases. Thus, such simple approximations cannot capture even the qualitative differences of the observed modes of plasticity. The only apparent difference, in addition to the hydrostatic pressure, is the initial stress distribution as seen in Figure 2d. At the lower orifice radii the shear stress is localised at the particle surface, and thus, even if dislocations attempting to accommodate the loading to the system would be nucleated, there would not be a shear to drive these inside the particle. Moreover, as the hydrostatic pressure of the system increases it becomes increasingly difficult for the dislocations nucleated at the surface to penetrate the material.

Conclusion

In summary, we have used molecular dynamics simulations to show how the formation of dislocation dendrites consisting of multiple different types of dislocations leads to strong strain hardening of individual Cu nanocrystallites. We also report a variety of dislocation interactions, not observed in the deformation of macroscopic metals, taking place during the plastic flow from the nanoparticle. We suggest a high pressure limit for displacive plasticity at which the surface amorphisation of the particle becomes the more favourable mode of plasticity. Our computational study further elucidates how the nanoscale processes differ from the familiar macroscopic counterparts and motivates more studies to understand the possible limits of displacive plasticity.

Methods

Molecular dynamics (MD) simulations were performed by using a modified version of the LAMMPS [14] simulation package. Interatomic interactions of Cu atoms were modelled by an EAM type inter atomic potential developed by Mishin et al. [15], which gives the correct generalised stacking fault energies [16]. In order to restrict the system to the regime of purely displacive plasticity, the system temperatures were kept close to 0 K by a Berendsen thermostat [17].

The nanoparticles were encapsulated inside a external repulsive spherical force field with a circular orifice interacting with the Cu atoms with a repulsive Lennard-Jones type potential. As the carbon atoms in a graphitic shell interact very weakly with the metal particle in equilibrium [18], and since during the contraction the interaction is repulsive, the exact functional form of this interaction is irrelevant, and such a simple model captures the essence of the process of a contracting carbon shell. Spherical nanoparticles were formed by cutting a sphere of radius 21.58 Å, with 3892 atoms, from an fcc Cu bulk. After cutting, the particle was annealed at 800 K for 500 ps and slowly cooled down to 0 K. Three different orientations aligning the {111} planes of the particle parallel, orthogonal, and tilted with respect to the extrusion direction, were chosen (referred to below as parallel, orthogonal and tilted).

The system was strained by reducing the radius of the external force field in 0.005 Å steps every 25 ps while keeping the radius and the position of the orifice constant. The radius of the extrusion orifice was varied from 16.6 to 10.6, which was found to capture the orifice-dependent changes in the plasticity. As the initial radius of the force field was 24.6 Å, this contraction rate corresponds to an initial strain rate of 8.1×10^{-6} ps^{-1} increasing to 8.5×10^{-6} ps^{-1} at the onset of plasticity. A constant contraction rate was selected over a constant strain rate, because it relates more accurately with the experimental setup modelled. A small time step of 0.5 fs was used to capture accurately the physics of the extremely fast processes taking place in the high-pressure nanosystem.

Atomic stresses and the pressure of the system were calculated from the atomic virials assuming constant atomic volumes, and the atomic stress tensors were diagonalised by using the Jacobi rotation method [19] for the analysis of shear components. With the multitude of possible dislocation interactions in a nanoscale system with a high dislocation density, it becomes cumbersome, or impossible, to identify the dislocations by using atomic energies, common neighbour analysis, or centrosymmetry parameters, which are often efficient and reliable in the studies of macroscopic systems in large-scale simulations. To overcome this problem, we employed a recent dislocation-detection algorithm developed by Stukowski et al. [20] and the related tool [21]. We found this method to be reliable and robust, even with the complicated surface effects and dense dislocation networks of our studied systems.

Supporting Information

The Supporting Information files show the evolution of the nanoparticle during extrusion from a 15 Å orifice showing displacive plasticity; evolution of the nanoparticle during extrusion from a 11 Å orifice showing surface amorphisation; and simultaneous dislocation nucleation at the onset of plasticity in different orientations of the nanoparticle during extrusion from a 15 Å orifice.

Supporting Information File 1

Extrusion from a 15 Å orifice
[http://www.beilstein-journals.org/bjnano/content/supplementary/2190-4286-4-17-S1.avi]

Supporting Information File 2

Extrusion from a 11 Å orifice
[http://www.beilstein-journals.org/bjnano/content/supplementary/2190-4286-4-17-S2.avi]

Supporting Information File 3

Simultaneous nucleation in different orientations of the system
[http://www.beilstein-journals.org/bjnano/content/supplementary/2190-4286-4-17-S3.pdf]

Acknowledgements

This work was supported by the Deutsche Forschungsgemeinschaft through project KO 3861/2. We are grateful for the DAAD travel grant and computational resources provided by the John von Neumann Institute for Computing in Jülich and HRZ at TU Darmstadt. We acknowledge the insightful comments of J. Schäfer and Y Ritter.

References

1. Van Swygenhoven, H.; Derlet, P. M.; Frøseth, A. G. *Nat. Mater.* **2004,** *3,* 399–403. doi:10.1038/nmat1136
2. Ikeda, H.; Qi, Y.; Çagin, T.; Samwer, K.; Johnson, W. L.; Goddard, W. A., III. *Phys. Rev. Lett.* **1999,** *82,* 2900–2903. doi:10.1103/PhysRevLett.82.2900
3. Koh, A. S. J.; Lee, H.-P. *Nano Lett.* **2006,** *6,* 2260–2267. doi:10.1021/nl061640o
4. Bobylev, S. V.; Ovid'ko, I. A. *Phys. Rev. Lett.* **2009,** *103,* No. 135501. doi:10.1103/PhysRevLett.103.135501
5. Valentini, P.; Gerberich, W. W.; Dumitrică, T. *Phys. Rev. Lett.* **2007,** *99,* No. 175701. doi:10.1103/PhysRevLett.99.175701
6. Wu, J. Y.; Nagao, S.; He, J. Y.; Zhang, Z. L. *Nano Lett.* **2011,** *11,* 5264–5273. doi:10.1021/nl202714n
7. Sun, L.; Krasheninnikov, A. V.; Ahlgren, T.; Nordlund, K.; Banhart, F. *Phys. Rev. Lett.* **2008,** *101,* No. 156101. doi:10.1103/PhysRevLett.101.156101
8. Krasheninnikov, A. V.; Banhart, F. *Nat. Mater.* **2007,** *6,* 723–733. doi:10.1038/nmat1996
9. Banhart, F.; Kotakoski, J.; Krasheninnikov, A. V. *ACS Nano* **2011,** *5,* 26–41. doi:10.1021/nn102598m
10. Wu, X. L.; Zhu, Y. T.; Wei, Y. G.; Wei, Q. *Phys. Rev. Lett.* **2009,** *103,* No. 205504. doi:10.1103/PhysRevLett.103.205504
11. Wang, L.; Han, X.; Liu, P.; Yue, Y.; Zhang, Z.; Ma, E. *Phys. Rev. Lett.* **2010,** *105,* No. 135501. doi:10.1103/PhysRevLett.105.135501
12. Bulatov, V.; Abraham, F. F.; Kubin, L.; Devincre, B.; Yip, S. *Nature* **1998,** *391,* 669–672. doi:10.1038/35577
13. Bulatov, V. V.; Hsiung, L. L.; Tang, M.; Arsenlis, A.; Bartelt, M. C.; Cai, W.; Florando, J. N.; Hiratani, M.; Rhee, M.; Hommes, G.; Pierce, T. G.; de la Rubia, T. D. *Nature* **2006,** *440,* 1174–1178. doi:10.1038/nature04658
14. Plimpton, S. *J. Comput. Phys.* **1995,** *117,* 1–19. doi:10.1006/jcph.1995.1039
15. Mishin, Y.; Mehl, M. J.; Papaconstantopoulos, D. A.; Voter, A. F.; Kress, J. D. *Phys. Rev. B* **2001,** *63,* No. 224106. doi:10.1103/PhysRevB.63.224106
16. Stukowski, A.; Albe, K.; Farkas, D. *Phys. Rev. B* **2010,** *82,* No. 224103. doi:10.1103/PhysRevB.82.224103
17. Berendsen, H. J. C.; Postma, J. P. M.; van Gunsteren, W. F.; DiNola, A.; Haak, J. R. *J. Chem. Phys.* **1984,** *81,* 3684–3690. doi:10.1063/1.448118
18. Rodríguez-Manzo, J. A.; Tolvanen, A.; Krasheninnikov, A. V.; Nordlund, K.; Demortière, A.; Banhart, F. *Nanoscale* **2010,** *2,* 901–905. doi:10.1039/C0NR00098A
19. Press, W. H.; Teukolsky, S. A.; Vetterling, W. T.; Flannery, B. P. *NUMERICAL RECIPES in Fortran 77,* 2nd ed.; Cambridge University Press, 1992.
20. Stukowski, A.; Albe, K. *Modell. Simul. Mater. Sci. Eng.* **2010,** *18,* 085001. doi:10.1088/0965-0393/18/8/085001
21. Stukowski, A. Dislocation extraction algorithm (DXA). http://dxa.ovito.org/.

License and Terms

Beilstein Journal of Nanotechnology

Grain boundaries and coincidence site lattices in the corneal nanonipple structure of the Mourning Cloak butterfly

Ken C. Lee and Uwe Erb*

Full Research Paper

Open Access

Address:
Department of Materials Science and Engineering, University of Toronto, Toronto, Ontario, M5S 3E4, Canada

Email:
Ken C. Lee - kenc.lee@mail.utoronto.ca; Uwe Erb* - erb@ecf.utoronto.ca

* Corresponding author

Keywords:
butterfly-eye structure; coordination defects; sigma grain boundaries

Beilstein J. Nanotechnol. **2013,** *4,* 292–299.
doi:10.3762/bjnano.4.32

Received: 30 January 2013
Accepted: 18 April 2013
Published: 02 May 2013

This article is part of the Thematic Series "Advances in nanomaterials".

Guest Editors: H. D. Gleiter and T. Schimmel

Abstract

In this study the highly ordered corneal nanonipple structure observed on the Mourning Cloak butterfly (*Nymphalis antiopa)* is analyzed with a particular emphasis on the high-angle grain-boundary-like defects that are observed between individual nanonipple crystals. It is shown that these grain boundaries are generated by rows of topological coordination defects, which create very specific misorientations between adjacent crystals. These specific orientations form coincidence site lattices, which (i) have unit cells larger than the unit cell in each individual crystal and (ii) extend from one crystal to the next, effectively creating order over areas larger than the individual crystals. A comparison to similar coincidence site lattices in engineering materials is made and the importance of such arrangements in terms of nipple packing density, corneal lens curvature and potential optical properties is discussed.

Introduction

The structure of moth and butterfly eyes consist of many repeating unit cells referred to as ommatidia. Thousands of ommatidia are closely packed together and typically form a nearly spherical or semispherical compound eye with the well-known surface facet structure [1]. Each ommatidium is composed of a corneal lens, a crystalline cone, a rhabdom and retinula cells. The signals detected by thousands of ommatidia are processed neurologically in the brain to form a complete image. The corneal lens incorporates chitin, a long chained semicrystalline natural polysaccharide with a refractive index of about 1.52. It is well known that the outer surfaces of the corneal lens of some moths and butterflies are covered with so-called corneal nipples, nanometer-sized protuberances distributed over the surface in patterns with varying degrees of regularity [2-6]. In an earlier study these nipple arrays were classified in different categories depending on nipple height, which can vary from less than 50 nm to over 200 nm [3]. The advantages of compound eyes with corneal nipple structures,

compared to flat lens surfaces observed in many other insects, have been discussed in numerous studies, e.g., [5-7]. Most importantly, these structures reduce the reflection of light from the surface of the eye, due to the gradient in the refractive index in the near surface region. This is important for nocturnal insects such as moths, because it gives a better low-light vision (moth-eye effect). The reduced light reflection also provides an antiglare effect, which provides some protection from predators. In recent years many artificial moth-eye-type surfaces have been developed as antireflection, antiglare surfaces by various methods such as photoresist patterning, porous aluminium oxide templating or direct reproduction, e.g., [7-9]. With respect to the topological arrangements of the nanometer sized nipples, both completely irregular and highly ordered structures have been observed on different species [2,6]. In an ongoing study, we analyze the highly ordered nipple structure of the Mourning Cloak butterfly (*Nymphalis antiopa*) in more detail and from a crystallography/defect-structure point of view. The results of this investigation will be published shortly [10]. Briefly, this study has shown that the highly ordered hexagonal structure is made up of nipples with average diameters on the order of 150 nm and a unit cell lattice parameter of about 200 nm. Perfect crystals with sizes on the order of a few micrometers cover the entire surface of each ommatidium. The crystals are separated by grain-boundary type defects created by rows of 5–7 coordination defects. While an individual 5–7 coordination defect in a perfect crystal creates a dislocation-type defect, rows of these defects with relatively large spacing form low-angle grain boundaries. With decreasing spacing between 5–7 coordination defects, high-angle grain boundaries are formed for which the misorientation between adjacent crystals is more than 10 degrees.

In the current investigation the type and nature of these high-angle grain boundaries was studied in more detail. It will be shown that these boundaries have preferential misorientation angles, such that adjacent crystallites are arranged in specific coincidence site lattices (CSLs). A comparison to similar CSLs observed in engineering materials will be made and the purpose and potential advantages of such unusual nipple array structures will be discussed in the current report.

Results and Discussion

Eye structure

The Mourning Cloak butterfly (*Nymphalis antiopa*) is a common butterfly in North America. It has a wing span of 4–8 cm and shows beige-yellow edges and several blue spots on brown colored wings.

A low magnification scanning electron micrograph of one of the eyes is shown in Figure 1. The hexagonal shape of the ommatidia is clearly visible with each facet measuring about 25 µm across. The entire eye of the Mourning Cloak butterfly is covered with randomly distributed tiny hairs (about 4 µm in diameter), which usually grow at the triple junctions between the ommatidia. In Figure 1, the bases of fractured hairs are visible on three of the triple junctions. Figure 1 also shows areas with contaminations/local damage, which are likely the result of the collection and the handling and/or preservation processes of the specimen.

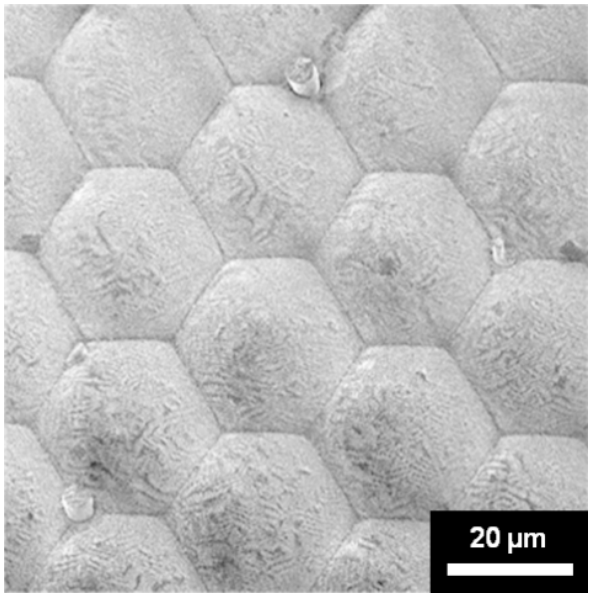

Figure 1: Scanning electron micrograph showing the facet structure of the Mourning Cloak butterfly. Note the bases of fractured hair at some of the triple junctions (magnification: 800×).

Figure 2 shows a triple junction between three ommatidia at higher magnification. In this micrograph the nanonipple structure on each of the facets is clearly visible. At the triple junction and the three facet boundaries the nipple structure is highly irregular showing no long-range order in their arrangement. However, with increasing distance from the triple junction and the facet boundaries, considerable structural order in the nipple arrangements can be seen as crystals, i.e., areas with close-packed, hexagonal nipple arrangements. These crystals can be several micrometers in diameter and are separated by topologically disordered or defective regions across which the orientation of the ordered regions changes by various rotational angles. In an earlier study on nipple arrangements on various butterflies similar structures were referred to as local domain arrangements [6].

For the remainder of this study, nipple arrangements located at least 4 µm away from triple junctions and facet boundaries in

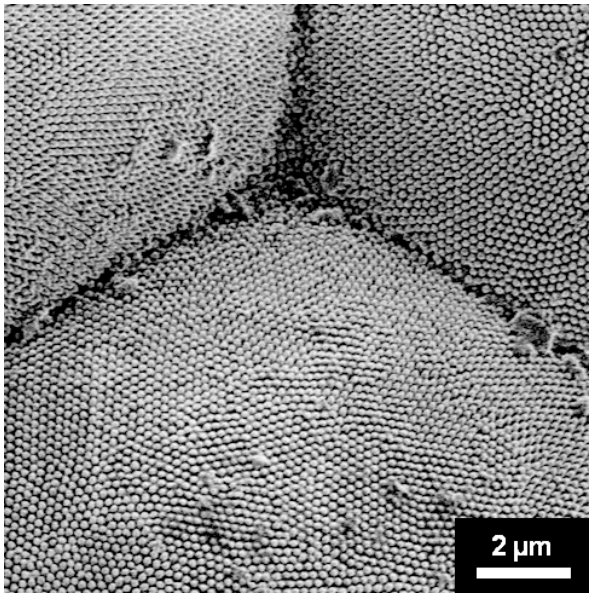

Figure 2: Triple junction in the facet structure and nanonipples in three adjacent facets (magnification: 6,000×).

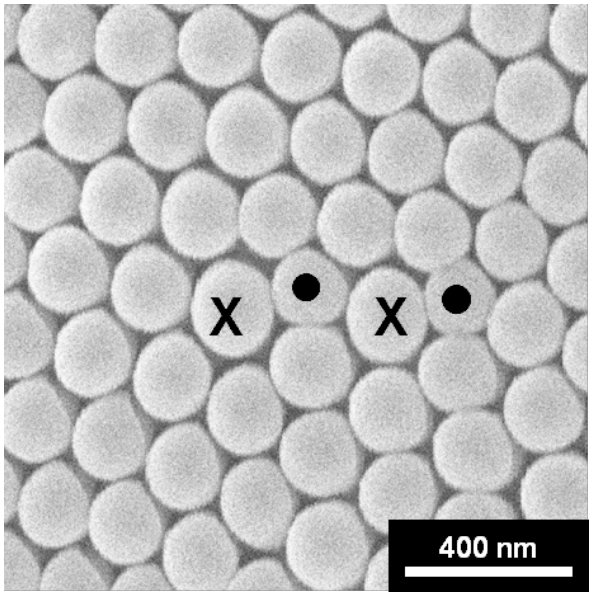

Figure 3: Topological disorder in the hexagonal nipple structure showing two pairs of 5–7 ("•"–"**X**") coordination defects (magnification: 52,000×).

contamination-free areas of the eye were selected. Figure 3 shows a high magnification micrograph of the nipple arrangement in one of the highly ordered regions. While most of the nipples are arranged in a regular hexagonal close-packed pattern, the structure is defective at the points marked with "•" and "**X**". We refer to these defects as 5–7 coordination defects, because the normal coordination number of six for the defect-free regions of the nipple arrangements is locally changed to five or seven nearest neighbors. It was observed that the nipples with seven nearest neighbors were usually slightly larger than the average nipple diameter (150 nm) while the nipples with five nearest neighbors were slightly smaller. These coordination defects usually occur in pairs. Only a small number of isolated 5-fold coordination defects were found. One pair of 5–7 coordination defects creates a dislocation-type defect in the crystalline structure [10].

Moreover, many 5–7 coordination defects were arranged in rows creating defects that can be described as high-angle grain boundaries [10]. In the current study we analyzed the type of these high-angle boundaries in more detail.

Figure 4 shows two different regions with rows of 5–7 coordination defects again marked with "•" and "**X**". It can be seen that these defect rows are clearly grain-boundary-type defects across which the orientations of otherwise defect-free crystals change. What is quite remarkable in both cases shown in Figure 4 is that some sort of superlattice can be identified as indicated by the nipples marked in white. This superlattice has the property of a regular repeat pattern with a unit cell several times larger than the unit cell in each of the crystals. The superlattice extends over adjacent crystals and is not interrupted by the grain boundaries separating two crystals. Another feature of the superlattice is that it subdivides the nipple array into regions of relatively good superlattice fit that are much larger than the crystal/domain size in the nipple array. It can be noted in both examples shown in Figure 4 that the superlattice is not 100% perfect for all nipple positions. Instead, some minor deviations from the perfect superlattice position are found for some of the nipples. The significance of these deviations will be discussed later.

The coincidence site lattice (CSL)

Superlattice structures such as those shown in Figure 4 have been studied in crystalline materials for several decades in the context of grain boundary analysis. For example, in 2D crystal structures produced by bubble rafts [11] or 3-D polycrystalline materials [12,13] such superlattices were studied for many different grain boundaries. Kronberg and Wilson [12] were likely the first researchers to point out the significance of superlattices for crystals rotated about the common <111> crystallographic direction and the preferred misorientations of crystals separated by <111>-type grain boundaries in recrystallized copper. In this work the term Σ was introduced to characterize such preferred orientations and the importance of Σ for grain boundaries in copper was discussed. The Σ-value is the size ratio of the superlattice unit cell divided by the original lattice unit cell. It should be noted that the motif arrangement of the

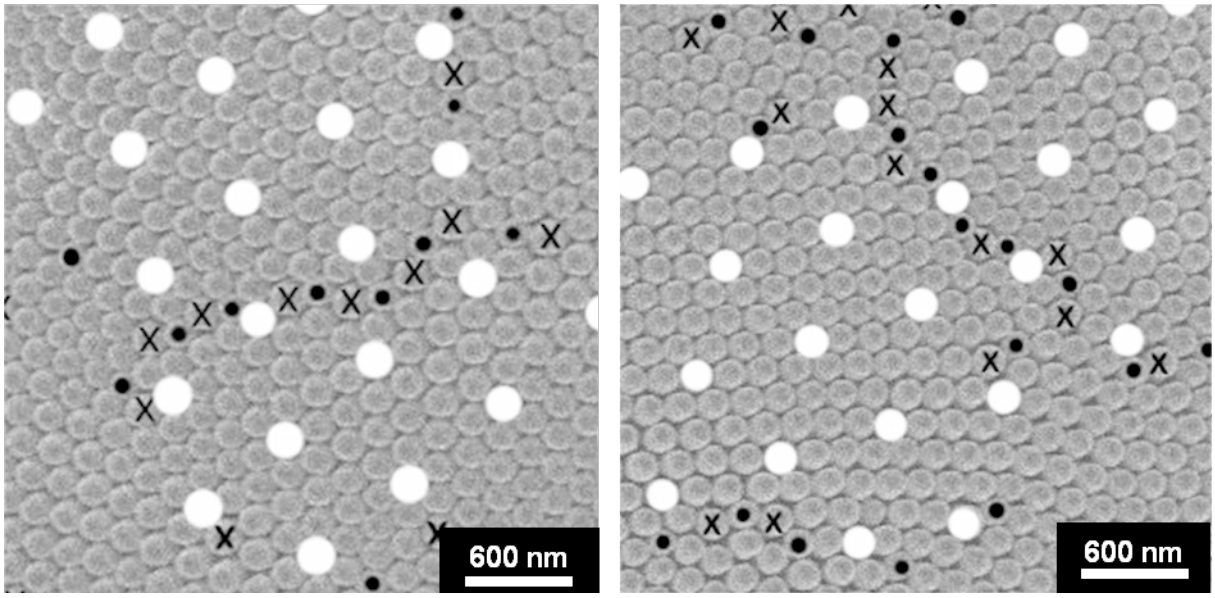

Figure 4: Examples of Σ13 grain boundaries between crystals (domains) in the nipple structure consisting of rows of 5–7 coordination-defects. White circles indicate nipple positions belonging to a coincidence site lattice (CSL) superlattice (magnification: 20,000×).

closest-packed (111) plane in face-centered cubic copper is identical to the hexagonal close packed plane in the 2-D crystal structure of the butterfly nipple structure arrangement.The work by Kronberg and Wilson was the foundation for numerous studies over the past six decades, which looked at the significance of so-called coincidence site lattices (CSLs) for grain-boundary structure and property analyses in engineering materials.

Ranganathan [13] derived the following mathematical relationships for the generation of general CSLs about any common rotation axis <*hkl*>, not only the <111> direction.

$$\theta = \left(2\tan^{-1}\left(x/y\right)\right)\left(N^{1/2}\right) \quad (1)$$

$$N = h^2 + k^2 + l^2 \quad (2)$$

$$\Sigma = x^2 + y^2 N \quad (3)$$

where θ is the misorientation angle between the two adjacent crystals, *h*, *k*, *l* are the Miller indices of the common rotation axis, and *x*, *y* are the coordinates of superlattice sites.

These CSL descriptions can be applied to both 2-D and 3-D crystal arrangements. It should be noted that all grain boundaries can be described by a Σ value. However, with increasing Σ number the physical significance of the superlattice becomes questionable as the unit cell of the lattice becomes very large. Many studies have shown that grain boundaries in materials associated with relatively low Σ values (small CSL unit cells) show special properties such as low energy or reduced susceptibility to intergranular degradation (e.g., intergranular corrosion, cracking, segregation) as summarized in several books, e.g., [14,15]. It was further shown that the special properties of grain boundaries were even maintained for small angular deviations (Δθ) from the special misorientations (θ). Several criteria were introduced for permissible angular deviations up to which the special properties of grain boundaries are maintained [16-19]. The most commonly used criterion is the Brandon criterion [16], which states

$$\Delta\theta = 15° \, \Sigma^{-1/2} \quad (4)$$

Table 1 summarizes all possible superlattices with Σ ≤ 19 that can be generated for increasing misorientation values up to θ = 60° about the <111> crystallographic axis, together with the corresponding deviation angles Δθ according to the Brandon criterion.

For a polycrystalline aggregate with crystals in random crystallographic orientations it has been shown that the fraction of grain boundaries with low Σ values is on the order of 10% [20]. In other words, a random material contains about 10% of grain boundaries with potentially enhanced resistance to intergranular degradation. In 1984, Watanabe suggested that the overall resistance of a material to intergranular degradation could be

Table 1: Σ-values for CSL lattices generated by misorientations θ about the common <111> rotation axis together with Δθ values according to Equation 4.

Σ	θ (°)	Δθ (°)
19	13.2	3.4
7	21.8	5.7
13	27.8	4.2
13	32.2	4.2
7	38.2	5.7
19	46.8	3.4
3	60.0	8.7

increased enormously by "grain-boundary design and control" which involves materials processing routes that increase the number of special boundaries [21]. This led to the new field of grain-boundary engineering, which has been successfully applied for many metals and alloys [22-24].

CSL structures on Mourning Cloak butterfly eyes

Returning to the importance of CSL grain boundaries for the 2-D nipple crystal structures found on the Mourning Cloak butterfly eye, Figure 5 shows three different special <111> tilt grain boundaries for three crystal rotations about the common <111> rotation axis. All three rotations correspond to low Σ values of Σ = 7 for θ = 21.8°, Σ = 13 for θ = 27.8° and Σ = 19 for θ = 13.2° (Table 1). It should be noted that in these figures the open circles show motif positions in the two crystals while the filled circles are the positions of CSL motifs belonging to both crystals. It can be clearly seen that the CSLs in all three cases extend across the grain boundaries over both crystals. The figures also show that the unit cell of the CSLs becomes larger with increasing Σ value. It should be pointed out that in Figure 5 the size of all motifs is the same, while in the nanonipple arrangement of the Mourning Cloak butterfly the grain boundary is introduced by rows of 5–7 coordination defects in which the nipple sizes vary to some extent. However, for the crystallographic description of the superlattice the actual nipple size distribution along the grain boundary is of secondary importance.

In order to assess the statistical significance of CSL boundaries within the nipple arrangements of the Mourning Cloak butterfly a total of 73 grain boundaries such as the ones shown in Figure 4 were analyzed. The results of this analysis are presented in Figure 6, which shows the number of boundaries found as a function of their misorientation θ about the common <111> tilt axis. Also shown in this Figure are the positions of various low Σ grain boundaries. This figure clearly demonstrates a strong preference for Σ7 and Σ13 boundaries, and even perhaps Σ19. Surprisingly, there is no preference for Σ3 boundaries expected at an angle of misorientation of 60°. Many engineering materials show a high preference for Σ3 boundaries [14,15]. Note that when the Brandon criterion is applied, all boundaries fall within the angular deviation given in

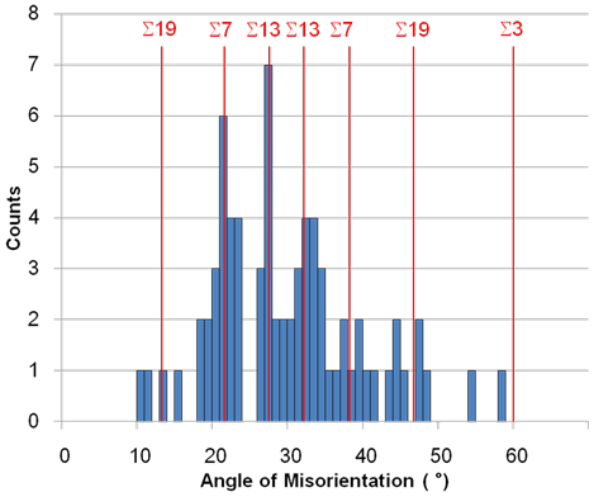

Figure 6: Histogram showing the misorientations around the common <111> direction between adjacent crystals in the Mourning Cloak nanonipple structure.

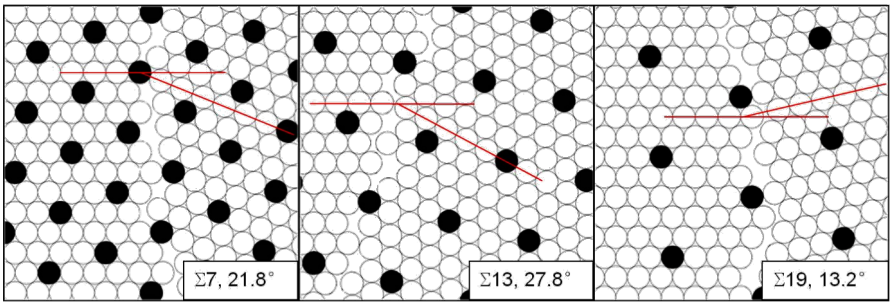

Figure 5: Coincidence site lattices for Σ = 7, Σ = 13 and Σ = 19.

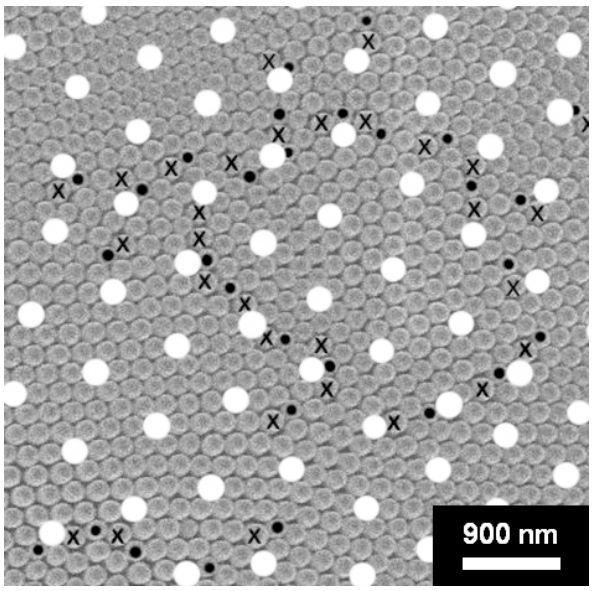

Figure 7: Extended Σ13 coincidence site lattice covering several crystals (magnification: 13,000×).

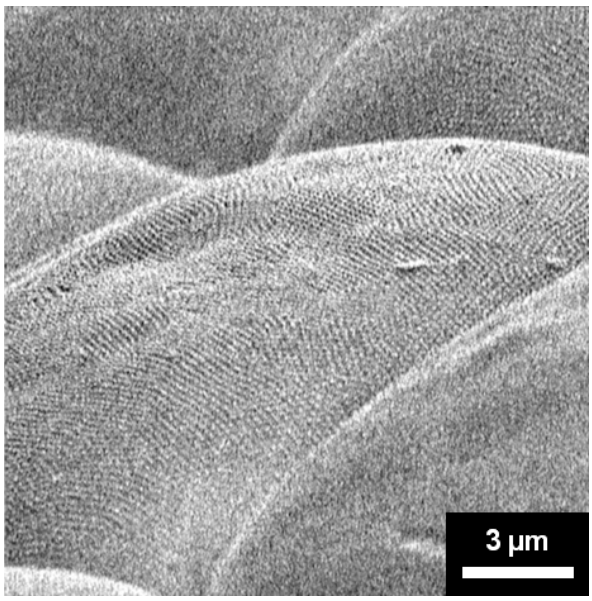

Figure 8: Several facets at very high tilt angle showing the curvature on each facet surface (magnification: 4,000×).

Equation 4. In other words, all 73 boundaries can be considered special boundaries.

It was observed that the nipple arrangement was not perfect for all CSL positions shown in Figure 4 and that some deviations did occur. This becomes more obvious when the area of analysis is increased as shown in Figure 7.

This figure clearly shows considerable distortions in the superlattice unit cell and a fairly pronounced waviness in rows of closest packed CSL lattice lines. However, this is perhaps not surprising because the SEM micrographs are 2-D projections of the ommatidia surfaces, which actually show a considerable curvature. This is observed in Figure 8, which is a micrograph of several ommatidia taken at a relatively high tilt angle to visualize their surface curvature. The radius of curvature can be estimated to be on the order of 16–20 µm. In addition, many ommatidia show some localized depressions, likely due to dehydration. It is therefore expected to see distortions of the superlattices shown in Figure 4 and Figure 7 as these are projections of curved 2-D crystals. In other words, the superlattice fit may actually extend over much larger areas if this curvature is taken into consideration.

In summary, the 2 mm hemispherical eyes of the Mourning Cloak butterfly consist of several thousand ommatidia, each covered with thousands of nanonipples. A total of about 100 million of these nipples are arranged in closest packed hexagonal crystals separated by grain boundaries. A small sample of 73 of these boundaries has shown that they are mainly of the Σ7 and Σ13 type and perhaps also Σ19 boundaries. These boundaries consist of rows of 5–7 coordination defects, which are generated by using slightly larger/smaller nipple sizes than the average nipple size. These Σ-related superlattices extend over areas larger than the average crystal size.

When looking at these surprising results two questions arise: (i) what is the purpose of this peculiar nipple arrangement, and (ii) what benefit does the Mourning Cloak butterfly derive from these structures? Perhaps it is instructive to first look at nipple arrangements on the moth eye, which has been studied much more extensively in the past. The moth eye has very similar nipple arrangements to the Mourning Cloak butterfly, although a detailed analysis of the exact arrangements of nipples along crystal interfaces has not been presented yet. One of the earliest theories [2] for the purpose of the nanonipples on the moth eye is that they effectively decrease the reflection of light from the eye because of the gradient in the refractive index as light travels from air (n = 1.0) to the ommatidia (chitin, n = 1.52). Thus, more light enters the eye, which is beneficial for moths as they are nocturnal and active in low light conditions. However, the Mourning Cloak is a diurnal butterfly, active during the day where low-light vision improvement may not be the most important. Nevertheless, the Mourning Cloak butterfly could benefit from less glare of the eye due to reduced reflection, which perhaps provides some protection from predators. However, a reduced eye reflection does not necessarily require ordered nipple arrangements.

Space filling due to the curved surfaces of the ommatidia could be another reason for the preference of coordination defects. If the intent is to create the highest possible density of nipples on the eye, a perfectly flat closed-packed crystal must include some sort of defects when curvature is introduced. In fact, nature uses this trick quite often to introduce curvature into hexagonal closely packed structures. For example, the combs of honey bees and social wasps, which also make use of space-filling hexagonal patterns, show interruptions to adjust for curvature, confined boundary conditions, or transition zones from smaller to larger cells [1]. Sometimes four-sided cells are found, but most commonly it is a row of five-sided cells that accommodates such obstructions. However, configurations of rows of several 5-fold coordination defects were not found in the nipple structures of the Mourning Cloak butterfly.

If the purpose of the CSL lattices is to create special properties of the eye, it is likely associated with an optical function. One such function could be a diffraction capability making the eye sensitive to diffraction phenomena for certain wavelengths. Table 2 shows the distances between rows of CSL sites for the three Σ boundaries Σ7, Σ13 and Σ19.

Table 2: Distances between coincident sites on the eye of the Mourning Cloak butterfly.

Σ	grating distance (nm)
7	d_1 = 529 d_2 = 917
13	d_1 = 721 d_2 = 1249
19	d_1 = 872 d_2 = 1509

If diffraction of light is indeed a primary role of the superlattices formed on this butterfly eye, the various CSLs could provide diffraction gratings that are sensitive to selective wavelengths in the visible and infrared wavelength range. It is suggested that a future study should be concerned with optical measurements to explore if there is indeed any wavelength sensitivity due to diffraction as a result of this unusual structure.

Although completely different in nature, the 5–7 coordination defects found as the most common defect in the Mourning Cloak butterfly eye are topologically similar to some of the defects found in other structures with closest packing. For example, in hexagonal graphene and carbon nanotubes, Stone–Wales 5–7 defects [25-27] have been found in numerous studies. Rows of 5–7–7–5 defects and other combinations have also been associated with grain boundaries in such structures [27]. Coordination defects are also common in other curved surfaces with closest packed structures such as polymer colloids assembled on water or oil droplets [28,29]. The importance of 5–7 topological coordination-number defects has further been discussed for the cases of grain growth in polycrystalline materials and the stability of periodic cellular structures [30,31]. All these examples show that, from a topological point of view there are similarities between inorganic materials and living structure patterns that should be further explored, as suggested earlier [32].

Experimental

The Mourning Cloak butterfly used in the current study was received from Thorne's Insect Shoppe Ltd, London, Ontario. It was collected in July 2008 at Miner's Bay, Ontario. The head of the butterfly was separated, mounted on a holder and carbon coated. Scanning electron micrographs were taken in a Hitachi 4500 field emission scanning electron microscope operated at 5 kV acceleration voltage. Micrographs were taken at various locations in contamination/macro-defect-free regions.

Acknowledgements

This paper is dedicated to Professor Horst Hahn on the occasion of his 60th Birthday. Financial support from the Natural Sciences and Engineering Research Council of Canada (NSERC) and Integran Technologies Inc., Toronto, is gratefully acknowledged.

References

1. Capinera, J. L., Ed. *Encyclopedia of Entomology,* 2nd ed.; Springer: Heidelberg, Germany, 2008. doi:10.1007/978-1-4020-6359-6
2. Bernhard, C. G.; Miller, W. H. *Acta Physiol. Scand.* **1962,** *56,* 385–386. doi:10.1111/j.1748-1716.1962.tb02515.x
3. Bernhard, C. G.; Gemne, G.; Sällström, J. Z. *Vgl. Physiol.* **1969,** *67,* 1–25. doi:10.1007/BF00298117
4. Smith, W. C.; Butter, J. F. *J. Insect Physiol.* **1991,** *37,* 287–296. doi:10.1016/0022-1910(91)90063-6
5. Watson, G. S.; Watson, J. A. *Appl. Surf. Sci.* **2004,** *235,* 139–144. doi:10.1016/j.apsusc.2004.05.129
6. Stavenga, D. G.; Foletti, S.; Palasantzas, G.; Arikawa, K. *Proc. R. Soc. London, Ser. B* **2006,** *273,* 661–667. doi:10.1098/rspb.2005.3369
7. Wilson, S. J.; Hutley, M. C. *Opt. Acta* **1982,** *29,* 993–1009. doi:10.1080/713820946
8. Sawitowski, T.; Beyer, N.; Schulz, F. Bio-inspired Anti-reflective Surfaces by Imprinting Processes. In *The Nano-Micro Interface;* Fecht, H. J.; Werner, M., Eds.; Wiley-VCH: Weinheim, Germany, 2004; pp 263–280.
9. Huang, J.; Wang, X.; Wang, Z. L. *Nanotechnology* **2008,** *19,* 025602. doi:10.1088/0957-4484/19/02/025602
10. Erb, U.; Lee, K. C.; Victor, J. J.; Chao, W.; Vakil, P.; Woo, P. to be published.
11. Ishida, Y. *J. Mater. Sci.* **1972,** *7,* 75–83. doi:10.1007/BF00549553

12. Kronberg, M. L.; Wilson, F. H. *Trans. Am. Inst. Min., Metall. Pet. Eng.* **1949,** *185,* 501–514.
13. Ranganathan, S. *Acta Crystallogr.* **1966,** *21,* 197–209. doi:10.1107/S0365110X66002615
14. Gleiter, H.; Chalmers, B. *High-Angle Grain Boundaries*. *Progress in Materials Science;* Pergamon Press: Oxford, UK, 1972; Vol. 16, pp 1–124.
15. Wolf, D.; Yip, S. *Materials Interfaces;* Chapman & Hall: London, UK, 1992; pp 1–716.
16. Brandon, D. G. *Acta Metall.* **1966,** *14,* 1479–1484. doi:10.1016/0001-6160(66)90168-4
17. Ishida, Y.; McLean, M. *Philos. Mag.* **1973,** *27,* 1125–1134. doi:10.1080/14786437308225821
18. Déschamps, M.; Baribier, F.; Marrouche, A. *Acta Metall.* **1987,** *35,* 101–108. doi:10.1016/0001-6160(87)90217-3
19. Palumbo, G.; Aust, K. T. *Acta Metall. Mater.* **1990,** *38,* 2343–2352. doi:10.1016/0956-7151(90)90101-L
20. Warrington, D. H.; Boon, M. *Acta Metall.* **1975,** *23,* 599–607. doi:10.1016/0001-6160(75)90100-5
21. Watanabe, T. *Res Mech.* **1984,** *11,* 47–84.
22. Aust, K. T.; Palumbo, G. Interface Control in Materials. In *Proceedings of the International Symposium on Advanced Structural Materials,* Montreal, Canada, Aug 28–31, 1988; Wilkinson, D. S., Ed.; Pergamon Press: New York, NY, 1989; pp 215–226.
23. Randle, V. *Mater. Sci. Technol.* **2010,** *26,* 253–261. doi:10.1179/026708309X12601952777747
24. Watanabe, T. *J. Mater. Sci.* **2011,** *46,* 4095–4115. doi:10.1007/s10853-011-5393-z
25. Stone, A. J.; Wales, D. J. *Chem. Phys. Lett.* **1986,** *128,* 501–503. doi:10.1016/0009-2614(86)80661-3
26. Suenaga, K.; Wakabayashi, H.; Koshino, M.; Sato, Y.; Urita, K.; Iijima, S. *Nat. Nanotechnol.* **2007,** *2,* 358–360. doi:10.1038/nnano.2007.141
27. Araujo, P. T.; Terrones, M.; Dresselhaus, M. S. *Mater. Today* **2012,** *15,* 98–109. doi:10.1016/S1369-7021(12)70045-7
28. Eisenmann, C.; Gasser, U.; Keim, P.; Maret, G.; von Grünberg, H. H. *Phys. Rev. Lett. 95,* No. 185502. doi:10.1103/PhysRevLett.95.185502
29. Irvine, W. T. M.; Vitelli, V.; Chaikin, P. M. *Nature* **2010,** *468,* 947–951. doi:10.1038/nature09620
30. Hillert, M. *Acta Metall.* **1965,** *13,* 227–238. doi:10.1016/0001-6160(65)90200-2
31. Morral, J. E.; Ashby, M. F. *Acta Metall.* **1974,** *22,* 567–575. doi:10.1016/0001-6160(74)90154-0
32. Bausch, A. R.; Boswick, M. J.; Cacciuto, A.; Dinsmore, A. D.; Hsu, M. F.; Neilson, D. R.; Nikolaides, M. G.; Travesset, A.; Weitz, D. A. *Science* **2003,** *229,* 1716–1718. doi:10.1126/science.1081160

License and Terms

The definitive version of this article is the electronic one which can be found at:
doi:10.3762/bjnano.4.32

Beilstein Journal of Nanotechnology

Grating-assisted coupling to nanophotonic circuits in microcrystalline diamond thin films

Patrik Rath[1], Svetlana Khasminskaya[1], Christoph Nebel[2], Christoph Wild[2,3] and Wolfram H.P. Pernice[*1]

Full Research Paper

Open Access

Address:
[1]Institute of Nanotechnology, Karlsruhe Institute of Technology, 76344 Eggenstein-Leopoldshafen, Germany, [2]Fraunhofer Institute for Applied Solid State Physics, Tullastr. 72, 79108 Freiburg, Germany and [3]Diamond Materials, Tullastr. 72, 79108 Freiburg, Germany

Email:
Wolfram H.P. Pernice[*] - wolfram.pernice@kit.edu

* Corresponding author

Keywords:
diamond devices; integrated optics; nanophotonics; waveguiding circuits

Beilstein J. Nanotechnol. **2013,** *4,* 300–305.
doi:10.3762/bjnano.4.33

Received: 21 February 2013
Accepted: 18 April 2013
Published: 07 May 2013

This article is part of the Thematic Series "Advances in nanomaterials".

Guest Editors: H. D. Gleiter and T. Schimmel

Abstract

Synthetic diamond films can be prepared on a waferscale by using chemical vapour deposition (CVD) on suitable substrates such as silicon or silicon dioxide. While such films find a wealth of applications in thermal management, in X-ray and terahertz window design, and in gyrotron tubes and microwave transmission lines, their use for nanoscale optical components remains largely unexplored. Here we demonstrate that CVD diamond provides a high-quality template for realizing nanophotonic integrated optical circuits. Using efficient grating coupling devices prepared from partially etched diamond thin films, we investigate millimetre-sized optical circuits and achieve single-mode waveguiding at telecoms wavelengths. Our results pave the way towards broadband optical applications for sensing in harsh environments and visible photonic devices.

Introduction

Integrated photonic circuits are of tremendous interest because they allow for realizing complex optical functionality in a compact and scalable fashion [1]. Alignment and stability issues commonly encountered in free-space setups can be avoided by moving to a chip-based architecture, in which photonic building blocks are laid out in much the same fashion as electronic integrated components. One of the most prominent materials for integrated optics is silicon, because of the availability of high-quality substrates, established fabrication routines, and a high refractive index [2-4]. For waveguiding in the telecommunications transmission window, thin silicon layers (surrounded by cladding material of lower refractive index) are required, which has led to the establishment of silicon-on-insulator (SOI) as a primary platform for nanophotonics [5,6]. However, silicon only provides a relatively small bandgap of 1.1 eV, which prevents waveguiding below 1100 nm. Furthermore, silicon is plagued be free-carrier absorption [7], which presents significant challenges for high-power applications and nonlinear

optics. Some of these material shortcomings can be addressed by using chalcogenide-based devices for realizing tunable photonic circuits [8-10]. Alternatively, material systems with a wider bandgap are also actively pursued to extend the capabilities of photonic integrated circuits. Among the various options, group-III/IV nitride semiconductors, such as silicon nitride (≈5 eV), gallium nitride (3.37 eV) and aluminium nitride (AlN, 6.14 eV), have been investigated [11-13]. Because of their larger bandgap, these materials allow for waveguiding throughout the visible spectrum and do not suffer from free-carrier-based absorption effects or instabilities. While waveguiding at visible wavelengths is of importance for applications in biological sensing and spectroscopy, materials that also provide transparency in the long-wavelength range are equally sought after. In this respect CVD diamond has found a wealth of applications for the fabrication of windows that permit transmission in the long-IR or microwave regions [14]. In addition, diamond provides attractive material properties, such as biocompatibility, chemical inertness, high thermal conductivity, and mechanical hardness [15]. In addition, a large bandgap of 5.5 eV also makes diamond a prime candidate for the realization of optical components [16]. To date, the possibility of fabricating nanophotonic devices out of diamond has mainly been explored in single-crystalline substrates [17-22]. In order to make suitable waveguides, single-crystal diamond foils are transferred onto oxidized silicon carrier wafers and subsequently etched down to the target thickness of a few hundred nanometres. This elaborate procedure inherently limits the size of the available substrates (and thus also the later photonic devices) and provides limited device yield.

Here, in contrast, we employ direct deposition of CVD diamond thin films as a convenient alternative for realizing wafer-scale diamond substrates for integrated optics. Using microwave-enhanced CVD we prepare diamond-on-insulator templates up to six inches in diameter, without the need for further post-growth treatment or thinning. In microcrystalline films we demonstrate waveguiding over millimetre distances in the fibre-optics C-band. To characterize our platform, we design efficient grating couplers, which provide out-of-plane access to integrated photonic circuits with insertion loss of −5.0 dB. Our approach holds promise for transferring established silicon photonics technology to a diamond platform for applications in broadband optics and biological sensing.

Results

Fabrication of diamond photonic circuits

Diamond provides a relatively high refractive index of 2.4, which is well suited for tightly confining light in subwavelength structures [16]. In order to prevent radiative loss into the surrounding medium, the diamond waveguiding layer needs to be surrounded by a material of lower refractive index. Here in analogy to silicon-on-insulator (SOI) substrates we employ silicon dioxide as the lower buffer layer and air as the top cladding, to realize diamond-on-insulator (DOI) substrates [17,19]. Commercial, high-purity silicon wafers with atomically flat surfaces are thermally oxidized to a thickness of 2 μm. The resulting amorphous silica provides the later buried oxide and serves as the template for the CVD diamond overgrowth. The oxide thickness is chosen to provide optimal coupling efficiency for the grating structures described further below. A diamond nanoparticle seed layer is deposited onto the SiO_2 film to initiate growth of polycrystalline diamond. We employ ultrasonification for 30 minutes in a water-based suspension of ultradispersed (0.1 wt %) diamond nanoparticles of typically 5–10 nm diameter to ensure uniform coverage of the underlying oxide surface [23]. Then the samples are rinsed with deionized water and methanol for cleaning and residual particle removal. After drying under nitrogen, the wafer is transferred into an ellipsoidal 915 MHz microwave plasma reactor [24]. Diamond films with a target thickness of 600 nm are grown at 1.8 kW microwave power. As feeding gas we employ a mixture containing 2% methane and 98% hydrogen at a base pressure of 80 mbar and a substrate temperature of 850 °C. Substrate rotation is applied to avoid angular nonuniformities arising from the gas flow. Growth rates are typically in the range of 1–2 μm/h. The diamond film thickness is controlled by timed growth combined with in situ interferometric measurement to allow for precise thickness monitoring. Because the growth rate is moderate and reproducible, the final film thickness can be controlled with high precision. After growth, the samples are cleaned in concentrated HNO_3/H_2SO_4 to remove remaining surface contamination.

Following the film growth the resulting DOI substrates are inspected for thickness uniformity and surface roughness. We employ atomic force microscopy (AFM) and scanning electron microscopy (SEM) imaging to estimate the CVD diamond grain size and height distribution. A typical measured surface profile is shown in Figure 1a. From the AFM scan we obtain a mean roughness of 15 nm and a typical grain size on the order of 100 nm. The surface roughness leads to occasional diamond peaks that extend out of the surface. In order to structure the diamond layer for the creation of photonic devices, we therefore employ a thick photoresist, which uniformly covers the entire diamond surface and does not leave any peaks unprotected. Here we use the negative-tone electron beam (e-beam) lithography resist Fox15, which is spun onto the prepared wafers to a thickness of 400 nm. After exposure, Fox15 cross-links to a silica-like inorganic matrix, which provides good etching resistance as well as high spatial resolution during e-beam writing.

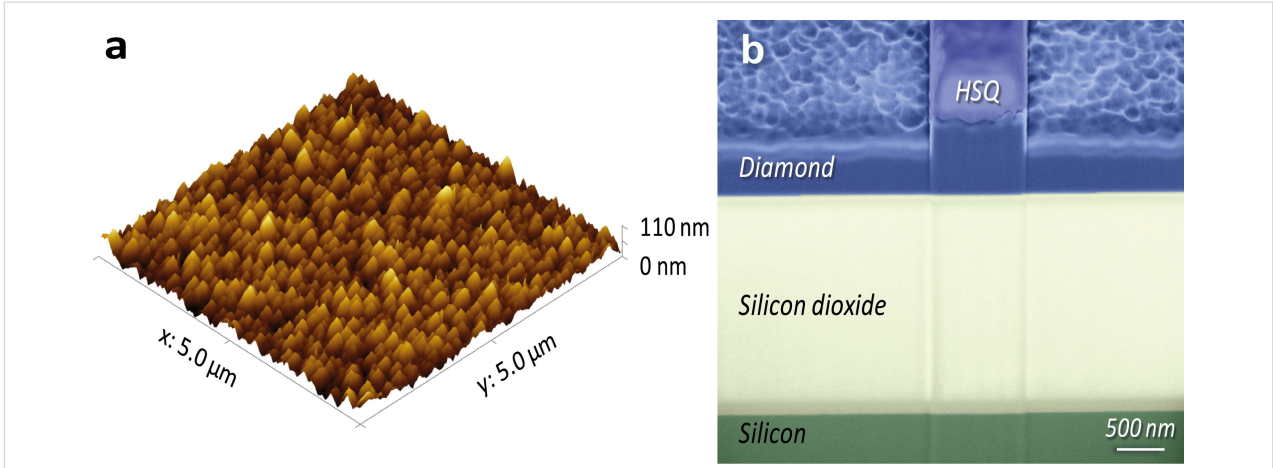

Figure 1: (a) AFM image of the as-grown surface of microcrystalline diamond-on-insulator substrates. Mean surface roughness of 15 nm rms is determined. (b) Cross-sectional SEM image of a nanophotonic waveguide cut by focussed-ion-beam milling. The diamond, e-beam resist, and buried oxide layers are marked in a false-colour overlay.

Photonic circuitry is designed and written into the Fox15 layer by using a JEOL 5300 50 kV e-beam system. After developing, the written structures are transferred into the diamond thin film by reactive ion etching (RIE) on an Oxford 80 system. We use oxygen/argon chemistry at high bias voltage in order to obtain highly anisotropic etching. Typical etch rates are around 25 nm/min, allowing us to precisely reach a desired etch depth. A false-colour SEM image of a typical ridge waveguide fabricated this way is shown in Figure 1b. Focussed ion beam (FIB) milling is used to cut through a waveguide cross-section, which is the reason for the line features at the edge of the waveguide. The FIB image reveals that the sidewalls resulting from the etching are near vertical, illustrating that the etch recipe is indeed highly anisotropic. Also visible in the image is the residual e-beam resist (labelled HSQ for Hydrogen silsesquioxane) on top of the waveguide.

Design of focussing grating couplers

We fabricate nanophotonic waveguides with a width of 1000 nm using the procedure outlined above. Here we employ partially etched ridge waveguides as shown in the image in Figure 1b. By using such a waveguide geometry, the optical mode is confined more deeply into the diamond thin film compared to fully etched strip waveguides. This way, scattering effects due to the remaining surface roughness are reduced. Furthermore, we do not remove the Fox15 silica layer on top of the waveguide, which provides a further alleviation of scattering on the diamond top surface.

In order to access the optical properties of the ridge waveguides light needs to be transmitted through on-chip devices. While traditional butt-coupling using optical fibres aligned to cleaved facets of photonic chips is commonly employed [25], such an approach requires careful positioning of the input–output fibres with respect to the waveguide, which is time consuming and not suitable for the investigation of large numbers of devices. Therefore, we employ an alternative approach using grating couplers, which scatter light propagating inside the diamond waveguide out of plane [26]. As a result, scattered light can be collected from the top of the chip, which makes the assessment of many devices on a chip much easier. We use focussing grating couplers as shown in the SEM image in Figure 2a. The design consists of a Bragg grating, that scatters light to first order into and out of the waveguide and then focusses it into the onset of the waveguide. The coupler provides a coupling bandwidth of 50 nm centred around a mean wavelength that is determined by the grating period [27,28]. As shown in the optical micrograph in Figure 2b we employ two grating couplers connected by a nanophotonic waveguide in order to assess the transmission properties of the device. The circuit is aligned to two optical fibres bundled into a fibre array with a fixed separation between the fibre cores.

To measure transmission through the device, light from a tunable laser source covering the wavelength range from 1510 nm to 1620 nm (New Focus Venturi 6600) is coupled into the input fibre. After propagating through the photonic device and being collected with a second fibre at the output coupling port, the transmitted signal is recorded with a low-noise photoreceiver (New Focus 2011). The device is aligned against the fibre array using a computer-controlled motorized three-axis piezo stage.

Typical spectra recorded from devices as shown in Figure 2b are shown in Figure 3a. The coupler provides a 3 dB coupling bandwidth of 50 nm centred in the fibre-optics C-band at

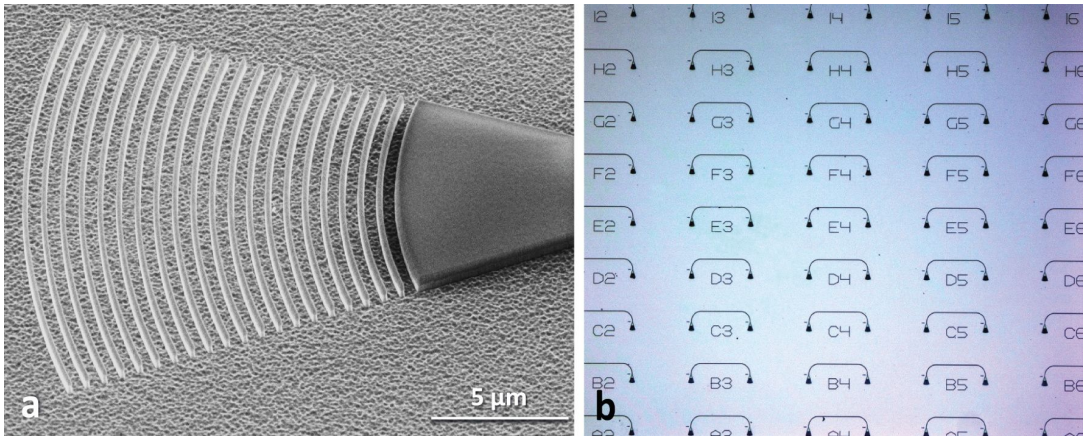

Figure 2: (a) SEM image of a fabricated focussing grating coupler. Light propagating through the incoming waveguide is scattered out of plane and collected by an optical fibre aligned to the grating section. (b) Optical microscope image of a fabricated chip containing several grating couplers connected by nanophotonic waveguides. The circuits enable characterization of the transmission profile of the grating couplers.

1555 nm. For optimized grating couplers we find a best coupling efficiency of −5.0 dB, which is on par with or slightly better than comparable structures reported in SOI [29]. For use at different wavelengths the coupler bandwidth can be shifted by adjusting the period of the grating. As shown in Figure 3b, the central coupling wavelength varies almost linearly with increasing grating period. The data is obtained by fitting measured spectra from different circuits of varying period with a Gaussian profile to extract the central coupling wavelength.

The coupler efficiency is strongly dependent on the depth of the grating etched into the diamond thin film. Therefore we fabricate several rounds of devices that are etched to different depths in order to find optimal coupling performance. In Figure 3c we show measured results for devices with varying etch depth. The best coupling efficiency of −5.0 dB per coupler is found for devices that are etched half way into the diamond layer (300 nm deep in our case). For weakly etched gratings the maximum coupling efficiency measured in the tuning range of the laser increases up to a depth of 300 nm. Upon further etching, the coupling efficiency decreases, due to increasing modal mismatch with the intensity profile of the input-coupling fibre. However, for each etching depth the linear dependence of the central coupling wavelength on the grating period is maintained. Therefore we select partial etching down to 300 nm as the default structure for the following section.

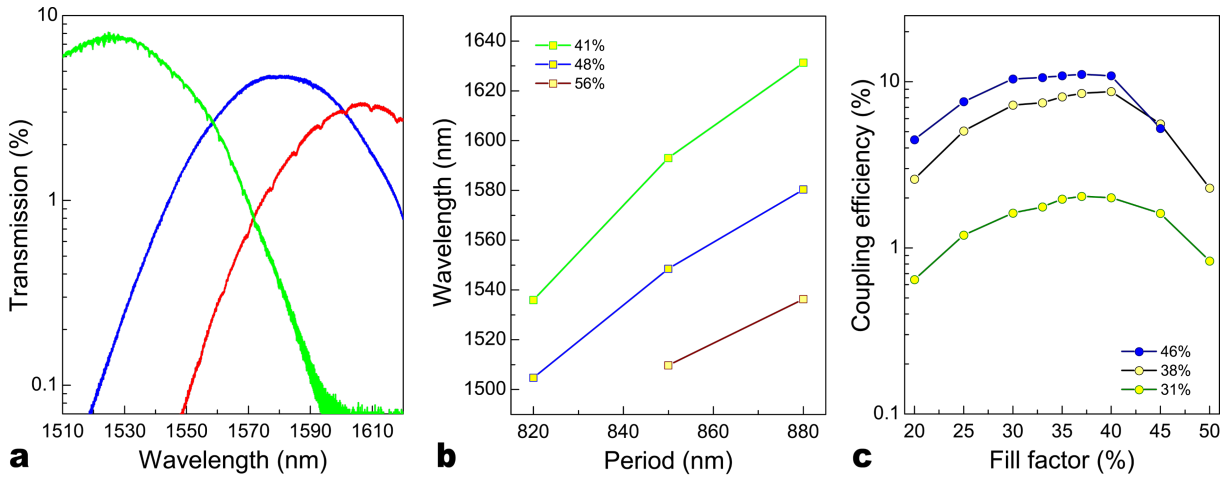

Figure 3: (a) Measured transmission spectrum of typical grating coupler devices. Best coupling loss at the central coupling wavelength of −5.0 dB is obtained. (b) The measured dependence of the central coupling wavelength on the grating period, which allows us to target specific wavelength windows over the coupler bandwidth of 50 nm. (c) The measured coupling efficiency for a pair of grating couplers in dependence of fill factor and etch depth. Optimal performance is obtained for gratings etched half way through the diamond layer.

Measurement of long waveguide devices

Having established a robust fabrication and measurement approach for diamond nanophotonic circuits we fabricate devices containing long waveguides in order to estimate the propagation loss on-chip. We fabricate photonic circuits with a waveguide length up to 4.6 mm. To accurately measure the propagation loss through such waveguides we design a three-terminal photonic circuit. Light coupled into the input waveguide is split evenly by using a 50/50 Y-shaped beam splitter. Half of the light is then guided towards a reference-grating coupling port. The other half of the light propagates through the long waveguide and is then collected at a third output port. By measuring the transmission through both the reference port and the output port we can thus perform balanced detection of the properties of the long waveguide. By normalizing the output intensity to the reference intensity, the coupling loss occurring at the grating coupler can be eliminated. Taking into account the propagation length of the reference arm, we then obtain a nominal propagation loss of 5.3 dB/mm. This value is a factor of five smaller than the propagation loss reported in [30]. As obvious from the AFM image in Figure 1a, the measured loss is likely due to scattering at the surface due to roughness. Such scattering loss can be quantitatively estimated by using the Payne–Laycey model [31,32]. The scattering loss α (in units of dB/unit length) scales quadratically with the surface roughness σ as

$$\alpha = 4.34 \frac{\sigma^2}{k_0 d^4 n} \cdot \frac{gf}{\sqrt{2}},$$

where k_0 is the free space wave vector, $2d$ is the height of the waveguide and n the refractive index of the waveguiding layer. The factor $\kappa = gf/\sqrt{2}$ consists of the analytical function g, which depends on the waveguide geometry and the function f, which depends on the index step of the waveguide and the correlation length of the surface roughness. Depending on the statistics used to describe the surface roughness, κ is bounded and an upper limit for α can be determined. For our waveguide geometry and the measured rms roughness of 15 nm the upper bound for scattering at the surface roughness is calculated as $\alpha \leq 6.0$ dB/mm for exponential statistics or $\alpha \leq 9.4$ dB/mm for Gaussian statistics, which is on the same order as the measured value for propagation loss in the diamond ridge waveguides. Since scattering loss is the dominant loss channel, in future work further improvement of the propagation loss will be possible by using surface polishing procedures to reduce the as-grown surface roughness.

Discussion

Our implementation of wafer-scale diamond-on-insulator substrates offers new possibilities for nanophotonic integrated circuits. In contrast to existing opinions, we show that microcrystalline CVD diamond provides a viable platform for fabricating nanophotonic waveguides. Here we have demonstrated essential components for the investigation of optical functionality on chip, including efficient coupling ports, optical wire waveguides, and on-chip beam splitters. The possibility to deposit diamond thin films on high quality substrates with diameters of commercial relevance enables the design and layout of large photonic circuits on-chip. Because of the broadband transparency of diamond and the good thermal properties, such devices may also be driven at high optical input power. Thus, our approach holds promise for the realization of optical functionality that is currently not available in silicon technology. While our initial demonstration proves the viability of the concept, in future work advanced concepts from the nanophotonic community may also be ported to our diamond platform in order to make DOI a new addition to integrated optics.

Acknowledgements

W.H.P. Pernice acknowledges support by DFG grant PE 1832/1-1. We also acknowledge support by the Deutsche Forschungsgemeinschaft (DFG) and the State of Baden-Württemberg through the DFG-Center for Functional Nanostructures (CFN) within subproject A6.04. The authors further wish to thank Silvia Diewald for assistance in device fabrication.

References

1. Kirchain, R.; Kimerling, L. *Nat. Photonics* **2007,** *1,* 303–305. doi:10.1038/nphoton.2007.84
2. Bruel, M. *Electron. Lett.* **1995,** *31,* 1201–1202. doi:10.1049/el:19950805
3. Celler, G. K.; Cristoloveanu, S. *J. Appl. Phys.* **2003,** *93,* 4955–4978. doi:10.1063/1.1558223
4. Bogaerts, W.; Baets, R.; Dumon, P.; Wiaux, V.; Beckx, S.; Taillaert, D.; Luyssaert, B.; Van Campenhout, J.; Bienstman, P.; Van Thourhout, D. *J. Lightwave Technol.* **2005,** *23,* 401–412. doi:10.1109/JLT.2004.834471
5. Jalali, B.; Fathpour, S. *J. Lightwave Technol.* **2006,** *24,* 4600–4615. doi:10.1109/JLT.2006.885782
6. Soref, R. *IEEE J. Sel. Top. Quantum Electron.* **2006,** *12,* 1678–1687. doi:10.1109/JSTQE.2006.883151
7. Lipson, M. *J. Lightwave Technol.* **2005,** *23,* 4222–4238. doi:10.1109/JLT.2005.858225
8. Eggleton, B. J.; Luther-Davies, B.; Richardson, K. *Nat. Photonics* **2011,** *5,* 141–148.
9. Wright, C. D.; Liu, Y.; Kohary, K. I.; Aziz, M. M.; Hicken, R. J. *Adv. Mater.* **2011,** *23,* 3408–3413. doi:10.1002/adma.201101060
10. Pernice, W. H. P.; Bhaskaran, H. *Appl. Phys. Lett.* **2012,** *101,* 171101. doi:10.1063/1.4758996
11. Hosseini, E. S.; Yegnanarayanan, S.; Atabaki, A. H.; Soltani, M.; Adibi, A. *Opt. Express* **2009,** *17,* 14543–14551. doi:10.1364/OE.17.014543

12. Xiong, C.; Pernice, W.; Ryu, K. K.; Schuck, C.; Fong, K. Y.; Palacios, T.; Tang, H. X. *Opt. Express* **2011,** *19,* 10462. doi:10.1364/OE.19.010462
13. Xiong, C.; Pernice, W. H. P.; Tang, H. X. *Nano Lett.* **2012,** *12,* 3562–3568. doi:10.1021/nl3011885
14. Koidl, P.; Wild, C.; Woerner, E.; Mueller-Sebert, W.; Fuener, M.; Locher, R. Diamond windows for infrared and multispectral applications. In *Proc. SPIE, Vol. 3436,* Infrared Technology and Applications XXIV, San Diego, CA, July 19, 1998; Andresen, B. F.; Strojnik, M., Eds.; SPIE Publications, 1998; pp 387–395. doi:10.1117/12.328035
15. May, P. W. *Philos. Trans. R. Soc., A* **2000,** *358,* 473–495. doi:10.1098/rsta.2000.0542
16. Aharonovich, I.; Greentree, A. D.; Prawer, S. *Nat. Photonics* **2011,** *5,* 397–405. doi:10.1038/nphoton.2011.54
17. Hausmann, B. J. M.; Shields, B.; Quan, Q.; Maletinsky, P.; McCutcheon, M.; Choy, J. T.; Babinec, T. M.; Kubanek, A.; Yacoby, A.; Lukin, M. D.; Lončar, M. *Nano Lett.* **2012,** *12,* 1578–1582. doi:10.1021/nl204449n
18. Faraon, A.; Barclay, P. E.; Santori, C.; Fu, K.-M. C.; Beausoleil, R. G. *Nat. Photonics* **2010,** *5,* 301–305. doi:10.1038/nphoton.2011.52
19. Babinec, T. M.; Hausmann, B. J. M.; Khan, M.; Zhang, Y.; Maze, J. R.; Hemmer, P. R.; Lončar, M. *Nat. Nanotechnol.* **2010,** *5,* 195–199. doi:10.1038/nnano.2010.6
20. Riedrich-Möller, J.; Kipfstuhl, L.; Hepp, C.; Neu, E.; Pauly, C.; Mücklich, F.; Baur, A.; Wandt, M.; Wolff, S.; Fischer, M.; Gsell, S.; Schreck, M.; Becher, C. *Nat. Nanotechnol.* **2012,** *7,* 69–74. doi:10.1038/nnano.2011.190
21. Beha, K.; Fedder, H.; Wolfer, M.; Becker, M. C.; Siyushev, P.; Jamali, M.; Batalov, A.; Hinz, C.; Hees, J.; Kirste, L.; Obloh, H.; Gheeraert, E.; Naydenov, B.; Jakobi, I.; Dolde, F.; Pezzagna, S.; Twittchen, D.; Markham, M.; Dregely, D.; Giessen, H.; Meijer, J.; Jelezko, F.; Nebel, C. E.; Bratschitsch, R.; Leitenstorfer, A.; Wrachtrup, J. *Beilstein J. Nanotechnol.* **2012,** *3,* 895–908. doi:10.3762/bjnano.3.100
22. Faraon, A.; Santori, C.; Huang, Z.; Acosta, V. M.; Beausoleil, R. G. *Phys. Rev. Lett.* **2012,** *109,* 033604. doi:10.1103/PhysRevLett.109.033604
23. Williams, O. A.; Douhéret, O.; Daenen, M.; Haenen, K.; Osawa, E.; Takahashi, M. *Chem. Phys. Lett.* **2007,** *445,* 255–258. doi:10.1016/j.cplett.2007.07.091
24. Füner, M.; Wild, C.; Koidl, P. *Appl. Phys. Lett.* **1998,** *72,* 1149. doi:10.1063/1.120997
25. Mahdi, S.; Grehn, M.; Al-Saadi, A.; Höfner, M.; Meister, S.; Eichler, H. J. *J. Nonlinear Opt. Phys. Mater.* **2011,** *20,* 509–523. doi:10.1142/S0218863511006315
26. Taillaert, D.; Bogaerts, W.; Bienstman, P.; Krauss, T. F.; Van Daele, P.; Moerman, I.; Verstuyft, S.; De Mesel, K.; Baets, R. R. *IEEE J. Quantum Electron.* **2002,** *14,* 949–955. doi:10.1109/JQE.2002.1017613
27. Li, M.; Pernice, W. H. P.; Tang, H. X. *Nat. Photonics* **2009,** *3,* 464–468. doi:10.1038/nphoton.2009.116
28. Fong, K. Y.; Pernice, W. H. P.; Li, M.; Tang, H. X. *Opt. Express* **2011,** *19,* 15098. doi:10.1364/OE.19.015098
29. Li, M.; Pernice, W. H. P.; Xiong, C.; Baehr-Jones, T.; Hochberg, M.; Tang, H. X. *Nature* **2008,** *456,* 480–484. doi:10.1038/nature07545
30. Checoury, X.; Neel, D.; Boucaud, P.; Gesset, C.; Girard, H.; Saada, S.; Bergonzo, P. *Appl. Phys. Lett.* **2012,** *101,* 171115. doi:10.1063/1.4764548
31. Payne, F. P.; Lacey, J. P. R. *Opt. Quantum Electron.* **1994,** *26,* 977–986. doi:10.1007/BF00708339
32. Yap, K. P.; Delâge, A.; Lapointe, J.; Lamontagne, B.; Schmid, J. H.; Waldron, P.; Syrett, B. A.; Janz, S. *J. Lightwave Technol.* **2009,** *27,* 3999–4008. doi:10.1109/JLT.2009.2021562

License and Terms

Beilstein Journal of Nanotechnology

Antiferromagnetic coupling of $TbPc_2$ molecules to ultrathin Ni and Co films

David Klar*[1], Svetlana Klyatskaya[2], Andrea Candini[3], Bernhard Krumme[1], Kurt Kummer[4], Philippe Ohresser[5], Valdis Corradini[3], Valentina de Renzi[3,6], Roberto Biagi[3,6], Loic Joly[7], Jean-Paul Kappler[7], Umberto del Pennino[3,6], Marco Affronte[3,6], Heiko Wende[1] and Mario Ruben[2,7]

Full Research Paper

Open Access

Address:
[1]Faculty of Physics and CENIDE, University Duisburg-Essen, Lotharstraße 1, 47048 Duisburg, Germany, [2]Institute of Nanotechnology, Karlsruhe Institute of Technology (KIT), 76344 Eggenstein-Leopoldshafen, Germany, [3]Centro S3, Istituto Nanoscienze - CNR, via Campi 213/a, I-41125 Modena, Italy, [4]ESRF, 6 rue Jules Horowitz, BP 220, F-38043 Grenoble Cedex, France, [5]Synchrotron SOLEIL, L'Orme des Merisiers, Saint-Aubin - BP 48, 91192 Gif-sur-Yvette, France, [6]Dipartimento di Scienze Fisiche, Informatiche e Matematiche, Università di Modena e Reggio Emilia, via Campi 213/A, I-41125 Modena, Italy and [7]Universite de Strasbourg, Institut de Physique et de Chimie des Materiaux de Strasbourg, CNRS UMP 7504, 23 Rue du Loess, 67034 Strasbourg Cedex 2, France

Email:
David Klar* - david.klar@uni-due.de

* Corresponding author

Keywords:
magnetic anisotropy; magnetic coupling; single molecule magnets; X-ray absorption spectroscopy

Beilstein J. Nanotechnol. **2013,** *4,* 320–324.
doi:10.3762/bjnano.4.36

Received: 04 March 2013
Accepted: 30 April 2013
Published: 21 May 2013

This article is part of the Thematic Series "Advances in nanomaterials". On the occasion of the 60th birthday of Professor Horst Hahn.

Guest Editors: H. D. Gleiter and T. Schimmel

Abstract

The magnetic and electronic properties of single-molecule magnets are studied by X-ray absorption spectroscopy and X-ray magnetic circular dichroism. We study the magnetic coupling of ultrathin Co and Ni films that are epitaxially grown onto a Cu(100) substrate, to an in situ deposited submonolayer of $TbPc_2$ molecules. Because of the element specificity of the X-ray absorption spectroscopy we are able to individually determine the field dependence of the magnetization of the Tb ions and the Ni or Co film. On both substrates the $TbPc_2$ molecules couple antiferromagnetically to the ferromagnetic films, which is possibly due to a super-exchange interaction via the phthalocyanine ligand that contacts the magnetic surface.

Introduction

Molecular spintronic devices as building blocks for future applications in information technology may be a big improvement and lead to higher efficiency [1-9]. Therefore several groups have studied the properties of potential organic molecules intensively over the past few years. Single-molecule magnets (SMMs) meet the requirements because of their magnetic remanence at low temperature without the need for long-range ordering. While most of the well-known SMMs consist of several interacting metal ions [10-13], bis(phthalocyaninato) terbium(III) ($TbPc_2$) has only one rare-earth ion, coordinated by two organic phthalocyanine ligands consisting of nitrogen, carbon and hydrogen atoms (Figure 1a). The SMM properties arise simply from the single ion anisotropy of the Tb ion exhibiting a total angular momentum of $J = 6$ [14]. The crucial point with regards to the applicability of magnetic molecules for industrial usage is the control of the magnetic properties. Mn- and Fe-porphyrin molecules were successfully coupled to ferromagnetic thin films, leading to the alignment of the magnetic moments of the metal ions parallel to the film [15-17] or antiparallel due to an interlayer of oxygen [18,19]. Recently, it was shown that $TbPc_2$ molecules can be magnetically coupled to a ferromagnetic Ni substrate [20]. The magnetic anisotropy and field dependence were also studied for $TbPc_2$ in a submonolayer on Cu(100) [21] and on antiferromagnetic substrates [22]. Spin quantum tunnelling at zero magnetic field leads to vanishing magnetization of the molecules, showing typical butterfly hysteresis [23-25]. Only at very low temperatures below 4 K is the relaxation slow enough for observation of magnetic remanence [26]. Here we demonstrate that it is possible to block this relaxation and conserve the magnetization without any external field by coupling the molecules to a ferromagnetic substrate. By X-ray absorption spectroscopy and X-ray magnetic circular dichroism we study the electronic and magnetic properties of a submonolayer coverage of $TbPc_2$ molecules on ultrathin Co and Ni films, focusing on the magnetic coupling between the substrate and the molecules.

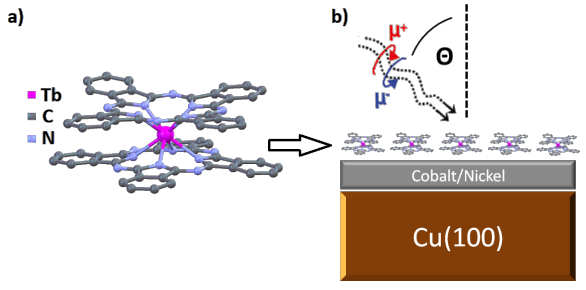

Figure 1: (a) The $TbPc_2$ molecule, consisting of two parallel phthalocyanine planes with the Tb ion centred in between and (b) a schematic illustration of the sample studied.

Results and Discussion

X-ray absorption spectroscopy of $TbPc_2$ molecules

Figure 2 shows spectra of circularly polarized (top) and linearly polarized X-rays (bottom) and the corresponding circular or linear dichroism at the Tb $M_{4,5}$ absorption edges of $TbPc_2$ on Cu(100). The XMCD signal has the shape typical for a Tb^{3+} ion, in agreement with what has been already reported for this molecule [20,21,24,25]. The high XMCD intensity at the M_5 edge and the low intensity at the M_4 edge indicate the large orbital moment of the Tb ion [27,28]. From the X-ray linear dichroism (XLD) at 45° X-ray incidence, one can deduce the orientation of the molecules. The typical shape at the M_5 edge, with the sign changing from negative to positive, indicates that the molecules lie flat, with the phthalocyanine planes parallel to the surface, as expected for the submonolayer coverage [25].

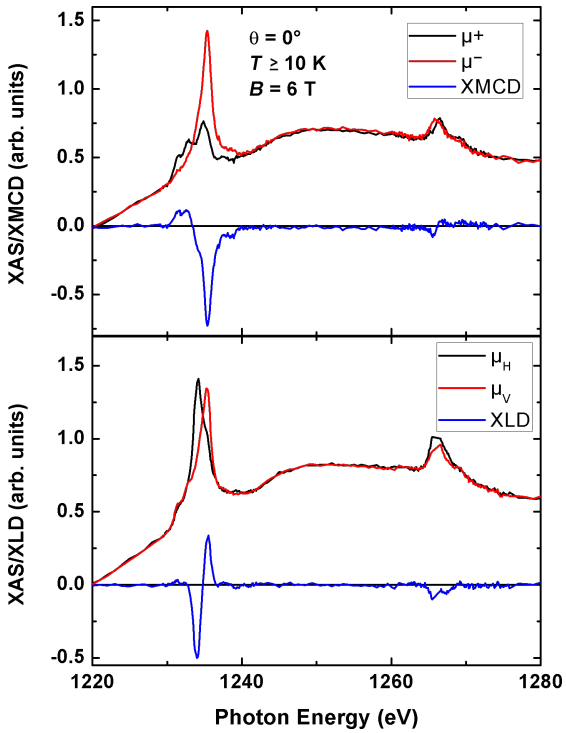

Figure 2: X-ray absorption spectra of the Tb $M_{4,5}$ edges for a submonolayer $TbPc_2$/Cu(100), measured at $T \geq 10$ K and $B = 6$ T. The top shows the spectra for circularly polarized X-rays (black and red) and the $\mu^+ - \mu^-$ = XMCD signal (blue) at perpendicular photon incidence (0°). The bottom figure shows the linearly polarized absorption spectra for an incidence angle of 45°. The red line corresponds to vertical polarization, where the electric field vector is parallel to the sample plane. The black line corresponds to horizontal polarization with an angle of 45° between the electric field vector and the sample surface. The blue line is the difference, i.e., the $\mu_V - \mu_H$ = XLD signal.

Magnetic coupling on a Ni surface

The 15 ML thick Ni film has a well-defined easy magnetic axis perpendicular to the plane [29] and the $TbPc_2$ molecule is known for its large magnetic anisotropy with the easy axis of magnetization perpendicular to the phthalocyanine plane [21]. Thus, the easy axis of the molecules is parallel to the one of the underlying Ni film. From the field-dependent XMCD at both Tb M_5 and Ni L_3 absorption edges presented in Figure 3, the influence of the Ni film on the magnetization of the molecules is visible. While the magnetic moments of Tb align parallel to the external magnetic field when the field is strong enough, they align antiparallel in a small magnetic field. This antiparallel alignment is caused by the magnetic coupling to the Ni substrate. At the top of Figure 3 one is able to identify the coupling by the magnetization sign changes. The signal crosses zero three times, twice when the exchange field and the external field cancel out each other and once when the Ni magnetization crosses zero. In the image below the coupling is even more visible. In this very small region around zero, one can see the remanence of the Ni substrate. For the Tb signal there is remanence as well, but with the opposite sign. The magnetization direction for Ni and Tb switch exactly at the same external field of about ±0.01 T, demonstrating the interaction between the molecules and the Ni film. Please note that the connecting lines for the Ni data in the upper picture of Figure 3 do not represent the Ni hysteresis curve, because of the low density of magnetic field steps. A more precise representation of the Ni hysteresis and the corresponding coercive field can be seen in the lower figure. Since the identical system was investigated by Lodi Rizzini et al. [20], it is remarkable that we obtain a significant difference in the exchange field and the amplitude of the antiparallel signal at the Tb M_5 edge, probably as a result of a weaker coupling. However, the main issue of the present manuscript is the demonstration of an antiferromagnetic coupling of rare-earth–Pc_2 molecules to ferromagnetic substrates. The quantitative analysis of the antiferromagnetic coupling strength goes beyond the scope of this manuscript. This can be achieved by experimental investigation by means of a detailed temperature-dependent XMCD study together with comparison to ab initio calculations, e.g., by utilizing density functional theory (DFT).

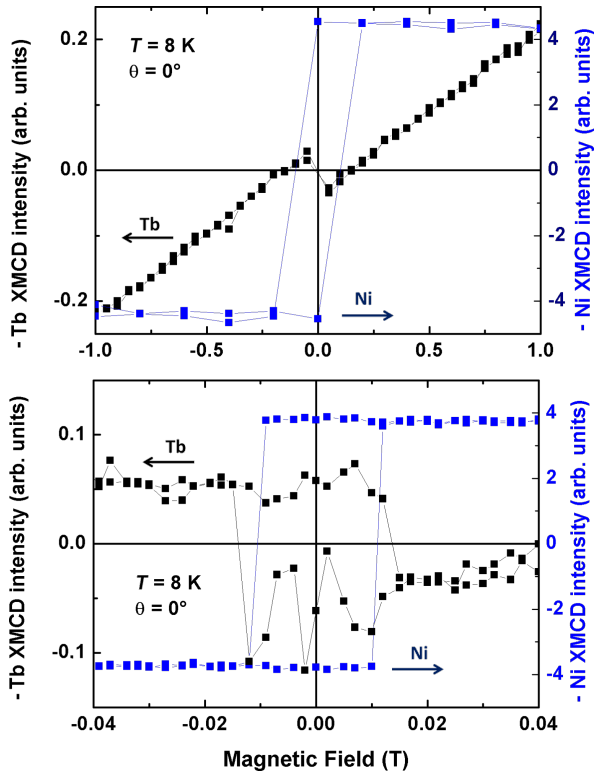

Figure 3: Element-specific field-dependent magnetization for the sample $TbPc_2$/Ni/Cu(100). The blue line is the magnetization curve at the maximum XMCD intensity of the Ni L_3 edge (852.5 eV), the black line is at the Tb M_5 edge (1235.4 eV). The top figure shows the curves from −1 T to 1 T and the bottom figure presents a zoom between −0.04 T and 0.04 T. The measurements were performed at T = 8 K under normal X-ray incidence (0°).

Magnetic coupling on a Co substrate

The important difference between the Co and the Ni substrate is the orientation of the magnetic easy axis that is parallel to the surface for the 10 ML thick Co film [30]. The magnetic coupling between the Co substrate and the molecule is therefore only between the out-of-plane component of the Co magnetization. The parallel component cannot polarize the molecules because of their large magnetic anisotropy [20]. The top graph of Figure 4 shows the magnetic signal of Tb in an external field between −6 T and 6 T. The shape is dominated by a paramagnetic signal that one would expect for a free molecule at a temperature of $T \approx 10$ K. But close to zero field the superposition of a second contribution becomes visible. In order to highlight the contribution, we subtracted the magnetization signal expected for the free molecule, which is simply a linear background at this temperature. The outcome is the lower graph of Figure 4. Compared to the Co magnetization curve (red line), one can see the antiparallel signal of the Tb magnetization. This antiferromagnetic contribution is very small compared to the dominating paramagnetic signal, because the Co magnetization direction is not in the direction of the molecular easy axis. If a very large coupling strength between the molecules and the Co substrate exceeds the magnetic anisotropy barrier, the magnetic moment of Tb could be forced in the plane. However, because of the large magnetic anisotropy barrier of the $TbPc_2$ molecules of 73 meV [20,31], we expect the magnetic moment of the Tb ions not to be forced to the in-plane direction by the Co magnetization since the coupling energies presented in [20] are in the regime of 1 meV. Nevertheless, this needs to be demonstrated, e.g., by angle-dependent measurements. In addition, the calcu-

lated coupling strength compared to the anisotropy energy would answer this question. But as mentioned above, this goes beyond the scope of this manuscript. Another reason for a smaller antiferromagnetic coupling strength may be the higher temperature for the measurements on Co (T ≥ 10 K) than on Ni (8 K). This temperature difference may cause changes in the field dependence of the XMCD, because a significant temperature dependence of the magnetic coupling is expected [20].

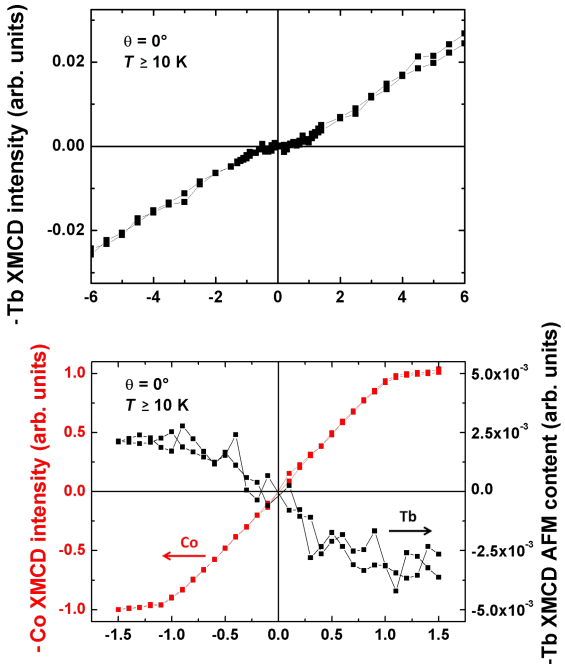

Figure 4: Magnetization curves for the sample $TbPc_2$/Ni/Cu(100). The top figure shows the magnetization curve at the maximum of the M_5 edge of Tb (1235.4 eV) from −6 T to 6 T. In the bottom figure one can see the magnetization curve at the maximum of the L_3 edge of the Co XMCD signal (778 eV) (red line) and the Tb M_5 curve after subtraction of a linear signal (black curve). The measurements were performed at perpendicular X-ray incidence at $T \geq 10$ K.

Conclusion

We have shown that the magnetic moments of $TbPc_2$ molecules can be ordered by coupling to a ferromagnetic substrate. At a temperature of 8 K it is possible to get a remanent magnetization, originating from an antiferromagnetic coupling to the Ni substrate. We observe an antiferromagnetic coupling also on the Co substrate, whose magnetic easy axis is in the plane and thus perpendicular to the one of the terbium(III) total angular momentum of $J = 6$. This antiferromagnetic contribution is much smaller than on the Ni film, partially due to the higher measuring temperature, but primarily because of the large magnetic anisotropy of the molecule. Therefore the magnetization curve is dominated by the paramagnetic signal.

Experimental

The samples were prepared in situ at a base pressure of 10^{-10} mbar directly before the measurements. By cycles of Ar^+ bombardment and annealing the Cu(100) surface was cleaned. Afterwards the ferromagnetic films were grown epitaxially via electron beam evaporation. The 10 ML thick Co film was produced with a rate of 0.5 ML/min and the 15 ML thick Ni film with a rate of 0.3 ML/min. The $TbPc_2$ molecules were thermally evaporated at a temperature of about 400 °C from a Knudsen cell onto the substrate held at room temperature.

The XAS measurements of the system $TbPc_2$/Co/Cu(100) were performed in magnetic fields up to 6 T at the DEIMOS beamline at the synchrotron SOLEIL, the XAS measurements of the system $TbPc_2$/Ni/Cu(100) in a magnetic field up to 4 T at the ID08 beamline at the ESRF. The lowest possible temperature was reached by cooling with liquid helium ($T = 4$ K), while the real temperature at the sample was limited by the quality of the thermal contact, leading to temperatures above 4 K. In detail we were able to measure at $T \approx 8$ K at the ESRF and $T \geq 10$ K at SOLEIL, although the temperature at the sample holder was 4 K.

To determine the thermal stability of $TbPc_2$, the sample was exposed to high-temperature sublimation under high vacuum in the sublimation apparatus consisting of a tube flask dipped into a heating mantle and a condenser. This method is carried out by heating 80 mg of the crude solid, while simultaneously evacuating the system. Upon reaching 400–420 °C at the bottom of the round flask and at a standard pressure in the system of about $2.8 \cdot 10^{-2}$ mbar, the sublimate appears on the cooled condenser. After 40 min about half of the crude solid was collected on the condenser. Both the sublimate and the residual molecules in the tube flask were exposed to mass-spectrometric and spectroscopic analysis as was the rest of the sample from a Knudsen cell. MALDI-TOF and UV–vis spectra did not reveal any difference compared to the initial sample. The presence of a binuclear complex (Tb_2Pc_3) in the MALDI-TOF spectrum as an evidence of thermal degradation was detected only in the rest of the sample in the tube flask after exposure to more than 450 °C for not less than 30 min. This allows us to assert that sublimation at 400 °C leaves the molecules unaffected.

Acknowledgements

One part of the experiments was performed on the DEIMOS beamline at SOLEIL Synchrotron, France (proposal number 20120073). We are grateful to the SOLEIL staff for smoothly running the facility. We also acknowledge the European Synchrotron Radiation Facility for financial support (Project HE 3739) and we would like to thank the beamline staff for assistance in using beamline ID08. This work was partially

supported also by the MIUR Project PRIN Contract No. 20105ZZTSE

References

1. Rocha, A. R.; García-Suárez, V. M.; Bailey, S. W.; Lambert, C. J.; Ferrer, J.; Sanvito, S. *Nat. Mater.* **2005,** *4,* 335–339. doi:10.1038/nmat1349
2. Bogani, L.; Wernsdorfer, W. *Nat. Mater.* **2008,** *7,* 179–186. doi:10.1038/nmat2133
3. Gambardella, P.; Stepanow, S.; Dmitriev, A.; Honolka, J.; de Groot, F. M. F.; Lingenfelder, M.; Sen Gupta, S.; Sarma, D. D.; Bencok, P.; Stanescu, S.; Clair, S.; Pons, S.; Lin, N.; Seitsonen, A. P.; Brune, H.; Barth, J. V.; Kern, K. *Nat. Mater.* **2009,** *8,* 189–193. doi:10.1038/nmat2376
4. Mannini, M.; Pineider, F.; Sainctavit, P.; Danieli, C.; Otero, E.; Sciancalepore, C.; Talarico, A. M.; Arrio, M.-A.; Cornia, A.; Gatteschi, D.; Sessoli, R. *Nat. Mater.* **2009,** *8,* 194–197. doi:10.1038/nmat2374
5. Urdampiletta, M.; Klyatskaya, S.; Cleuziou, J.-P.; Ruben, M.; Wernsdorfer, W. *Nat. Mater.* **2011,** *10,* 502–506. doi:10.1038/nmat3050
6. Candini, A.; Klyatskaya, S.; Ruben, M.; Wernsdorfer, W.; Affronte, M. *Nano Lett.* **2011,** *11,* 2634–2639. doi:10.1021/nl2006142
7. Vincent, R.; Klyatskaya, S.; Ruben, M.; Wernsdorfer, W.; Balestro, F. *Nature* **2012,** *488,* 357–360. doi:10.1038/nature11341
8. Schwöbel, J.; Fu, Y.; Brede, J.; Dilullo, A.; Hoffmann, G.; Klyatskaya, S.; Ruben, M.; Wiesendanger, R. *Nat. Commun.* **2012,** *3,* 953. doi:10.1038/ncomms1953
9. Ganzhorn, M.; Klyatskaya, S.; Ruben, M.; Wernsdorfer, W. *Nat. Nanotechnol.* **2013,** *8,* 165–169. doi:10.1038/NNANO.2012.258
10. Sessoli, R.; Gatteschi, D.; Caneschi, A.; Novak, M. A. *Nature* **1993,** *365,* 141–143. doi:10.1038/365141a0
11. Christou, G.; Gatteschi, D.; Hendrickson, D. N.; Sessoli, R. *MRS Bull.* **2000,** *25,* 66–71. doi:10.1557/mrs2000.226
12. Gatteschi, D.; Sessoli, R. *Angew. Chem., Int. Ed.* **2003,** *42,* 268–297. doi:10.1002/anie.200390099
13. Wernsdorfer, W.; Aliaga-Alcalde, N.; Hendrickson, D. N.; Christou, G. *Nature (London)* **2002,** *416,* 406–409. doi:10.1038/416406a
14. Rinehard, J. D.; Long, J. R. *Chem. Sci.* **2011,** *2,* 2078–2085. doi:10.1039/c1sc00513h
15. Scheybal, A.; Ramsvik, T.; Bertschinger, R.; Putero, M.; Nolting, F.; Jung, T. A. *Chem. Phys. Lett.* **2005,** *411,* 214–220. doi:10.1016/j.cplett.2005.06.017
16. Wende, H.; Bernien, M.; Luo, J.; Sorg, C.; Ponpandian, N.; Kurde, J.; Miguel, J.; Piantek, M.; Xu, X.; Eckhold, P.; Kuch, W.; Baberschke, K.; Panchmatia, P. M.; Sanyal, B.; Oppeneer, P. M.; Eriksson, O. *Nat. Mater.* **2007,** *6,* 516–520. doi:10.1038/nmat1932
17. Bernien, M.; Xu, X.; Miguel, J.; Piantek, M.; Eckhold, P.; Luo, J.; Kurde, J.; Kuch, W.; Baberschke, K.; Wende, H.; Srivastava, P. *Phys. Rev. B* **2007,** *76,* 214406. doi:10.1103/PhysRevB.76.214406
18. Bernien, M.; Miguel, J.; Weis, C.; Ali, M. E.; Kurde, J.; Krumme, B.; Panchmatia, P. M.; Sanyal, B.; Piantek, M.; Srivastava, P.; Baberschke, K.; Oppeneer, P. M.; Eriksson, O.; Kuch, W.; Wende, H. *Phys. Rev. Lett.* **2009,** *102,* 047202. doi:10.1103/PhysRevLett.102.047202
19. Chylarecka, D.; Wäckerlin, C.; Kim, T. K.; Müller, K.; Nolting, F.; Kleibert, A.; Ballav, N.; Jung, T. A. *J. Phys. Chem. Lett.* **2010,** *1,* 1408–1413. doi:10.1021/jz100253c
20. Lodi Rizzini, A.; Krull, C.; Balashov, T.; Kavich, J. J.; Mugarza, A.; Miedema, P. S.; Thakur, P. K.; Sessi, V.; Klyatskaya, S.; Ruben, M.; Stepanow, S.; Gambardella, P. *Phys. Rev. Lett.* **2011,** *107,* 177205. doi:10.1103/PhysRevLett.107.177205
21. Stepanow, S.; Honolka, J.; Gambardella, P.; Vitali, L.; Abdurakhmanova, N.; Tseng, T.-C.; Rauschenbach, S.; Tait, S. L.; Sessi, V.; Klyatskaya, S.; Ruben, M.; Kern, K. *J. Am. Chem. Soc.* **2010,** *132,* 11900–11901. doi:10.1021/ja105124r
22. Lodi Rizzini, A.; Krull, C.; Balashov, T.; Mugarza, A.; Nistor, C.; Yakhou, F.; Sessi, V.; Klyatskaya, S.; Ruben, M.; Stepanow, S.; Gambardella, P. *Nano Lett.* **2012,** *12,* 5703–5707. doi:10.1021/nl302918d
23. Gonidec, M.; Davies, E. S.; McMaster, J.; Amabilino, D. B.; Veciana, J. *J. Am. Chem. Soc.* **2010,** *132,* 1756–1757. doi:10.1021/ja9095895
24. Gonidec, M.; Biagi, R.; Corradini, V.; Moro, F.; De Renzi, V.; del Pennino, U.; Summa, D.; Muccioli, L.; Zannoni, C.; Amabilino, D. B.; Veciana, J. *J. Am. Chem. Soc.* **2011,** *133,* 6603–6612. doi:10.1021/ja109296c
25. Margheriti, L.; Chiappe, D.; Mannini, M.; Car, P.-E.; Sainctavit, P.; Arrio, M.-A.; Buatier de Mongeot, F.; Cezar, J. C.; Piras, F. M.; Magnani, A.; Otero, E.; Caneschi, A.; Sessoli, R. *Adv. Mater.* **2010,** *22,* 5488–5493. doi:10.1002/adma.201003275
26. Ishikawa, N.; Sugita, M.; Wernsdorfer, W. *Angew. Chem., Int. Ed.* **2005,** *44,* 2931–2935. doi:10.1002/anie.200462638
27. Thole, B. T.; Carra, P.; Sette, F.; van der Laan, G. *Phys. Rev. Lett.* **1992,** *68,* 1943–1946. doi:10.1103/PhysRevLett.68.1943
28. Carra, P.; Thole, B. T.; Altarelli, M.; Wang, X. *Phys. Rev. Lett.* **1993,** *70,* 694–697. doi:10.1103/PhysRevLett.70.694
29. Schulz, B.; Baberschke, K. *Phys. Rev. B* **1994,** *50,* 13467–13471. doi:10.1103/PhysRevB.50.13467
30. Schneider, C. M.; Bressler, P.; Schuster, P.; Kirschner, J.; de Miguel, J. J.; Miranda, R. *Phys. Rev. Lett.* **1990,** *64,* 1059–1062. doi:10.1103/PhysRevLett.64.1059
31. Ishikawa, N.; Sugita, M.; Okubo, T.; Tanaka, N.; Iino, T.; Kaizu, Y. *Inorg. Chem.* **2003,** *42,* 2440–2446. doi:10.1021/ic026295u

License and Terms

Beilstein Journal of Nanotechnology

Ferromagnetic behaviour of Fe-doped ZnO nanograined films

Boris B. Straumal[*1,2,3,4], Svetlana G. Protasova[2,3], Andrei A. Mazilkin[2,3], Thomas Tietze[3], Eberhard Goering[3], Gisela Schütz[3], Petr B. Straumal[4,5] and Brigitte Baretzky[1]

Full Research Paper

Open Access

Address:
[1]Karlsruher Institut für Technologie, Institut für Nanotechnologie, Hermann-von-Helmholtz-Platz 1, 76344 Eggenstein-Leopoldshafen, Germany, [2]Institute of Solid State Physics, Russian Academy of Sciences, Ac. Ossipyan str. 2, 142432 Chernogolovka, Russia, [3]Max-Planck-Institut für Intelligente Systeme, Heisenbergstrasse 3, 70569 Stuttgart, Germany, [4]National University for Research and Technology "MISiS", Leninsky prospect 4, 119991 Moscow, Russia and [5]Institute of Metallurgy and Materials Science, Russian Academy of Sciences, Leninsky prospect 49, 117991 Moscow, Russia

Email:
Boris B. Straumal[*] - straumal@mf.mpg.de

* Corresponding author

Keywords:
Fe; ferromagnetism; grain boundaries; ZnO

Beilstein J. Nanotechnol. **2013,** *4,* 361–369.
doi:10.3762/bjnano.4.42

Received: 23 February 2013
Accepted: 23 May 2013
Published: 13 June 2013

This article is part of the Thematic Series "Advances in nanomaterials".

Guest Editors: H. D. Gleiter and T. Schimmel

Abstract

The influence of the grain boundary (GB) specific area s_{GB} on the appearance of ferromagnetism in Fe-doped ZnO has been analysed. A review of numerous research contributions from the literature on the origin of the ferromagnetic behaviour of Fe-doped ZnO is given. An empirical correlation has been found that the value of the specific grain boundary area s_{GB} is the main factor controlling such behaviour. The Fe-doped ZnO becomes ferromagnetic only if it contains enough GBs, i.e., if s_{GB} is higher than a certain threshold value $s_{th} = 5 \times 10^4$ m^2/m^3. It corresponds to the effective grain size of about 40 μm assuming a full, dense material and equiaxial grains. Magnetic properties of ZnO dense nanograined thin films doped with iron (0 to 40 atom %) have been investigated. The films were deposited by using the wet chemistry "liquid ceramics" method. The samples demonstrate ferromagnetic behaviour with J_s up to 0.10 emu/g (0.025 μ_B/f.u.ZnO) and coercivity $H_c \approx 0.03$ T. Saturation magnetisation depends nonmonotonically on the Fe concentration. The dependence on Fe content can be explained by the changes in the structure and contiguity of a ferromagnetic "grain boundary foam" responsible for the magnetic properties of pure and doped ZnO.

Introduction

The possibility of ferromagnetism (FM) in oxides has been widely debated since 2000. In their theoretical work, Dietl et al. discussed the chances for oxides to possess saturation of magnetisation in an external magnetic field, coercivity, and a Curie temperature above room temperature (RT) [1]. According to their theory, FM could appear if one dopes the oxides (especially ZnO) with "magnetic" atoms such as Co, Mn, or Fe. Such transition-metal (TM) ions induce FM ordering into a magnetically polarized oxide lattice modified by doping. After publication of their paper [1] a lot of theoretical and experimental works were carried out in order to find the "promised" FM behaviour of zinc oxide (see [2-6] and references therein). However, the obtained results were quite contradictory. Several teams of experimentalists reported observations of weak but quite reproducible ferromagnetism. Other research groups never succeeded in synthesizing ferromagnetic ZnO. The huge interest in FM in ZnO is because it is a cheap semiconductor that is widely used in various devices and technologies. The FM behaviour, in addition to the attractive optical and semiconductor properties, could open the way for the future applications of FM ZnO in spintronics [2]. Recently we proposed an explanation for the contradictory results in the investigations of FM ZnO [6]. We observed, that FM behaviour does not appear in bulk ZnO (even doped by Mn or Co), but only in polycrystalline samples with very high specific area s_{GB} of grain boundaries (GBs), i.e., the ratio of GB area to grain volume [6]. Only in the case where the specific area of grain boundaries in ZnO exceeds a certain threshold called s_{th}, does the ferromagnetism appear. If s_{GB} is high enough, even the doping by TM ions is not essential, and FM appears in pure, undoped ZnO. The viewpoint that GBs are the reason for FM in ZnO became generally accepted in the past few years [3,7-16]. Therefore, it is important to continue the investigations into the GB-induced ferromagnetic behaviour of TM-doped ZnO. We were able to observe the FM behaviour even in pure ZnO due to the extremely small grain size in our films deposited by the original method of so-called "liquid ceramics", which is based on the application of organic acids for the solution of metallic ions for pure and Mn- and Co-doped ZnO [6,17,18].

The observed dependence of the saturation magnetization of Mn- and Co-doped ZnO on the Mn and Co concentration showed complicated nonmonotonic behaviour [17,18]. The concentration dependence for Co-doped ZnO films has one maximum [18], and the concentration dependence for Mn-doped ZnO films has two maxima [17]. The shape of the dependence of the saturation magnetization on the Mn and Co concentration is different for the Mn- and Co-doped nanograined ZnO manufactured by different methods. It is most probably controlled by the topology of the GB network (ferromagnetic GB foam) in the ZnO polycrystals. Our findings strongly suggest that GBs and related vacancies are the intrinsic origin of RT ferromagnetism. We can also suppose another reason for the fact that the concentration dependence of the saturation magnetization for Co-doped ZnO films has one maximum [18], and the concentration dependence for Mn-doped ZnO films has two maxima [17]. It is probably due to the fact that cobalt demonstrates only one oxidation state Co^{3+} whereas manganese can possess several oxidation states, namely +2, +3 and +4 [17,18]. Together with cobalt and manganese, iron is one of the most important dopants in ZnO. Similar to manganese, iron has different oxidation states (Fe^{2+} and Fe^{3+}). This fact prompts us to check, whether the concentration dependence of the saturation magnetization for Fe-doped ZnO films has one or two maxima. Therefore, the goals of this work are to determine the threshold value s_{th} of the specific GB area for Fe-doped zinc oxide and to analyse experimentally the influence of Fe on the saturation magnetization of ZnO in a broad interval of Fe concentrations.

Experimental

Pure and Fe-doped ZnO thin films consisting of dense equiaxial nanograins were produced by using the novel method of liquid ceramics [19]. Zinc(II) butanoate diluted in an organic solvent with zinc concentrations between 1 and 4 kg/m^3 was used as a precursor for the preparation of pure ZnO films. For the ZnO films that were doped with 0.1, 5, 12, 20, 31, and 40 atom % Fe, zinc(II) butanoate solution was mixed with an iron(III) butanoate solution in suitable proportions. The butanoate precursor was deposited onto (102) single-crystalline sapphire substrates. Drying at 100 °C in air for about 30 min was followed by thermal pyrolysis in an electrical furnace in air at 550 °C. The Zn and Fe content in doped oxides was measured by atomic absorption spectroscopy in a Perkin-Elmer spectrometer and electron-probe microanalysis (EPMA). EPMA investigations were carried out in a Tescan Vega TS5130 MM microscope equipped by the LINK energy-dispersive spectrometer produced by Oxford Instruments. The presence of other magnetic impurities, such as Mn, Co, and Ni, was below 0.001 atom %. During the long preparation procedure all possible precautions were taken to exclude any additional FM contaminations (for example, nonmagnetic ceramic scissors and tweezers, etc., were used). It is known from the literature [20] that the effect of a contaminated substrate can completely conceal the ferromagnetic signal of ZnO itself. We carefully measured the magnetization curves for bare Al_2O_3 substrates and subtracted them from data for the substrates including ZnO films. The films were transparent and sometimes with a very slight greenish finish. The films had a thickness between 50 and 200 nm, determined using edge-on transmission electron micro-

scopy (TEM) and EPMA. TEM investigations were carried out on a Jeol JEM–4000FX microscope at an accelerating voltage of 400 kV. X-ray diffraction (XRD) data were obtained on a Siemens diffractometer (Cu Kα radiation). Evaluation of the grain size D from the X-ray peak broadening was performed by using the Scherrer equation [21]. The magnetic properties were measured on a superconducting quantum interference device (Quantum Design MPMS-7 and MPMS-XL). The magnetic field was applied parallel to the sample plane ("in plane"). The diamagnetic background signals, generated by the sample holder and the substrate, were carefully subtracted, due to the small absolute magnetic moments measured in the range of 10^{-6} to 10^{-4} emu.

Results

Using the method of liquid ceramics, we deposited nanograined (the size of equiaxial grains was 10 to 30 nm) and poreless pure and Fe-doped ZnO thin films (see micrographs in Figure 1a). In the samples with 0.1, 5, 12, and 20 atom % Fe only pure quartzite grains are present, according to the studies with selected area diffraction (Figure 1b), TEM and XRD. These methods reveal the presence of ternary cubic zinc–iron oxide $ZnFe_2O_4$ in samples with 31 and 40 atom % Fe. No visible texture can be observed in the deposited thin films, namely the diffraction rings shown in Figure 1b are uniform without any preferred orientations of ZnO grains.

The observed FM behaviour in doped nanocrystalline as well as in dense ZnO films with 0.1 atom % Fe is depicted in Figure 2. Shown is the pronounced FM indicated by the saturation of magnetization ($J_s \approx 0.10$ emu/g or 0.025 μ_B/f.u.ZnO (units of Bohr magnetons per formula unit of ZnO) above the applied field ≈1.5 T) and hysteretic behaviour with coercivity $H_c \approx 0.03$ T (see the inset). These magnetization and coercivity values are close to those obtained by other methods for the Fe-doped samples [22-47].

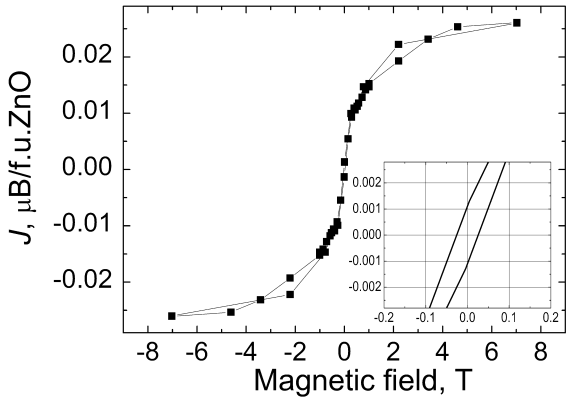

Figure 2: Magnetization (calibrated in units of Bohr magnetons per formula unit of ZnO) at RT for ZnO thin films doped with 0.1 atom % Fe deposited on the sapphire substrate. The curve was obtained after subtracting the magnetic contribution from the substrate and the sample holder. The inset shows the magnified central part of the magnetisation curve.

The saturation magnetization depends nonmonotonically on the Fe concentration (Figure 3). It increases more than ten times upon increase of the Fe content from 0 to 0.1 atom %. The magnetization drops down on further increase in Fe concentration and becomes almost indistinguishable from the background at around 20 atom % Fe. Above a concentration of 20 atom % Fe the magnetization increases again and reaches a value of about 0.09 emu/g (0.022 μ_B/f.u.ZnO) at 40 atom % Fe.

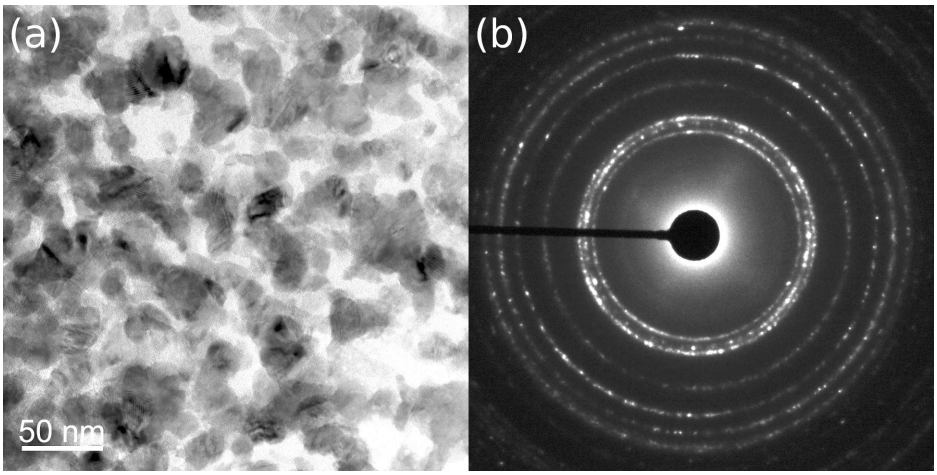

Figure 1: (a) Bright-field TEM micrograph of the nanograined pure ZnO thin film deposited on a sapphire substrate by the novel liquid ceramics method. Electron diffraction pattern (b) shows only rings from the ZnO wurtzite structure; no texture is visible. Bright spots originate from the sapphire substrate.

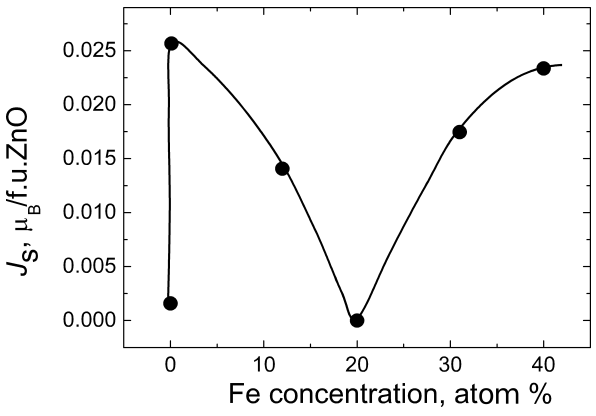

Figure 3: Dependence of the saturation magnetization J_s (magnetic moment in units of Bohr magnetons per ZnO formula units) on the Fe concentration in ZnO nanograined polycrystals obtained by the "liquid ceramics" method.

Discussion

We critically analysed the published papers on the search for possible ferromagnetic behaviour in the Fe-doped ZnO [22-66]. The results are summarized in Figure 4 in a T–s_{GB} plot (here T represents the annealing or synthesis temperature). They can be divided into three groups, depending on the s_{GB} value. First, the samples obtained by the magnetron and ion-beam sputter deposition or pulsed laser deposition (PLD) having small and very small grains are almost always ferromagnetic [22-47]. The respective (filled) points are grouping in the right part of the diagram in Figure 4. Second, the coarse-grained samples synthesised by the conventional powder sintering method, bulk single crystals or single-crystalline films are always diamagnetic or paramagnetic [48-55]. They are positioned in the left part of the diagram in Figure 4. In between one finds the third group of the data, namely obtained for the samples produced by chemical vapour deposition (CVD), solution combustion or wet chemistry methods. They have intermediate properties and can be either paramagnetic or FM [56-66].

We used different approaches in order to determine the value s_{GB}, the ratio of grain boundary area to volume, basing on the published data [22-66]. Quite frequently the grain size has been carefully measured in published works (using TEM micrographs or XRD peak broadening) and directly quoted in the text. For other works we estimated the grain size ourselves basing again on the published TEM micrographs or XRD spectra. In such cases the points in Figure 4 have substantial error bars. The single crystals and single crystalline films [26,49] have no GBs, and formally the s_{GB} value is zero for them. We choose the value of $s_{GB} = 4 \times 10^2$ m^2/m^3 in order to indicate such data in Figure 4 (open squares). If the samples studied in the literature were poreless and contain equiaxial

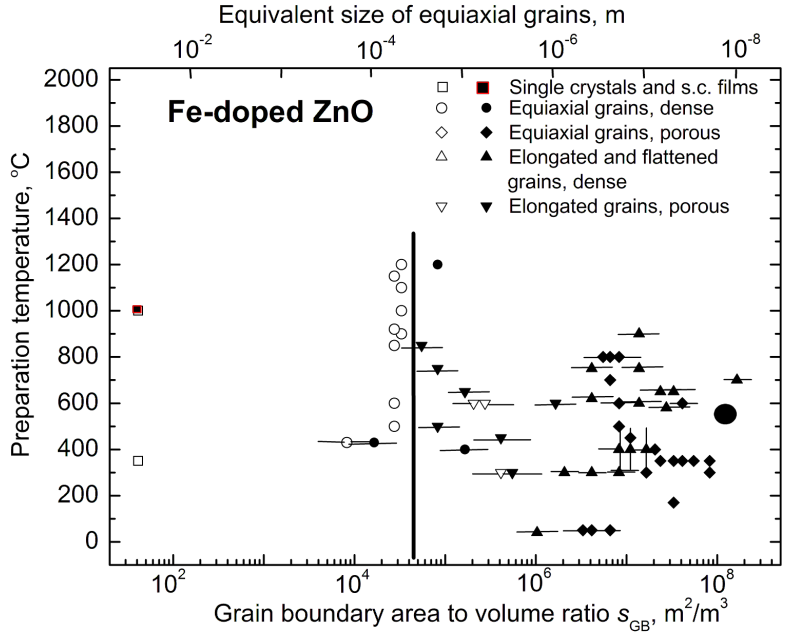

Figure 4: FM (full symbols) and para- or diamagnetic (open symbols) behaviour of Fe-doped ZnO in dependence on the specific GB area, s_{GB}, the ratio of GB area to volume, at different preparation temperatures T. A vertical line marks the estimated threshold value s_{th}. The enlarged symbol indicates the experimental data obtained by the authors' own investigations (for symbols and references see the text).

grains with mean grain size D, we calculated the s_{GB} as $s_{GB} = 1.65/D$. This formula is true for the space optimally filled with tetrakaidecahedrons (i.e., polyhedrons with 14 faces) [6]. It was used for the samples obtained by sintering of conventional [30,37,44,48-52,54,55,58,64] or nanopowders [24,29,32,41,42,46,53,56,59,65,66], or for films obtained by sol–gel method, pyrolysis, CVD or PLD [22,23,25,27,28,45]. If the samples mentioned in the analysed papers were not poreless, such as in the partly sintered powders (open and filled diamonds) [29,32,37,44,50,52,53,56,59,62,65], nanorods, or nanowires (open and filled down-triangles) [34,43,57,61], we introduced the additional porosity coefficient, p, for the s_{GB}. p varies from 0 for nonsintered powders to 1 for the fully compacted polycrystals. We estimated p values using the published micrographs. In many cases the samples were poreless; however, the grains were not equiaxial but elongated [31,33,38-40,60] or flattened [35,36,45,47,66] (open and filled up-triangles). In these cases $s_{GB} = 1.65a/D$, D is the mean grain width and a is the aspect ratio (ratio of grain width to grain height). For the flattened grains $a > 1$, for the elongated ones $a < 1$.

The results for Fe-doped ZnO are summarized in Figure 4 in a T-s_{GB} plot. Indeed, the results clearly reveal a dependence of the FM behaviour on s_{GB}. The samples are FM only for a certain threshold value s_{th}. For the Fe-doped ZnO $s_{th} = 5 \times 10^4$ m^2/m^3. For pure ZnO $s_{th} = 5.3 \times 10^7$ m^2/m^3 [6], for Mn-doped ZnO $s_{th} = 2.4 \times 10^5$ m^2/m^3 [6], and for Co-doped ZnO $s_{th} = 1.5 \times 10^6$ m^2/m^3 [18]. This means that the addition of "magnetic" TM atoms to the pure ZnO did indeed drastically improve the FM properties of pure ZnO, as originally supposed in [1]. Moreover, Fe improved the FM properties of pure zinc oxide more effectively than Co and Mn. For the transition from paramagnetic to FM behaviour in the Fe-doped ZnO one needs many times fewer GBs than in the Co- and Mn-doped ZnO. The reason for the s_{th} difference for the pure ZnO and ZnO doped by Fe, Mn and Co could be also the strong segregation of Fe, Mn and Co in ZnO GBs. According to the estimations made in [4,5], the GB concentration of Mn or Co in the ferromagnetic nanograined samples can be several times higher than in the bulk. Our samples (large filled circle in the right part of the Figure 4) have very fine grains (10–30 nm). The grains are almost the smallest among the Fe-doped ZnO samples reported in the literature [22-66]. This means that the minimum in the concentration dependence $J_s(c_{Fe})$ (Figure 3) or the minima in the equivalent dependences $J_s(c_{Co})$ [18] and $J_s(c_{Mn})$ [17] for Co- and Mn-doped ZnO cannot be attributed to the fact that the s_{GB} value is larger than s_{th}. On the other hand, it follows from Figure 3 that the s_{th} value could be different for different Fe concentrations. In other words, $s_{th} = s_{th}(c_{Fe})$ is generally concentration-dependent. For example for pure ZnO $s_{th} = 5.3 \times 10^7$ m^2/m^3. This means that the value $s_{th} = 5 \times 10^4$ m^2/m^3 (Figure 4) should be considered actually as the minimum possible one for the iron-doped ZnO.

In Figure 4 only the synthesis temperature and specific area of GBs are taken into account. However, the saturation magnetization J_s of the doped ZnO depends on the dopant concentration in a nontrivial manner (see for example [17]). In the case of Co-doped ZnO we also observed a strong increase of J_s for small amounts of Co added to pure ZnO [18]. The saturation magnetization decreased again above 5 atom % Fe. The presence of only one maximum in Co-doped ZnO [18] in comparison with Mn-doped ZnO [17] can be explained by the fact that the valence of Mn-ions changes from +2 to +3 and +4 with increasing Mn content and in the Co-doped ZnO Co always remains trivalent. Fe in ZnO can also change the valence from +2 to +3 [42,47,64,65]. Indeed, we observe a similar strong increase of J_s for small amounts of Fe added to pure ZnO (Figure 3). J_s increases more than ten times by the increase of Fe content from 0 to 0.1 atom %. The magnetization drops down at further increase in Fe concentration and becomes almost indistinguishable from the background at around 20 atom % Fe. The magnetization increases again above 20 atom % Fe and reaches a value above 0.09 emu/g (0.022 μ_B/f.u.ZnO) at 40 atom % Fe. However, we do not observe a second drop of J_s with increasing Fe content (as took place in Mn-doped ZnO). This means that the concentration dependence of J_s in Fe-doped ZnO (Fe can be either di- or trivalent) is indeed, as we supposed in the Introduction, in a certain sense intermediate between the dependences for Co- (always trivalent) and Mn-doped ZnO (the valence of Mn-ions changes from +2 to +3 and +4 with increasing Mn content).

A strong increase of J_s by the addition of the first portions of "magnetic" TM atoms to the pure ZnO appears to be a general phenomenon, as reported in [17,18] and this work. At least, we observed it in all three cases of Mn-, Co- and Fe-doping. This means that the arguments of seminal work [1] are quite reasonable. However, the important difference is that Dietl et al. [1] predicted the transition to TM behaviour in bulk ZnO and, as we can see from the Figure 4 and respective plots in [6] and [18], the bulk ZnO (single crystals or coarse-grained polycrystals) remains non-FM even after the strong doping. The presence of grain boundaries is critically important for the FM behaviour of the zinc oxide. Moreover, it is specifically the grain boundaries and not the free surfaces that are crucial for FM behaviour. For example, it has been observed that the nonsintered ZnO nanoparticles doped with 16 atom % Co obtained by forced hydrolysis were not ferromagnetic [67]. This was despite the fact that their grain size of 40 nm was well below the threshold value of 1 μm for the Co-doped ZnO [18].

However, the same powder becomes FM after annealing at 400 °C. The TEM investigations revealed that the annealing leads to the partial sintering of nanoparticles [67]. In other words, the annealing formed the grain boundaries and they, in turn, caused the ferromagnetism.

In [4,5] we compared the adsorption of Co and Mn in GBs and at free surfaces of zinc oxide. It has been observed that the presence of GBs and free surfaces drastically increases the total solubility of Co and Mn in ZnO. For example, the second bulk phase (Co_2O_3 or Mn_3O_4) appears at 550 °C in single-crystalline or coarse-grained ZnO if the concentration of Co exceeds 2 atom % [4] and that of Mn exceeds 12 atom % [5]. In fine-grained poreless ZnO films (D < 20 nm) the total solubility of Co at 550 °C exceeds 33 atom % [4] and that of Mn exceeds 30 atom % [5]. In the fine-grained (D < 20 nm) powders only free surfaces and almost no GBs are present. The solubility of Co and Mn in such powders also increases but to a much lower extent (up to about 8 atom % Co and 20 atom % Mn) [4,5]. Similar investigations of the grain size influence on the total solubility of Fe-doped ZnO are now in progress; they give comparable results and will be published elsewhere. Simple calculations performed in [4,5] showed that the drastic increase of the total solubility of Co and Mn with decreasing grain size is due to the multilayer adsorption of dopants in GBs (up to 10 monolayers) and free surfaces (2–4 monolayers). From this point of view, the doped ZnO differs a lot from the metallic alloys where such a multilayer adsorption was not observed and the grain-size effect on the total solubility is much weaker [68-70]. Moreover, it has been observed in the Cu–Bi alloys that the Bi segregation in free surfaces is much stronger than that in GBs [70]. Therefore, it seems that the internal porosity in pure and doped ZnO cannot bring a significant input into FM behaviour.

The drop of J_s at a few percent of Co, Mn or Fe also seems to be a general feature of ZnO doped by the "magnetic" TM atoms. We supposed in our first paper on Mn-doped ZnO that the first minimum in the $J_s(c_{Mn})$ dependence is caused by the valence change from Mn^{2+} to Mn^{3+} and further to Mn^{4+} [17]. However, later we observed that J_s in Co-doped ZnO also drops down between 10 and 15 atom % Co after it reached a maximum at 1.2 atom % Co [18]. This happens despite of the fact that the valence of Co ions in ZnO is constant at Co^{2+}. This means that the reason for the "first decrease" of J_s at a few per cent of "magnetic" TM atoms is not the valence change with increasing c_{TM}. Most probably, the change of valence is responsible for the $J_s(c_{TM})$ behaviour at higher concentrations of TM atoms (above 10 atom % TM). As we can see, Mn has three different valence states (Mn^{2+}, Mn^{3+} and Mn^{4+}) and the respective $J_s(c_{Mn})$ curve has three minima and two maxima [17]. Fe has two different valence states (Fe^{2+} and Fe^{3+}) and the respective $J_s(c_{Fe})$ curve has two minima and two maxima (Figure 4 in this work). The curve $J_s(c_{Co})$ for Co has only one maximum and two minima [18]. Therefore, we suppose that the "first minimum" between 1 atom % and 5–6 atom % of TM can be explained by the redistribution of doping atoms in the network of grain boundaries in TM-doped ZnO.

The nonmonotonic dependence of J_s on the Fe concentration has been observed in this work (Figure 3). A strong increase of J_s with the addition of small proportions of Fe atoms has been observed also in thin films with nanograined columnar structure deposited by magnetron sputtering (Figure 5, filled triangles) [38-40,63] and in samples synthesized by the conventional solid-state reaction having rather large (>10 μm) equiaxial grains [59]. If the ZnO films are deposited by magnetron sputtering, their J_s decreases above 5–8 atom % Fe with increasing iron content [39,63]. The ZnO samples obtained by mechanical alloying behave in a different way [64]. They demonstrate a very weak dependence of J_s on Fe content (see Figure 5, open circles).

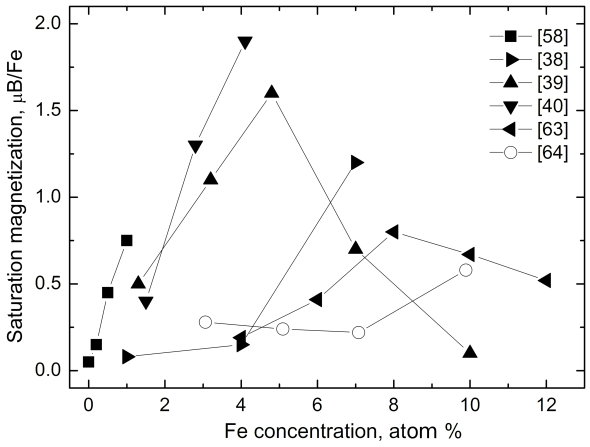

Figure 5: Dependence of the saturation magnetization (magnetic moment per iron atom in units of Bohr magnetons) on the Fe concentration in ZnO obtained by other methods such as magnetron sputtering (filled right- [38], up- [39], down- [40] and left-triangles [63]), solid-state reaction (filled squares [58]) and mechanical alloying (open circles [64]).

The plot in Figure 4 and respective plots in [6,18] demonstrate that the presence of a certain amount of GBs is needed to transform non-FM zinc oxide into a FM state. The comparison between Figure 3 and Figure 5 shows that not only the specific area of GBs but also their character distribution (i.e., the spectrum of GB misorientations and inclinations) influences the J_s

value. We observed previously that the texture or the amount of intergranular amorphous phase in the nanograined pure ZnO films drastically influences the FM properties even at the same grain size [68-70]. The GB structure also changes with increasing dopant content [71]. Moreover, by varying the synthesis conditions one can tailor the thickness of the amorphous intergranular layer and, thus, increase or decrease the J_s value [70]. It is well known that GBs with different character possess different adsorption ability [72,73]. If the GB networks have different topology, the GBs having various adsorption ability will be connected with each other in a different way. For example, the ZnO samples synthesized by the liquid ceramics method possess the uniform, equiaxial grains without visible pores inside [6,17,18,72-74]. The films deposited by the magnetron sputtering are also poreless and have columnar grains aligned perpendicular to the substrate [31,33,38-40,63]. Such samples, as well as sintered powders with equiaxial grains [58], have at low c_{Fe} the most similar $J_s(c_{TM})$ dependences (Figure 5) to our samples (Figure 3). The same is true also for the Mn- and Co-doped ZnO films [17,18]. If the contiguity of the GB network becomes weaker, as for example, in the samples composed of equiaxed nanograined balls, which in turn are loosely packed with each other (see Refs 25–29 in [17]), the first maximum in the $J_s(c_{TM})$ dependence becomes lower in comparison with the second one [17]. By further decrease of contiguity, such as in poreless samples with flattened grains (see Refs 24, 26, 28, and 92 in [18]), the $J_s(c_{TM})$ dependences becomes "stretched" along the c_{TM} axis, and the first maximum becomes shifted from 1 to about 10 atom % Co [18]. The continuous increase of J_s with increasing Co content in samples obtained by autocombustion or partly sintered nanorods (Refs 94 and 101 in [18]) can be considered as further "stretching" of the generic dependence shown in Figure 3. In other words, if the contiguity of the GB network (of "FM foam") becomes low, the "first maximum" is not reached even at c_{TM} = 20–25 atom % [18]. In the samples obtained by mechanical alloying the $J_s(c_{Fe})$ dependence is very weak [64].

Thus, if we compare the $J_s(c_{TM})$ dependences for the Co-, Mn- and Fe-doped ZnO films having a dense, poreless structure with equiaxial grains, on the one hand, with samples having lower contiguity of the GB network (porosity, flattened grains, etc.) on the other hand, we can suppose that there is a kind of "generic" $J_s(c_{TM})$ dependence. This can be observed in the poreless, dense samples with equiaxial grains. This "generic" $J_s(c_{TM})$ dependence becomes "stretched" in the c_{TM} direction if the contiguity of the GB network decreases. As a result, the first J_s maximum moves from 1 atom % to 5–10 atom % and then disappears above 20–25 atom %. As a result, in the samples with low contiguity of the GB network only a weak increase of J_s with increasing c_{TM} remains.

Conclusion

The influence of the specific area of grain boundaries s_{GB} on the presence or absence of ferromagnetism in Fe-doped ZnO has been analysed based on a review of numerous research contributions from the literature on the origin of the ferromagnetic behaviour of Fe-doped ZnO. An empirical correlation has been found that the value of the specific grain boundary area s_{GB} is the controlling factor for such behaviour. The Fe-doped ZnO becomes ferromagnetic only if it contains enough GBs, i.e., if s_{GB} is higher than a certain threshold value s_{th} = 5×10^4 m^2/m^3. It corresponds to the effective grain size of about 40 μm, assuming a full, dense material and equiaxial grains. The value of $s_{th} = 5 \times 10^4$ m^2/m^3 is lower than that for pure ZnO $s_{th} = 5.3 \times 10^7$ m^2/m^3, that for Mn-doped ZnO s_{th} = 2.4×10^5 m^2/m^3 and that for Co-doped ZnO $s_{th} = 1.5 \times 10^6$ m^2/m^3. This means that the addition of "magnetic" TM atoms to the pure ZnO did indeed drastically improve the FM properties of pure ZnO. Moreover, Fe improved the FM properties of pure zinc oxide more effectively than Co and Mn. We experimentally investigated the magnetic properties of Fe-doped ZnO thin films. The Fe concentration varies from 0 to 40 atom %. The thin films were deposited by using the wet-chemistry "liquid ceramics" method onto a sapphire substrate. The dense nanograined samples demonstrate ferromagnetic behaviour with J_s up to 0.10 emu/g (0.025 μ_B/f.u.ZnO) and coercivity $H_c \approx$ 0.03 T. Saturation magnetisation depends nonmonotonically on the Fe concentration. It increases more than tenfold by the increase of Fe content from 0 to 0.1 atom %. The magnetization drops down at a further increase in Fe concentration and becomes almost indistinguishable from the background at around 20 atom % Fe. Above 20 atom % Fe the magnetization increases again and reaches a value of about 0.09 emu/g (0.022 μ_B/f.u.ZnO) at 40 atom % Fe. In other published papers similar nonmonotonous dependences were observed in nanostructured films with elongated grains deposited by magnetron sputtering. These differences can be explained by the changes in the structure and contiguity of a ferromagnetic "grain boundary foam" responsible for the magnetic properties of pure and doped ZnO.

Acknowledgements

Authors thank the Russian Foundation for Basic Research (grants 11-03-00029, 11-08-90439, and 12-08-31185) for financial support.

References

1. Dietl, T.; Ohno, H.; Matsukura, F.; Cibert, J.; Ferrand, D. *Science* **2000,** *287,* 1019–1022. doi:10.1126/science.287.5455.1019
2. Sato, K.; Katayama-Yoshida, H. *Semicond. Sci. Technol.* **2002,** *17,* 367. doi:10.1088/0268-1242/17/4/309
3. Dietl, T. *Nat. Mater.* **2010,** *9,* 965–974. doi:10.1038/NMAT2898

4. Straumal, B. B.; Mazilkin, A. A.; Protasova, S. G.; Myatiev, A. A.; Straumal, P. B.; Baretzky, B. *Acta Mater.* **2008,** *56,* 6246–6256. doi:10.1016/j.actamat.2008.08.032
5. Straumal, B.; Baretzky, B.; Mazilkin, A.; Protasova, S.; Myatiev, A.; Straumal, P. *J. Eur. Ceram. Soc.* **2009,** *29,* 1963–1970. doi:10.1016/j.jeurceramsoc.2009.01.005
6. Straumal, B. B.; Mazilkin, A. A.; Protasova, S. G.; Myatiev, A. A.; Straumal, P. B.; Schütz, G.; van Aken, P. A.; Goering, E.; Baretzky, B. *Phys. Rev. B* **2009,** *79,* 205206. doi:10.1103/PhysRevB.79.205206
7. Karmakar, R.; Neogi, S. K.; Banerjee, A.; Bandyopadhyay, S. *Appl. Surf. Sci.* **2012,** *263,* 671–677. doi:10.1016/j.apsusc.2012.09.133
8. Hsu, C. Y. *Appl. Phys. Lett.* **2012,** *101,* 062416. doi:10.1063/1.4745845
9. Mohanty, P.; Mishra, N. C.; Choudhary, R. J.; Banerjee, A.; Shripathi, T.; Lalla, N. P.; Annapoorni, S.; Rath, C. *J. Phys. D* **2012,** *45,* 325301. doi:10.1088/0022-3727/45/32/325301
10. Zou, W. Q.; Ge, C. N.; Venkataiah, G.; Su, H. L.; Hsu, H. S.; Huang, J. C. A.; Liu, X. C.; Zhang, F. M.; Du, Y. W. *J. Appl. Phys.* **2012,** *111,* 113704. doi:10.1063/1.4720381
11. Burova, L. I.; Perov, N. S.; Semisalova, A. S.; Kulbachinskii, V. A.; Kytin, V. G.; Roddatis, V. V.; Vasiliev, A. L.; Kaul, A. R. *Thin Solid Films* **2012,** *520,* 4580–4585. doi:10.1016/j.tsf.2011.10.198
12. Chakrabarty, A.; Patterson, C. H. *Phys. Rev. B* **2011,** *84,* 054441. doi:10.1103/PhysRevB.84.054441
13. Liu, W.; Li, W.; Hu, Z.; Tang, Z.; Tang, X. *J. Appl. Phys.* **2011,** *110,* 013901. doi:10.1063/1.3601107
14. Potzger, K.; Osten, J.; Levin, A. A.; Shalimov, A.; Talut, G.; Reuther, H.; Arpaci, S.; Bürger, D.; Schmidt, H.; Nestler, T.; Meyer, D. C. *J. Magn. Magn. Mater.* **2011,** *323,* 1551–1562. doi:10.1016/j.jmmm.2011.01.018
15. Lin, M. N.; Hsu, H. S.; Lai, J. Y.; Guo, M. C.; Lin, C. Y.; Li, G. Y.; Chen, F. Y.; Huang, J. J.; Chen, S. F.; Liu, C. P.; Huang, J. C. A. *Appl. Phys. Lett.* **2011,** *98,* 212509. doi:10.1063/1.3593384
16. Zippel, J.; Lorenz, M.; Setzer, A.; Wagner, G.; Sobolev, N.; Esquinazi, P.; Grundmann, M. *Phys. Rev. B* **2010,** *82,* 125209. doi:10.1103/PhysRevB.82.125209
17. Straumal, B. B.; Protasova, S. G.; Mazilkin, A. A.; Myatiev, A. A.; Straumal, P. B.; Schütz, G.; Goering, E.; Baretzky, B. *J. Appl. Phys.* **2010,** *108,* 073923. doi:10.1063/1.3486044
18. Straumal, B. B.; Mazilkin, A. A.; Protasova, S. G.; Straumal, P. B.; Myatiev, A. A.; Schütz, G.; Goering, E.; Tietze, T.; Baretzky, B. *Philos. Mag.* **2013,** *93,* 1371–1383. doi:10.1080/14786435.2012.736693
19. Straumal, B.; Mazilkin, A.; Straumal, P.; Myatiev, A. *Int. J. Nanomanuf.* **2008,** *2,* 253–270. doi:10.1504/IJNM.2008.018948
20. Belghazi, Y.; Schmerber, G.; Colis, S.; Rehspringer, J. L.; Dinia, A.; Berrada, A. *Appl. Phys. Lett.* **2006,** *89,* 122504. doi:10.1063/1.2355462
21. Lábár, J. L. *Microsc. Microanal.* **2008,** *14,* 287–295. doi:10.1017/S1431927608080380
22. Shinagawa, T.; Izaki, M.; Inui, H.; Murase, K.; Awakura, Y. *Phys. Status Solidi A* **2006,** *203,* 2760–2764. doi:10.1002/pssa.200669600
23. Dorneles, L. S.; O'Mahony, D.; Fitzgerald, C. B.; McGee, F.; Venkatesan, M.; Stanca, I.; Lunney, J. G.; Coey, J. M. D. *Appl. Surf. Sci.* **2005,** *248,* 406–410. doi:10.1016/j.apsusc.2005.03.044
24. Liu, H.; Yang, J.; Zhang, Y.; Wang, Y.; Wei, M. *Mater. Chem. Phys.* **2008,** *112,* 1021–1023. doi:10.1016/j.matchemphys.2008.07.004
25. Feng, Q. J.; Shen, D. Z.; Zhang, J. Y.; Li, B. H.; Zhang, Z. Z.; Lu, Y. M.; Fan, X. W. *Mater. Chem. Phys.* **2008,** *112,* 1106–1109. doi:10.1016/j.matchemphys.2008.07.037
26. Tamura, T.; Ozaki, H. *J. Phys.: Condens. Matter* **2009,** *21,* 026009. doi:10.1088/0953-8984/21/2/026009
27. Zhang, B.; Li, Q. H.; Shi, L. Q.; Cheng, H. S.; Wang, J. Z. *J. Vac. Sci. Technol., A* **2008,** *26,* 1469–1473. doi:10.1116/1.2990855
28. Kumar, R.; Pratap Singh, A.; Thakur, P.; Chae, K. H.; Choi, W. K.; Angadi, B.; Kaushik, S. D.; Patnaik, S. *J. Phys. D: Appl. Phys.* **2008,** *41,* 155002. doi:10.1088/0022-3727/41/15/155002
29. Wei, Z.-R.; Li, Z.-Q.; Dong, G.-Y. *J. Magn. Magn. Mater.* **2008,** *320,* 916–918. doi:10.1016/j.jmmm.2007.09.017
30. Wang, Y. Q.; Yuan, S. L.; Liu, L.; Li, P.; Lan, X. X.; Tian, Z. M.; He, J. H.; Yin, S. Y. *J. Magn. Magn. Mater.* **2008,** *320,* 1423–1426. doi:10.1016/j.jmmm.2007.10.007
31. Seo, S.-Y.; Kwak, C.-H.; Lee, Y.-B.; Kim, S.-H.; Park, S.-H.; Han, S.-W. *J. Korean Phys. Soc.* **2008,** *52,* 805–809. doi:10.3938/jkps.52.805
32. Kimishima, Y.; Uehara, M.; Irie, K.; Ishihara, S.; Yamaguchi, T.; Saitoh, M.; Kimoto, K.; Matsui, Y. *J. Magn. Magn. Mater.* **2008,** *320,* e674–e677. doi:10.1016/j.jmmm.2008.04.025
33. Lee, H. Y.; Lee, J.; Na, G.; Nam, S.; Park, I.-H.; Park, J. H. *J. Korean Phys. Soc.* **2008,** *52,* 249–252. doi:10.3938/jkps.52.249
34. Xin, M.; Chen, Y.; Jia, C.; Zhang, X. *Mater. Lett.* **2008,** *62,* 2717–2720. doi:10.1016/j.matlet.2008.01.024
35. Jin, Z.; Fukumura, T.; Kawasaki, M.; Ando, K.; Saito, H.; Sekiguchi, T.; Yoo, Y. Z.; Murakami, M.; Matsumoto, Y.; Hasegawa, T.; Koinuma, H. *Appl. Phys. Lett.* **2001,** *78,* 3824–3826. doi:10.1063/1.1377856
36. Venkatesan, M.; Fitzgerald, C. B.; Lunney, J. G.; Coey, J. M. D. *Phys. Rev. Lett.* **2004,** *93,* 177206. doi:10.1103/PhysRevLett.93.177206
37. Zhang, H.-W.; Wei, Z.-R.; Li, Z.-Q.; Dong, G.-Y. *Mater. Lett.* **2007,** *61,* 3605–3607. doi:10.1016/j.matlet.2006.11.139
38. Wei, X. X.; Song, C.; Geng, K. W.; Zeng, F.; He, B.; Pan, F. *J. Phys.: Condens. Matter* **2006,** *18,* 7471–7479. doi:10.1088/0953-8984/18/31/037
39. Wang, X. C.; Mi, W. B.; Kuang, D. F. *Appl. Surf. Sci.* **2010,** *256,* 1930–1935. doi:10.1016/j.apsusc.2009.10.040
40. Wang, C.; Chen, Z.; He, Y.; Li, L.; Zhang, D. *Appl. Surf. Sci.* **2009,** *255,* 6881–6887. doi:10.1016/j.apsusc.2009.03.008
41. Kataoka, T.; Kobayashi, M.; Song, G. S.; Sakamoto, Y.; Fujimori, A.; Chang, F.-H.; Lin, H.-J.; Huang, D. J.; Chen, C. T.; Mandal, S. K.; Nath, T. K.; Karmakar, D.; Dasgupta, I. *Jpn. J. Appl. Phys.* **2009,** *48,* 04C200. doi:10.1143/JJAP.48.04C200
42. Liu, H.; Yang, J.; Zhang, Y.; Yang, L.; Wei, M.; Ding, X. *J. Phys.: Condens. Matter* **2009,** *21,* 145803. doi:10.1088/0953-8984/21/14/145803
43. Chen, X.; Zhou, Z.; Wang, K.; Fan, X.; Hu, S.; Wang, Y.; Huang, Y. *Mater. Res. Bull.* **2009,** *44,* 799–802. doi:10.1016/j.materresbull.2008.09.014
44. Karamat, S.; Ke, C.; Tan, T. L.; Zhou, W.; Lee, P.; Rawat, R. S. *Appl. Surf. Sci.* **2009,** *255,* 4814–4820. doi:10.1016/j.apsusc.2008.11.077
45. Hong, N. H.; Sakai, J.; Brizé, V. *J. Phys.: Condens. Matter* **2007,** *19,* 036219. doi:10.1088/0953-8984/19/3/036219
46. Mandal, S. K.; Das, A. K.; Nath, T. K.; Karmakar, D. *Appl. Phys. Lett.* **2006,** *89,* 144105. doi:10.1063/1.2360176
47. Wu, P.; Saraf, G.; Lu, Y.; Hill, D. H.; Gateau, R.; Wielunski, L.; Bartynski, R. A.; Arena, D. A.; Dvorak, J.; Moodenbaugh, A.; Siegrist, T.; Raley, J. A.; Yeo, Y. K. *Appl. Phys. Lett.* **2006,** *89,* 012508. doi:10.1063/1.2213519
48. Kolesnik, S.; Dabrowski, B.; Mais, J. *J. Appl. Phys.* **2004,** *95,* 2582–2586. doi:10.1063/1.1644638

49. Blasco, J.; Bartolomé, F.; García, L. M.; García, J. *J. Mater. Chem.* **2006,** *16,* 2282–2288. doi:10.1039/b518418e
50. Yoon, S. W.; Cho, S.-B.; We, S. C.; Yoon, S.; Suh, B. J.; Song, H. K.; Shin, Y. J. *J. Appl. Phys.* **2003,** *93,* 7879–7881. doi:10.1063/1.1556126
51. Hörlin, T.; Svensson, G.; Olsson, E. *J. Mater. Chem.* **1998,** *8,* 2465–2473. doi:10.1039/A805291C
52. Blasco, J.; Bartolomé, F.; García, L. M.; García, J. *J. Magn. Magn. Mater.* **2007,** *316,* e177–e180. doi:10.1016/j.jmmm.2007.02.080
53. Alaria, J.; Venkatesan, M.; Coey, J. M. D. *J. Appl. Phys.* **2008,** *103,* 07D123. doi:10.1063/1.2833840
54. Glaspell, G.; Dutta, P.; Manivannan, A. *J. Cluster Sci.* **2005,** *16,* 523–536. doi:10.1007/s10876-005-0024-y
55. Ahn, G. Y.; Park, S.-I.; Shim, I.-B.; Kim, C. S. *J. Magn. Magn. Mater.* **2004,** *282,* 166–169. doi:10.1016/j.jmmm.2004.04.039
56. Mandal, S. K.; Nath, T. K.; Karmakar, D. *Philos. Mag.* **2008,** *88,* 265–275. doi:10.1080/14786430701823205
57. Uum, Y. R.; Han, B. S.; Lee, H. M.; Hong, S. M.; Kim, G. M.; Rhee, C. K. *Phys. Status Solidi C* **2007,** *4,* 4408–4411. doi:10.1002/pssc.200777208
58. Han, S.-J.; Song, J. W.; Yang, C.-H.; Park, S. H.; Park, J.-H.; Jeong, Y. H.; Rhie, K. W. *Appl. Phys. Lett.* **2002,** *81,* 4212–4214. doi:10.1063/1.1525885
59. Mandal, S. K.; Nath, T. K.; Das, A. *J. Appl. Phys.* **2007,** *101,* 123920. doi:10.1063/1.2748614
60. Presmanes, L.; Capdeville, S.; Bonningue, C.; Datas, L.; Tailhades, P. *Thin Solid Films* **2007,** *515,* 6676–6681. doi:10.1016/j.tsf.2007.01.006
61. Kumar, S.; Kim, Y. J.; Koo, B. H.; Sharma, S. K.; Vargas, J. M.; Knobel, M.; Gautam, S.; Chae, K. H.; Kim, D. K.; Kim, Y. K.; Lee, C. G. *J. Appl. Phys.* **2009,** *105,* 07C520. doi:10.1063/1.3073933
62. Sharma, P. K.; Dutta, R. K.; Pandey, A. C.; Layek, S.; Verma, H. C. *J. Magn. Magn. Mater.* **2009,** *321,* 2587–2591. doi:10.1016/j.jmmm.2009.03.043
63. Zhao, R. B.; Hou, D. L.; Wei, Y. Y.; Zhou, Z. Z.; Pan, C. F.; Zhen, C. M.; Tang, G. D. *Mod. Phys. Lett. B* **2009,** *23,* 815–824. doi:10.1142/S0217984909019089
64. Lin, Y.; Jiang, D.; Lin, F.; Shi, W.; Ma, X. *J. Alloys Compd.* **2007,** *436,* 30–33. doi:10.1016/j.jallcom.2006.07.011
65. Karmakar, D.; Mandal, S. K.; Kadam, R. M.; Paulose, P. L.; Rajarajan, A. K.; Nath, T. K.; Das, A. K.; Dasgupta, I.; Das, G. P. *Phys. Rev. B* **2007,** *75,* 144404. doi:10.1103/PhysRevB.75.144404
66. Srivastava, A. K.; Deepa, M.; Bahadur, N.; Goyat, M. S. *Mater. Chem. Phys.* **2009,** *114,* 194–198. doi:10.1016/j.matchemphys.2008.09.005
67. Boubekri, R.; Beji, Z.; Elkabous, K.; Herbst, F.; Viau, G.; Ammar, S.; Fiévet, F.; von Bardeleben, H. J.; Mauger, A. *Chem. Mater.* **2009,** *21,* 843–855. doi:10.1021/cm802605u
68. Straumal, B.; Mazilkin, A.; Protasova, S.; Myatiev, A.; Straumal, P.; Goering, E.; Baretzky, B. *Phys. Status Solidi B* **2011,** *248,* 1581–1586. doi:10.1002/pssb.201001182
69. Straumal, B. B.; Mazilkin, A. A.; Protasova, S. G.; Myatiev, A. A.; Straumal, P. B.; Goering, E.; Baretzky, B. *Thin Solid Films* **2011,** *520,* 1192–1194. doi:10.1016/j.tsf.2011.04.154
70. Straumal, B. B.; Protasova, S. G.; Mazilkin, A. A.; Baretzky, B.; Myatiev, A. A.; Straumal, P. B.; Tietze, T.; Schütz, G.; Goering, E. *Mater. Lett.* **2012,** *71,* 21–24. doi:10.1016/j.matlet.2011.11.082
71. Straumal, B. B.; Myatiev, A. A.; Straumal, P. B.; Mazilkin, A. A.; Protasova, S. G.; Goering, E.; Baretzky, B. *JETP Lett.* **2010,** *92,* 396–400. doi:10.1134/S0021364010180074
72. Chang, L. S.; Rabkin, E.; Straumal, B. B.; Hofmann, S.; Baretzky, B.; Gust, W. *Defect Diffus. Forum* **1998,** *156,* 135–146. doi:10.4028/www.scientific.net/DDF.156.135
73. Chang, L.-S.; Rabkin, E.; Hoffmann, S.; Gust, W. *Acta Mater.* **1999,** *47,* 2951–2959. doi:10.1016/S1359-6454(99)00168-8
74. Straumal, B. B.; Mazilkin, A. A.; Protasova, S. G.; Dobatkin, S. V.; Rodin, A. O.; Baretzky, B.; Goll, D.; Schütz, G. *Mater. Sci. Eng., A* **2009,** *503,* 185–189. doi:10.1016/j.msea.2008.03.052

License and Terms

Beilstein Journal of Nanotechnology

Porous polymer coatings as substrates for the formation of high-fidelity micropatterns by quill-like pens

Michael Hirtz*[1], Marcus Lyon[2], Wenqian Feng[3], Andrea E. Holmes[2], Harald Fuchs[1,4] and Pavel A. Levkin*[3,5]

Full Research Paper

Open Access

Address:
[1]Institute of Nanotechnology (INT) and Karlsruhe Nano Micro Facility (KNMF), Karlsruhe Institute of Technology (KIT), Germany, [2]Department of Chemistry, Doane College, Crete, Nebraska, and the Center for Nanohybrid Functional Materials (CNFM), University of Nebraska-Lincoln, USA, [3]Institute of Toxicology and Genetics (ITG), Karlsruhe Institute of Technology (KIT), Germany, [4]Physical Institute and Center for Nanotechnology (CeNTech), University of Münster, Germany and [5]Applied Physical Chemistry, Heidelberg University, Germany

Email:
Michael Hirtz* - michael.hirtz@kit.edu; Pavel A. Levkin* - levkin@kit.edu

* Corresponding author

Keywords:
microarrays; microscale printing; microspotting; polymeric porous support; polymethacrylate; quill-like pens

Beilstein J. Nanotechnol. **2013,** *4,* 377–384.
doi:10.3762/bjnano.4.44

Received: 16 March 2013
Accepted: 29 May 2013
Published: 19 June 2013

This article is part of the Thematic Series "Advances in nanomaterials".

Guest Editors: H. D. Gleiter and T. Schimmel

Abstract

We explored the potentials of microarray printing using quill-like microcantilevers onto solid supports that are typically used in microspot printing, including paper, polymeric nitrocellulose and nylon membranes. We compared these membranes with a novel porous poly(2-hydroxyethyl methacrylate-*co*-ethylene dimethacrylate) support (HEMA) with narrow pore size distribution in the 150 nm range, which demonstrated advantages in pattern definition, spot homogeneity, and consistent spot delivery of different dyes (phloxine B and bromophenol blue) with diameters of several micrometres. The bromophenol blue arrays on HEMA support were used to detect the presence of bovine serum albumin (BSA). In the presence of BSA, the fluorescence spectrum observed from the bromophenol blue microarray exhibited a significant red shift of the maximum emission wavelength. Our results show that the porous HEMA substrates can improve the fidelity and quality of microarrays prepared by using the quill-like microcantilevers. The presented method sets the stage for further studies using chemical and biochemical recognition elements, along with colorimetric and fluorometric sensors that can be spotted by this method onto flat porous polymer substrates.

Introduction

Microarrays are of immense importance in many fields of biological research (e.g., genomics, proteomics, and cell analysis) and medical applications in diagnostics such as the detection of pathogens or antibodies. Nitrocellulose films and nylon membranes are widely used as carriers for microarrays, usually with spot sizes in the range of 100 to 500 µm, easily accessible for current inkjet and spotting techniques [1]. For scales of 100 µm and above, even plain paper was proposed as an inexpensive substrate for microfluidic devices [2,3]. However, when downsizing microarrays to the lower micrometer range with spot features in the range of a few tens of micrometres, the intrinsic granularity and broad pore size distribution of these substrates impairs pattern fidelity, quality and reproducibility. In addition, porous substrates that feature a large porous morphology are usually nontransparent due to the extensive light scattering, which reduces the sensitivity of readout systems utilizing such substrates.

Recently we introduced a method for the preparation of a porous biocompatible polymer coating on a solid substrate, using in situ free radical polymerization of methacrylate monomers in the presence of porogens [4]. Porous poly(2-hydroxyethyl methacrylate-*co*-ethylene dimethacrylate, HEMA) was shown to possess very high hydrophilicity due to the combination of the porous structure with the hydrophilic nature of the 2-hydroxyethyl methacrylate used as a monomer [5]. The small size and narrow size distribution of both pores and polymer globules (about 20–200 nm) resulted in high transparency of the polymer in the wetted state [4]. Such porous HEMA substrates were used for creating superhydrophilic–superhydrophobic micropatterned surfaces for cell-patterning [6] and cell-screening applications [7,8].

Here, we present an approach for the formation of high-fidelity microarrays of three-dimensional 20–50 micrometer sized spots inside a HEMA film, using quill-like microcantilevers. In contrast to nonporous substrates, porous films allow for the noncovalent infiltration of fluorescent sensors or dyes that can accommodate a greater volume and increased surface area for analyte binding. This should enhance sensitivity and yield a more reliable read out due to higher signal strength and less potential for cross contamination of sensors due to bleeding or trailing. The increased transparency of the porous HEMA substrates also allows for detection in transmission mode, which increases the versatility of this technique. Combined, these advantages of the porous HEMA substrates over plain surfaces and other porous substrates with larger pores or broader pore size distribution make them ideal candidates for creating high-fidelity micropatterns and microarrays by using the quill-like pens.

Results and Discussion

Pattern generation

The microarrays were fabricated by spotting the dye solution with quill-like microchannel cantilevers, called surface patterning tools (SPTs) [9], attached to a dip-pen nanolithography (DPN) platform (NLP 2000, NanoInk, USA) for precise control in *x*- *y*- and *z*-direction (Figure 1). After filling of the reservoir on the SPT with the dye solution, it is brought into contact with the substrate surface for a defined dwell time to allow a flow to the substrate by capillary forces. The SPT is retracted and moved to the next spotting position. The process of relocation, contacting and retracting is repeated until the desired spot features are created. The writing procedure can be relatively fast: our standard pattern of 100 spots arranged in a square with pitch of 50 µm (yielding a patterned area of 500 × 500 µm^2) with a dwell time of 0.5 s was written with a single cantilever in about a minute. However, technically the writing speed can be increased by the use of cantilever arrays, with the added option of intrinsic multiplexing [10].

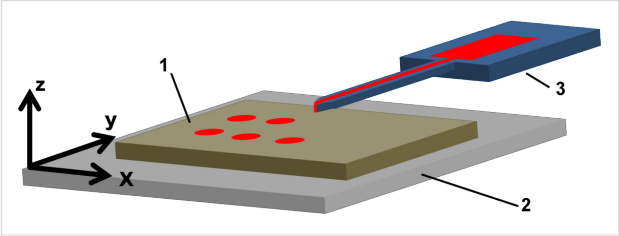

Figure 1: Dye delivery by microchannel cantilever. The substrate (1) is placed on the stage (2), which can be actuated with a precision of less than 100 nm in the *x*-, *y*-, and *z*-direction by piezoelectric actuators. By raising the stage in the *z*-direction the substrate can be brought into contact with the apex of the microchannel cantilever of the SPT (3) on which the dye solution reservoir is located.

Comparison of substrates

First, we compared four different substrate systems (i.e., plain paper, nylon membrane, nitrocellulose, and a HEMA porous polymer film, see Experimental section for exact type and suppliers) for their capability to serve as platforms for the microarrays generated by spotting with SPTs. Since porosity was considered as a key aspect for pattern fidelity, scanning electron microscopy (SEM) images of the different substrates were recorded to estimate pore size distribution and morphology (Figure 2).

The plain paper is of fibrous morphology, with dense fibres in the width range of 10 to 50 µm (Figure 2a) and gaps of about 50 µm. The microporous nylon membrane has a nominal pore size of 0.45 µm and is positively charged by quaternary ammonium groups (supplier specification). The average pore size obtained from SEM amounts to (0.79 ± 0.57) µm and is

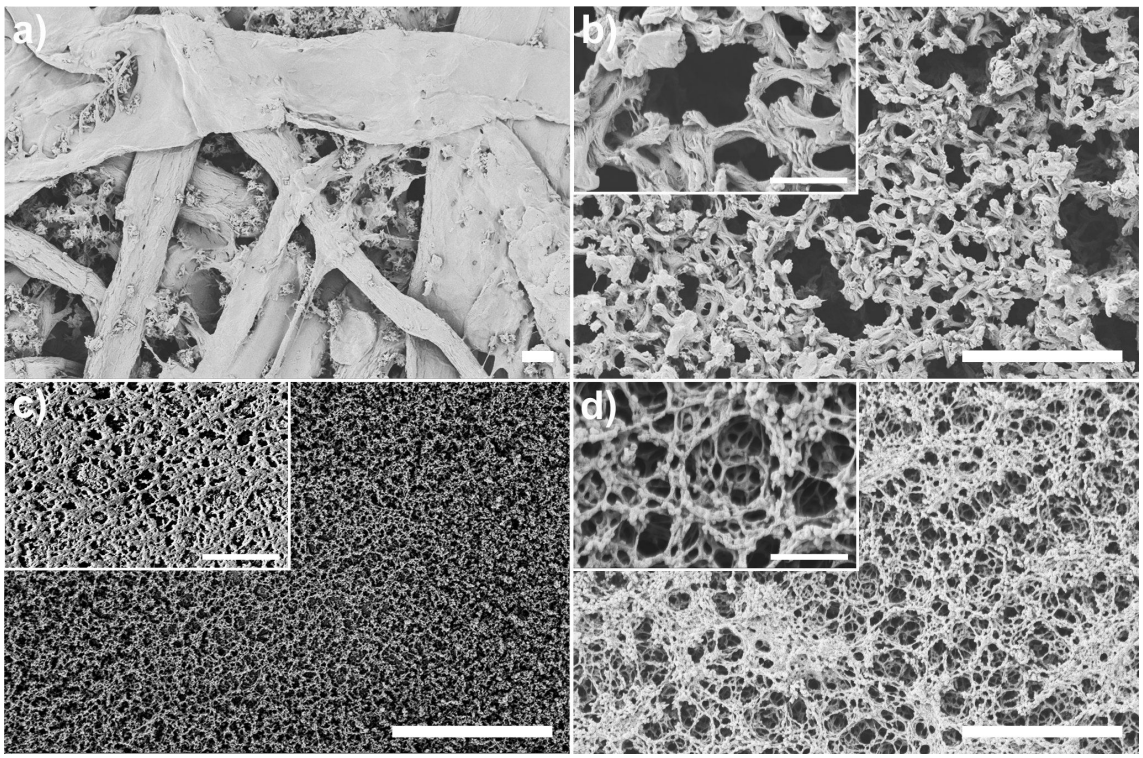

Figure 2: SEM images of the (a) plain paper, (b) nylon membrane, (c) HEMA polymer and (d) nitrocellulose substrates used for patterning. The scale bars respresent 10 µm in the main images and 2 µm in the insets.

compatible with the specification within one standard deviation, but the overall pore size distribution seems broad with many pores sizing up to almost 2 µm (Figure 2b). The porous HEMA substrate shows a highly porous (60% porosity based on the prepolymer mixture) structure of interconnected polymer globules, with the size of pores and globules being in the range of (0.15 ± 0.06) µm (Figure 2c). The thickness of the film is about 12.5 µm as adjusted by the spacers used in the preparation process. The nitrocellulose membranes with a thickness of 10 to 15 µm (supplier specification) is also highly porous with the average pore size estimated from SEM being (0.94 ± 0.37) µm. Figure 3 presents a histogram of the pore size distribution in the three different porous substrates. The HEMA substrate shows a much narrower distribution and smaller average pore size compared to the nylon membrane and nitrocellulose film. The paper substrate was not included in the plot due to its significantly larger pores and pore size distribution.

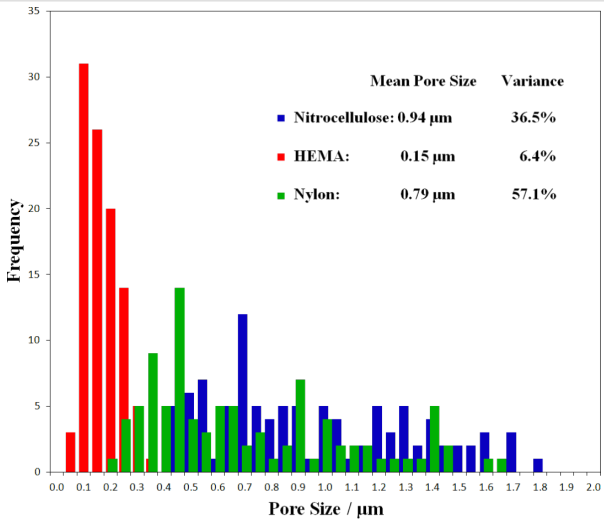

Figure 3: Pore size distribution based on SEM micrographs for the three different porous substrates, measured over 100 pores for each substrate. The mean pore size and variance for each porous substrate is given in the inset.

As shown in Figure 4, four different substrates were tested as platforms for the microarray spotting using SPTs. A pattern of 10 × 10 spots with a 50 µm pitch and dwell time of 0.5 s was written on each of the substrates by using a 10 mM solution of phloxine B in isopropanol mixed with 30 vol % glycerol (87% in water) to prevent drying of the dye solution in the SPT reservoir.

Bright field and fluorescent microscopy images demonstrate huge differences in the patterning outcome for the different substrates. Plain paper (Figure 4a and Figure 4e) does not consistently take up phloxine B from the SPT, presumably in part because of a large surface roughness (that might have

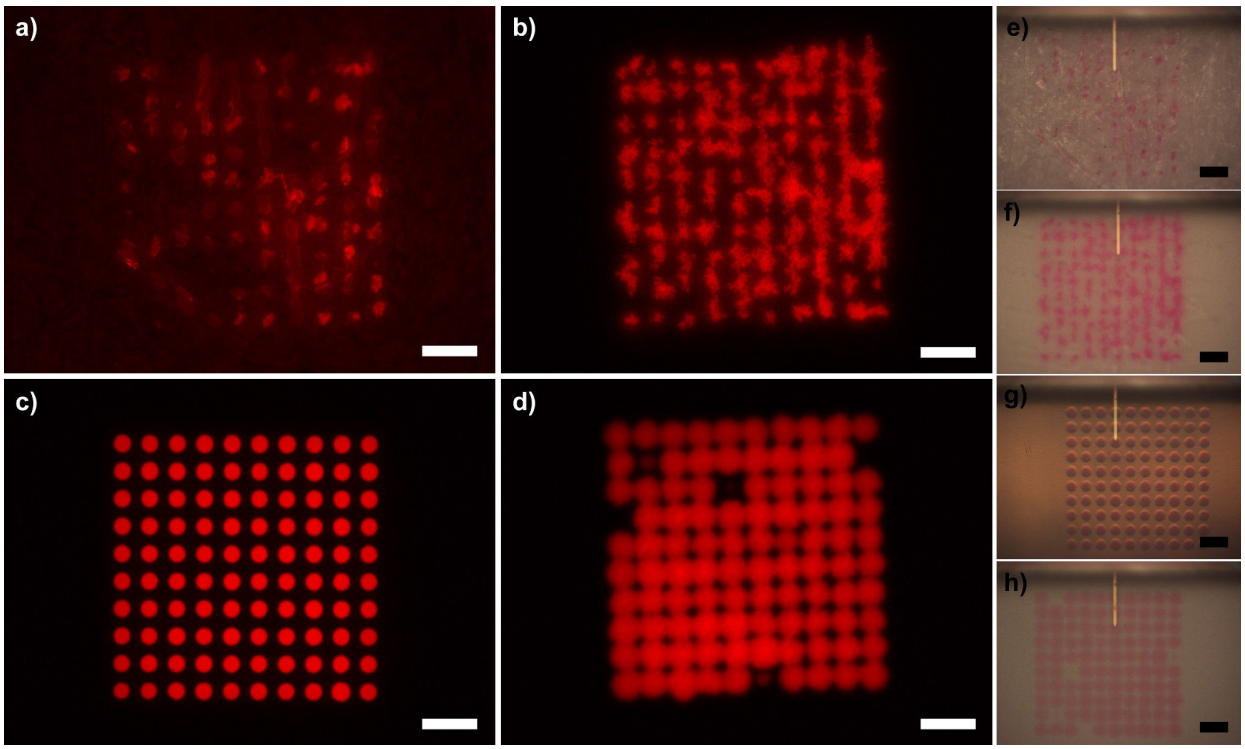

Figure 4: Comparison of printed phloxine B solution on different substrates. Fluorescence microscopy images of the printed solution on (a) paper, (b) nylon, (c) porous HEMA polymer film, and (d) nitrocellulose. Corresponding in situ bright-field images with delivery microchannel cantilever still in place for (e) paper, (f) nylon, (g) porous HEMA polymer film, and (h) nitrocellulose, respectively. Scale bars equal 100 µm.

prevented the SPT from touching the surface in some places) and because of inhomogeneous wetting behaviour due to the fibrous structure of the paper, as seen by sometimes brighter and sometimes fainter features. Overall the rough surface structure prevents clear homogenous patterning of phloxine B, and spreading is observed along the fibres that are tens to hundreds of micrometers long (see Supporting Information File 1, Figure S1 for combined bright field and fluorescence images). This behaviour is consistent with the observation that hydrophobic barriers have to be on the order of at least 200 µm to be effective in paper-based microfluidics [3]. Patterning on nylon membranes (Figure 4b and Figure 4f) shows a uniform wetting behaviour over the whole substrate area (visible by equal fluorescence intensity in the different features). However, similar distortions, as seen on the paper substrate, caused by the solution trailing along the nylon fibres of the membrane were observed. In both cases, this trailing is on the order of few tens of micrometers, which may be acceptable for spot sizes in the range of hundreds of micrometers as in conventional microarrays. However, patterning of microarrays with spot sizes in the lower micron range on such substrates becomes impractical. The porous nitrocellulose performs much better with regard to pattern fidelity (Figure 4d and Figure 4h), reflecting the fact that it is more homogeneous with smaller fibres and pore organisation as compared to paper and nylon membrane. However, compared with the pattern on porous HEMA (Figure 4c and Figure 4g) the pattern on nitrocellulose still has a much lower definition, with more diffuse spot edges and some missing features. The pattern on porous HEMA has by far the sharpest spot edges and most homogeneous spot distribution within the features.

Characterization of printing on porous HEMA substrate

Several experiments on the porous HEMA were performed to evaluate reproducibility and tunability. Three spot patterns of 100 spots (0.5 s dwell time) are shown in Figure 5a with an average spot radius of (16.0 ± 0.7) µm. The size distribution is narrow (Figure 5d) and symmetrical, showing very good pattern reproducibility with variance in radius of only 3.3%. The intensity within a spot is very uniform, with fluctuations of around 3% (profile inset in Figure 5a).

The size of the spots can be tuned by varying the dwell time (Figure 5b). By increasing the dwell time from 0.1 s to 2.0 s the radius of the spot features grows from (12.6 ± 0.1) µm to (22.8 ± 0.1) µm as seen in Figure 5e. Theoretically, for a liquid being absorbed by a porous media from a point source one

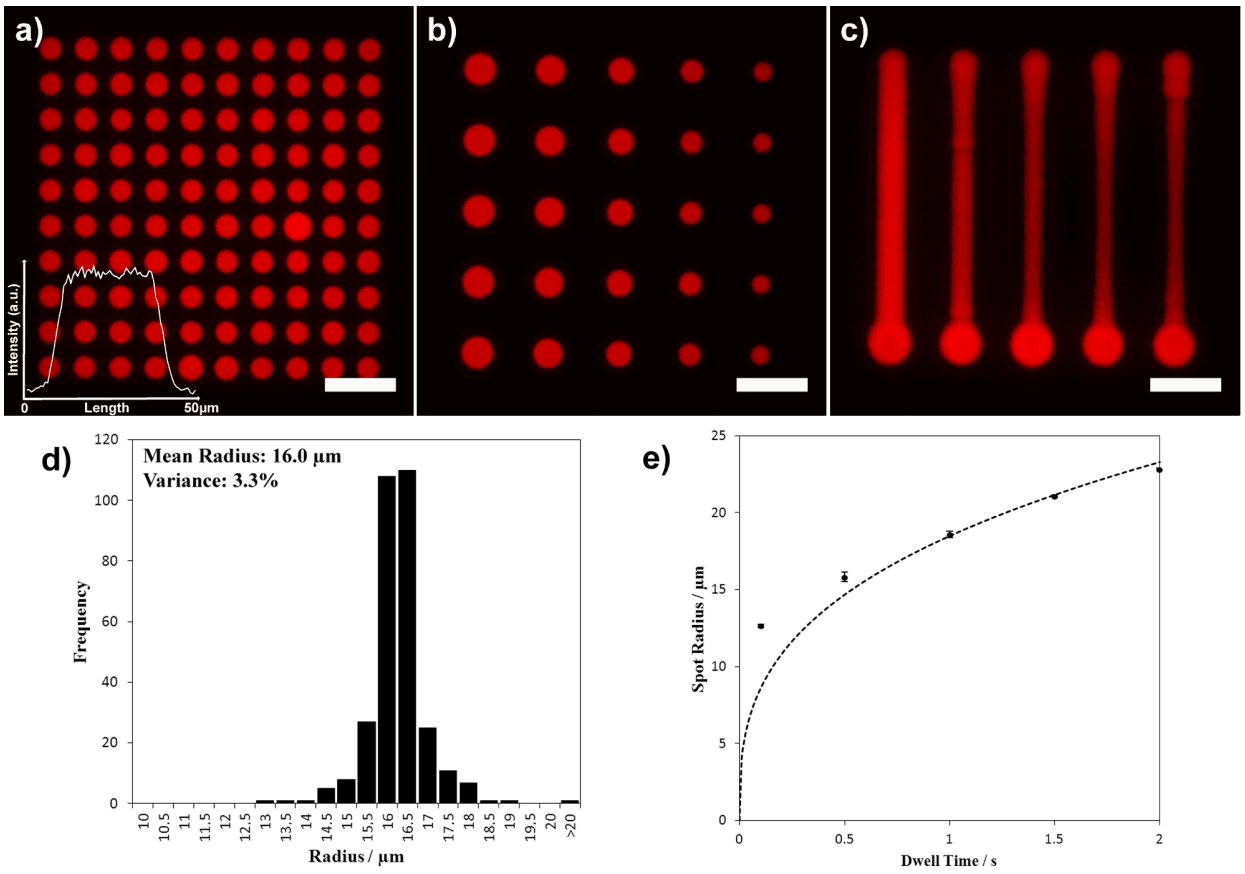

Figure 5: Time dependence and homogeneity of microprinting on porous polymer HEMA films. Fluorescent micrographs of (a) a spot pattern with 0.5 s dwell time, the inset shows the intensity profile of a typical spot, (b) spot pattern with varying dwell time (from left column to right 2.0 s, 1.5 s, 1.0 s, 0.5 s, and 0.1 s, respectively), and (c) lines written with different speeds (from left to right 50 µm/s, 100 µm/s, 150 µm/s, 200 µm/s, and 250 µm/s, respectively). Lines were written from bottom to top. All scale bars equal 100 µm. A histogram of the spot radius of the image in (a) combined with two more patterns generated under the same conditions for more statistics is given in (d). The dependence of spot radius on the dwell time as derived from the image in (c) is given in (e), dashed line denotes a plot of $y = A \cdot x^{1/3}$ with $A = 18.5$.

should expect a growth in radius with a dependence $r \sim t^{1/3}$, denoted by the dashed line [11]. Our results deviate from this trend for the low dwell time of 0.1 s, which can be understood when taking into account that the theory postulates a point source for the liquid flow. In contrast, the SPT used in our experiments has a finite apex opening in the low micrometre range, therefore generating bigger spots than may be theoretically expected for short dwell times.

By moving the SPT over the substrate while keeping contact, line patterns can be generated with the line width depending on the speed of movement (Figure 5c). The lines were written from bottom to top with speeds of 50 µm/s (left line) up to 250 µm/s (right line) yielding line widths from about 22 µm to 12 µm width. The start point of the line is demarked by a bigger spot, since the DPN instrument pauses shortly after contacting the SPT with the surface before drawing the line. Especially for the higher velocity lines, there is a widening visible at the start and end of the lines. This is caused by the acceleration and deceleration, respectively, of the piezo positioning table of the instrument before reaching the target speed or when slowing down before the end of a line.

For microarray printing, the inherent three-dimensional porosity is advantageous over flat substrates, such as glass, because subsurface regions under a spot can act as a binding area for the spotted sensor solution and later on for the target analyte.

In our experiments, five times longer exposure times were needed for the plain paper and nylon substrates in comparison to the HEMA substrate to reach equal fluorescence intensity in the images (50 ms for plain paper and nylon membrane compared to 10 ms to HEMA, the nitrocellulose falls in between with 40 ms). This could be explained by the larger surface area and better transparency of the porous HEMA in comparison to the other substrates. The three-dimensional

porous structure, improved transparency, and the large specific surface area can lead to considerably higher sensitivity when compared to substrates with the same surface area (see Supporting Information File 1 for comparison to a flat glass substrate, Figure S2).

Detection of BSA with bromophenol blue pattern

We used the HEMA substrate as a platform for demonstrating a microarray sensor application using bromophenol blue as a sensor, which is a dye commonly used in lateral flow devices to detect proteins in biological samples [12,13]. After preparing 10 × 10 spot microarrays using bromophenol blue solution as shown in the inset of Figure 6b, the patterns were either incubated with a 0.5 µL droplet of an analyte solution containing bovine serum albumin (BSA) or a clear solution to give a negative control. Fluorescence spectra obtained on the samples prior to and after incubation are shown in Figure 6b. Additionally, Figure 6a gives the corresponding fluorescence spectra of macroscopic droplets of the dye solutions with and without the addition of BSA for comparison.

All spectra were normalized to have equal intensity at the filter cut-off wavelength of 510 nm. The spectra of the patterns in Figure 6b were multiplied by a factor of 2 to demonstrate the spectroscopic changes more clearly. Figure 6a shows the fluorescence spectra of macroscopic droplets as shown in the inset. The fluorescence spectrum of the bromophenol in a macroscopic droplet (black curve) shows a very pronounced shift to the red after addition of BSA containing analyte solution (red

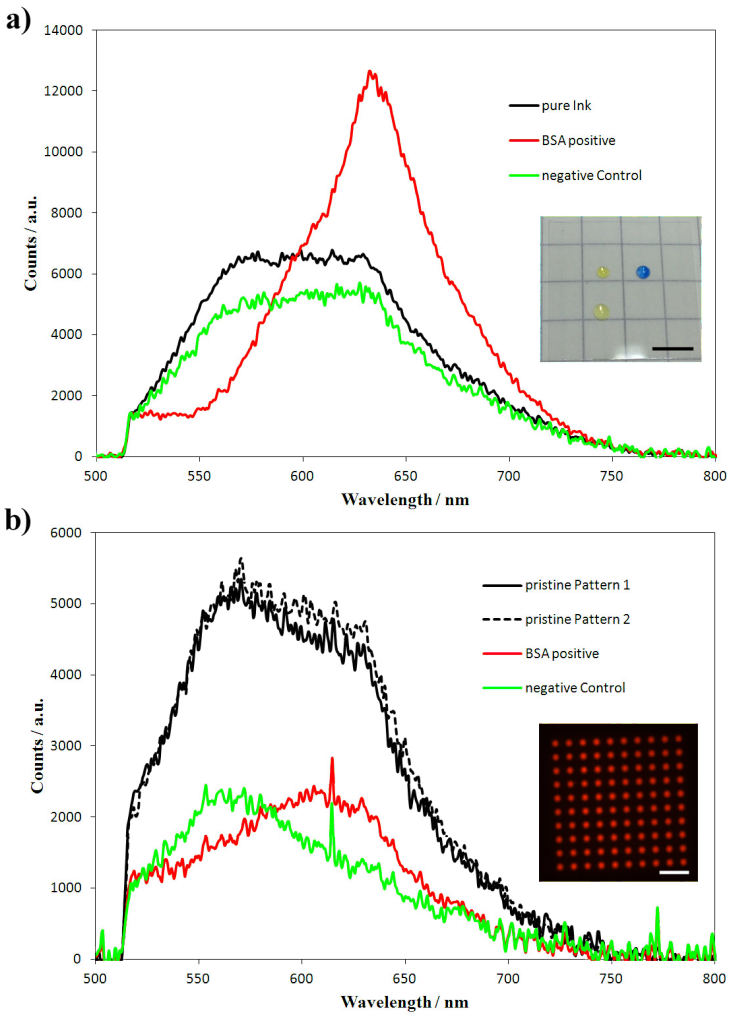

Figure 6: Fluorescence spectra of (a) macroscopic droplets of pure bromophenol blue dye solution (black), dye solution admixed with BSA (red), and dye solution admixed with a BSA free solution (green) as negative control (inset shows a photograph of the macroscopic droplets on a cover glass, pure dye solution at the top left, BSA positive at the top right and negative control at the bottom left position; scale bar equals 5 mm) and (b) of the pristine bromophenol blue pattern after lithography (black) and after incubation with BSA solution (red) or a solution not containing BSA (green), respectively (inset shows a fluorescence microscopy image of one of the pristine bromophenol blue patterns, scale bar equals 100 µm).

curve), while the spectrum shape remains unaltered on addition of a control solution containing no BSA (green curve). For the bromophenol blue microarrays we obtain similar results (Figure 6b). The spectra of two patterns are given in black; the green curve shows the spectrum after incubation with a test solution containing no BSA and the red curve after incubation with a test solution containing 10% BSA. Again a substantial bathochromic shift in fluorescence distinguishes the control sample from a sample incubated with BSA.

Conclusion

Four different substrates were tested for low-micrometre microarray printing with quill-like microcantilevers. We demonstrated that the porous HEMA polymer films exhibited advantageous properties for creating micropatterns with feature sizes below 50 µm. We showed that the narrow pore size distribution as well as the small average pore size is crucial for achieving high pattern fidelity and reproducibility. Additionally, the three-dimensional morphology in nanoporous substrates like the HEMA polymer films presents a higher surface area for binding of analytes, potentially giving rise to increased sensitivity in sensor applications. The pattern formation by SPTs can be tuned by varying the dwell time, or in the case of line patterns, by using different writing speeds. The basic feasibility of the HEMA as substrate for microarray-based sensor applications was demonstrated by the detection of BSA with a bromophenol blue pattern. This avenue should be followed further by the generation of sensor arrays aiming at more than one analyte and preferably incorporation into microfluidic systems for the delivery of analyte solutions under controlled conditions. This would open the door for the miniaturization of array sensor platforms like DETECHIP [14,15] and make them less expensive and more compatible with in-field applications.

Experimental

Spotting Setup: All patterns were written on a NLP 2000 system (NanoInk, USA) equipped with SPT pens (SPT-S-C10S, Bioforce Nanosciences). The SPTs were freshly plasma cleaned by oxygen plasma (10 sccm O_2, 100 mTorr, 30 W for 2 min) prior to use. The SPT was mounted onto the tip holder by double-sided sticky tape, and the pen reservoir was filled with 1 µL of dye solution. The spotting took place at a relative humidity of 60% and with the sample stage tilted by 8° with respect to the SPT tip to minimize the chance of contact between the dye solution in the reservoir and sample. For all patterns, except for the pattern used for spot size versus dwell time analysis, a dwell time of 0.5 s was used.

Substrates: Plain paper (Black Label Zero 80 g/m^2, Canon) and nylon membrane (Nytran SuPerCharge (SPC), Whatman) were cut down into pieces of about 1 × 1 cm^2 before spotting. The nitrocellulose slides (FAST Slides, Whatman) were used as received. HEMA polymer films were prepared as follows by using the previously described procedure [7]:

Schott (Germany) Nexterion Glass B glass plates were activated in NaOH (1 M) for 1 h followed by 30 min in 1 M HCl. A set of glass slides was modified with 3-(trimethoxysilyl)propyl methacrylate (20% v/v in ethanol) for 1 h. Another set of activated glass slides was fluorinated with tridecafluoro-(1,1,2,2)-tetrahydrooctyltrichlorosilane in a vacuumed desiccator. In the next step, the polymerization mixture consisted of 2-hydroxyethyl methacrylate (24 wt %), ethylene dimethacrylate (16 wt %), 1-decanol (12 wt %), cyclohexanol (48 wt %), and 2,2-dimethoxy-2-phenylacetophenone (1 wt % with respect to monomers) was injected between fluorinated and modified glass slides separated by 12.5 µm thick strips of Teflon film (American Durafilm Co.), and irradiated for 15 min at 12 mW·cm^{-2} with a 260 nm UV light to form a hydrophilic porous polymer layer. Polymerization was carried out on an OAI Model 30 deep-UV collimated light source (San Jose, CA) fitted with an USHIO 500 W Hg-xenon lamp (Japan). Irradiation intensity was calibrated by using an OAI 360 UV power meter with a 260 nm probe head. Monomers were purchased from Sigma-Aldrich (Germany). Further details can be found in our previous papers [6,7].

Dye and analyte solutions: All chemicals were obtained from Sigma-Aldrich and used as received if not otherwise noted. Ultrapure water (18.2 MΩ·cm) for the solutions was obtained from an Arium water supply (Sartorius, Germany). Phloxine B solution: 10 mM phloxine B in isopropanol was mixed 7:3 with a glycerol stock solution of 87% glycerol in water. Bromophenol blue solution: 1.4 mg/mL bromophenol blue in water was mixed 7:3 with a glycerol stock solution of 87% glycerol in water. Analyte solution: A mix of 10% BSA in water and glycerol stock solution (87% in water) 7:3 was used as the analyte solution in the bromophenol blue experiments. As the negative control, a mix of pure water and glycerol solution (87% in water) 7:3 was used.

Scanning electron microscopy (SEM) analysis: The surface morphologies of the substrates were analysed by using a ZEISS Leo 1530 scanning electron microscope (Carl Zeiss NTS GmbH, Germany) after gold sputtering (20 nm) using the Balzers Union MED 10.

Microscope setup: All fluorescent microscopic images were obtained on an Eclipse 80i upright fluorescence microscope (Nikon) equipped with an Intensilight (Nikon) for illumination and a CoolSNAP HQ^2 camera (Photometrics). Phloxine B patterns were observed in Texas Red filter (Nikon Y-2E/C) with

exposure times ranging from 10 ms (HEMA substrates) over 40 ms (nitro cellulose substrate) to 50 ms (plain paper and nylon). The fluorescent spectra were recorded on the same microscope through an AHF F36-QLP filter (excitation: 415–455 nm, dichroic mirror: 510 nm, emission: long-pass 500 nm) with an Avaspec-2048 Spectrometer (Avantes). Recording time for the spectra of the macroscopic droplets and the pristine microarray patterns was 1 s; the spectra of the incubated patterns were recorded with 3 s exposure.

Image analysis: To obtain the size distribution of the spotted features, fluorescent microscopy images were analysed with ImageJ [16,17]. The images were first converted into black and white by a threshold filter, and then spot sizes were obtained by particle analyses. Particles smaller than 20 pixels were excluded from analysis to exclude noise-induced artefacts.

Supporting Information

Supporting Information File 1

Figures S1 and S2.
[http://www.beilstein-journals.org/bjnano/content/supplementary/2190-4286-4-44-S1.pdf]

Acknowledgements

This work was carried out with the support of the Karlsruhe Nano Micro Facility (KNMF, www.kmf.kit.edu), a Helmholtz Research Infrastructure at Karlsruhe Institute of Technology (KIT, www.kit.edu). PAL and WF are grateful to the Helmholtz Association's Initiative and Networking Fund (Grant VH-NG-621) for financial support. We also thank the SEM facility at the Institute of Nanotechnology (INT, KIT) for the help with the SEM measurements. ML thanks the Fulbright Fellowship Program for financial support for a stay at INT/KIT. This research was supported in part by the NIH, P20 RR016469 (AEH) from the INBRE Programs of the National Center for Research Resources; the NSF CHE-0747949 (AEH) and NSF-EPSCoR-EPS-1004094 (AEH and ML).

References

1. Haab, B. B. *Proteomics* **2003,** *3,* 2116–2122. doi:10.1002/pmic.200300595
2. Martinez, A. W.; Phillips, S. T.; Butte, M. J.; Whitesides, G. M. *Angew. Chem., Int. Ed.* **2007,** *46,* 1318–1320. doi:10.1002/anie.200603817
3. Martinez, A. W.; Phillips, S. T.; Wiley, B. J.; Gupta, M.; Whitesides, G. M. *Lab Chip* **2008,** *8,* 2146–2150. doi:10.1039/b811135a
4. Levkin, P. A.; Svec, F.; Fréchet, J. M. J. *Adv. Funct. Mater.* **2009,** *19,* 1993–1998. doi:10.1002/adfm.200801916
5. Ueda, E.; Levkin, P. A. *Adv. Mater.* **2013,** *25,* 1234–1247. doi:10.1002/adma.201204120
6. Efremov, A. N.; Stanganello, E.; Welle, A.; Scholpp, S.; Levkin, P. A. *Biomaterials* **2013,** *34,* 1757–1763. doi:10.1016/j.biomaterials.2012.11.034
7. Geyer, F. L.; Ueda, E.; Liebel, U.; Grau, N.; Levkin, P. A. *Angew. Chem., Int. Ed.* **2011,** *50,* 8424–8427. doi:10.1002/anie.201102545
8. Ueda, E.; Geyer, F. L.; Nedashkivska, V.; Levkin, P. A. *Lab Chip* **2012,** *12,* 5218–5224. doi:10.1039/c2lc40921f
9. Xu, J.; Lynch, M.; Huff, J. L.; Mosher, C.; Vengasandra, S.; Ding, G.; Henderson, E. *Biomed. Microdevices* **2004,** *6,* 117–123. doi:10.1023/B:BMMD.0000031748.13353.10
10. Xu, J.; Lynch, M.; Nettikadan, S.; Mosher, C.; Vegasandra, S.; Henderson, E. *Sens. Actuators, B* **2006,** *113,* 1034–1041. doi:10.1016/j.snb.2005.03.113
11. Xiao, J.; Stone, H. A.; Attinger, D. *Langmuir* **2012,** *28,* 4208–4212. doi:10.1021/la204474f
12. Schosinsky, K. H.; Vargas, M.; Luz Esquivel, A.; Chavarria, M. A. *Clin. Chem.* **1987,** *33,* 223–226.
13. Jung, K.; Nickel, E.; Pergande, M. *Clin. Chim. Acta* **1990,** *187,* 163–172. doi:10.1016/0009-8981(90)90343-Q
14. Burks, R. M.; Pacquette, S. E.; Guericke, M. A.; Wilson, M. V.; Symonsbergen, D. J.; Lucas, K. A.; Holmes, A. E. *J. Forensic Sci.* **2010,** *55,* 723–727. doi:10.1111/j.1556-4029.2010.01323.x
15. Lyon, M.; Groathouse, J.; Beaber, J.; Turner, L. M.; Rouhier, K. A.; Wilson, M. V.; Symonsbergen, D. J.; Sikich, S. M.; Holmes, A. E. J. *Forensic Res.* **2011,** *2,* 126. doi:10.4172/2157-7145.1000126
16. Abràmoff, M. D.; Magalhães, P. J.; Ram, S. J. *Biophoton. Int.* **2004,** *11,* 36–42.
17. Schneider, C. A.; Rasband, W. S.; Eliceiri, K. W. *Nat. Methods* **2012,** *9,* 671–675. doi:10.1038/nmeth.2089

License and Terms

Beilstein Journal of Nanotechnology

In situ monitoring magnetism and resistance of nanophase platinum upon electrochemical oxidation

Eva-Maria Steyskal[1,§], Stefan Topolovec[1,§], Stephan Landgraf[2], Heinz Krenn[3] and Roland Würschum[*1]

Letter

Open Access

Address:
[1]Institute of Materials Physics, Graz University of Technology, Petersgasse 16, 8010 Graz, Austria, [2]Institute of Physical and Theoretical Chemistry, Graz University of Technology, Stremayrgasse 9, 8010 Graz, Austria and [3]Institute of Physics, University of Graz, Universitätsplatz 5, 8010 Graz, Austria

Email:
Roland Würschum[*] - wuerschum@tugraz.at

* Corresponding author
§ Both authors contributed equally to this work.

Keywords:
electrical resistance; electrochemistry; magnetism; porous nanocrystalline Pt; tunable properties

Beilstein J. Nanotechnol. **2013,** *4,* 394–399.
doi:10.3762/bjnano.4.46

Received: 13 March 2013
Accepted: 28 May 2013
Published: 24 June 2013

This article is part of the Thematic Series "Advances in nanomaterials".

Guest Editors: H. D. Gleiter and T. Schimmel

Abstract

Controlled tuning of material properties by external stimuli represents one of the major topics of current research in the field of functional materials. Electrochemically induced property tuning has recently emerged as a promising pathway in this direction making use of nanophase materials with a high fraction of electrode-electrolyte interfaces. The present letter reports on electrochemical property tuning of porous nanocrystalline Pt. Deeper insight into the underlying processes could be gained by means of a direct comparison of the charge-induced response of two different properties, namely electrical resistance and magnetic moment. For this purpose, four-point resistance measurements and SQUID magnetometry were performed under identical in situ electrochemical control focussing on the regime of electrooxidation. Fully reversible variations of the electrical resistance and the magnetic moment of 6% and 1% were observed upon the formation or dissolution of a subatomic chemisorbed oxygen surface layer, respectively. The increase of the resistance, which is directly correlated to the amount of deposited oxygen, is considered to be primarily caused by charge-carrier scattering processes at the metal–electrolyte interfaces. In comparison, the decrease of the magnetic moment upon positive charging appears to be governed by the electric field at the nanocrystallite–electrolyte interfaces due to spin–orbit coupling.

Introduction

Porous nanophase materials with electrochemically induced tunability of properties [1] have become a topic of growing research interest in the past few years. Studies on the tunability of mechanical (e.g., [2-4]), electrical (e.g., [4-9]) and magnetic (e.g., [9-14]) properties have been presented for various materials. Besides field-induced tuning due to the accumulation of

excess charges at the electrode–electrolyte interface of nanophase materials, the physical material properties may also be changed by electrochemical surface reactions, as for instance documented for nanoporous Au [6]. Based on tunability studies of the electrical resistance of porous nanocrystalline Pt [5] or nanoporous Pt [7] and of the magnetic moment of porous nanocrystalline Pd [10], the present work aims at a direct comparison of electrical resistance and magnetic moment with respect to in situ electrochemical oxidation by using porous nanocrystalline Pt as a model system. These different electronic properties represent an ideal combination to provide a deeper understanding of the underlying charge-related processes since both properties are expected to respond differently on charging and chemical modification. The studies make use of a specifically designed electrochemical cell that allows in situ magnetic studies in a SQUID magnetometer under electrochemical control [12].

Experimental

Porous nanophase platinum samples were produced from commercially available platinum powder (Platinum Black, 20–40 m^2/g, Chempur GmbH). For resistance measurements, 104 mg of Platinum Black were compacted into a PTFE groove with embedded electrical contacts similar to our previous work [5], improved by adding a fifth wire providing an independent contact for electrochemical charging (further referred to as sample Pt_{ER}). For magnetic measurements, 17.8 mg of the powder were compacted to a cylindrical pellet, which was carefully wrapped by a gold wire, applying an electrical contact (further referred to as sample Pt_{SQUID}).

All measurements were carried out at ambient temperature in a 1 molar aqueous solution of KOH. Resistance measurements were performed in a standard electrochemical cell with a PGZ-100 potentiostat (Radiometer Analytical). The Pt_{ER} sample served as the working electrode and was charged via the Pt wire contacted to the center of the sample. Porous carbon fabric and a commercial Ag/AgCl (sat. KCl) electrode (Radiometer Analytical) were used as counter and reference electrode, respectively. The electrical resistance was measured in a four-point geometry with a Keithley 2400 multimeter using the outer contact pair for current supply and the inner contact pair for voltage measurement. SQUID magnetometry was performed in a MPMS-XL-7 device (Quantum Design) at a constant magnetic field of 5 kOe upon in situ electrochemical charging with an Autolab PGSTAT128N potentiostat (Metrohm). The magnetic measurements were performed in a miniaturized electrochemical cell by using porous carbon fabric and a gold wire as counter and quasi-reference electrode, respectively, similar to our setup presented recently [12]. In the present improved setup a long borosilicate glass NMR tube (Wilmad-LabGlass, length 17.78 cm, diameter 4.96 mm) was used as the electrolyte container. By this means, the part filled with electrolyte extended well beyond the SQUID detection coils, and the counter electrode was located outside the coils, so that neither the electrolyte nor the counter electrode caused changes of the SQUID signal while scanning the tube through the detection coils. In the following, all potential values are given relative to Ag/AgCl, i.e., the data taken with the Au quasi-reference electrode are converted to corresponding values relative to Ag/AgCl. As reference values for the resistance and the magnetic moment, the initial values R_0 and m_0 of the respective measurement were used.

Results

Charging was performed by the electrochemical methods of cyclic voltammetry, with a constant scan rate of 0.5 mV/s, or chronoamperometry (CA). Prior to the measurements the electrode was activated by repeatedly cycling between the oxygen- and hydrogen-evolution regimes. A typical cyclic voltammogram (CV) taken for sample Pt_{ER} is shown by the gray curve in Figure 1. As the potential is varied with triangular characteristics, the CV curve is run through clockwise. The behavior well-known from the literature (e.g., [15,16]) can be discerned, i.e., upon anodic scanning, the peak system due to hydrogen desorption (−950 mV to −550 mV), the double-layer region characterized by low charging currents (−500 mV to −300 mV), as well as the shoulder and plateau of oxygen adsorption/sample oxidation (−200 mV to 600 mV) followed finally by O_2 evolution. In the opposite direction, oxygen remains on the surface until the desorption peak is reached (extremum at −460 mV), fol-

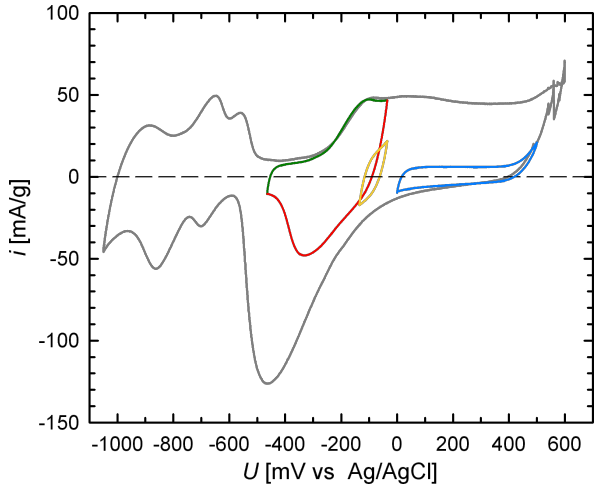

Figure 1: Steady-state cyclic voltammograms (CVs) of porous nanocrystalline Pt (sample Pt_{ER}) measured at a scan rate of v = 0.5 mV/s in different potential ranges from −1050 mV to +600 mV (gray), −465 mV to −35 mV (green, red), −135 mV to −35 mV (yellow), 0 mV to +500 mV (blue) in 1 M KOH.

lowed by the region of hydrogen adsorption (−650 mV to −1050 mV), and finally by the onset of H_2 evolution.

The colored CV curves in Figure 1 characterize the various potential regions, which will be discussed in the following with respect to charge-induced variations of the electrical resistance and the magnetic moment. Each CV is located within the oxygen-governed regime and shown in steady state, which means that subsequent cycles perfectly superpose each other, and thus, identical electrochemical processes take place in all cycles. The CV between −465 mV and −35 mV characterizes the formation (anodic direction, green line) and subsequent removal (cathodic direction, red line) of a thin oxygen layer to an extent of less than one oxygen atom per Pt surface atom [16]. This layer is modified without being entirely removed in the narrow CV-regime between −135 mV and −35 mV (yellow line). The CV in the higher potential regime (0 mV to +500 mV, blue line) corresponds to the state of further strong oxygen adsorption.

The CV between −465 mV and −35 mV (green and red) is shown in more detail in Figure 2a along with the corresponding variation of the electrical resistance (b) and of the magnetic moment of the platinum samples (c). The green- and red-colored data in (b) and (c) again indicate the anodic and cathodic scan direction, respectively. In each plot two subsequent voltammetric cycles are plotted, which can hardly be discerned, illustrating the good reversibility of the measurements in the steady-state CV. The electrical resistance R reversibly increases upon positive charging, exhibiting a total variation $\Delta R/R_0$ of about 6% (Figure 2b). The variation of R with the potential U exhibits a pronounced hysteresis, which indicates a high sensitivity of R with respect to superficial oxygen adsorption. This sensitivity is also clearly reflected by the steep increase or decrease of R right in the CV regime where oxygen adsorption or desorption takes place, respectively. Taking a closer look at the high potential edge, a further increase in R can be observed when the scan direction is reversed (start of red-colored data) as the charging current i is still positive. When i finally changes its sign at about −75 mV, the resistance also starts to decrease. Thus the R-variation is proportional to the transferred charge as presented in more detail below (Figure 4). The magnetic moment m, on the other hand, decreases (increases) with increasing (decreasing) potential showing a total variation $\Delta m/m_0$ of approximately 1% (Figure 2c). The variation of the magnetic moment also changes strongly with the onset of oxygen adsorption, yet in contrast to R, the slope of the $\Delta m/m_0$-potential characteristic remains at a high value in the entire oxygen adsorbed regime, reversing its sign immediately at the high potential edge. This indicates a correlation to the capacitive charging currents (i.e., the electric field), which also reverse sign directly with the potential scan direction, explaining the lack of hysteresis for $\Delta m/m_0$.

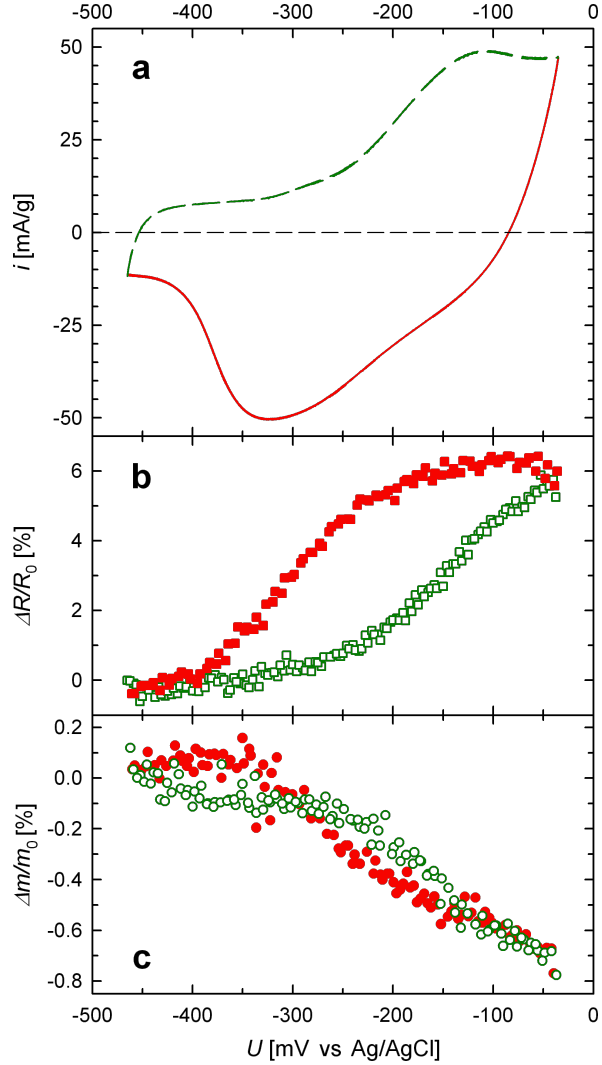

Figure 2: Relative variation of resistance ($\Delta R/R_0$, b) and magnetic moment ($\Delta m/m_0$, c) of porous nanocrystalline Pt upon electrochemical CV-cycling in 1 M KOH between −465 mV and −35 mV. (a) CV measured for sample Pt_{ER}. Measurements of m were performed at 5 kOe. Anodic scan indicated by green dashed line and green open symbols. Cathodic scan indicated by red solid line and red full symbols. To demonstrate the good reproducibility and reversibility two cycles are shown in each plot.

The variation of m with applied potential has been studied in more detail by cycling in the potential range between −135 mV and −35 mV (see Figure 3). The cycling was performed after oxidation (green-colored data) and followed by reduction (red-colored data), similar to the measurement in the potential range between −465 mV and −35 mV. The same variation $\Delta m/m_0$ with potential is observed for the range between −135 mV and −35 mV, irrespective of whether the CV cycling is limited to this regime (yellow-colored data in Figure 3) or whether the

potential is scanned through the entire regime of electrochemical oxidation (green-colored data) and reduction (red-colored data). Since in the narrow CV regime the adsorbed oxygen remains on the sample, this leads again to the conclusion that the variation $\Delta m/m_0$ is more directly governed by the potential (i.e., the electric field) than by the superficial adsorption or desorption of oxygen. In contrast to these findings for m, no significant variation in R can be observed in this narrow potential range (data not shown).

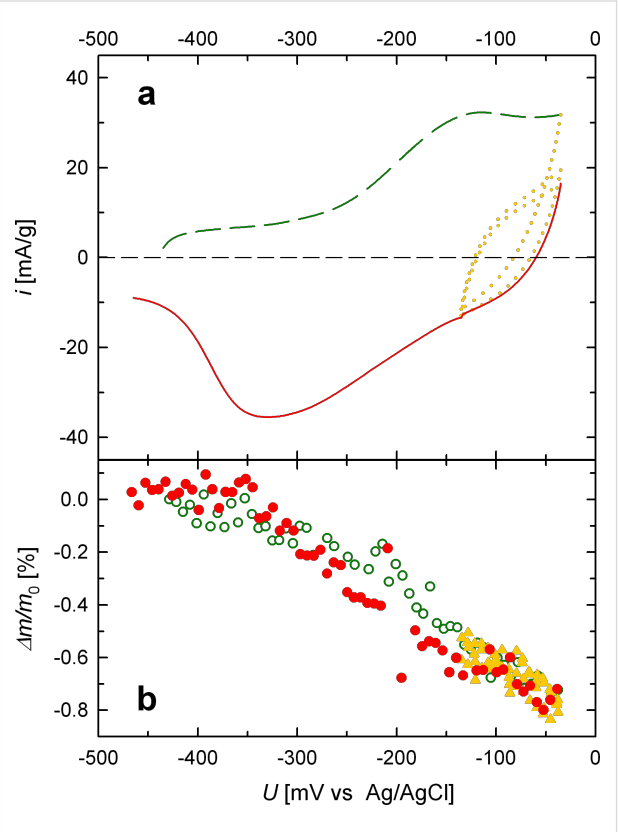

Figure 3: Relative variation of magnetic moment ($\Delta m/m_0$, b) of porous nanocrystalline Pt upon electrochemical oxidation (−435 mV to −35 mV, green: dashed line, open circles), electrochemical cycling between −135 mV and −35 mV (yellow: dotted line, full triangles), and electrochemical reduction (−35 mV to −465 mV, red: solid line, full circles). (a) CV measured in situ at the identical sample (Pt_{SQUID}). Measurements performed in 1 M KOH at 5 kOe.

The dependence of $\Delta R/R_0$ on the applied charge was investigated using the electrochemical method of chronoamperometry (CA), where a correction of the leak current is possible, allowing for a higher accuracy of charge determination. Two different potential regimes were investigated, which are illustrated by cyclic voltammograms in Figure 4a. The regime between −465 mV and −35 mV, which is identical to that applied in the CV-mode measurement (Figure 2b), characterizes adsorption and desorption, whereas the regime between 0 mV and +500 mV corresponds to the steady state of strong oxygen adsorption (blue). In each potential region, CA measurements were performed in consecutive step intervals of 86 mV (green/red) or 100 mV (blue). After an equilibration time of 60 minutes at a given potential, the transferred charge ΔQ per sample mass, relative to the first measurement point in the respective regime, was determined from the monitored charging current and the electrical resistance was measured. The data $\Delta R/R_0$ in dependence of ΔQ obtained in this way are presented in Figure 4b. Again, two successive cycles are shown in each region, to illustrate the reversibility of $\Delta R/R_0$. The regime of adsorption/desorption (green, red) is characterized by a high charge coefficient $[(\Delta R/R_0)/(\Delta Q)]_{Chem} = 0.31\ \%\cdot(C/g)^{-1}$. The measurements performed in this regime allow for a comparison of the CA- (see Figure 4b) and CV-mode (see Figure 2b), which yield self-consistent results, both indicating a strong sensitivity of R to the surface modifications. In the regime of strong oxygen adsorption (blue), besides a significantly smaller total variation of $\Delta R/R_0$, also the relative dependence on ΔQ is significantly weaker as reflected by a reduced value $[(\Delta R/R_0)/(\Delta Q)]_{Ox}$ of $0.14\ \%\cdot(C/g)^{-1}$.

Discussion

For the discussion of the present results, first of all, it has to be pointed out that the voltage-induced responses of the magnetic moment and electrical resistance, although nicely correlated, exhibit distinctly different behavior as outlined above. As discussed earlier neither the variation of the magnetic moment nor that of the resistance can simply be attributed to a variation $\Delta n/n$ of the charge carrier density upon electrochemical charging [7,10]. A simple $\Delta n/n$-dependence for both effects can further be excluded, because for that, an equal magnitude of variation $|\Delta R/R_0| = |\Delta m/m_0|$ would have to be expected. The obviously weaker sensitivity of the magnetic moment to the formation and removal of a thin oxygen layer, compared to the electrical resistance, can yet be understood by looking more closely at the different magnetic and electronic responses of the metal–electrolyte interface upon adsorption and desorption of oxygen species.

On the one hand, the increase in R with increasing potential can be understood as being dominated directly by surface effects, in good agreement with previous results [5,7]. Besides a reduced charge carrier density due to positive charging [17] and a shrinking conductor cross-section of Pt in favor of a superficial formation of platinum oxide with ongoing oxidation, the electrical resistance is strongly affected by charge-carrier scattering processes at the metal–electrolyte interface [5-7]. In the potential regime indicated by the green/red curves (Figure 2a and Figure 4a), oxygen adsorption takes place at a clean platinum surface. Since the ion transfer in this regime corresponds to less than one oxygen atom per platinum surface atom [16], each

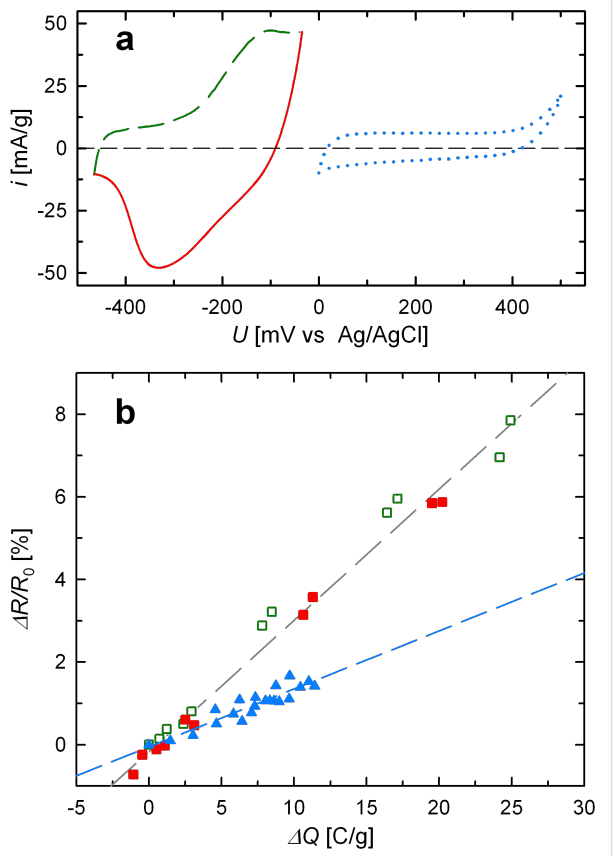

Figure 4: Relative variation of electrical resistance $\Delta R/R_0$ of sample Pt_{ER} upon adsorption (green: dashed line, open squares) and desorption (red: solid line, full squares), and upon charging in the regime of strong oxygen adsorption (blue: dotted line, full triangles) in 1 M KOH. (a) CVs measured in the respective potential ranges. (b) Variation of $\Delta R/R_0$ with charge ΔQ imposed upon chronoamperometry (CA) in the potential regimes shown in (a).

adsorbed ion may effectively act as an additional charge-carrier scattering center at the platinum surface. Therefore, the resistance increases strongly in this regime and, moreover, is directly related to the transferred charge, which reflects the amount of adsorbed oxygen.

Compared to the preceding regime of oxidation and reduction, the blue-colored regime (Figure 4a) denotes a steady-state condition well above the oxygen desorption peak where reversible charging is performed entirely within the oxygen adsorbed steady state without removing it. Since the corresponding currents in this steady-state CV are similar to that of the double layer regime of platinum (see Figure 1), the charge transfer in this regime can be considered as "double-layer-like" charging of a previously oxygen-covered surface. This results in weaker response of the resistance, because charging does not directly affect the underlying platinum surface. This explains the reduced charge coefficient in this regime (Figure 4b).

It is worth mentioning that, compared to the present case of cluster-assembled porous Pt, the charge-induced resistance variation of nanoporous Pt prepared by electrochemical dealloying in addition showed a sign inversion at high potentials [7]. This different behavior has to be assigned to the strongly different types of surface states originating from the preparation, which is a chemical reduction process for the commercial Pt powder, whereas dealloying takes place under strongly oxidizing conditions. In fact, as shown by Viswanath et al. [18], strongly differing surface states may respond rather differently with respect to charging. Regarding dealloyed nanoporous Pt, the sign-inversion of the charge-induced resistance variation was associated with the semiconducting behavior of the partially oxidized surface [7].

The electrochemical tunability of the magnetic moment is more than one half of an order of magnitude lower than that of the electrical resistance. The magnetic response is less sensitive to charging since the macroscopic magnetic moment of nanocrystalline Pt represents a volume average of the interior and surface region of the nanocrystallites, only the latter part being affected by charging. In contrast to that, the electrical resistance, which is governed by interfacial charge-carrier scattering, selectively probes the crystallite–electrolyte interfaces. The observed decrease of the magnetic moment of nanocrystalline Pt with electrochemically induced oxygen adsorption nicely fits with earlier studies of the influence of chemisorbed oxygen on the magnetic susceptibility of Pt [19]. The trend of decreasing magnetic moment is also supported by recent DFT calculations according to which the density of states at the Fermi level of Pt monotonically decreases with increasing oxygen coverage [20]. This also demonstrates that a simple picture of voltage-induced filling or depletion of rigid electronic bands fails, because within such a picture positive charging, i.e., extraction of electrons from the nearly filled d-band of Pt would give rise to an increase of the density of states rather than to a decrease.

Although oxygen adsorption causes a decrease of the magnetic moment, it may not fully account for the observed voltage-induced variation of m. In fact, in contrast to the voltage-induced variation of R, the $\Delta m/m_0$–U behavior shows no hysteresis (Figure 2c) but, on the other hand, m changes also in the narrow potential regime between −135 mV and −35 mV where oxygen is not removed from the surface (Figure 3). This indicates that the variation $\Delta m/m_0$ is governed by the electric field at the nanocrystallite–electrolyte interface. As well known for surfaces, the asymmetric potential drop at a surface causes strong spin–orbit coupling with mobile spins (Rashba effect) [21]. This is reflected by the formation of an effective magnetic field due to unbalanced orbital currents, which polarizes the electron spins. Since this Rashba spin–orbit coupling varies

with an applied electric field E [21,22], this may give rise to an E-dependence of the magnetization, directly. In addition the Rashba effect is also associated with magnetic surface anisotropy [22]. The E-dependence of the latter may also cause variations of the magnetic moment in nanophase systems according to recent theoretical studies of Subkow and Fähnle [23]. Spin–orbit coupling in combination with potential-dependent surface stress or charge-induced relaxation of the outermost atomic layer may also influence the magnetization, as suggested by Ghosh [14]. More detailed in situ electrochemical SQUID studies, in particular measurements in dependence of the applied magnetic field, will be necessary in order to further elucidate the chemical or/and electric-field-induced character of the $\Delta m/m_0$–U behavior.

Conclusion

In conclusion, the variations of the electrical resistance and magnetic moment upon electrooxidation show similar trends but differ in detail, since the former is due to charge-carrier scattering processes at the metal–electrolyte interfaces, whereas the latter seems to be governed by the electric field at the nanocrystallite–electrolyte interface. Consistent results for the resistance variation were found by chronoamperometry and cyclic voltammetry. The combination of SQUID magnetometry and in situ cyclic voltammetry opens up attractive potentials for studying nanophase materials under full electrochemical control.

References

1. Gleiter, H.; Weissmüller, J.; Wollersheim, O.; Würschum, R. *Acta Mater.* **2001,** *49,* 737. doi:10.1016/S1359-6454(00)00221-4
2. Weissmüller, J.; Viswanath, R. N.; Kramer, D.; Zimmer, P.; Würschum, R.; Gleiter, H. *Science* **2003,** *300,* 312. doi:10.1126/science.1081024
3. Jin, H.-J.; Weissmüller, J. *Science* **2011,** *332,* 1179. doi:10.1126/science.1202190
4. Biener, J.; Dasgupta, S.; Shao, L.; Wang, D.; Worsley, M. A.; Wittstock, A.; Lee, J. R. I.; Biener, M. M.; Orme, C. A.; Kucheyev, S. O.; Wood, B. C.; Willey, T. M.; Hamza, A. V.; Weissmüller, J.; Hahn, H.; Baumann, T. F. *Adv. Mater.* **2012,** *24,* 5083. doi:10.1002/adma.201202289
5. Sagmeister, M.; Brossmann, U.; Landgraf, S.; Würschum, R. *Phys. Rev. Lett.* **2006,** *96,* 156601. doi:10.1103/PhysRevLett.96.156601
6. Wahl, P.; Traußnig, T.; Landgraf, S.; Jin, H.-J.; Weissmüller, J.; Würschum, R. *J. Appl. Phys.* **2010,** *108,* 073706. doi:10.1063/1.3490789
7. Steyskal, E.-M.; Besenhard, M.; Landgraf, S.; Zhong, Y.; Weissmüller, J.; Pölt, P.; Albu, M.; Würschum, R. *J. Appl. Phys.* **2012,** *112,* 073703. doi:10.1063/1.4755808
8. Dasgupta, S.; Gottschalk, S.; Kruk, R.; Hahn, H. *Nanotechnology* **2008,** *19,* 435203. doi:10.1088/0957-4484/19/43/435203
9. Mishra, A. K.; Bansal, C.; Ghafari, M.; Kruk, R.; Hahn, H. *Phys. Rev. B* **2010,** *81,* 155452. doi:10.1103/PhysRevB.81.155452
10. Drings, H.; Viswanath, R. N.; Kramer, D.; Lemier, C.; Weissmüller, J.; Würschum, R. *Appl. Phys. Lett.* **2006,** *88,* 253103. doi:10.1063/1.2216897
11. Traußnig, T.; Topolovec, S.; Nadeem, K.; Szabó, D. V.; Krenn, H.; Würschum, R. *Phys. Status Solidi RRL* **2011,** *5,* 150. doi:10.1002/pssr.201004483
12. Topolovec, S.; Jerabek, P.; Szabó, D. V.; Krenn, H.; Würschum, R. *J. Magn. Magn. Mater.* **2013,** *329,* 43. doi:10.1016/j.jmmm.2012.09.071
13. Weisheit, M.; Fähler, S.; Marty, A.; Souche, Y.; Poinsignon, C.; Givord, D. *Science* **2007,** *315,* 349. doi:10.1126/science.1136629
14. Ghosh, S.; Lemier, C.; Weissmüller, J. *IEEE Trans. Magn.* **2006,** *42,* 3617. doi:10.1109/TMAG.2006.880922
15. Hamann, C. H.; Vielstich, W. *Elektrochemie;* Wiley-VCH: Weinheim, Germany, 1998.
16. Angerstein-Kozlowska, H.; Conway, B. E.; Sharp, W. B. A. *J. Electroanal. Chem. Interfacial Electrochem.* **1973,** *43,* 9. doi:10.1016/S0022-0728(73)80307-9
17. Tucceri, R. *Surf. Sci. Rep.* **2004,** *56,* 85. doi:10.1016/j.surfrep.2004.09.001
18. Viswanath, R. N.; Kramer, D.; Weissmüller, J. *Electrochim. Acta* **2008,** *53,* 2757. doi:10.1016/j.electacta.2007.10.049
19. Gray, T.; McCain, C. The Chemisorption of Oxygen and Hydrogen on Platinum. In *Proceedings of the second international congress of surface activity. Vol. 2 Solid/gas interface;* Schulman, J., Ed.; Butterworths: London, 1957; pp 260 ff.
20. Pang, Q.; Zhang, Y.; Zhang, J.-M.; Xu, K.-W. *Appl. Surf. Sci.* **2011,** *257,* 3047. doi:10.1016/j.apsusc.2010.10.114
21. Bihlmayer, G.; Koroteev, Yu. M.; Echenique, P. M.; Chulkov, E. V.; Blügel, S. *Surf. Sci.* **2006,** *600,* 3888. doi:10.1016/j.susc.2006.01.098
22. Xu, L.; Zhang, S. *J. Appl. Phys.* **2012,** *111,* 07C501. doi:10.1063/1.3670002
23. Subkow, S.; Fähnle, M. *Phys. Rev. B* **2011,** *84,* 220409. doi:10.1103/PhysRevB.84.220409

License and Terms

Beilstein Journal of Nanotechnology

Magnetic anisotropy of graphene quantum dots decorated with a ruthenium adatom

Igor Beljakov[1], Velimir Meded[1], Franz Symalla[1], Karin Fink[1], Sam Shallcross[2] and Wolfgang Wenzel[*1]

Letter

Open Access

Address:
[1]Institute of Nanotechnology (INT), KIT, Karlsruhe, Germany and [2]Friedrich-Alexander-Universität Erlangen-Nürnberg (FAU), Erlangen, Germany

Email:
Wolfgang Wenzel[*] - wolfgang.wenzel@kit.edu

* Corresponding author

Keywords:
adsorbate; grapheme; graphene quantum dot; magnetic anisotropy; transition metal

Beilstein J. Nanotechnol. **2013,** *4,* 441–445.
doi:10.3762/bjnano.4.51

Received: 28 February 2013
Accepted: 13 June 2013
Published: 10 July 2013

This article is part of the Thematic Series "Advances in nanomaterials".

Guest Editors: H. D. Gleiter and T. Schimmel

Abstract

The creation of magnetic storage devices by decoration of a graphene sheet by magnetic transition-metal adatoms, utilizing the high in-plane versus out-of-plane magnetic anisotropy energy (MAE), has recently been proposed. This concept is extended in our density-functional-based modeling study by incorporating the influence of the graphene edge on the MAE. We consider triangular graphene flakes with both armchair and zigzag edges in which a single ruthenium adatom is placed at symmetrically inequivalent positions. Depending on the edge-type, the graphene edge was found to influence the MAE in opposite ways: for the armchair flake the MAE increases close to the edge, while the opposite is true for the zigzag edge. Additionally, in-plane pinning of the magnetization direction perpendicular to the edge itself is observed for the first time.

Introduction

Since 2004, graphene [1], a one-atom-thick sheet of carbon atoms arranged in a regular hexagonal lattice, has been investigated intensively [2]. Outstanding mechanical and electronic properties, both predicted and measured [3], make it one of the most studied materials both theoretically and experimentally [4-11]. High magnetic anisotropies were predicted for graphene decorated with transition-metal (TM) adatoms and dimers [12,13]. Inspired by its application potential in the fields of spintronics and magnetic storage as well as fundamental science, a number of works were published on the properties of such structures [14-17]. The studies mostly describe two extreme cases of substrates, i.e., single benzene molecules, less suitable for a realistic device, because of their size and problematic realization (benzene is an easily flammable toxic liquid), or infinite graphene with a certain periodic coverage of metal adatoms. A homogeneous distribution of adatoms on a graphene sheet may pose further experimental difficulties, due to the possibility of adatom clustering. The magnetic anisotropy energy (MAE) is known to be profoundly influenced by the symmetry of the environment. On the other hand, graphene flakes both provide a natural interpolation between the two limits, i.e., the infinite graphene sheet and the benzene ring,

which have already been studied in the literature, as well as provide a possible template for the adsorption of magnetic adatoms, by preferential adsorption at the edges. Considering the higher spin-orbit coupling of 4d TMs compared to 3d TMs, as well as the fact that the first observation of 4d ferromagnetism was made for a ruthenium monolayer on a graphite substrate [18], Ru appeared as an attractive candidate for the adatom. All of these reasons motivate our present study of the MAE of Ru adatoms on a graphene flake.

Methods

As the system of choice, triangular hydrogen-saturated graphene flakes (or graphene quantum dots) were investigated, comprising 90 and 97 carbon atoms for two different edge types, armchair and zigzag (AGQD and ZGQD), respectively. The triangular shape was chosen as the simplest geometry, providing the same edge type on all sides. On a chosen hollow site (above a carbon ring center) a ruthenium adatom was placed, and the distance was optimized by minimization of the total energy using density functional theory. The stability of the Ru adatom on the hollow site, surrounded by less preferable positions over the C–C bridge and atop a C-atom, was reported for infinite graphene [15]. The graphene flake is considered fixed, as it would be on a substrate.

Within our work we used density functional theory (DFT) [19] with the B-P86 generalized gradient approximation (GGA) functional and the hybrid functional B3-LYP as implemented in TURBOMOLE [20,21]. The (Grimme) empirical dispersion correction (DFT-D2) [22] was used for geometry optimizations. To calculate the magnetic anisotropy we used the two-component calculation [23] with dhf-TZVP-2c basis [24]. For the spin–orbit interaction the two-component effective core potential dhf-ecp-2c [25] was used.

To determine the magnetic anisotropy of the system at hand, the magnetization direction was varied, and the resulting total energies were compared. Three magnetization directions and corresponding energies were used: (1) the out-of-plane ($E_{\perp}$) direction, pointing perpendicular to the flake plane; (2) the in-plane-minimum ($E_{\parallel,\min}$) direction, i.e., the direction parallel to the flake plane with the lowest total energy; and (3) the in-plane-maximum ($E_{\parallel,\max}$) direction, for the highest total energy in-plane. Note, direction 2 may depend on the chosen site, and directions 2 and 3 are not necessary perpendicular to each other. Using the defined directions, the following two kinds of MAE are defined. The in- versus out-of-plane (E_{IO}) MAE is defined as

$$E_{\mathrm{IO}} = E_{\perp} - E_{\parallel,\min}, \tag{1}$$

and is negative when the easy axis points out of plane. If E_{IO} is positive, the easy axis points along the direction 2. The in-plane MAE (E_{IP}) is defined as

$$E_{\mathrm{IP}} = E_{\parallel,\max} - E_{\parallel,\min}. \tag{2}$$

The E_{IP} is per definition always positive and would be equal to zero for an adatom on an infinite graphene sheet, due to the underlying symmetry.

Results

We first consider the electronic structure of the armchair-graphene (AGQD) and zigzag-graphene (ZGQD) quantum dots in the pristine state, i.e., without decoration by a Ru atom. (The geometric structure may be seen in Figure 1.) While the AGQD has no intrinsic moment, the ZGQD in contrast is found to have an intrinsic moment of 7 μ_B. This spin polarisation of the ZGQD arises from a highly localized p_z-type edge state [26], and the total moment of the quantum dot is exactly equal to the difference in number between the A-type atoms and B-type atoms, in agreement with the theorem of magnetism in a bipartite lattice at half filling reported by Lieb [27]. As we shall subsequently see, this difference in the magnetic state of the pristine graphene quantum dots leads to a qualitatively different behaviour of the magnetic anisotropy of the absorbed Ru atom.

Before considering in detail the magnetic state of the Ru adatom, however, we shall consider the nature of its bonding to the graphene flake. We find the calculated Ru–flake separation to be 1.75 Å, strongly indicating chemisorption, a fact supported by the significant reduction in the Ru moment from the atomic state (we find the moment to be always less than 2 μ_B while the atomic moment of Ru is 4 μ_B, see below), as well as the large binding energy of the Ru adatom which we find to be of the order of eV (see Table 1). In addition we note that the most energetically preferred position on the graphene flake is, for both the AGQD and ZQGD, the apex site (see Table 1). This finding is compatible with previous work on the absorption of transition-metal atoms on graphene nanoribbons [28].

We now turn to the question of the detailed magnetic structure of the graphene flake with the Ru adatom. Considering first the in-plane versus out-of-plane anisotropy (E_{IO}) we find that (i) $E_{\mathrm{IO}} > 0$ for all absorption positions on both flakes, i.e., the easy axis is in-plane and (ii) E_{IO} is significantly larger on the AGQD as compared to the ZGQD, see Figure 1b in which the E_{IO} is plotted for all 9 (8) symmetrically inequivalent sites of the AGQD (ZGQD).

As we shall now demonstrate that the origin of this difference in the magnitude of E_{IO} between the two flakes can be traced back

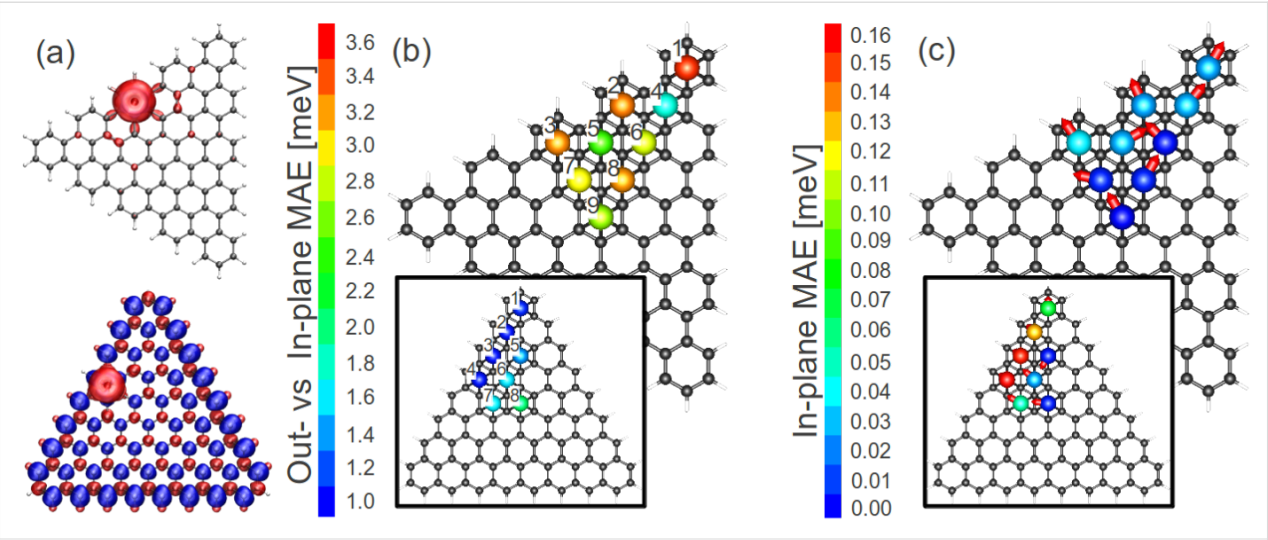

Figure 1: (a) The magnetization density of an armchair (top) and zigzag (bottom) graphene flake decorated with a single ruthenium adatom at a separation of 1.75 Å from the flake plane; positive (negative) m(r) indicated by the red (blue) colour. Shown in panel (b) are the in-plane versus out-of-plane magnetic anisotropy energies for all symmetry-inequivalent adatom positions, see Equation 1 for the definition of this quantity, for both the armchair and zigzag (as inset) graphene flakes. In panel (c) are similarly presented the in-plane magnetic anisotropy energies (see Equation 2), with the red arrows indicating the direction of the minimum-energy in-plane position.

Table 1: Total energy of the graphene flakes decorated with a Ru atom. The Ru atom was put on 9(8) sites with nonequivalent symmetry on armchair (zigzag) graphene flakes. The sites are numbered according to Figure 1b. As a zero-point system the corresponding flake was chosen with a Ru atom placed 100 Å away from the flake plane.

Position AGQD	E_{Tot} [eV]	Position ZGQD	E_{Tot} [eV]
1	−2.249	1	−2.369
2	−1.987	2	−2.036
3	−1.980	3	−2.026
4	−1.451	4	−2.031
5	−1.485	5	−1.697
6	−1.328	6	−1.637
7	−1.372	7	−1.628
8	−1.590	8	−1.568
9	−1.474		

to the fact that, while the bare ZGQD is spin polarised, the AGQD is not. To this end we first note that spin coupling of the Ru adatom to the p_z spin-split edge state on the ZGQD is antiferromagnetic. This we illustrate in Figure 1a, in which isosurfaces of the magnetisation density (m(r)) for Ru on the AGQD and ZGQD are shown. Clearly while in the former case the Ru acts to weakly polarise the flake with ferromagentic coupling, in the latter case the coupling is strongly antiferromagnetic (note that blue and red indicate negative and positive m isosurfaces). The net result of this antiferromagnetic coupling is to strongly reduce the moment of the Ru adatom on the ZGQD: while moments of 1.7–1.8 μ_B are found for the AGQD, for the ZGQD these values fall to 0.8–1.4 μ_B. To bring out the relation to the in-plane versus out-of-plane anistropy, E_{IO}, we plot this quantity against the Ru adatom moment in Figure 2. As can be seen the clear trend that emerges is that the larger the moment the greater the value attained for the anisotropy. In this plot the impact of the AFM coupling of Ru is clearly made visible: while the Ru moment increases at the edge sites for the AGQD, as there are fewer C atoms with which to share the unpaired electrons of Ru, towards the edge sites of the ZGQD the moment, in contrast, is seen to decrease.

In short, the electronic structure of the graphene substrate determines the polarisation of the absorbed Ru atom and this in turn governs the value of E_{IO}. This is, in fact, a rather natural result as the physics of anisotropy is, upon expansion of the Dirac equation in powers of v/c, governed by the spin–orbit coupling term which is proportional to $\mathcal{L}\cdot\mathcal{S}$ with $\mathcal{S}$ the spin moment.

Having thoroughly probed the physics of the in-plane versus out-of-plane anisotropy we now consider the question of which in-plane direction the Ru moment assumes, i.e., the question of what is the in-plane easy axis of the spin. To this end we calculated E_{IP} for all the symmetry-inequivalent absorbate positions, as shown in Figure 1c. As may be seen, E_{IP} is generally an order of magnitude smaller than E_{IO} and attains its maximum value, as one would expect, at the edges of the graphene flakes. This follows from the fact that it is the lowering of the symmetry of the local environment that is crucial for the anisotropy (as the existence of orbital currents implies local magnetism), and hence, in the centre of even the rather small flakes presented here the anisotropy is substantially lower than

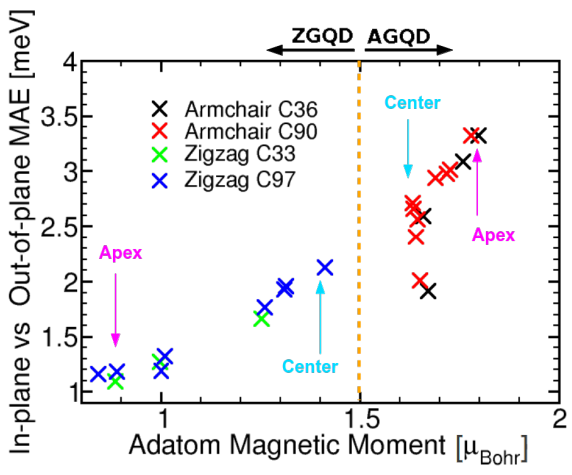

Figure 2: Correlation between the magnetic moment and the in-plane versus out-of-plane anisotropy, E_{IO}, see Equation 1, for armchair-graphene quantum dots (AGQDs) and zigzag-graphene quantum dots (ZGQDs) consisting of 36 and 90 carbon atoms for the AGQDs, and 33 and 97 carbon atoms for the ZGQDs. Each of the points represents the spin moment and E_{IO} for an adsorbate position of the Ru adatom. Evidently, the larger the Ru moment the greater the value attained for E_{IO}. Specific absorbate positions (edge, apex) are indicated by the text. Note that the edge positions of the ZGQD have the lowest adatom moment (and so lowest E_{IO}) while, in contrast, on the AGQD these positions have the highest adatom moment and E_{IO}. Points that deviate from the overall trend reflect a specific electronic structure associated with low symmetry positions of the AGQDs.

at the edges. Interestingly, we find that for the edge positions the spin always points perpendicular to the boundary of the flake.

Conclusion

Using first-principles DFT methods we have investigated the magnetic properties of Ru adatoms on two types of graphene flakes: the armchair (AGQD) and zigzag (ZGQD) edged triangular graphene quantum dots. The geometry of these flakes is such that each has only one specific type high-symmetry edge (armchair or zigzag), allowing the clear separation of the physics of these two common edge types. We find that for all flakes and adatom positions investigated, the Ru magnetic moment prefers to lie in the plane of the island, and that the difference in energy between the most favourable and least favourable in-plane positions for the moment is of the order of 0.1 eV. For adatoms at the edge positions we find that the moment points perpendicular to the edge of the island.

Interestingly, the in-plane versus out-of-plane anisotropy dramatically depends on the edge type, with the zigzag edge showing a marked reduction in both the Ru moment and the corresponding E_{IO} as compared to values at the centre of the flake, with the opposite trend seen for the armchair-edge flakes. The origin of this lies in the antiferromagnetic coupling of the adatom to the spin-polarised p_z edge state in the ZGQD.

Acknowledgements

We acknowledge financial support from EC FP7 e-infrastructures project MMM@HPC (GA 261594). KF thanks for support by the DFG-funded Transregional Collaborative Research Center SFB/TRR 88 “3 MET”. SS acknowledges the financial support of the Collaborative Research Center SFB 953.

References

1. Novoselov, K. S.; Geim, A. K.; Morozov, S. V.; Jiang, D.; Zhang, Y.; Dubonos, S. V.; Grigorieva, I. V.; Firsov, A. A. *Science* **2004,** *306,* 666–669. doi:10.1126/science.1102896
2. Wee, A. T. S. *ACS Nano* **2012,** *6,* 5739–5741. doi:10.1021/nn302799p
3. Geim, A.; Novoselov, K. S. *Nat. Mater.* **2007,** *6,* 183–191. doi:10.1038/nmat1849
4. Novoselov, K. S.; Geim, A. K.; Morozov, S. V.; Jiang, D.; Katsnelson, M. I.; Grigorieva, I. V.; Dubonos, S. V.; Firsov, A. A. *Nature* **2005,** *438,* 197–200. doi:10.1038/nature04233
5. Meyer, J. C.; Geim, A. K.; Katsnelson, M. I.; Novoselov, K. S.; Booth, T. J.; Roth, S. *Nature* **2006,** *446,* 60–63. doi:10.1038/nature05545
6. Heersche, H. B.; Jarillo-Herrero, P.; Oostinga, J. B.; Vandersypen, L. M. K.; Morpurgo, A. F. *Nature* **2007,** *446,* 56–59. doi:10.1038/nature05555
7. Stankovich, S.; Dikin, D. A.; Dommett, G. H. B.; Kohlhaas, K. M.; Zimney, E. J.; Stach, E. A.; Piner, R. D.; Nguyen, S. T.; Ruoff, R. S. *Nature* **2006,** *442,* 282–286. doi:10.1038/nature04969
8. Berger, C.; Song, Z.; Li, X.; Wu, X.; Brown, N.; Naud, C.; Mayou, D.; Li, T.; Hass, J.; Marchenkov, A. N.; Conrad, E. H.; First, P. N.; de Heer, W. A. *Science* **2006,** *312,* 1191–1196. doi:10.1126/science.1125925
9. Danneau, R.; Wu, F.; Craciun, M. F.; Russo, S.; Tomi, M. Y.; Salmilehto, J.; Morpurgo, A. F.; Hakonen, P. J. *Phys. Rev. Lett.* **2008,** *100,* 196802. doi:10.1103/PhysRevLett.100.196802
10. Geim, A. K. *Science* **2009,** *324,* 1530–1534. doi:10.1126/science.1158877
11. Candini, A.; Klyatskaya, S.; Ruben, M.; Wernsdorfer, W.; Affronte, M. *Nano Lett.* **2011,** *11,* 2634–2639. doi:10.1021/nl2006142
12. Xiao, R.; Fritsch, D.; Kuz'min, M. D.; Koepernik, K.; Richter, M.; Vietze, K.; Seifert, G. *Phys. Rev. B* **2010,** *82,* 205125. doi:10.1103/PhysRevB.82.205125
13. Sargolzaei, M.; Gudarzi, F. *J. Appl. Phys.* **2011,** *110,* 064303. doi:10.1063/1.3636112
14. Pandey, R.; Rao, B. K.; Jena, P.; Newsam, J. M. *Chem. Phys. Lett.* **2000,** *321,* 142–150. doi:10.1016/S0009-2614(00)00287-6
15. Zólyomi, V.; Rusznyák, A.; Kürti, J.; Lambert, C. J. *J. Phys. Chem. C* **2010,** *114,* 18548–18552. doi:10.1021/jp107669b
16. Cao, C.; Wu, M.; Jiang, J.; Cheng, H.-P. *Phys. Rev. B* **2010,** *81,* 205424. doi:10.1103/PhysRevB.81.205424
17. Zhang, H.; Lazo, C.; Blügel, S.; Heinze, S.; Mokrousov, Y. *Phys. Rev. Lett.* **2012,** *108,* 056802. doi:10.1103/PhysRevLett.108.056802
18. Pfandzelter, R.; Steierl, G.; Rau, C. *Phys. Rev. Lett.* **1995,** *74,* 3467–3470. doi:10.1103/PhysRevLett.74.3467
19. Treutler, O.; Ahlrichs, R. *J. Chem. Phys.* **1995,** *102,* 346–354. doi:10.1063/1.469408

20. Ahlrichs, R.; Bär, M.; Häser, M.; Horn, H.; Kölmel, C. *Chem. Phys. Lett.* **1989,** *162,* 165–169. doi:10.1016/0009-2614(89)85118-8
21. *A development of University of Karlsruhe and Forschungszentrum Karlsruhe GmbH, 1989-2007,* TURBOMOLE V6.4 2012; TURBOMOLE GmbH.
Since 2007; available from http://www.turbomole.com.
22. Grimme, S. *J. Comput. Chem.* **2006,** *27,* 1787–1799. doi:10.1002/jcc.20495
23. Armbruster, M. K.; Weigend, F.; van Wüllen, C.; Klopper, W. *Phys. Chem. Chem. Phys.* **2008,** *10,* 1748–1756. doi:10.1039/B717719D
24. Weigend, F.; Baldes, A. *J. Chem. Phys.* **2010,** *133,* 174102. doi:10.1063/1.3495681
25. Peterson, K. A.; Figgen, D.; Dolg, M.; Stoll, H. *J. Chem. Phys.* **2007,** *126,* 124101. doi:10.1063/1.2647019
26. Fernández-Rossier, J.; Palacios, J. J. *Phys. Rev. Lett.* **2007,** *99,* 177204. doi:10.1103/PhysRevLett.99.177204
27. Lieb, E. H. *Phys. Rev. Lett.* **1989,** *62,* 1201–1204. doi:10.1103/PhysRevLett.62.1201
28. Sevinçli, H.; Topsakal, M.; Durgun, E.; Ciraci, S. *Phys. Rev. B* **2008,** *77,* 195434. doi:10.1103/PhysRevB.77.195434

License and Terms

Beilstein Journal of Nanotechnology

Plasticity of nanocrystalline alloys with chemical order: on the strength and ductility of nanocrystalline Ni–Fe

Jonathan Schäfer* and Karsten Albe

Full Research Paper

Open Access

Address:
Technische Universität Darmstadt, Fachbereich Material- und Geowissenschaften, Fachgebiet Materialmodellierung, Petersenstr. 32, D-64287 Darmstadt, Germany

Email:
Jonathan Schäfer* - schaefer@mm.tu-darmstadt.de

* Corresponding author

Keywords:
nanocrystalline materials; grain boundary structure; grain boundary segregation; plastic deformation; molecular dynamics

Beilstein J. Nanotechnol. **2013,** *4,* 542–553.
doi:10.3762/bjnano.4.63

Received: 21 June 2013
Accepted: 26 August 2013
Published: 19 September 2013

This article is part of the Thematic Series "Advances in nanomaterials" and is dedicated to Professor Horst Hahn on the occasion of his 60th birthday.

Guest Editors: H. D. Gleiter and T. Schimmel

Abstract

Plastic deformation and alloying of nanocrystalline Ni–Fe is studied by means of atomic scale computer simulations. By using a combination of Monte-Carlo and molecular dynamics methods we find that solutes have an ordering tendency even if grain sizes are in the nanometer regime, where the phase field of the ordered state is widened as compared to larger grain sizes. Tensile testing of disordered structures with various elemental distributions and the simultaneous analysis of intragranular defects reveal that solid solution strengthening is absent for the studied grain sizes. The composition and relaxation state of the grain boundary control the strength of the material, which is also found for ordered structures ($L1_2$), where dislocation activity is suppressed.

Introduction

In intermetallics grain refinement to the nanometer scale has been considered as a possible route for achieving room temperature ductility in this otherwise brittle class of materials [1,2]. The underlying assumption is that for very small grain sizes plasticity can be carried by grain boundary (GB) mediated processes rather than by energetically expensive superlattice dislocations [3,4].

The experimental realization of a nanocrystalline (nc) microstructure of an ordered alloy, however, strongly depends on the route of preparation. For electrodeposited nc Ni–Fe alloys (up to 28% Fe) a solid solution with no chemical order was observed [5]. In Ni_3Al, a partially ordered state was found after rolling at liquid nitrogen temperature to obtain a nanometer grain size [6]. In nanostructured Ni_3Al processed by ball milling [7] or high pressure torsion [8], on the contrary, a complete loss of order is observed during preparation. Grain refinement by severe plastic deformation (SPD) of B2 FeAl leads to a partial destruction of the long range order and the formation of ordered nanodomains,

which can grow to the size of grains upon heating and restore the order [9].

Concerning the mechanical properties of nc intermetallics, grain refinement often leads to a severe strengthening but does not increase the room temperature ductility [10]. It was demonstrated experimentally, that additional modifications, e.g., a bimodal grain structure and nanotwins can enhance the ductility while conserving the strength [10]. For nc Ni–Fe alloys, several observations were made: For nc disordered Ni–Fe, prepared by electrodeposition, where the Fe content was modulated to control the grain size, an inverse Hall–Petch relationship was reported with a critical grain size around 15 nm [5]. Nc disordered Ni–Fe (5.6% Fe) with an average grain size of 10 nm showed a tensile yield strength in the order of 2 GPa and an increase in strength after annealing even though some grain growth was observed [11]. It was reported that plastic deformation processes in nc Ni–Fe (15% Fe) undergo a transition with applied strain, where at low strains the strain is mainly accommodated by the grain boundaries while at large strains dislocation motion becomes dominant [12].

Computational attempts such as molecular dynamics simulations (MD) can help to understand the macroscopic properties by means of the atomistic processes. For intermetallic phases, MD simulations have been successfully employed, to investigate, e.g., the nucleation of dislocations from surfaces [13] or at GBs [14]. Furthermore, the mechanical response of intermetallic nanostructures such as nanowires has been studied by MD [15].

For understanding the atomistic processes that are carrying and controlling plastic deformation in nc intermetallics (Ni–Fe), we present a set of MD simulations. Samples with 5 and 15 nm average grain size are constructed according to the Voronoi tessellation method [16], then chemically equilibrated via a hybrid MD/Monte-Carlo (MD/MC) scheme and finally tested in tensile straining tests. By this scheme we are able to generate samples of different compositions and a varying internal order for a given average grain size. This allows to explore their respective influence on the macroscopic strength. We perform a detailed analysis of the virtual structures and investigate the influence of composition, element distribution and the degree of order on the interplay of intergranular and intragranular deformation mechanisms.

Methodology

We employ a hybrid simulation method [17] that has been used for describing miscible random alloys [18] as well as segregating systems [19]. The atomic interaction is modeled by an embedded-atom (EAM) type potential which reproduces the phase diagram of Ni–Fe [20]. The hybrid method allows for structural relaxation by MD and for chemical equilibration by interleaving MC steps, yielding structurally equilibrated samples with an equilibrium distribution of the constituents. The MC algorithm, which is sampling a semi-grandcanonical ensemble [17,18,21], equilibrates the distribution of the constituents and the composition of the system for a given difference of chemical potentials $\Delta\mu = \mu_{Ni} - \mu_{Fe}$. The method is used within the framework of the freely-available molecular dynamics code LAMMPS [22], which was extended to perform the MC steps [17].

Initially, we created nc model structures of perfectly ($L1_2$) ordered $FeNi_3$ with average grain sizes of 5 and 15 nm consisting of 432 and 54 grains, respectively. The Voronoi tesselation method [16] was used to set up the grain shapes based on randomly placed center points in 3-dimensional periodic cubic simulation box. The lattice orientations of the grains were taken from a random isotropic distribution. For avoiding spurious configurations in the as-prepared Voronoi samples, we deleted atoms from the grain boundaries that were closer than 2.0 Å to other atoms prior to relaxation. Relaxation and equilibration of the composition and distribution of the constituents was then performed at 600 K for 1 ns at zero hydrostatic pressure using Berendsen's [23] thermostat and barostat. During this MD equilibration, one full MC step was performed every 40 fs, i.e., 25,000 trial exchanges were performed on each atom in the system on average. For obtaining the equilibrium chemical distribution at a given composition, the temperature parameter for the MC algorithm was the same as in the MD stage. For the variation of the global composition, we choose different values for $\Delta\mu$ to chemically equilibrate the system at a global composition, deviating from the stoichiometric concentration.

The short range order in the system was evaluated by computing the Warren and Cowley [24] order parameter for each atom surrounded by its 12 nearest neighbors as $\alpha_i = 1 - Z_j/(12 \times (1 - c_i))$, where α_i denotes the ordering parameter for atom of type i, Z_j is the number of atoms of the according other type among the 12 nearest neighbors and c_i is the global concentration of atoms of type i. For distinguishing atoms located in grain boundaries from those in the bulk, we use the common neighbor analysis (CNA) [25]. The cutoff parameter R_{CNA} for identifying nearest neighbors was chosen between the first and second nearest neighbor shells: $R_{CNA} = a_0(x) \cdot \left(1 + \sqrt{1/2}\right)/2$, with $a_0(x)$ being the static lattice parameter for a given concentration x. Analysis of the defects within the microstructure was done by a novel algorithm, which allows for the extraction and analysis of dislocations from simulation data in a fully automated way [26].

The local atomic volume of each atom was calculated by means of the Voronoi tessellation method [27]. We define the free volume of the GB atoms as the difference between the average atomic volume of all GB atoms and the average atomic volume within a fcc single crystal of random solid solution and a chemical composition identical to the composition of the GB.

Samples were quenched from annealing temperature to 300 K. Then they were deformed by imposing a constant engineering strain rate (10^8 1/s) in uniaxial direction on the simulation cell. The cell size was allowed to relax perpendicular to the strain axis.

Results

Structural characterization

In a first step, the elemental distribution in the model structures relaxed by the hybrid MD/MC scheme were analyzed in order to quantify the amount of ordering in the grain interior. At finite temperature the instantaneous element distribution is fluctuating and it is therefore useful to introduce the concept of an "effective atom" [28], namely the average occupancy of an atomic position. By taking the ensemble average over a large number of MC steps, the site occupancy for each atomic position was computed in the semi-grandcanonical ensemble. Figure 1 shows the local site occupancy for the different structural elements (grains and GB), which were identified according to CNA. It can be seen that the chemical composition of the GBs is strongly dependent on the global composition, whereas the grain interior is less affected and stays close to the stoichiometric composition of the $L1_2$ structure (25% of Fe). The GB therefore acts as source or sink for solutes accommodating any excess of Fe or Ni, respectively. This allows the grain interior to stay in the ordered and stoichiometric state. Furthermore, it can be seen, that the change in GB composition shows a stronger dependence on the global composition for the case of a 15 nm grain size. Since the GBs need to accommodate the excess in either Ni or Fe, this can be explained by the smaller volume fraction of GB atoms as compared to the 5 nm case. For the atomic arrangement inside the grains we find $L1_2$ ordering, irrespective of global composition. It shall be noted, that this finding is independent of the initial configuration prior to equilibration, i.e., whether we start from a perfectly ordered or a disordered state (not shown). Figure 2 shows representative slices through individual grains and the surrounding GBs for different grain sizes and composition. In the inset, the slice is colored according to the deviation from perfect $L1_2$ short range order, where green refers to a perfect $L1_2$ structure. For all atoms in the grain interior perfect $L1_2$ short range order (and consequently also long range order) is conserved for both studied grain sizes. Furthermore, it is visualized (for the 5 nm case), that also for a deviation from stoichiometric composition, the grain interior stays ordered while the GB accommodates the excess in either Ni or Fe. Interestingly, for the maximum deviation from stoichiometric composition, the GB is either almost free of Fe or enriched up to 50%, respectively (Figure 1). It shall be noted that some of the compositions reported here, which show an ordered $L1_2$ structure inside the grains, lie outside the phase field of the $L1_2$ structure (at 600 K) in the bulk phase diagram reproduced by the interatomic potential [20]. The stability range of the ordered $L1_2$ structure in the phase diagram is therefore widened at reduced average grain sizes, where the grains stay ordered and the GBs act as a buffer layer. The experimentally observed disordered state of nc Ni–Fe with an Fe content of up to 28% [5] produced by electrodeposition is therefore considered to result from the route of processing, leading to a kinetically trapped disordered elemental distribution and not due to a differing stable configuration for the case of a nanometer grain size as observed for other systems [29].

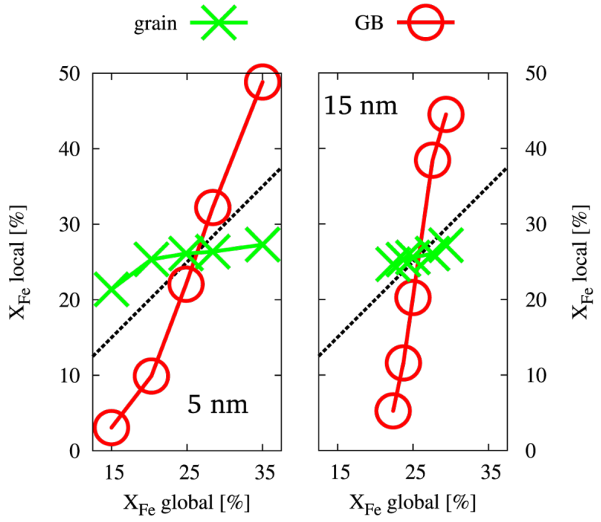

Figure 1: Local composition of the grain interior and the GBs as a function of the global composition for two different grain sizes (5 nm and 15 nm).

Random alloy: fixed GB composition, varying grain composition (15 nm)

For coarse grained material, the strengthening effect of substitutional solutes (i.e., solid solution strengthening) is well understood, where an increase in strength according to $\tau_c \sim \sqrt{c}$ is expected [31]. In order to investigate, whether substitutional solutes in the grain interior have an effect on the macroscopic mechanical properties for the case of a nc solid solution, samples with differing composition inside the grains but identical GB (composition and structure) were compared. The initially equilibrated structure was identical for all cases with a concentration of 20% Fe in the GBs. Different amounts of Fe

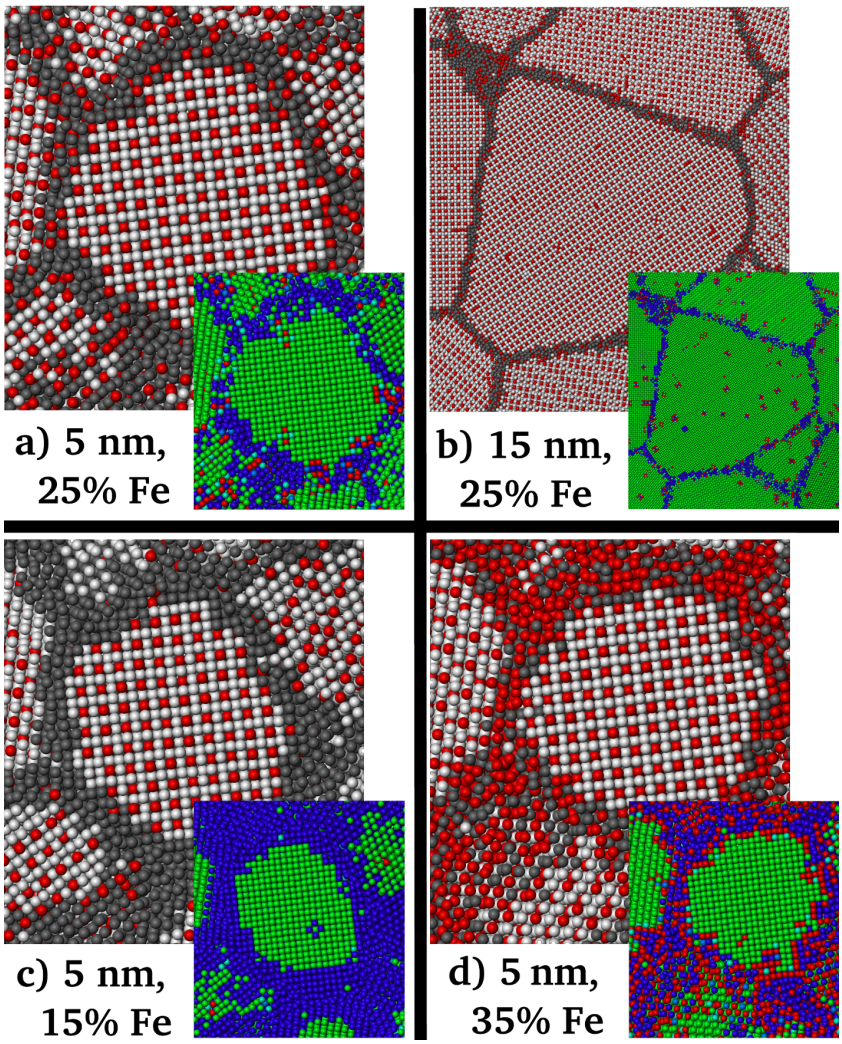

Figure 2: Atomic configurations after annealing with the hybrid MD/MC scheme. Ni atoms in the grain interior are white, Ni atoms in the GB are dark grey, Fe atoms are red. In the inset, the color coding is according to the deviation from perfect $L1_2$ short range order, where green refers to perfect $L1_2$ structure, while red and blue refer to a positive and negative deviation, respectively. a) 5 nm grain size with a global concentration of 25% Fe. b) 15 nm grain size with a global concentration of 25% Fe. c) 5 nm grain size with an (understoichiometric) global concentration of 15% Fe. d) 5 nm grain size with an (overstoichiometric) global concentration of 35% Fe. Snapshots were generated using OVITO [30].

(5%, 15% and 25%) were then distributed randomly in the grain interior and equilibrated via successive MD steps at 300 K and zero hydrostatic pressure prior to deformation.

Figure 3 shows slices through the initial microstructure for two different compositions, where the random distribution and differing amount of solute in the grain interior is visualized. Figure 3 furthermore shows the stress–strain behavior and the evolution of dislocations in the microstructure under tensile load. It can be seen that a differing composition of the grain interior but identical GB structure (and composition) has little effect on the macroscopic behavior. Neither the stress–strain behavior nor the dislocation density show a dependence on the amount of solute, distributed randomly in the grain interior, even though dislocations are the major carrier of plasticity under the given conditions [32]. We conclude that for the presented case stresses required for dislocation nucleation from the GBs are so high that pinning by solutes inside the grains does not provide an additional barrier for dislocation motion. The stresses required for dislocation nucleation might, however, depend on the state and composition of the GBs. To test a potential effect on the macroscopic properties, we focus on the GB composition in the next section.

Random alloy: varying GB composition, fixed grain composition (15 nm)

The delicate interplay between solute distribution and mechanical response of this nc alloy was further studied on samples,

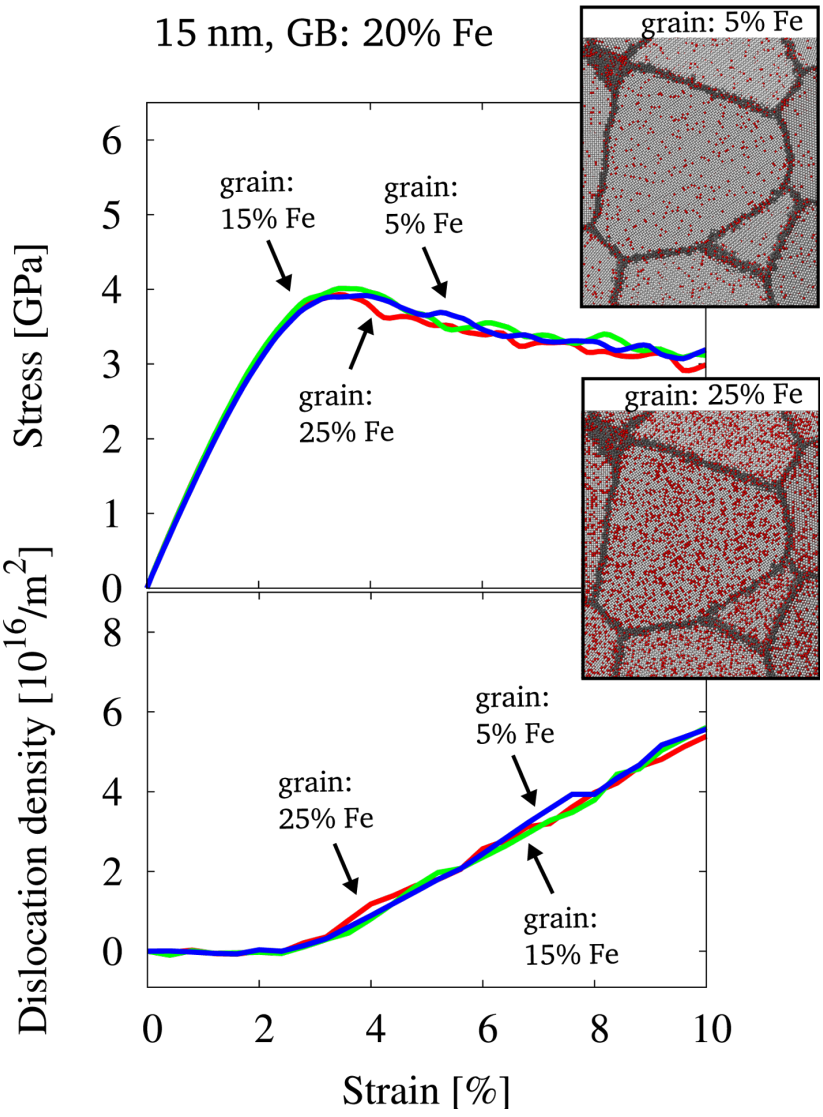

Figure 3: Stress-strain behavior and dislocation density for structures of 15 nm grain size, which were equilibrated by the hybrid MD/MC scheme at a global composition of 25% Fe. The distribution of solutes in the grain interior only was then randomized and the composition inside the grains was changed prior to deformation. The data for three different concentrations inside the grains is shown. Additionally, two snapshots of the initial configuration visualize the solute distribution for two different compositions. Color coding is identical to Figure 2.

where the random solid solution inside the grain interior was held at a constant composition of 25% Fe, but different amounts of solute were introduced into the GB during equilibration. That is, the nc structures were equilibrated via the MD/MC scheme at differing global compositions, leading to the described variation in the GB composition (Figure 1). For all studied samples, the grain interior stays close to the stoichiometric composition after equilibration via the MD/MC scheme (Figure 1). To eliminate any effect due to the slight variation in grain composition and to allow for dislocation processes, the grain interior in all samples was manually brought to a random solid solution with an identical composition for all structures. Prior to deformation, the structures were equilibrated via MD steps at 300 K and zero hydrostatic pressure. Since the composition and relaxation state of the grain interior is identical for all samples, any differences in the macroscopic behavior must result from the changes in GB composition. Figure 4 shows snapshots of a representative grain and the surrounding GBs inside the microstructure for two different cases, where a similar distribution of solutes is present inside the grains, but the GB composition is varied. The corresponding stress–strain behavior (Figure 4) reveals that there is a dependence on the amount of solute added to the GB via the MD/MC scheme, while the evolution of dislocations stays similar for all cases and is therefore not affected. The effect of different amounts of solute in the GB is more pronounced for the onset of plastic deformation. This is consistent with other

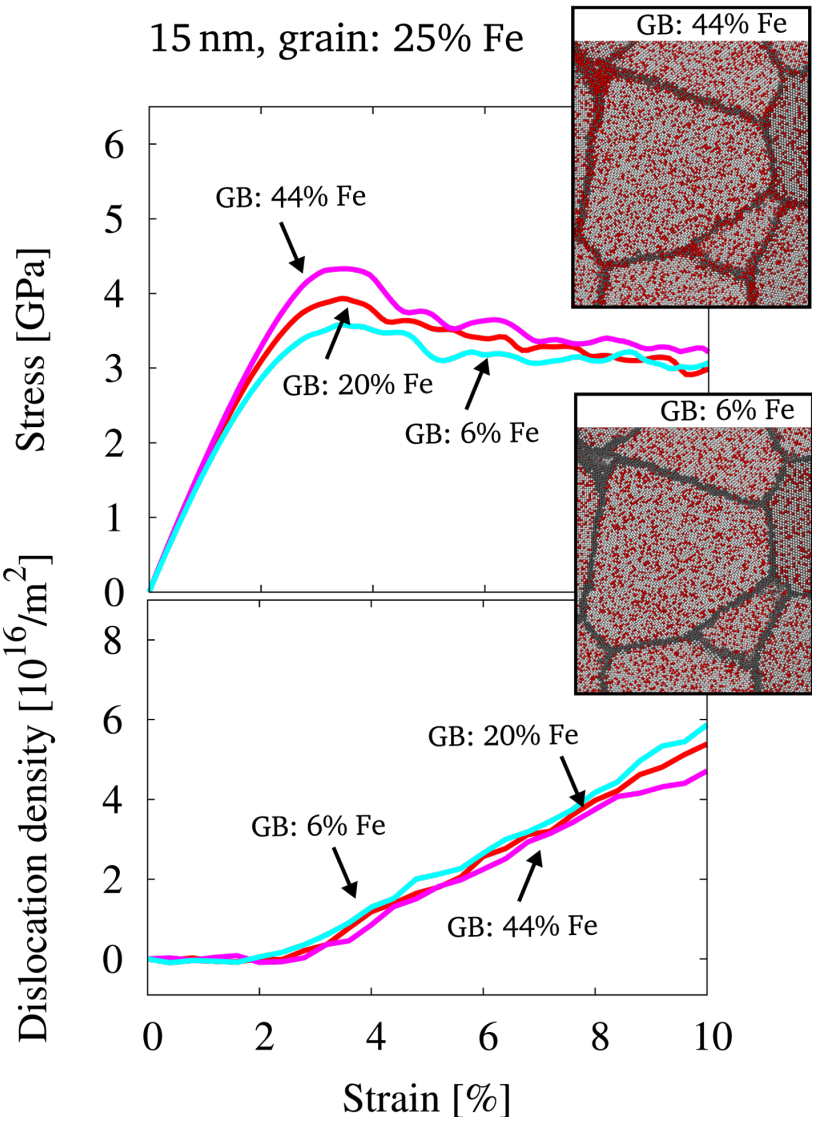

Figure 4: Stress-strain behavior and dislocation density for structures of 15 nm grain size, which were equilibrated by the hybrid MD/MC scheme at different global compositions (22, 25 and 29% Fe). The distribution of solutes in the grain interior only was then randomized with a constant composition of 25% inside the grains prior to deformation. The data for three different concentrations in the GB is shown. Additionally, two snapshots of the initial configuration visualize the solute distribution for two different GB compositions. Color coding is identical to Figure 2.

studies, where it was reported that during the initial stages of deformation, GB plasticity contributes more significantly to the overall plastic deformation [32].

We conclude that the amount of solutes inside the GB or the equilibration state of the GBs is of critical importance for the strength of this nc alloy, which was observed also for completely miscible systems [18]. After demonstrating the important role of the GB equilibration state, we want to discuss the case, where deformation processes are restricted to the GBs. Therefore, we will focus on samples with an ordered grain interior in the next section. Here, dislocation motion in the grain interior is suppressed by the presence of the intermetallic phase.

Ordered alloy: varying GB composition, fixed grain composition

15 nm grain size

In a next step samples with an ordered grain interior with fixed composition were tested. Here, dislocation processes can be excluded, since the nucleation of superdislocations cannot be expected for the presented strain rates and no fcc-like slip planes are available in the $L1_2$ structure. The structures with an ordered grain interior as obtained by equilibration via the MD/MC scheme are therefore expected to deform mainly by GB mediated processes. Figure 5 shows the stress–strain behavior and evolution of dislocations under tensile load for the structures of 15 nm grain size and varying composition. Obviously,

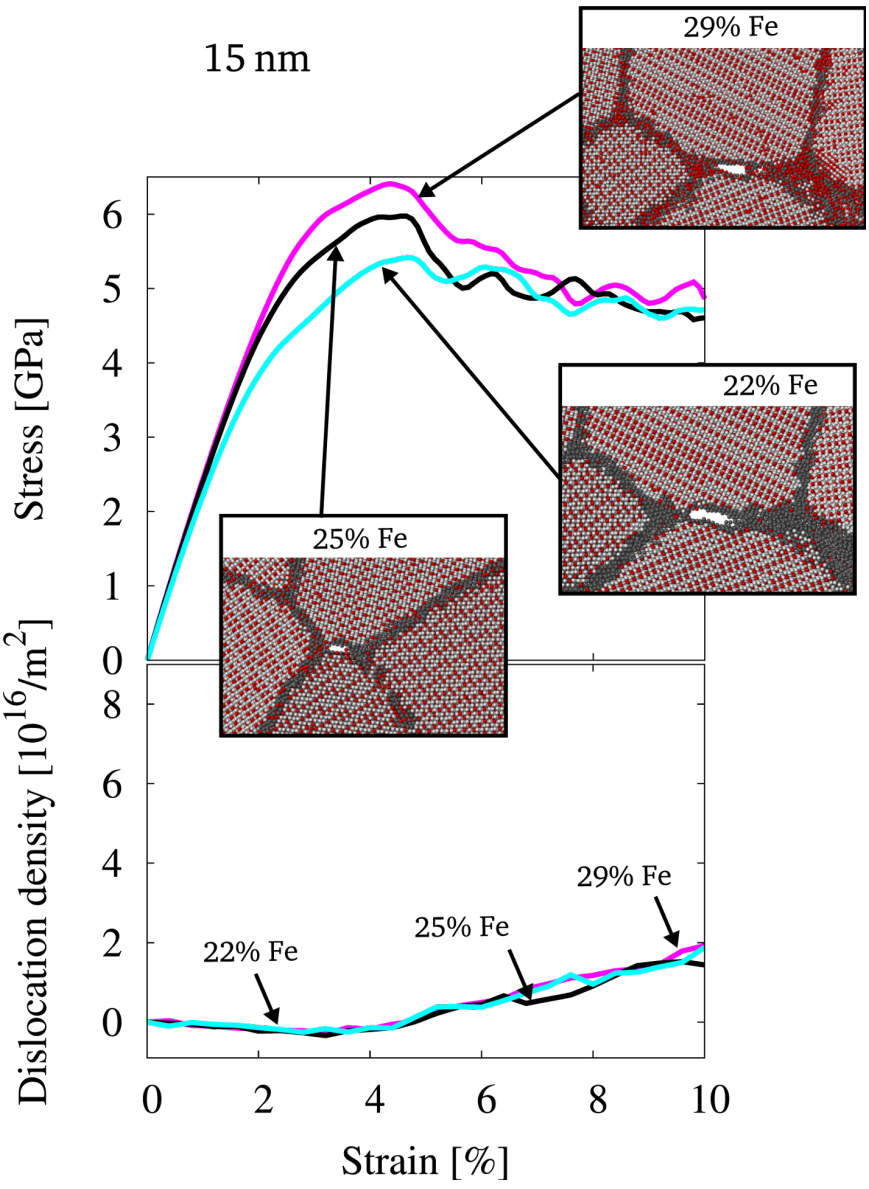

Figure 5: Stress-strain behavior and dislocation density for structures of 15 nm grain size, which were equilibrated by the hybrid MD/MC scheme at different global compositions (22, 25 and 29% Fe). The snapshots of the atomic configuration at the according strain visualize the onset of intergranular fracture. Color coding is identical to Figure 2.

the stress–strain behavior shows a clear dependence on GB composition, while dislocation activity is suppressed. The yield stress is also here increased for the case of a structure with GBs enriched in Fe and decreased for a structure with GBs fully depleted in Fe. This is similar to the case of a disordered grain interior as reported above, but even more pronounced.

At the onset of plastic deformation, however, intergranular fracture occurs within the presented structures. This is visualized in the snapshots shown in Figure 5, where slices through the atomic configuration are presented for various stages of deformation. Apparently, suppression of dislocation activity inside the grain interior leads to intergranular fracture, since GB mediated processes cannot be accommodated in samples with relatively large grains (15 nm).

5 nm grain size

Since the suppression of dislocation activity leads to intergranular fracture for the 15 nm grain size, the data for the 5 nm grain size is presented here, where a larger contribution to plastic deformation by GB mediated processes can be expected. Figure 6 shows the corresponding stress–strain behavior, evolution of dislocations and change in GB volume under tensile load. Representative slices through the microstructure at 10%

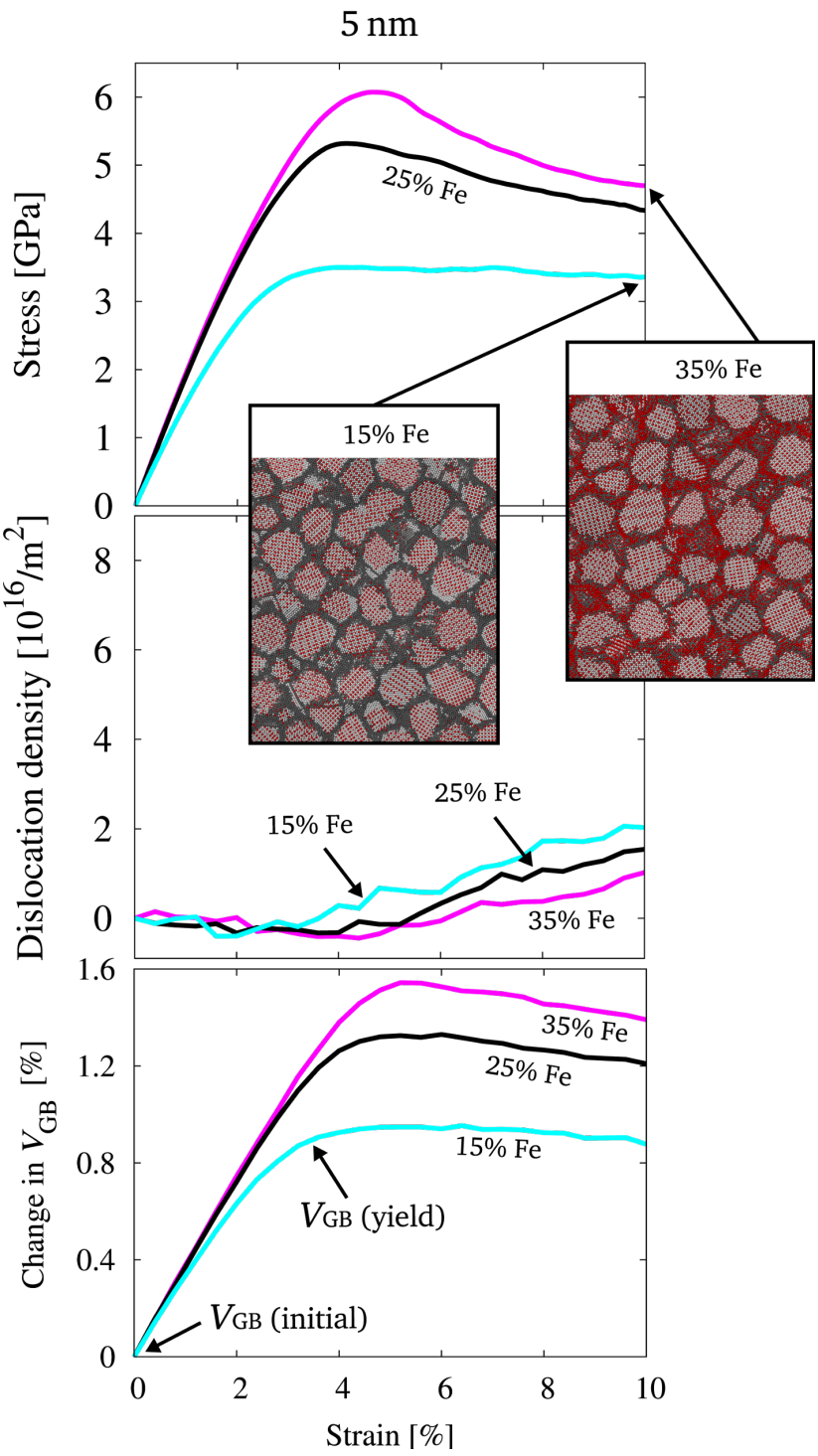

Figure 6: Stress-strain behavior, dislocation density and evolution of GB volume for structures of 5 nm grain size, which were equilibrated by the hybrid MD/MC scheme at different global compositions (15, 25 and 35% Fe). The representative slices through the microstructure at a total strain of 10% visualize, that no intergranular fracture occurred. Color coding is identical to Figure 2.

total strain are shown, which indicate that intergranular fracture did not occur for the structures with a grain size of 5 nm. From the stress–strain behavior, we find a strong dependence on the GB composition. The dislocation density reveals, that this is not caused by the evolution of intragranular defects, what is consistent with expectations based on the small grain size. It has been shown for other material systems, that the energetic state of the GB, which is closely related to the GB free volume drastically

influences the macroscopic mechanical properties of nc microstructures [18,19]. Monitoring the state of the GB for the presented samples in terms of the change in GB free volume (V_{GB}) shows that there is a strong similarity between the evolution of the GB volume and the stress during straining.

Obviously, for the structures with a higher yield stress, the GB volume needs to increase more drastically. This increase in GB volume is not only caused by elastic straining but by a general and irreversible increase of the GB volume and therefore also the sample volume. To quantify the amount of irreversible volume change during straining, the samples presented in Figure 6 were unloaded at different stages during deformation (every 0.4% of total strain). The GB volume as well as the total volume was then computed for the unloaded state of the samples. Figure 7 shows the irreversible change in GB volume (V_{GB}) as a function of the irreversible change in sample volume (V_{tot}) for three different samples of 5 nm grain size. It can be seen, that the total volume as well as the GB volume of the unloaded structures increase as a consequence of the deformation. It furthermore becomes evident, that the relative change in GB volume is higher than the relative change in the total volume. This means, that the volume of the grain interior is less affected by the overall deformation, which is consistent with GB mediated deformation processes. Comparing the data for the three different structures visualizes, that the irreversible change in GB volume (as well as in total volume) is the highest for the structure with the highest yield stress. Obviously, here, the free volume in the GBs must be raised more significantly in order to deform plastically. This leads to a stronger resistance to plastic deformation and therefore to an increased yield strength.

Controlling the strength - state of the GB

For quantifying the relaxation state of the GB, we compute the change in free volume in the GBs during straining for all structures. The correlation between the yield stress of the material and the change in GB free volume at the yield point is analyzed in order to quantify the relation between the onset of plastic deformation and the increase in free volume in the GBs. Experimentally, it was observed, that the 0.2% offset cannot be used as a yield criterion for nc metals (nc Ni–Fe) [12]. From in-situ X-ray peak profile analysis it was reported, that the transition from micro- to macroplasticity rather occurs around 0.7% for nc Ni [33]. We therefore took the 0.7% offset as a yield criterion for the presented data and extracted the yield stress as the stress at a plastic strain of 0.7%. For the same plastic strain, the change in GB free volume was extracted from the data. (It shall be noted, that the results are rather insensitive to the choice of the offset or employing the maxima in the stress–strain behavior as a criterion for yielding.) Figure 8 shows the correlation between the yield stress and the change in free volume in the GB. Obviously, the data for different stages of equilibration and different stages of ordering falls on the same trend. Remarkably, even the data for different grain sizes lies on the same trend, irrespective of the state of the grain interior. (The data for structures, which were not discussed in detail is also shown.) It becomes evident, that the state of the GB and therefore the necessary increase in GB free volume controls the yield strength of the material. This is consistent with observations made for miscible systems [18] and observations on materials where dislocation slip is completely inactive (ultrananocrystalline diamond), where it was observed, that the yield stress scales with the stress required for GB sliding [34].

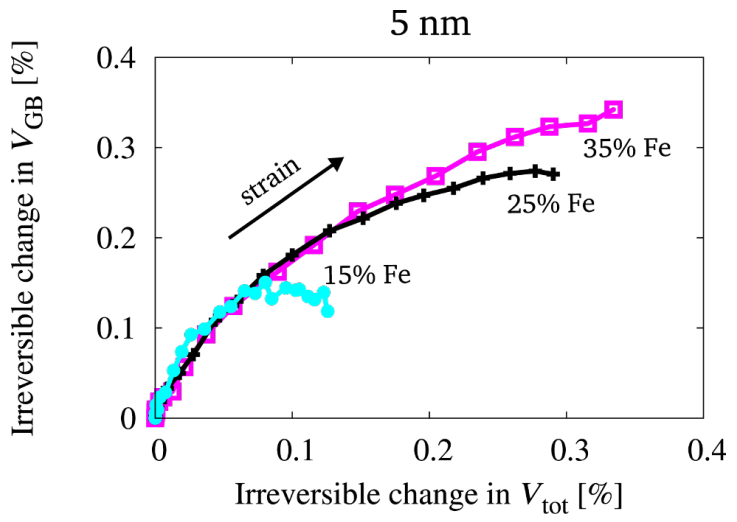

Figure 7: Irreversible change in GB volume (V_{GB}) as a function of the irreversible change in total sample volume (V_{tot}) measured at different stages of deformation (every 0.4% of total strain) after unloading. The data for structures of 5 nm grain size, which were equilibrated by the hybrid MD/MC scheme at different global compositions (15, 25 and 35% Fe) is shown.

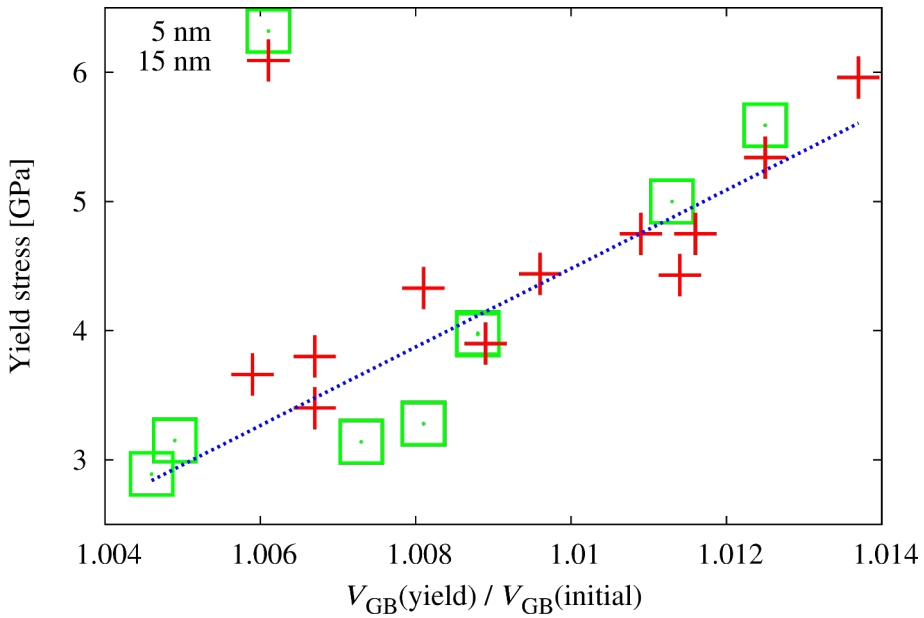

Figure 8: Correlation between yield stress (stress at plastic strain of 0.7%) and the change in free volume in the GBs during deformation for 5 and 15 nm grain size and different states of relaxation. Open squares refer to the data for 5 nm grain size and crosses to the data for 15 nm grain size. (Also data for samples, which were not discussed in detail is shown here.)

Conclusion

For studying plasticity in nc alloys with an ordering tendency, we performed hybrid MD/MC simulations of nc Ni–Fe of different grain sizes and compositions. We have shown that a nanocrystalline microstructure widens the stability range of the ordered $L1_2$ phase. Furthermore we could proof that conventional solid solution hardening is absent. For the presented conditions and samples, the equilibration state of the GBs controls the strength of the material, irrespective of the grain size.

The employed algorithm allowed us to obtain the equilibrium solute distribution for a given microstructure. For grain sizes in the nanometer range, ordering in Ni–Fe alloys was not observed experimentally [5] and it is reported, that nc materials can have a different ground state crystal structure than coarse crystalline material at the same composition and temperature [29,35]. For the case of Ni–Fe, however, our simulations reveal that the ground state of this alloy (at an Fe content of 25%) is the $L1_2$ ordered phase also for a 5 nm grain size. Equilibrating a nc model structure by the hybrid MD/MC scheme leads to an ordered grain interior, irrespective of the starting configuration. We can thus conclude that the experimental preparation procedure is producing metastable nc structures in the chemically disordered state. Our simulations furthermore show that decreasing the grain size into the nanometer range is extending the compositional phase field of the $L1_2$ structure, where perfect ordering in the grain interior is observed, since the GBs act as buffer layer accommodating excess components. The segregation of either Ni or Fe to the GB is therefore energetically in favor as compared to the loss of order inside the grains.

For studying the influence of solute distribution on the mechanical properties, additional configurations of solute distribution were obtained by randomly distributing the solute within individual parts of the microstructure, e.g., the GBs or grain interiors. Successive uniaxial straining simulations for the different samples then allowed to evaluate the influence of individual effects. For the structures with an equilibrated GB and a random solid solution of varying composition inside the grain interior we find that there is little effect of the composition of the grain interior on the macroscopic mechanical properties. The dislocation extraction algorithm [26] reveals that there is a considerable amount of dislocation activity inside the grains. It is, however, concluded that solid solution hardening is not present in the described structures since the stresses necessary for GB sliding and dislocation nucleation obviously exceed the stresses required for dislocation motion in the presence of substitutional solutes. For the structures with an equilibrated GB of varying composition and a random solid solution with constant composition inside the grains, we observe that the composition of the GB has an effect on the macroscopic mechanical properties. Here, an excess in Fe strengthens the structure, while a depletion in Fe decreases the strength. This is consistent with findings for miscible systems, where a maximum in the strengthening effect of solutes was observed for intermediate composi-

tions [18]. Also in this case, the dislocation density inside the grains does not change. The differing strength must therefore result from the state of the GB. The drastic increase in dislocation density, however, shows that a large fraction of plastic deformation is carried by intragranular defects. This could explain, why the difference in the response vanishes for larger strains, where intragranular defects contribute more significantly, which is reported also from experiment [12]. Suppressing dislocation motion by leaving the grain interior in the energetically favored, ordered state resulted in an even stronger dependence on GB composition. For the 15 nm grain size, however, an ordered grain interior also resulted in intergranular fracture. The processes in the GB can apparently not accommodate themselves for this grain size. Ductility could here be conserved by increasing the volume fraction of the GBs, i.e., by a smaller grain size. For the 5 nm samples, we find no intergranular fracture during straining and a strong dependence of strength on GB composition. For the 5 nm grain size, where GB mediated processes contribute stronger to plastic deformation, the material stays ductile also for the case of ordered grains. Here, the macroscopic mechanical properties are controlled by the state of the GB only.

Acknowledgements

Financial support of the Deutsche Forschungsgemeinschaft (FOR714) and grants of computer time from Forschungszentrum Jülich are gratefully acknowledged.

References

1. Bohn, R.; Haubold, T.; Birringer, R.; Gleiter, H. *Scr. Metall. Mater.* **1991,** *25,* 811–816. doi:10.1016/0956-716X(91)90230-X
2. Haubold, T.; Bohn, R.; Birringer, R.; Gleiter, H. *Mater. Sci. Eng., A* **1992,** *153,* 679–683. doi:10.1016/0921-5093(92)90270-B
3. Marcinkowski, M. J.; Brown, N.; Fisher, R. M. *Acta Metallurgica* **1961,** *9,* 129–137. doi:10.1016/0001-6160(61)90057-8
4. Kear, B. H.; Wilsdorf, H. G. *Trans. Metall. Soc. AIME* **1962,** *224,* 382.
5. Cheung, C.; Djuanda, F.; Erb, U.; Palumbo, G. *Nanostruct. Mater.* **1995,** *5,* 513–523. doi:10.1016/0965-9773(95)00264-F
6. Bojar, Z.; Jóźwik, P.; Bystrzycki, J. *Scr. Mater.* **2006,** *55,* 399–402. doi:10.1016/j.scriptamat.2006.03.062
7. Jang, J. S. C.; Koch, C. C. *J. Mater. Res.* **1990,** *5,* 498–510. doi:10.1557/JMR.1990.0498
8. Rentenberger, C.; Karnthaler, H. P. *Acta Mater.* **2005,** *53,* 3031–3040. doi:10.1016/j.actamat.2005.03.016
9. Gammer, C.; Mangler, C.; Karnthaler, H. P.; Rentenberger, C. *Scr. Mater.* **2011,** *65,* 57–60. doi:10.1016/j.scriptamat.2011.03.002
10. Edalati, K.; Toh, S.; Iwaoka, H.; Watanabe, M.; Horita, Z.; Kashioka, D.; Kishida, K.; Inui, H. *Scr. Mater.* **2012,** *67,* 814–817. doi:10.1016/j.scriptamat.2012.07.030
11. Schwaiger, R.; Reszat, J.-T.; Bade, K.; Aktaa, J.; Kraft, O. *Int. J. Mater. Res.* **2009,** *100,* 68–75. doi:10.3139/146.101785
12. Li, H. Q.; Choo, H.; Ren, Y.; Saleh, T. A.; Lienert, U.; Liaw, P. K.; Ebrahimi, F. *Phys. Rev. Lett.* **2008,** *101,* 015502. doi:10.1103/PhysRevLett.101.015502
13. DaSilva, C. J.; Rino, J. P. *Comput. Mater. Sci.* **2012,** *62,* 1–5. doi:10.1016/j.commatsci.2012.04.046
14. Farkas, D. *Philos. Mag. A* **2000,** *80,* 1425–1444. doi:10.1080/01418610008212128
15. Sutrakar, V. K.; Mahapatra, D. R. *Intermetallics* **2010,** *18,* 1565–1571. doi:10.1016/j.intermet.2010.04.009
16. Voronoi, G. *J. Reine Angew. Math.* **1908,** 198. doi:10.1515/crll.1908.134.198
17. Sadigh, B.; Erhart, P.; Stukowski, A.; Caro, A.; Martinez, E.; Zepeda-Ruiz, L. *Phys. Rev. B* **2012,** *85,* 184203. doi:10.1103/PhysRevB.85.184203
18. Schäfer, J.; Stukowski, A.; Albe, K. *Acta Mater.* **2011,** *59,* 2957–2968. doi:10.1016/j.actamat.2011.01.036
19. Vo, N. Q.; Schäfer, J.; Averback, R. S.; Albe, K.; Ashkenazy, Y.; Bellon, P. *Scr. Mater.* **2011,** *65,* 660–663. doi:10.1016/j.scriptamat.2011.06.048
20. Bonny, G.; Pasianot, R. C.; Malerba, L. *Philos. Mag.* **2009,** *89,* 711–725. doi:10.1080/14786430902720994
21. Erhart, P.; Caro, A.; de Caro, M. S.; Sadigh, B. *Phys. Rev. B* **2008,** *77,* 134206. doi:10.1103/PhysRevB.77.134206
22. Plimpton, S. *J. Comput. Phys.* **1995,** *117,* 1–19. doi:10.1006/jcph.1995.1039
23. Berendsen, H. J. C.; Postma, J. P. M.; van Gunsteren, W. F.; DiNola, A.; Haak, J. R. *J. Chem. Phys.* **1984,** *81,* 3684–3690. doi:10.1063/1.448118
24. Cowley, J. M. *Phys. Rev.* **1950,** *77,* 669–675. doi:10.1103/PhysRev.77.669
25. Honeycutt, J. D.; Andersen, H. C. *J. Phys. Chem.* **1987,** *91,* 4950–4963. doi:10.1021/j100303a014
26. Stukowski, A.; Albe, K. *Modelling Simul. Mater. Sci. Eng.* **2010,** *18,* 085001. doi:10.1088/0965-0393/18/8/085001
27. Rycroft, C. H.; Grest, G. S.; Landry, J. W.; Bazant, M. Z. *Phys. Rev. E* **2006,** *74,* 021306. doi:10.1103/PhysRevE.74.021306
28. Wang, H. Y.; Najafabadi, R.; Srolovitz, D. J.; Lesar, R. *Philos. Mag. A* **1992,** *65,* 625–655. doi:10.1080/01418619208201541
29. Mayo, M. J.; Suresh, A.; Porter, W. D. *Rev. Adv. Mater. Sci.* **2003,** *5,* 100–109.
30. Stukowski, A. *Modelling Simul. Mater. Sci. Eng.* **2010,** *18,* 015012. doi:10.1088/0965-0393/18/1/015012
31. Fleischer, R. L. *Acta Metall.* **1963,** *11,* 203–209. doi:10.1016/0001-6160(63)90213-X
32. Vo, N. Q.; Averback, R. S.; Bellon, P.; Odunuga, S.; Caro, A. *Phys. Rev. B* **2008,** *77,* 134108. doi:10.1103/PhysRevB.77.134108
33. Brandstetter, S.; Van Swygenhoven, H.; Van Petegem, S.; Schmitt, B.; Maaß, R.; Derlet, P. M. *Adv. Mater.* **2006,** *18,* 1545–1548. doi:10.1002/adma.200600397
34. Mo, Y. F.; Stone, D.; Szlufarska, I. *J. Phys. D: Appl. Phys.* **2011,** *44,* 405401. doi:10.1088/0022-3727/44/40/405401
35. Jiang, Q.; Yang, C. C. *Curr. Nanosci.* **2008,** *4,* 179–200. doi:10.2174/157341308784340949

Beilstein Journal of Nanotechnology

Deformation-induced grain growth and twinning in nanocrystalline palladium thin films

Aaron Kobler[*1,2], Jochen Lohmiller[3], Jonathan Schäfer[4], Michael Kerber[2], Anna Castrup[1,2], Ankush Kashiwar[5,6], Patric A. Gruber[3], Karsten Albe[4], Horst Hahn[1,2] and Christian Kübel[*2,7,§]

Full Research Paper

Open Access

Address:
[1]Technische Universität Darmstadt (TUD), KIT-TUD Joint Research Laboratory Nanomaterials, 64287 Darmstadt, Germany, [2]Karlsruhe Institute of Technology (KIT), Institute of Nanotechnology (INT), 76021 Karlsruhe, Germany, [3]Karlsruhe Institute of Technology (KIT), Institute for Applied Materials (IAM), P.O. Box 3640, 76021 Karlsruhe, Germany, [4]Technische Universität Darmstadt (TUD), Petersenstr. 32, 64287 Darmstadt, Germany, [5]Department of Metallurgical and Materials Engineering, Visvesvaraya National Institute of Technology (VNIT), Nagpur 440 010, Maharashtra, India, [6]Department of Materials Engineering, Indian Institute of Science (IISc), Bangalore 560 012, Karnataka, India and [7]Karlsruhe Institute of Technology (KIT), Karlsruhe Nano Micro Facility (KNMF), 76021 Karlsruhe, Germany

Email:
Aaron Kobler[*] - aaron.kobler@kit.edu;
Christian Kübel[*] - christian.kuebel@kit.edu

* Corresponding author
§ Hermann-von-Helmholtz-Platz 1, 76344 Eggenstein-Leopoldshafen, Germany; Tel.: +49 721 608 28970; Fax: +49 721 608 26368

Keywords:
ACOM-TEM; deformation mechanism; nanostructured metals; tensile testing; XRD

Beilstein J. Nanotechnol. **2013,** *4,* 554–566.
doi:10.3762/bjnano.4.64

Received: 14 June 2013
Accepted: 26 August 2013
Published: 24 September 2013

This article is part of the Thematic Series "Advances in nanomaterials" and is dedicated to Prof. Horst Hahn on the occasion of his 60th birthday.

Guest Editors: H. D. Gleiter and T. Schimmel

Abstract

The microstructure and mechanical properties of nanocrystalline Pd films prepared by magnetron sputtering have been investigated as a function of strain. The films were deposited onto polyimide substrates and tested in tensile mode. In order to follow the deformation processes in the material, several samples were strained to defined straining states, up to a maximum engineering strain of 10%, and prepared for post-mortem analysis. The nanocrystalline structure was investigated by quantitative automated crystal orientation mapping (ACOM) in a transmission electron microscope (TEM), identifying grain growth and twinning/detwinning resulting from dislocation activity as two of the mechanisms contributing to the macroscopic deformation. Depending on the initial twin density, the samples behaved differently. For low initial twin densities, an increasing twin density was found during straining. On the other hand, starting from a higher twin density, the twins were depleted with increasing strain. The findings from ACOM-TEM were confirmed by results from molecular dynamics (MD) simulations and from conventional and in-situ synchrotron X-ray diffraction (CXRD, SXRD) experiments.

Introduction

Nanocrystalline (nc) metals and alloys exhibit different mechanical behavior compared to their coarse-grained counterparts [1]. They show extraordinary strength but often lack ductility and suffer from rapid strain localization [2]. Understanding the underlying deformation mechanisms operating in these structures is important, for example to guarantee the reliability of nc materials in next-generation micro- and nano-scale devices.

In nc metals, with grain sizes well below 100 nm, the conventional deformation mechanisms based on dislocation motion and multiplication, which govern deformation in coarse-grained metals, are increasingly limited by grain boundaries with decreasing grain size. It is believed that their low ductility is associated with this [3]. Although nc metals are under investigation for a number of years, there still is an ongoing debate on the deformation mechanisms active in these materials. Discussed are grain boundary sliding, grain rotation, emission and annihilation of dislocations at grain boundaries, intragranular dislocation glide resulting in twinning/detwinning processes, stress-driven grain boundary migration and the formation of shear bands [4-7].

When studying the mechanical properties of nc metals and the associated deformation mechanisms, it is important to consider the preparation technique for the corresponding bulk nc metal. Bulk nc metals are typically produced by severe plastic deformation [8-11], inert gas condensation [4,12] or electrochemical deposition [13]. The different approaches result in significant differences in dislocation and twin density, porosity and impurity levels of the nc metals, where, e.g., pores and impurities may pin grain boundaries [14,15]. Furthermore, the different production techniques may also lead to different grain boundary structures with varying free volume and defect structure [4,16,17]. All these factors will affect the mechanical behavior of the material, making it difficult to determine and compare the inherent properties. As an alternative approach to prepare dense and very pure nc metals, we employed interrupted magnetron sputtering of thin metallic films [3,18,19]. The drawback of this approach is that mechanical testing and handling of the films is difficult. However, this can be improved by sputtering onto compliant polyimide substrates to stabilize the specimens and to avoid strain localization during tensile testing [20-22]. Such samples were successfully used in the present work.

The goal of the present work is to investigate the deformation processes active in ncPd films deposited by magnetron sputtering onto compliant substrates. The microstructural analysis is mainly performed by quantitative automated crystal orientation mapping TEM (ACOM-TEM) [23,24] and supplemented with grain size measurement using dark-field TEM (DF-TEM) and conventional X-ray diffraction (CXRD) after straining to different deformation levels. The evaluation presented in this paper concentrates on grain growth and twinning due to straining. The findings from the ex-situ investigations were compared to results obtained during in-situ deformation experiments using synchrotron X-ray diffraction (SXRD) on equivalent samples. Furthermore, the experimental results for the twin density evolution are qualitatively supported by molecular dynamics (MD) simulations.

Results

Microstructural characterization of the as deposited Pd films

The sputtering parameters were chosen to minimize residual stress and to obtain dense and high purity ncPd films [18]. Although the sputter parameters were chosen to be the same for each sample set, small fluctuations in the pressure have led to sample sets with slightly different residual stresses and different initial twin densities. Table 1 gives an overview of the samples analyzed.

BF-TEM images of the as-deposited sputtered Pd films exhibit a comparable microstructure for sample ncPd 1 and ncPd 2 (Figure 1). Figure 2 displays the microstructure as revealed by ACOM-TEM in plane-view and cross section. It shows an elongated columnar grain structure in growth direction compared to the isotropic structure in plane-view typical for sputter-deposited thin films.

CXRD analysis revealed an increased ratio between the XRD intensity of the (111) peak and the (200) peak of 9.8:1 for sample ncPd 1 and 7:1 for sample ncPd 2 compared to 2.1:1 for an isotropic palladium powder (Figure 3a). This indicates a <111> texture component in growth direction, which was also observed in the ACOM orientation density function in growth direction for both ncPd sample sets (Figure 3b).

Grain size evolution

Different characterization techniques result in slightly different absolute values for the grain size, but the trends observed during straining for each sample set are systematic and comparable for all investigation techniques used. The microstructural evolution during deformation of sample sets ncPd 1 and ncPd 2 was investigated by ACOM-TEM. Orientation and crystallite boundary maps corresponding to 0%, 5% and 10% strain are displayed in Figure 4. The grain size increases, with no noticeable evolution of a bimodal size distribution and no significant preferential growth direction is observed in plane-view. In Figure 5a, a quantitative analysis of the crystallite size as a

Table 1: Overview of the structural properties of the three ncPd sample sets analyzed using different techniques before straining.

		sample sets	ncPd 1	ncPd 2	ncPd 3
crystallite size [nm]	plane-view	ACOM-TEM	23 ± 13	24 ± 15	—
		in-situ SXRD	—	—	17
	growth direction	ACOM-TEM	34 ± 35	43 ± 23	—
		CXRD (111) peak	68	61	—
grain size [nm]	plane-view	ACOM-TEM	36 ± 19	34 ± 22	—
		DF-TEM	—	49	—
		in-situ SXRD	—	—	38
twin boundaries/ per grain		ACOM-TEM	1.3	1.1	—
		DF-TEM	—	0.005	—
		in-situ SXRD	—	—	1.2[a]
		CXRD residual stress [MPa]	−47 ± 25	16 ± 25	—
		CXRD micro strain	0.004	0.004	—

[a]Determined only by comparing grain size and crystallite size, assuming that the difference arises only from twinning. For details see section 'Twin density evolution'.

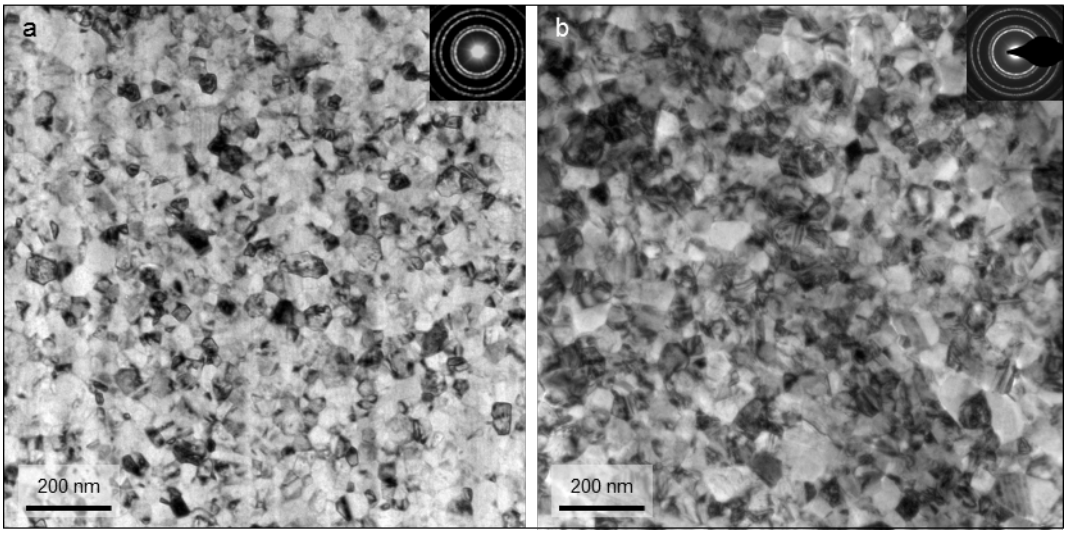

Figure 1: BF-TEM images of the initial microstructure of ncPd 1 (a) and ncPd 2 (b) with the corresponding selected electron diffraction pattern (SAED) as insets.

function of strain is given for all sample sets and analysis methods. Independent of sample set and method, an increase in in-plane crystallite size with increasing strain was observed, leading to an increase in crystallite diameter of ca. 45% at 10% strain for sample sets ncPd 1 and ncPd 2. This trend was also confirmed by in-situ SXRD and sample set ncPd 3. On the other hand, the CXRD crystallite size, representing the crystallite size perpendicular to the film surface, only increased by ca. 22%. Comparing the out-of-plane grain size evolution observed by CXRD and the in-plane ACOM-TEM analysis suggests a non-isotropic crystallite growth within the plane of the thin film and perpendicular to it with a ratio of around 2. This observed difference in crystallite growth is probably the result of stress coupled grain boundary motion, with a higher stress within the

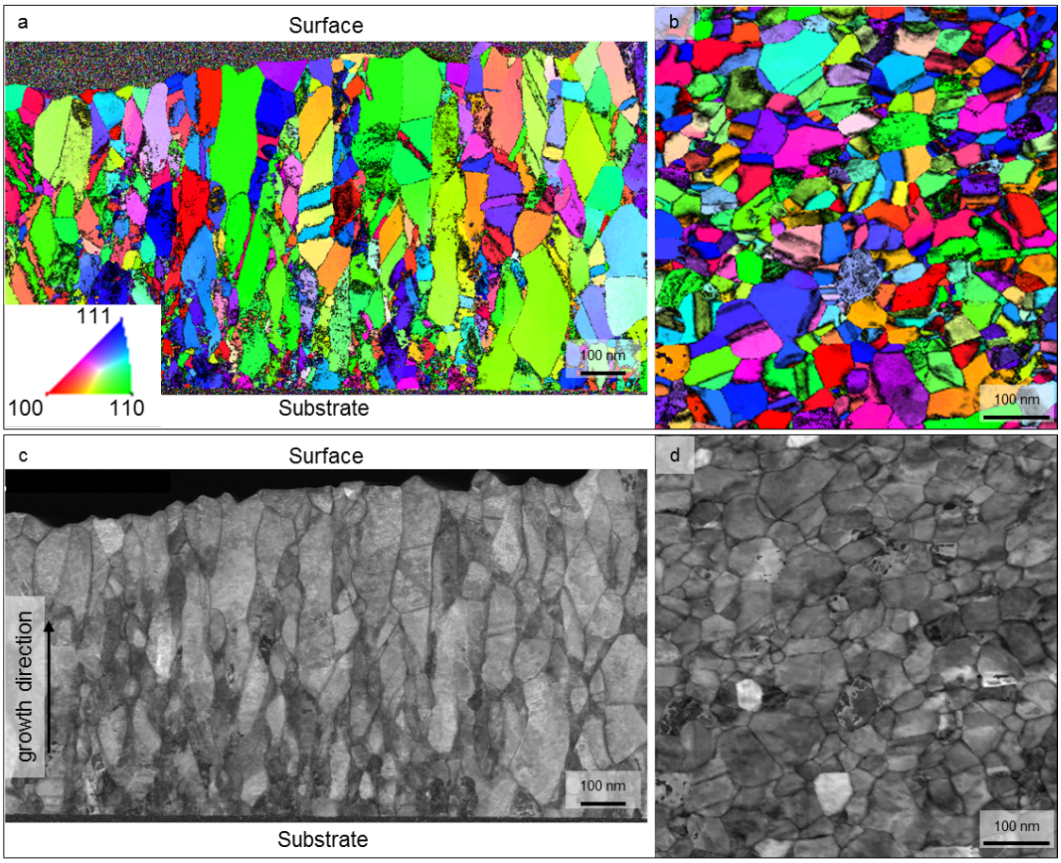

Figure 2: Orientation maps overlaid with reliability derived from ACOM-TEM of the as deposited sample in a) cross section and b) plane view (insets shows the color code for the orientation maps), c) and d) are the corresponding ACOM-TEM cross correlation index maps of the cross section and plane view, respectively.

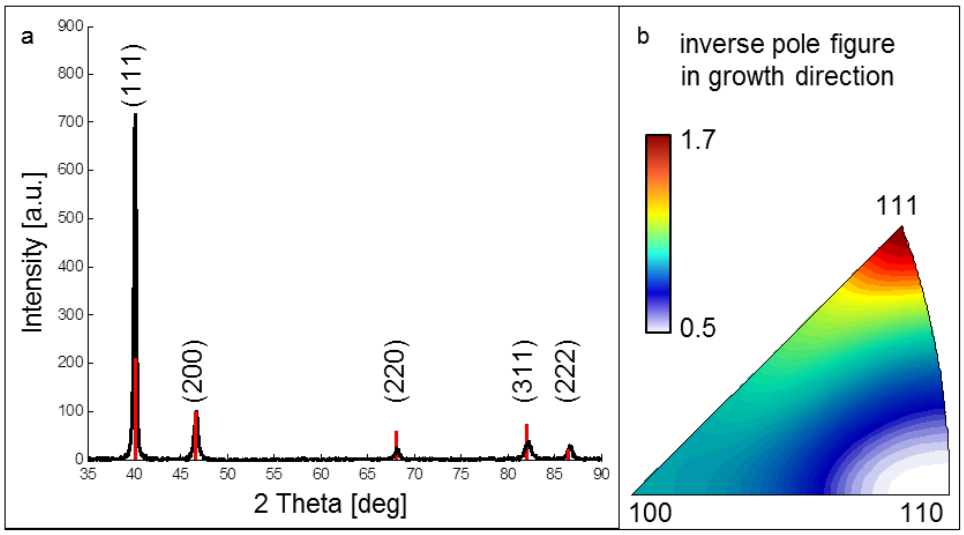

Figure 3: Orientation analysis of the as prepared sputtered ncPd film. a) X-ray diffraction pattern of the as deposited sample (black) (ncPd 2) overlaid with the isotropic Pd intensity profile (red) (normalized to the (200) peak intensity). b) Orientation density function (inverse pole figure) determined by ACOM-TEM in growth direction (ncPd 1).

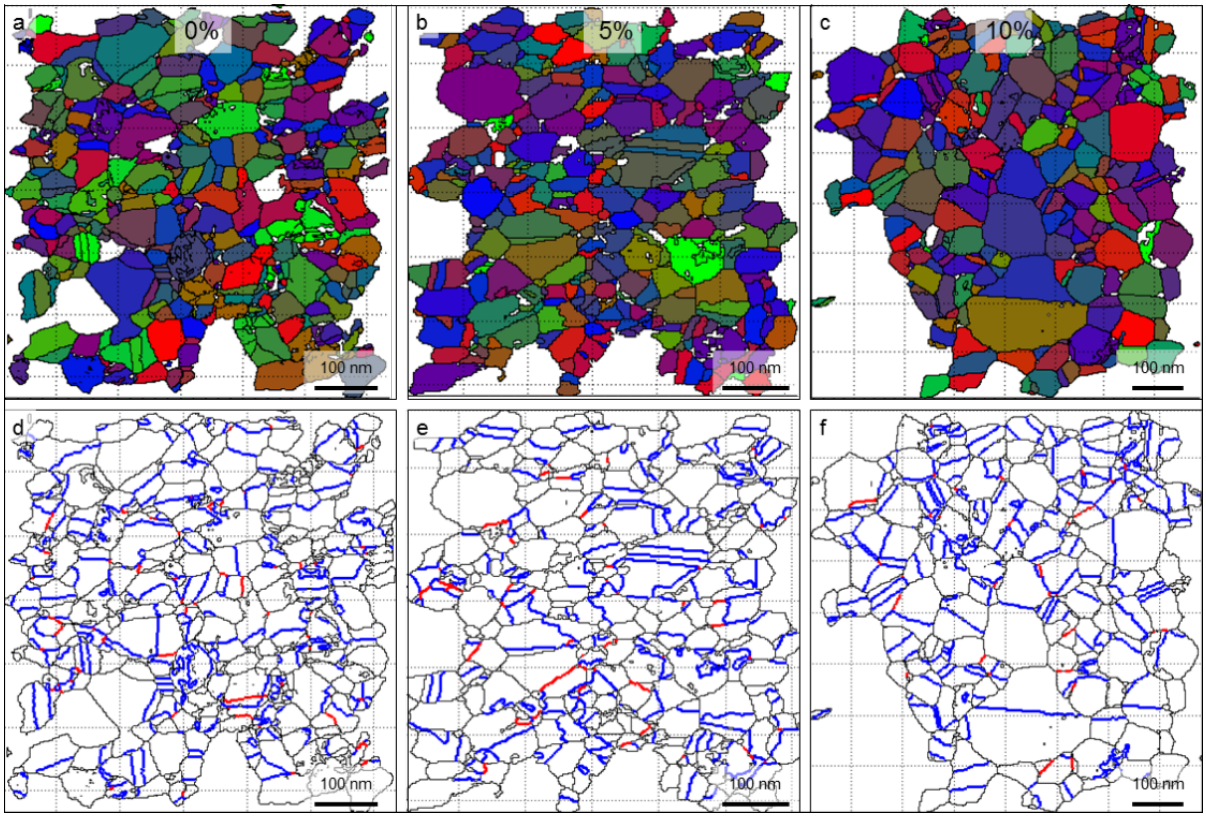

Figure 4: Crystallites recognized by ACOM-TEM for the as deposited sample and samples deformed to 5% and 10% strain (a–c). d–f) Crystallite boundaries (black), twin boundaries (CSL Σ3) (blue) and CSL Σ9 boundaries (red).

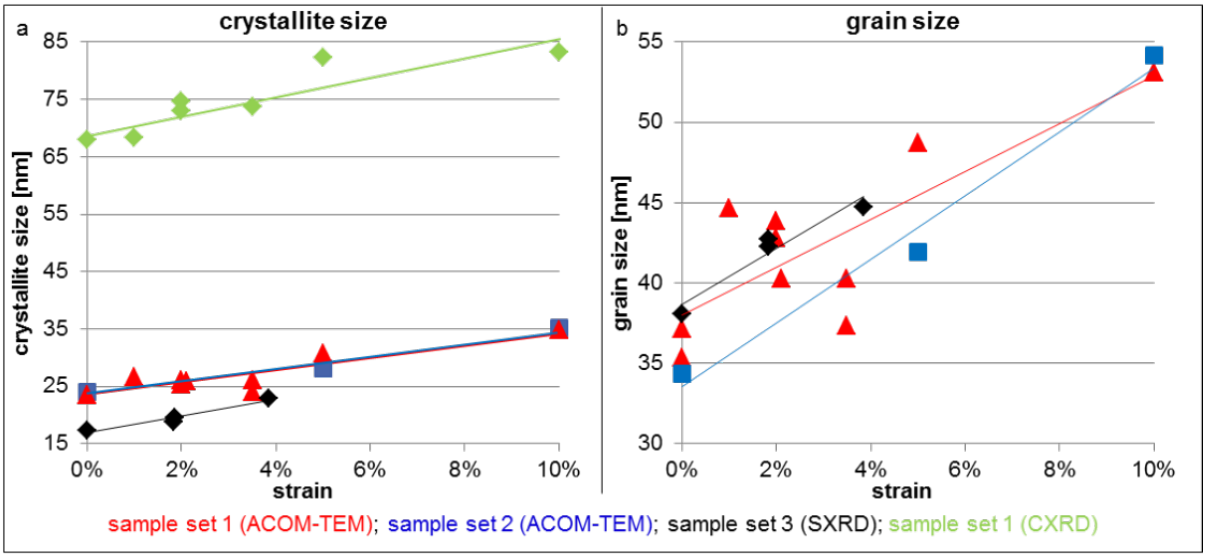

Figure 5: a) Crystallite and b) grain size as a function of strain based on ACOM-TEM (equivalent in-plane diameter) (ncPd 1: red, ncPd 2: blue), CXRD (out-of-plane grain size) (ncPd 1: green) and in-situ SXRD (area weighted in-plane diameter) (ncPd 3: black) analysis.

plain of the sample compared to the perpendicular direction. However, as we compare the crystallite size only we cannot exclude differences in the twin boundary motion behavior in both directions, which could contribute further to the crystallite size changes. Further, the columnar structures of the metal films may contribute to the observed difference in crystallite growth within the film and perpendicular to it.

When analyzing the grain size instead of the crystallite size, the effect of twinning is removed from the grain growth (Figure 5b). In the case of sample ncPd 1, this reveals a similar trend for the grain growth as observed for the crystallite growth, but a significantly more pronounced grain growth of about 58% for sample ncPd 2. The difference is due to the different twinning behavior of both sample sets, described in the next section.

Twin density evolution

Twinning was analyzed using ACOM-TEM, in-situ SXRD and MD simulations. In order to understand the twin density evolution during straining, the measurement metric is very important. When analyzing the twin density as twins per area, all sample sets exhibit a decrease in twin density during straining up to 10% total strain, namely by 82% for sample ncPd 1 and by 50% for sample ncPd 2, respectively (Figure 6a). However, this metric is mixing grain size changes and twin density evolution. To separate the twin density evolution from grain growth, we evaluated the number of twin boundaries per grain (Figure 6b). With this metric, the two sample sets showed a significantly different behavior. While the twin boundaries per grain decreased with increasing strain for sample ncPd 1 by 26%, it increased for sample ncPd 2 by 22%. The twin boundaries per grain determined for the initial structure of sample ncPd 1 do not seem to fit to the overall trend observed during straining. However, contrary to all the other samples, the analysis for the initial structure of sample ncPd 1 was performed close to the end of the sample stripe which was used for clamping of the sample during mechanical testing. Although the sputtering was conducted with substrate rotation, there might be a slight difference in the microstructure between the middle of the sample and the edge of the test samples. Therefore, the grain size/twin density of the initial sample ncPd 1 is not considered for the analysis. The number of twin boundaries per grain in both sample sets after 10% straining are quite similar, despite the different initial levels, suggesting that the twin boundary density might converge to an equilibrium value during deformation.

The trend of decreasing twin density per area seen by ACOM-TEM was also observed for sample ncPd 3 using in-situ SXRD and subsequent X-ray line profile analysis (Figure 6a). However, the metric accessible from XRD is the twin boundary frequency. It describes the mean probability (in percent) that a lattice plane within the ensemble of (111) planes is a twin plane and is based on a purely statistical analysis established for single crystals with randomly distributed twin boundaries. For example, here the initial twin boundary frequency of $f_{twin}(0)$ = 1.57% means that on average every 67th (111) lattice plane is a twin plane, corresponding to an average spacing between two twin boundaries of about 15 nm for (111) twins in Pd. It is known that the twin boundary frequency obtained by XRD

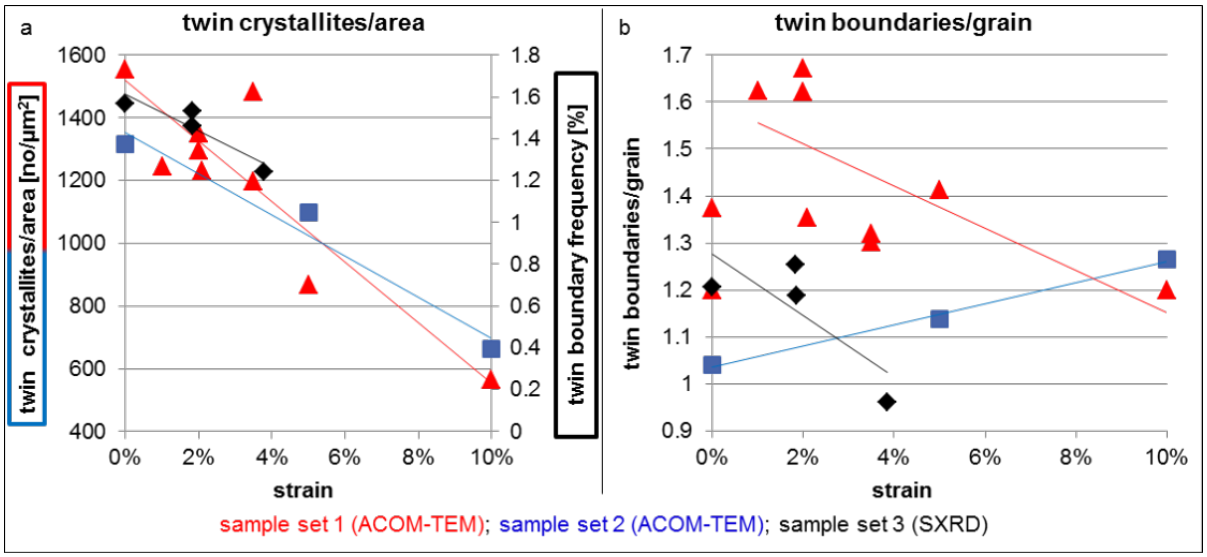

Figure 6: a) Twin crystallites/area as a function of strain based on the ACOM-TEM analysis (ncPd 1: red, ncPd 2: blue) and twin boundary frequency (f_{twin}) as a function of strain (ncPd 3: black) derived from in-situ SXRD data. b) Twin boundaries/grain as a function of strain based on the ACOM-TEM (ncPd 1: red, ncPd 2: blue) and in-situ SXRD analysis (ncPd 3: black).

tends to overestimate the number of twin boundaries, especially if they are located close to the center of a grain [25-27] which is preferentially the case here for the growth twins in the as-deposited Pd film (Figure 4d). Consequently, the twin spacing given above is difficult to directly compare with the ACOM-TEM analysis. As an alternative approach for a direct comparison between SXRD and ACOM-TEM analysis, we, therefore, propose the ratio of grain and crystallite size to estimate the number of twin boundaries per grain. It can be approximated as

$$\frac{twin\,boundaries}{grains} \approx \frac{grain\,size}{crystallite\,size} - 1 \qquad (1)$$

leading to 1.2 twin boundaries/grain based on the in-situ SXRD analysis. This is in good agreement with the corresponding values obtained via ACOM-TEM. The twin boundary frequency obtained by SXRD decreases from $f_{twin}(0) = 1.57\%$ to $f_{twin}(3.8) = 1.24\%$ upon straining to 3.8% (Figure 6a) and the resulting values for the twin boundaries/grain are in agreement with the trend observed by ACOM-TEM (Figure 6b).

In addition to the experimental investigations, MD simulations were conducted to elucidate the twinning evolution during straining, starting from different initial configurations. Figure 7 shows the stress–strain behavior and the corresponding evolution of the twin boundary density during straining for 4 different cases with varying initial twin density and different grain size. Starting from a high initial density of twin boundaries (e.g., growth twins), the twin density decreases with increasing strain (Figure 7a,b). In the slices through representative grains at different stages of the deformation, it is shown that twin boundaries (highlighted in red) disappear from the microstructure. This occurs by nucleation of partial dislocations at twin boundaries and their successive motion (not shown). In contrast, samples with an initially defect free grain interior showed an increase of the twin boundary density during straining (Figure 7c,d). Twins nucleate at the grain boundaries under an

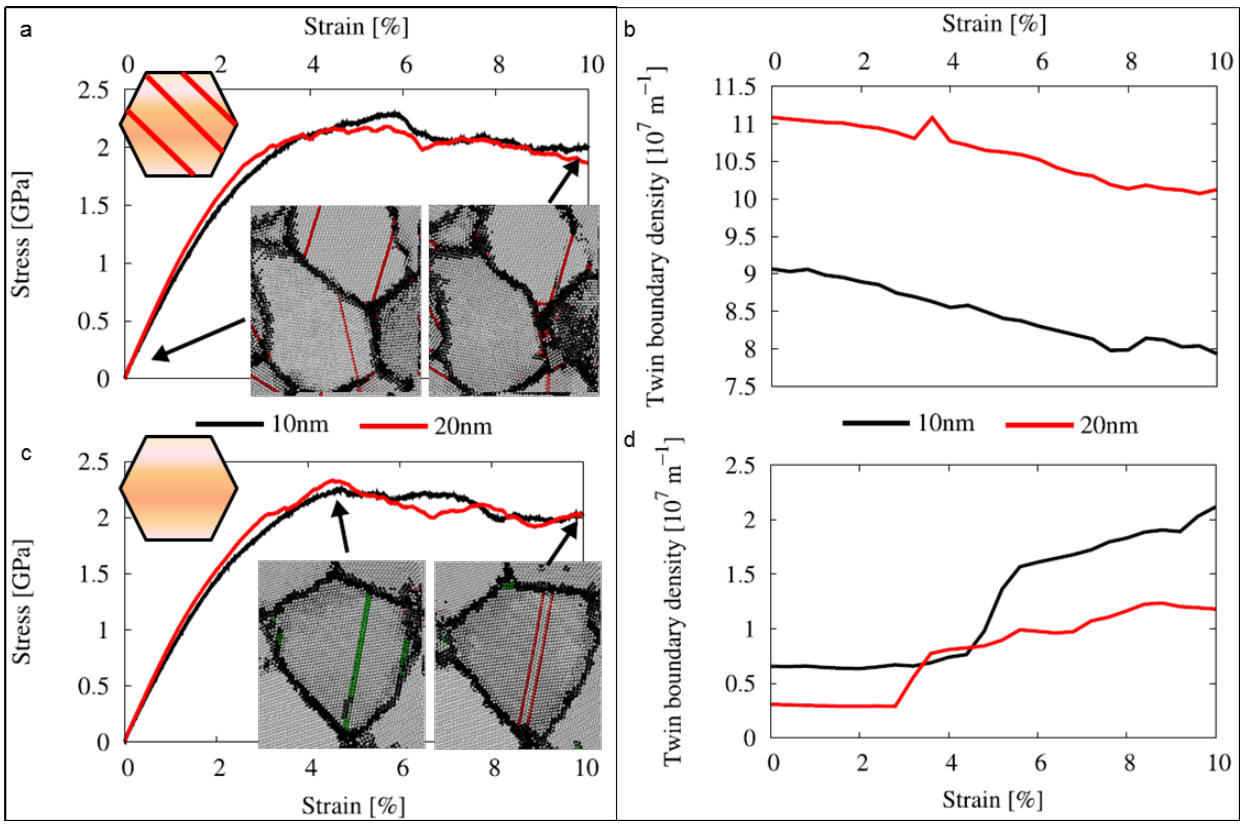

Figure 7: Stress strain behavior and evolution of twin boundary density as a function of strain for grain sizes of 10 and 20 nm based on MD simulations. Two different initial microstructures are compared: a) and b) show the data for structures initially loaded with growth twins (50% of the grains are loaded with twin boundaries) and c) and d) without twin boundaries present prior to straining. The snapshots show representative slices through the microstructure at different stages of the deformation. Atoms in the grain boundary are highlighted in black and atoms located in a stacking fault or a twin boundary are highlighted in green and red.

applied stress by emission of partial dislocations, which lead to stacking faults and eventually twin embryos. These trends are independent of the studied grain sizes.

Discussion

Grain growth of magnetron sputtered ncPd films was evaluated by comparing analysis of ex-situ and in-situ tensile tests. For ex-situ investigations, individual samples of two sample sets (ncPd 1 and ncPd 2) were strained to defined states and investigated using TEM and CXRD. A third sample (ncPd 3) was analyzed by in-situ SXRD during cyclic loading. The results from SXRD given here represent unloaded sample states to ensure comparability with the ex-situ results. Both approaches provide results in good qualitative agreement. In all three sample sets investigated, grain growth as a result of increasing strain was evident. With both ACOM-TEM and SXRD, we showed that not only the crystallite size increases with increasing strain but also the grain size. This indicates that the applied stress was accommodated by grain boundary motion in addition to the observed twinning/detwinning. The observed grain growth is in line with a recent in-situ XRD study on the deformation behavior of similar sputter-deposited ncPd thin films [28], but is in contrast to measurements performed on electron beam evaporated Pd samples where no grain growth was reported up to 4% strain [29]. However, the same authors also compared the microstructure of electron-beam evaporated and magnetron sputtered samples [30] and found significantly higher initial twin densities in electron-beam evaporated Pd films. This difference in microstructure along with slightly different impurity levels may alter the grain boundary mobility and may explain the different grain growth behavior of sputtered and electron-beam evaporated Pd films. The comparison between in-situ and ex-situ analysis shows that ex-situ analysis of different straining states is possible with a quantitative evaluation of grain growth by ACOM-TEM as the nc structure is sufficiently homogeneous in case of the magnetron sputter deposited ncPd films. Grain growth as a result of aging at room temperature can be excluded to contribute to our evaluation based on the XRD analysis of undeformed parts of the tensile samples after 12 weeks, which did not exhibit a significant change in grain size.

Twinning is a possible mode for plastic deformation that is mainly observed in fcc metals with low stacking fault energy, but also in fcc metals with high stacking fault energy if deformed under extreme conditions, like cryogenic temperatures, shock loading, or large strains [13]. The high stacking fault energy of Pd (169 mJ/m^2) [31] should lead to a low number of twinned grains. However, ACOM-TEM analysis reveals that the investigated system inherently contains 1.3 (ncPd 1) / 1.1 (ncPd 2) growth twin boundaries per grain. This has not been evident from classical DF-TEM (see Supporting Information File 1).

The two sample sets examined here in detail, show different initial microstructures: the sample grown with slight compressive residual stress (Table 1) exhibits a higher twin density compared to the sample grown with slight tensile stress. The higher amount of growth twins did not affect the flow stress in our experiments (not shown here). This was also confirmed by the MD-simulations, which showed no significant difference in the stress strain behavior after introducing twin boundaries to 50% of the grains (Figure 7a,c). However, simulations by Stukowski et al. showed a softening effect due to twin boundaries in Pd [32]. The simulations of Stukowski et al. and the simulations presented here differ in two ways. In the study by Stukowski et al., all grains were loaded with twins and a symmetrical grain shape was chosen, which suppresses grain boundary mediated processes. If all grains in our samples are loaded with twin boundaries, we also see a softening effect. Experiments and simulations further show, that the softening of Pd due to twin boundaries differs from observations made for nano-twinned Cu, where twin boundaries led to strengthening [32-34]. The difference between Cu and Pd can be explained by the preferred nucleation site of partial dislocations: In case of nano-twinned Cu, partial dislocations nucleate from the grain boundaries onto planes with the highest Schmid-factor (the highest resolved shear stress). Here, randomly oriented twin boundaries can act as barriers to dislocation motion. In nano-twinned Pd, however, partial dislocations nucleate preferentially at twin boundaries. The twin boundaries then act as nucleation site and do not hinder successive dislocation motion in the twinning plane [32]. The preferential nucleation of partial dislocations at twin boundaries is consistent, with the evolution of the twin boundary density in the present work, where a high initial density leads to an annihilation of twin boundaries during straining.

The present experiments and simulations have shown that twinning/detwinning as a result of partial dislocation activity contributes to the accommodation of the induced strain. Figure 8 illustrates two competing processes taking place during deformation, depending on the initial twin boundary density. In case of a high initial growth twin density, partial dislocations nucleate preferentially at the twin boundaries and lead to movement and thus a reduction of twin boundaries [35]. If no twin boundaries are present, partial dislocations need to nucleate from the grain boundaries into defect free grains and may form stacking faults and subsequently individual twins by successive motion of partial dislocations [36]. The initial nucleation is controlled by the Schmid factor. As soon as stacking faults or twins are formed, the tendency is identical to the twinned case.

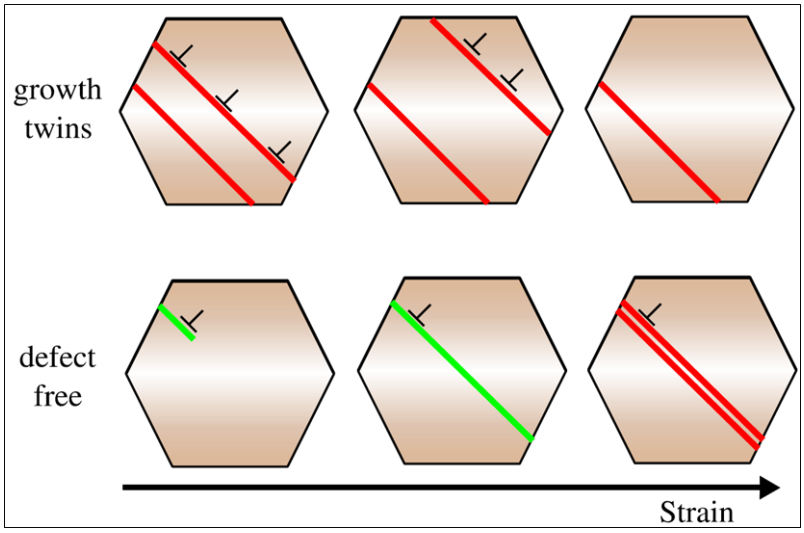

Figure 8: Model of the deformation pathways: If growth twins are initially present, partial dislocations nucleate at twin boundaries and lead to twin boundary migration out of the grain. If the grains are initially defect free, partial dislocations nucleate into a defect free grain and can form stacking faults and twinning faults by successive nucleation of partial dislocations.

Presumably this competition between annihilation and nucleation of twin boundaries consequently leads to a steady state twin density during straining, which is seen experimentally for the twin density of samples ncPd 1 and ncPd 2 approaching similar values at 10% strain. In the simulations, where the initial twin density difference was significantly higher, this steady state was not reached within 10% strain. Twinning and Detwinning have been reported in several experimental studies. Twinning has been reported for Cu [37] with a low stacking fault energy, for Al with a high stacking fault energy [38] and for the compound material NiFe [39]. Detwinning on the other side has been also reported for Cu [40], Al [41] and NiFe [42]. It has been proposed that twinning and detwinning occur at the same time with one process prevailing over the other depending on grain size [43]. In our measurements we could not confirm a grain size effect for the competing mechanisms as both investigated sample sets showed comparable grain sizes in the initial state, but a dependence on the initial twin density is evident.

The present simulation shows that dislocation plasticity is active and as a consequence twinning/detwinning processes take place during deformation. Carlton et al. estimated the dislocations required for purely dislocation based plasticity by

$$N = \frac{d\varepsilon_{grain}}{b} \qquad (2)$$

with d the grain size, ε_{grain} the strain in the grain (here considered to be 4%) and b the burgers vector, here considered for the slip system {111} and <110>, resulting in an average of 6.1 dislocations per grain [44]. On the experimental side, Lohmiller et al. showed for comparable samples that the dislocation density begins to increase in the micro plastic regime starting from 0.3–0.4% applied strain [28,45]. A dislocation density of $\rho = 3.5 \cdot 10^{-3}$ nm^{-2} was reported at 0% strain and $6 \cdot 10^{-3}$ nm^{-2} at 4% strain. This corresponds to an average dislocation spacing of about 17 nm (0%) and 13 nm (4%), or about 2 (0%) and 3 (4%) dislocations per grain for a grain size of 35 nm (0%) and 41 nm (4%). This dislocation activity can explain the twin boundary mobility leading to the changes in twin density seen by ACOM-TEM. However, Carlton's estimation for the dislocations needed for a purely dislocation based deformation is noticeably higher compared to the experimentally estimated dislocation density. The difference suggests that grain boundary mediated deformation mechanisms have to be active to compensate for the remaining strain that does not come from dislocation/twin activity. Lohmiller et al. has already reported other mechanisms, such as GB shear and slip, as well as GB migration resulting in grain growth [28,45].

Conclusion

NcPd thin films with a grain size of about 35 nm (plane view) were sputter deposited onto flexible polyimide substrates. The samples were tensile tested ex-situ up to defined maximum strains and the resulting microstructure as a function of imposed strain was investigated using ACOM-TEM and CXRD after deformation. Two sets of sputtered samples were directly compared by ACOM-TEM. In addition, the results

were confirmed with in-situ SXRD and with observations from MD simulations. The conclusions can be summarized as follows:

1. ACOM-TEM revealed a notable amount of growth twins present in the sputtered samples. 64–75% of the grains in the as prepared microstructure contain about 1–2 twins, with the absolute value depending on minute difference in the sputtering conditions.
2. Grain growth as a result of stress coupled grain boundary motion was identified as one of the deformation mechanism. The grain growth observed within the plane of the film was about a factor of 2 higher compared to the grain growth along the thickness of the film.
3. Partial dislocation activity leading to twinning/detwinning was identified as a second deformation mechanism. Samples with a high density of growth twins exhibit detwinning with increasing strain, whereas samples with a low density of growth twins react with twinning to increasing strain in qualitative agreement with MD simulations.
4. The main findings by ACOM-TEM on grain growth and twin density evolution were confirmed by careful in-situ SXRD analysis.

Experimental

Sample preparation

Palladium thin films were deposited by radio frequency (RF) magnetron sputtering using 2'' diameter planar targets with 99.95% purity. Three sets of pure Pd samples were prepared with constant sputtering power of 60 W at a working gas pressure (Ar) of 0.005 mbar at room temperature. Pd films of 1 μm nominal thickness were grown in 100 steps of 10 nm film thickness, each interrupted for 10 s using a fast rotational shutter in front of the Pd-target. Polyimide Kapton E (DuPont) sheets with a thickness of 50 and 25 μm were used as substrate. Prior to film deposition, the substrates were cut into strips of 30 mm length and 5 mm width using a razor blade, cleaned in an ultrasonic acetone bath for 15 min, and rinsed with isopropanol on a resist spinner. This cleaning procedure, developed by Lohmiller et al. [20], provides enhanced adhesive support of the thin metallic film preventing strain localization and film delamination, allowing for a homogeneous deformation up to very high total strain. Directly after rinsing, the samples were clamped onto special sample holders and transferred into ultra-high vacuum of $2.0 \cdot 10^{-8}$ mbar within the sputtering chamber.

Mechanical testing and microstructural characterization

Ex-situ uniaxial tensile tests were carried out at room temperature using a dedicated tensile stage for miniature specimens at a strain rate of $5 \cdot 10^{-5}$ s^{-1}. The tensile tester was equipped with a special thin film sample clamping to avoid sample deformation during mounting of the delicate thin films. The elongation was measured using a laser extensometer (P-50, Fiedler Optoelectronics) to read paper marks applied to the backside of the polyimide substrate. The individual samples were pulled to maximum elongations of 1%, 2%, 3.5%, 5% and 10.0% engineering strain and relaxed for post-mortem TEM and CXRD analysis.

Specimens for post-mortem TEM analysis were prepared either by focused ion beam (FIB) using a FEI Strata 400S DualBeam at 5 kV and 8 pA beam current for final polishing (sample ncPd 1) or by mechanical dimpling and Argon ion milling from the polyimide side at 2.5 kV in a PIPS (Gatan) (sample ncPd 2). FIB prepared samples have the advantage that the loading direction can be tracked down to the TEM sample and the user can define the height inside the metal film for plane-view preparation. The later has an influence on the observed microstructure as the crystallite size shrinks towards the substrate [18]. Therefore, plane-view FIB samples shown here were always prepared close to the surface, typically from the middle of the straining section.

ACOM-TEM analysis was performed using a FEI Tecnai F20 ST operated at 200 kV in micro-probe (μp) STEM mode with spot size 8, camera length 100 mm, condenser aperture 30 μm, gun lens 6 and extraction voltage 4.5 kV, resulting in a spot size of about 1 nm and a semi convergence angle of 1.4 mrad. An ASTAR system (Nanomegas) was used for ACOM diffraction data acquisition. Data processing consisted of the following steps [23]:

1. Pixel filtering of the orientation maps with a median filter of the combined Euler angles.
2. Grain recognition in the orientation maps with an expanded Mtex version 3.3.1 [46]. The chosen disorientation between neighbors for the recognition is 3°.
3. Grain filtering: Removal of grains that contain less than 50% pixel having a combined reliability greater than 0.15 and index greater than 20.
4. Crystallite filtering: Removal of crystallites with an equivalent diameter <8 nm (ncPd 1) <10 nm (ncPd 2).
5. No re-filling of any of the removed pixels was performed.

Independent of the exact filter settings used in steps 2–4, the trends revealed in this study remain the same. Only slight changes in the absolute values result from using different filter settings. The general trends have also been confirmed using the TEAM^{TM} (EDAX) software as a well-established analysis

package. The crystallite and grain sizes given for the ACOM results are the number-averaged equivalent diameters of the crystallites/grains. Only the histograms in Figure 4 show area weighted grain sizes. Here, a crystallite is defined as the smallest uniform crystallographic unit based on the disorientation to its neighbors. If a crystallite is separated from a neighbor by a twin boundary (recognized by the CSL Σ3 condition within the Brandon criteria) each of them are called twin crystallites. Grains can be single crystallites or consist of one or more twins. The twin density is defined as twin boundaries per grain.

BF/DF-TEM analysis was performed using an image corrected FEI Titan 80-300 equipped with a Gatan US1000 slow scan CCD camera operated at 300 kV. DF-TEM images were acquired with a 10 µm objective aperture at a scattering angle around 0.6°. Crystallite sizes were evaluated manually measuring at least 200 crystallites in different orientations for each straining level. The observed twin density is calculated as twin boundaries per grain detected by human inspection of the DF-TEM images.

Conventional XRD measurements were performed in Bragg–Brentano geometry using a Bruker D 8 Discover diffractometer to determine the crystallite size and residual stress. The measured profiles were evaluated in MATLAB using a home-built script. Peak analysis was performed based on the Single Line Method [47,48]. The crystallite size was determined from the broadening of the (111) peak. The (200) reflection was also analyzed showing a considerably smaller crystallite size compared to the (111) peak analysis. However, as the (200) peak has a considerable lower signal-to-noise ratio, in the present work only the crystallite size determined from the (111) reflection is given. The residual stress was investigated via the $\sin^2\Psi$ method using the (311) and (331) peaks.

Additionally, similar samples were used for in-situ SXRD deformation experiments at the Material Science Beamline of the Swiss Light Source [28,45]. These samples were also subjected to tensile deformation at room temperature at a similar strain rate. In these experiments the samples were loaded in two cycles, first to a maximum elongation of 2% and subsequent unloading, followed by a second cycle to 3.8% and unloading. X-ray diffraction profiles were recorded continuously during deformation using 17.5 keV synchrotron radiation. For comparison with the ex-situ investigations in this work, only the results from the initial state, after the first cycle and at the end of the second cycle were used here (sample ncPd 3). The evaluation of the X-ray profiles was done using CMWP-fit [49] to determine the parameters of the grain-size distribution as well as the twin frequencies. The contribution of twinning in the evaluation of the X-ray data is a diffraction-order dependent part of the size broadening. If one does not consider the effect of twinning in the model, the broadening due to twinning manifests itself in a smaller CSD-size as the twin-faults are then treated as boundaries breaking the coherent scattering. According to the definition given earlier this is exactly the case referred to as the crystallite size. If twinning is considered in the model for the data evaluation, the size effect is reduced as the twin fault is considered as a special defect within a bigger volume. In this situation the size determined from the SXRD evaluation gives the grain size as defined in the ACOM section. More details on this experiment and the analysis can be found in references [28,45,50].

Simulations

MD simulations were carried out assuming pure ncPd as described by an embedded atom method potential [51]. For all simulations, the LAMMPS MD code [52] was used. The input structures were constructed following the Voronoi tessellation method [53], with an average grain size of 10 and 20 nm consisting of 64 and 36 grains, respectively. After initial relaxation at 300 K, in one sample of each grain size, 50% of the grains were loaded with twin boundaries with an average spacing of 4 nm. All samples were then annealed for 1 ns at 500 K to minimize the enthalpy. Successive uniaxial straining simulations were carried out with a strain rate of 10^8 s^{-1}. The evolution of defects during straining was extracted, using a dislocation extraction algorithm [54], which allows to identify the atoms in twin boundaries. The twin boundary density as a function of strain was computed as the atomic area of all atoms inside a twin boundary normalized by the total volume. Analysis and visualization was carried out using DXA [54] and OVITO [55].

Supporting Information

Supporting Information File 1

Comparison between ACOM- and DF-TEM evaluation of grain growth and twin activity.
[http://www.beilstein-journals.org/bjnano/content/supplementary/2190-4286-4-64-S1.pdf]

Acknowledgements

Special thanks are dedicated to Florian Bachmann, TU Bergakademie Freiberg, Institut für Geomathematik und Geoinformatik, Bernhard-von-Cotta-Str. 2, D-09599 Freiberg, Germany for the supportive information about Mtex.

Financial support through the DFG grant “DFG Forschergruppe714: Plastizität in nanokristallinen Metallen und

Legierungen" and the Karlsruhe Nano Micro Facility (KNMF) is gratefully acknowledged.

The authors would also like to thank A. Bergamaschi, A. Cervellino, F. Gozzo and B. Schmitt for their excellent support at the MS beamline of the Swiss Light Source.

References

1. Gleiter, H. *Acta Mater.* **2000,** *48,* 1–29. doi:10.1016/S1359-6454(99)00285-2
2. Kurmanaeva, L.; Ivanisenko, Yu.; Markmann, J.; Kübel, C.; Chuvilin, A.; Doyle, S.; Valiev, R. Z.; Fecht, H.-J. *Mater. Sci. Eng., A* **2010,** *527,* 1776–1783. doi:10.1016/j.msea.2009.11.001
3. Gianola, D. S.; Van Petegem, S.; Legros, M.; Brandstetter, S.; Van Swygenhoven, H.; Hemker, K. J. *Acta Mater.* **2006,** *54,* 2253–2263. doi:10.1016/j.actamat.2006.01.023
4. Meyers, M. A.; Mishra, A.; Benson, D. J. *Prog. Mater. Sci.* **2006,** *51,* 427–556. doi:10.1016/j.pmatsci.2005.08.003
5. Haslam, A. J.; Phillpot, S. R.; Wolf, D.; Moldovan, D.; Gleiter, H. *Mater. Sci. Eng., A* **2001,** *318,* 293–312. doi:10.1016/S0921-5093(01)01266-7
6. Cahn, J. W.; Mishin, Y.; Suzuki, A. *Acta Mater.* **2006,** *54,* 4953–4975. doi:10.1016/j.actamat.2006.08.004
7. Zhu, Y. T.; Liao, X. Z.; Wu, X. L. *Prog. Mater. Sci.* **2012,** *57,* 1–62. doi:10.1016/j.pmatsci.2011.05.001
8. Chinh, N. Q.; Gubicza, J.; Langdon, T. G. *J. Mater. Sci.* **2007,** *42,* 1594–1605. doi:10.1007/s10853-006-0900-3
9. Starink, M. J.; Qiao, X. G.; Zhang, J.; Gao, N. *Acta Mater.* **2009,** *57,* 5796–5811. doi:10.1016/j.actamat.2009.08.006
10. Valiev, R. Z.; Islamgaliev, R. K.; Alexandrov, I. V. *Prog. Mater. Sci.* **2000,** *45,* 103–189. doi:10.1016/S0079-6425(99)00007-9
11. Valiev, R. Z.; Estrin, Y.; Horita, Z.; Langdon, T. G.; Zehetbauer, M. J.; Zhu, Y. T. *JOM* **2006,** *58,* 33–39. doi:10.1007/s11837-006-0213-7
12. Tjong, S. C.; Chen, H. *Mater. Sci. Eng., R* **2004,** *45,* 1–88. doi:10.1016/j.mser.2004.07.001
13. Kumar, K. S.; Van Swygenhoven, H.; Suresh, S. *Acta Mater.* **2003,** *51,* 5743–5774. doi:10.1016/j.actamat.2003.08.032
14. Tang, F.; Gianola, D. S.; Moody, M. P.; Hemker, K. J.; Cairney, J. M. *Acta Mater.* **2012,** *60,* 1038–1047. doi:10.1016/j.actamat.2011.10.061
15. Schäfer, J.; Albe, K. *Scr. Mater.* **2012,** *66,* 315–317. doi:10.1016/j.scriptamat.2011.11.031
16. Suryanarayana, C.; Koch, C. C. *Hyperfine Interact.* **2000,** *130,* 5–44. doi:10.1023/A:1011026900989
17. Padilla II, H. A.; Boyce, B. L. *Exp. Mech.* **2009,** *50,* 5–23. doi:10.1007/s11340-009-9301-2
18. Castrup, A.; Kübel, C.; Scherer, T.; Hahn, H. *J. Vac. Sci. Technol., A* **2011,** *29,* 021013. doi:10.1116/1.3554265
19. Hodge, A. M.; Wang, Y. M.; Barbee, T. W., Jr. *Mater. Sci. Eng., A* **2006,** *429,* 272–276. doi:10.1016/j.msea.2006.05.109
20. Lohmiller, J.; Woo, N. C.; Spolenak, R. *Mater. Sci. Eng., A* **2010,** *527,* 7731–7740. doi:10.1016/j.msea.2010.08.043
21. Yu, D. Y. W.; Spaepen, F. *J. Appl. Phys.* **2004,** *95,* 2991. doi:10.1063/1.1644634
22. Hommel, M.; Kraft, O. *Acta Mater.* **2001,** *49,* 3935–3947. doi:10.1016/S1359-6454(01)00293-2
23. Kobler, A.; Kashiwar, A.; Hahn, H.; Kübel, C. *Ultramicroscopy* **2013,** *128,* 68–81. doi:10.1016/j.ultramic.2012.12.019
24. Rauch, E. F.; Portillo, J.; Nicolopoulos, S.; Bultreys, D.; Rouvimov, S.; Moeck, P. *Z. Kristallogr.* **2010,** *225,* 103–109. doi:10.1524/zkri.2010.1205
25. Scardi, P.; Leoni, M.; Beyerlein, K. R. *Z. Kristallogr.* **2011,** *226,* 924–933. doi:10.1524/zkri.2011.1448
26. Beyerlein, K. R.; Snyder, R. L.; Scardi, P. *Acta Crystallogr., Sect. A: Found. Crystallogr.* **2011,** *67,* 252–263. doi:10.1107/S0108767311009482
27. Beyerlein, K. R.; Leoni, M.; Snyder, R. L.; Scardi, P. *Mater. Sci. Forum* **2011,** *681,* 13–18. doi:10.4028/www.scientific.net/MSF.681.13
28. Lohmiller, J.; Baumbusch, R.; Kraft, O.; Gruber, P. A. *Phys. Rev. Lett.* **2013,** *110,* 066101. doi:10.1103/PhysRevLett.110.066101
29. Wang, B.; Idrissi, H.; Galceran, M.; Colla, M. S.; Turner, S.; Hui, S.; Raskin, J. P.; Pardoen, T.; Godet, S.; Schryvers, D. *Int. J. Plast.* **2012,** *37,* 140–156. doi:10.1016/j.ijplas.2012.04.003
30. Wang, B.; Idrissi, H.; Shi, H.; Colla, M. S.; Michotte, S.; Raskin, J. P.; Pardoen, T.; Schryvers, D. *Scr. Mater.* **2012,** *66,* 866–871. doi:10.1016/j.scriptamat.2012.01.038
31. Crampin, S.; Vvedensky, D. D.; Monnier, R. *Philos. Mag.* **1993,** *67,* 1447–1457. doi:10.1080/01418619308225366
32. Stukowski, A.; Albe, K.; Farkas, D. *Phys. Rev. B* **2010,** *82,* 224103. doi:10.1103/PhysRevB.82.224103
33. Lu, L.; Schwaiger, R.; Shan, Z. W.; Dao, M.; Lu, K.; Suresh, S. *Acta Mater.* **2005,** *53,* 2169–2179. doi:10.1016/j.actamat.2005.01.031
34. Lu, L.; Chen, X.; Huang, X.; Lu, K. *Science* **2009,** *323,* 607–610. doi:10.1126/science.1167641
35. Wang, J.; Li, N.; Anderoglu, O.; Zhang, X.; Misra, A.; Huang, J. Y.; Hirth, J. P. *Acta Mater.* **2010,** *58,* 2262–2270. doi:10.1016/j.actamat.2009.12.013
36. Weissmüller, J.; Markmann, J. *Adv. Eng. Mater.* **2005,** *7,* 202–207. doi:10.1002/adem.200400211
37. Zhang, J.-Y.; Liu, G.; Wang, R. H.; Li, J.; Sun, J.; Ma, E. *Phys. Rev. B* **2010,** *81,* 172104. doi:10.1103/PhysRevB.81.172104
38. Liao, X. Z.; Zhou, F.; Lavernia, E. J.; Srinivasan, S. G.; Baskes, M. I.; He, D. W.; Zhu, Y. T. *Appl. Phys. Lett.* **2003,** *83,* 632. doi:10.1063/1.1594836
39. Ni, S.; Wang, Y. B.; Liao, X. Z.; Figueiredo, R. B.; Li, H. Q.; Ringer, S. P.; Langdon, T. G.; Zhu, Y. T. *Acta Mater.* **2012,** *60,* 3181–3189. doi:10.1016/j.actamat.2012.02.026
40. Wen, H.; Zhao, Y.; Li, Y.; Ertorer, O.; Nesterov, K. M.; Islamgaliev, R. K.; Valiev, R. Z.; Lavernia, E. J. *Philos. Mag.* **2010,** *90,* 4541–4550. doi:10.1080/14786435.2010.514579
41. Li, B. Q.; Sui, M. L.; Li, B.; Ma, E.; Mao, S. X. *Phys. Rev. Lett.* **2009,** *102,* 205504. doi:10.1103/PhysRevLett.102.205504
42. Cheng, S.; Zhao, Y.; Wang, Y.; Li, Y.; Wang, X.-L.; Liaw, P. K.; Lavernia, E. J. *Phys. Rev. Lett.* **2010,** *104,* 255501. doi:10.1103/PhysRevLett.104.255501
43. Ni, S.; Wang, Y. B.; Liao, X. Z.; Li, H. Q.; Figueiredo, R. B.; Ringer, S. P.; Langdon, T. G.; Zhu, Y. T. *Phys. Rev. B* **2011,** *84,* 235401. doi:10.1103/PhysRevB.84.235401
44. Carlton, C. E.; Ferreira, P. J. *Mater. Sci. Eng., A* **2008,** *486,* 672–674. doi:10.1016/j.msea.2007.09.038
45. Lohmiller, J.; Baumbusch, R.; Kerber, M. B.; Castrup, A.; Hahn, H.; Schafler, E.; Zehetbauer, M.; Kraft, O.; Gruber, P. A. *Mech. Mater.* **2013,** in press. doi:10.1016/j.mechmat.2013.04.010
46. Bachmann, F.; Hielscher, R.; Schaeben, H. *Ultramicroscopy* **2011,** *111,* 1720–1733. doi:10.1016/j.ultramic.2011.08.002
47. De Keijser, T. H.; Langford, J. I.; Mittemeijer, E. J.; Vogels, A. B. P. *J. Appl. Crystallogr.* **1982,** *15,* 308–314. doi:10.1107/S0021889882012035

48. Langford, J. I. *J. Appl. Crystallogr.* **1978,** *11,* 10–14. doi:10.1107/S0021889878012601
49. Ribárik, G.; Gubicza, J.; Ungár, T. *Mater. Sci. Eng., A* **2004,** *387–389,* 343–347. doi:10.1016/j.msea.2004.01.089
50. Kerber, M. B. Ph.D. Thesis, University of Vienna, 2011; pp 1–315.
51. Foiles, S. M.; Hoyt, J. J. *Computer Simulation of Bubble Growth in Metals Due to He;* Albuquerque, NM, and Livermore: CA, 2001; p 28.
52. Plimpton, S. *J. Comput. Phys.* **1995,** *117,* 1–19. doi:10.1006/jcph.1995.1039
53. Voronoi, G. Z. J. *Reine Angew. Math.* **1908,** *134,* 198. doi:10.1515/crll.1908.134.198
54. Stukowski, A.; Albe, K. *Modelling Simul. Mater. Sci. Eng.* **2010,** *18,* 085001. doi:10.1088/0965-0393/18/8/085001
55. Stukowski, A. *Modelling Simul. Mater. Sci. Eng.* **2010,** *18,* 015012. doi:10.1088/0965-0393/18/1/015012

License and Terms

Beilstein Journal of Nanotechnology

Spin relaxation in antiferromagnetic Fe–Fe dimers slowed down by anisotropic Dy^{III} ions

Valeriu Mereacre[*1], Frederik Klöwer[1], Yanhua Lan[1], Rodolphe Clérac[2,3], Juliusz A. Wolny[4], Volker Schünemann[4], Christopher E. Anson[1] and Annie K. Powell[*1,5]

Full Research Paper

Open Access

Address:
[1]Institute of Inorganic Chemistry, Karlsruhe Institute of Technology, Engesserstr. 15, D-76128 Karlsruhe, Germany, [2]CNRS, CRPP, UPR 8641, F-33600 Pessac, France, [3]Univ Bordeaux, CRPP, UPR 8641, F-33600 Pessac, France, [4]Institute of Physics, University of Kaiserslautern, Erwin Schrödingerstr. 56, D-67653 Kaiserslautern, Germany and [5]Institute of Nanotechnology, Karlsruhe Institute of Technology, Postfach 3640, D-76021 Karlsruhe, Germany

Email:
Valeriu Mereacre[*] - valeriu.mereacre@kit.edu;
Annie K. Powell[*] - annie.powell@kit.edu

* Corresponding author

Keywords:
anisotropy; dysprosium; iron; Mössbauer spectroscopy

Beilstein J. Nanotechnol. **2013,** *4,* 807–814.
doi:10.3762/bjnano.4.92

Received: 23 August 2013
Accepted: 14 November 2013
Published: 27 November 2013

This article is part of the Thematic Series "Advances in nanomaterials".

Guest Editors: H. D. Gleiter and T. Schimmel

Abstract

By using Mössbauer spectroscopy in combination with susceptibility measurements it was possible to identify the supertransferred hyperfine field through the oxygen bridges between Dy^{III} and Fe^{III} in a $\{Fe_4Dy_2\}$ coordination cluster. The presence of the dysprosium ions provides enough magnetic anisotropy to "block" the hyperfine field that is experienced by the iron nuclei. This has resulted in magnetic spectra with internal hyperfine fields of the iron nuclei of about 23 T. The set of data permitted us to conclude that the direction of the anisotropy in lanthanide nanosize molecular clusters is associated with the single ion and crystal field contributions and ^{57}Fe Mössbauer spectroscopy may be informative with regard to the the anisotropy not only of the studied isotope, but also of elements interacting with this isotope.

Introduction

The huge Ising-type magnetic anisotropy of many lanthanide ions, which can be controlled by designing the ligand field, can slow down the relaxation of magnetisation and can be an effective source for the modulation of properties of transition metal molecular magnets [1]. The anisotropy of the lanthanide is severely affected by the symmetry of the crystal field and it can be controlled by a suitable design of the ligand field environment [2,3]. Today, the orientation of the principal axes of the

magnetization of the lanthanide ions in low-symmetry environments can be determined theoretically and experimentally [4-9]. For molecular magnetism the Dy^{III} ion has proved to be the most attractive [4-12] not only because of its large flexibility regarding the interaction between the single-ion electron density and the crystal field environment, and its predicted hard anisotropy using simple ligand field considerations, but also because of its huge field dependence of the relaxation time [13].

Designing the ligand field environment can help to control the magnetic anisotropy of some of the later lanthanides [2,3], but this is less useful for the Dy^{III} ion. The unpredictable behaviour and the strong dependence of magnetic anisotropy and orientation of the easy axis of the magnetization of the Dy^{III} ion on very small changes in the ligand environment was predicted by ab-initio calculations [5]. But only recently, we have shown that such radical changes can also be seen experimentally. By using Mössbauer spectroscopy we have shown how minor changes in the electronegativity of the atoms in the ligand sphere and in the donor–acceptor nature of the substituents, and their position on the aromatic ring, can control the shape anisotropy of the Dy^{III} ions and, thus, their interaction with the iron centres [14,15]. Moreover, the reported compounds [14,15] – with an antiferromagnetic coupling in the central iron dimer – show a very intriguing effect: the collapse of the magnetic hyperfine splitting under the effect of the external magnetic field. This apparently paradoxical behaviour reveals how complex and case-sensitive the properties of the Fe–Ln clusters can be. One of the reasons for this effect may well be that the externally applied magnetic field can affect the ground state of Dy^{III} by lowering the energy of the system: This can result in a change of the direction of polarization, and thus the shape anisotropy of the Dy^{III} ion and its interaction with the iron centres can be controlled. This means that the Ln anisotropy can be influenced not only by altering crystal field, but also by an external source. But, surprisingly, this is not always the case. It seems that the structural aspect can prevail over the others. Here, we report how, contrary to reported Fe_2Dy_2 compounds [14,15], the application of an external magnetic field does not always affect the ground state of the Dy^{III} ion and its relaxation time. Two compounds $[Fe_4Ln_2(\mu_3\text{-}OH)_2(L)_4((CH_3)_3CCOO)_6(N_3)_2]\cdot(solv)$ (Ln = Dy^{III}, L = *N*-(*n*-butyl)diethanolamine, solv = 3(MeCN), **1**, see below in Figure 1) and Ln = Y^{III}, L = *N*-methyldiethanolamine, solv = phenol, **2**) are magnetically and spectroscopically studied and their properties are compared.

Results and Discussion

Compound **1** crystallizes in the triclinic space group $P\bar{1}$ with $Z = 2$; each Fe_4Dy_2 aggregate (Figure 1) occupies a general site with no crystallographically imposed symmetry. The central core of the aggregate possesses a $\{Fe^{III}_4Dy_2(\mu_3\text{-}OH)_2(\mu_3\text{-}OR)_2\}$ architecture, in which two of the Fe^{III} (Fe(1) and Fe(3)) and the two Dy^{III} ions, together with the two hydroxo ligands, are arranged in the well-known "butterfly" shape. The two Fe^{III} ions form the “wingtips” and the Dy^{III} ions define the “body” of the butterfly, with the two hydroxo ligands each bridging a $FeDy_2$ triangle. The typical butterfly topology has a planar Fe_2Dy_2 unit, with the two (μ_3-OH) bridges on opposite faces of the Fe_2Dy_2 plane. In contrast, in **1** the Fe_2Dy_2 butterfly is not planar; the two $FeDy_2$ triangles show a dihedral angle of 43.8°, and the two hydroxo ligands are on the same face of the Fe_2Dy_2 unit.

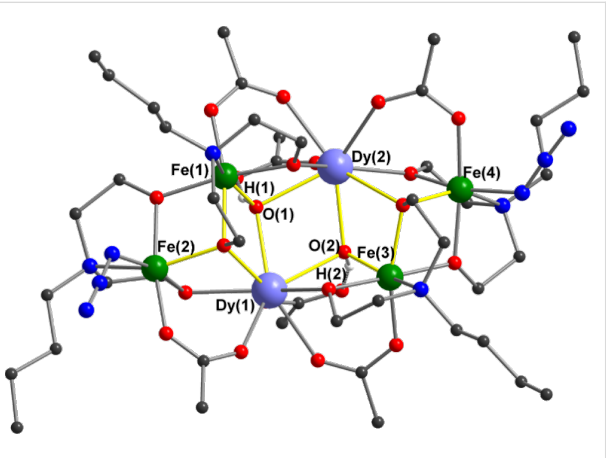

Figure 1: Molecular structure of $[Fe_4Dy_2(OH)_2(N\text{-}nbdea)_4((CH_3)_3CCOO)_6(N_3)_2]$ and its core. Solvent molecules, disordered atoms and organic H atoms have been omitted for clarity. Dy blue; Fe green; O red; N blue; C black, H white.

Each of the four Fe^{III} ions in the aggregate is chelated by a fully-deprotonated (*n*-butyl)diethanolamine (nbdea) ligand. Of those chelating Fe(1) and Fe(3), one alkoxo arm bridges an Fe–Dy edge of the butterfly, while the other forms a (μ_3-alkoxo) bridge between a Fe–Dy edge in the butterfly and a further Fe^{III} centre (Fe(2) or Fe(4)). The nbdea ligands chelating Fe(2) and Fe(4) then each form two (μ2-alkoxo) bridges, to a Dy atom and to an Fe atom in the butterfly. Peripheral ligation is provided by four μ-pivalato ligands in their common *syn,syn* bridging mode. Two further unidentate pivalates each coordinate to a dysprosium, with the non-coordinated carboxylate oxygen atom accepting a hydrogen bond from a (μ_3-OH) ligand. The coordination is completed by two azido anions coordinated to the outer iron atoms (Fe(2) and Fe(4)). All four Fe ions are six-coordinate with distorted octahedral geometries, while the Dy^{III} ions are eight-coordinate with coordination polyhedra that may best be described as distorted bicapped trigonal prisms. The molecular structure of the Fe_4Y_2 aggregate in **2** is very similar to that of the Fe_4Dy_2 in **1**, and differs only in the replacement of the *n*-butyl groups in **1** by methyl groups and the replacement of Dy^{III} by Y^{III}.

At temperatures higher than 20 K the Mössbauer spectra (MS) of **1** are paramagnetic (Figure 2) and show two symmetric quadrupole doublets with average isomer shifts, δ, of 0.42 and 0.46 mm/s and quadrupole splittings, ΔE_Q, of 0.51 and 1.08 mm/s, respectively, (Table 1). This is typical for high spin, $S = 5/2$, Fe^{III} ions of iron-oxo proteins and other relevant model compounds [16-18]. The presence of two doublets with different quadrupole splittings (ΔE_Q) indicates two Fe sites with different coordination spheres, in agreement with both the molecular structure and bond length distortion (BLD) calculations: Fe(1) and Fe(3) = 3.95 and 3.82, Fe(2) and Fe(4) = 3.30 and 3.19, respectively [19]. Consequently, we constrained the area ratio of doublets to 1:1. The low temperature (30 K) MS (not given here) for **1** is broad and shows a small onset of relaxation at an intermediate rate superimposed on the absorption peaks at the centre of the spectrum. At 3 K (Figure 2), a magnetic spectrum is obtained, indicating that the spin-relaxation time is slow with respect to the Mössbauer time scale. The spectrum has been fitted with two sextets with the parameters listed in Table 1. The best fits for the zero-field spectrum at 3 K were achieved through a free iteration method with two sextets with the effective hyperfine fields $B_{eff} = 23.5$ and 23.2 T, respectively, at the nuclei.

When applying an external magnetic field one cannot see significant changes in the values of the hyperfine parameters. The spectra represent a superposition of two sextets with an area ratio 1:1. When the applied magnetic field is increased a behaviour that is typical for antiferromagnetically coupled molecular clusters can be seen [20,21]. The MS for **1** at 3 K, under the application of an external field ($B_{appl} = 1$, 3 and 5 T), are shown in Figure 2. Since the high-spin Fe^{III} ions are considered isotropic, it is expected that the local spins will align along (parallel or antiparallel) the direction of the applied field. Information about such an alignment can be derived from the relative intensity of the $\Delta m = 0$ and $\Delta m = 1$ lines of the sextet, which yield information about the angle θ between B_{eff} and the γ-rays. It is important to note that upon application of the external field the intensity of the Δm = 0 lines does not change considerably (θ is almost constant) as it is to be expected for systems dominated by internal magnetic anisotropies. This indicates that even though the net moment of the cluster may be aligned along the direction of the applied magnetic field, the local magnetic moments tend to align approximately perpendicular to it. It appears that for **1** an applied field much larger than 5 T would be necessary to align the local magnetic moments completely along the direction of the field. An obvious change of the magnetization direction is suggested by the variation of the angle φ between the principal axis (V_{zz}) of the electrical field gradient (EFG) and B_{int}. This angle can be calculated from the magnetic spectra according to the formula

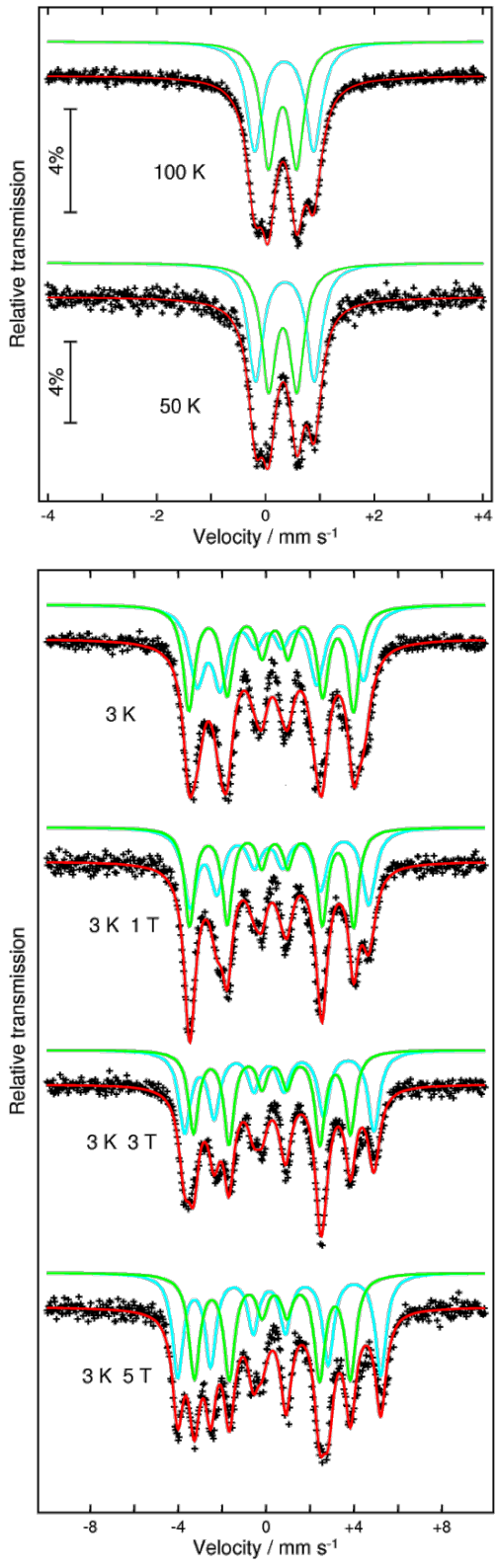

Figure 2: The ^{57}Fe Mössbauer spectra for $[Fe_4Dy_2(OH)_2(N\text{-nbdea})_4((CH_3)_3CCOO)_6(N_3)_2]$ at 100 and 50 K (top); at 3 K in zero-applied magnetic field and at 3 K in applied magnetic fields of 1, 3 and 5 T (bottom). See Table 1 for the fitting parameters.

Table 1: Mössbauer data for $[Fe_4Dy_2(OH)_2(N\text{-nbdea})_4((CH_3)_3CCOO)_6(N_3)_2]$ (**1**).

T [K]	Fe sites	δ[a] [mm/s]	ΔE_Q or ε[b] [mm/s]	Γ [mm/s]	θ [°]	φ [°]	B_{eff} [T][c]
100	$Fe_{1,3}$	0.45(1)	1.09(1)	0.35(3)	—	—	—
	$Fe_{2,4}$	0.42(1)	0.52(2)	0.32(3)			
50	$Fe_{1,3}$	0.47(2)	1.08(5)	0.32(1)	—	—	—
	$Fe_{2,4}$	0.43(2)	0.52(4)	0.31(1)			
3	$Fe_{1,3}$	0.48(1)	0.52(1)	0.83(1)	58	36	23.5(1)
	$Fe_{2,4}$	0.43(2)	−0.17(1)	0.64(1)	52	70	23.2(1)
3 K, 1 T	$Fe_{1,3}$	0.48[d]	0.49(1)	0.73(1)	51	37	25.2(5)
	$Fe_{2,4}$	0.43[d]	−0.14(1)	0.55(1)	62	67	23.1(1)
3 K, 3 T	$Fe_{1,3}$	0.48[d]	0.47(1)	0.63(1)	50	38	26.7(2)
	$Fe_{2,4}$	0.43[d]	−0.11(1)	0.56(1)	63	64	22.1(1)
3 K, 5 T	$Fe_{1,3}$	0.48[d]	0.45(1)	0.59(1)	49	39	28.6(1)
	$Fe_{2,4}$	0.43[d]	−0.09(1)	0.60(2)	64	62	22.0(1)

[a]Relative to α-Fe at room temperature; [b]For magnetically-split spectra the quadrupole shifts, $\varepsilon = \frac{1}{2}\Delta E_Q(3\cos^2\varphi - 1)$. φ - Euler angle between the internal hyperfine field, B_{int}, and the principal axis (V_{zz}) of the electrical field gradient. The quadrupole shifts are easy to observe from the magnetic spectra as a difference in the splitting of 1 and 2 and 5 and 6 iron(III) lines. δ - isomer shift, ΔE_Q - quadrupole splitting, θ - angle between B_{eff} and the direction of the γ-rays. The statistical errors are given in parentheses. The relative areas for the doublets and sextets have been constrained to a 1:1 ratio. [c]$B_{eff} = B_{int} + B_{appl}$; [d]Fixed values.

$\varepsilon = 1/2\ \Delta E_Q(3\ \cos^2\varphi - 1)$, where ε are the quadrupole shift values determined from the magnetically ordered spectra and ΔE_Q are the quadrupole splitting values determined from the paramagnetic spectra. A clear variation of the φ values for both sextets is observed from 36° at 3 K (without a magnetic field) to 39° at 3 K (magnetic field 5 T) for $Fe_{1,3}$ and from 70° at 3 K (without a magnetic field) to 62° at 3 K (magnetic field 5 T) for $Fe_{2,4}$, respectively.

Another peculiarity observed from the magnetic spectra under an applied magnetic field is that one sextet is showing decreasing B_{eff} values regardless of the increased B_{appl}, while the second one shows an increased value for B_{eff}. This is a microscopic confirmation of the magnetic structure with $Fe_{1,3}$ and $Fe_{2,4}$ moments being antiferromagnetically coupled. The decrease and increase of the B_{eff} values at the nuclei with an increasing value of applied magnetic field is proof that the directions of the effective magnetic flux densities at the iron nuclei of iron have either the same or the opposite direction as the applied magnetic field. However, the difference in the change in the measured effective magnetic field for $Fe_{1,3}$ and $Fe_{2,4}$ sites is very different: 5.1 T and 1.2 T, respectively. The change of B_{eff} with B_{appl} for the $Fe_{1,3}$ sites is close to 1.0, which is simply the applied field. This means that B_{int} (≈23.4 T) for these iron centers has a maximum (saturation) value. Contrary to $Fe_{1,3}$, the change for $Fe_{2,4}$ is very small. We anticipate an almost identical B_{int} for all sites and the above mentioned difference is due to a different reaction of the iron moments from the spin-coupled pairs to the applied field. It seems that the $Fe_{1,3}$ moments tend to align themselves parallel to the applied field, but those of $Fe_{2,4}$ have a spin-flop tendency into the plane perpendicular to the applied magnetic field. This could also be an explanation for the opposite evolution of the θ values (one is increasing and the other one is decreasing) with increasing B_{appl}. Since the applied external magnetic field is perpendicular to the direction of γ-rays, the θ values should increase. The same conclusion can be made from the evolution of the Euler angles with B_{appl}. While the angle φ for $Fe_{1,3}$ is almost invariable (it changes from 36° to 39°), a more visible and opposite change from 70° to 62° can be seen for $Fe_{2,4}$, together with a tendency to smaller angles, i.e., angles that deviate less from the direction perpendicular to B_{appl}, or parallel to the γ-rays, respectively. Such unusual features can be attributed to the presence of an antisymmetric exchange in the diferric units. But such conclusions should be treated with caution, because of the unknown role of the very anisotropic Dy^{III} ions in this exchange.

To shed some light on the interaction inside of these clusters, the direct-current (dc) magnetic susceptibility of **1** has been measured in an applied magnetic field of 0.1 T between 300 and 1.8 K (Figure 3). At room temperature, the $\chi_M T$ value of 43.44 $cm^3 \cdot K \cdot mol^{-1}$ is close to the expected value of 28.33 $cm^3 \cdot K \cdot mol^{-1}$ for two uncoupled Dy^{III} ions (S = 5/2,

$L = 5$, $^6H_{15/2}$, $g = 4/3$) plus the value obtained for the iron fragments from the Y^{III} analogue. As shown in Figure 3, $\chi_M T$ decreases with lowering temperatures in the range from 300 to 8 K and then increases sharply to reach a maximum of 33.00 $cm^3 \cdot K \cdot mol^{-1}$ at 1.8 K, which may be because of an intramolecular ferromagnetic interaction. If the Fe–Fe (Fe(1)–Fe(2) and Fe(3)–Fe(4)) interaction is antiferromagnetic and the Fe–Dy exchange interaction is negligible, then the only ferromagnetic interaction is between the Dy ions of the central dimer. This is not unusual taking into consideration the relatively small Dy–Dy separation (3.87 Å) and angles of the Dy(1)–O(1)–Dy(2) and Dy(1)–O(2)–Dy(2) bridges (≈ 108°). To confirm the antiferromagnetism for the Fe(1)–Fe(2) and Fe(3)–Fe(4) units, the Y^{III} analogue **2** has been synthesized. At room temperature the value of $\chi_M T$ is 13.5 $cm^3 \cdot K \cdot mol^{-1}$ (Figure 3, inset), a value below the theoretical value for four uncoupled Fe^{III} ions (17.5 $cm^3 \cdot K \cdot mol^{-1}$). This indicates a weak antiferromagnetic interaction between the spin centers. When the temperature is lowered, $\chi_M T$ decreases and reaches zero at 1.8 K. This indicates clearly that the complex possesses an $S = 0$ ground state at low temperatures. The experimental data of **2** were fitted to the expression for the molar susceptibility derived from the Hamiltonian $H = -2J \cdot S_1 \cdot S_2$. The best fit to the χT-vs-T curve gave g = 1.94(1) and an exchange parameter $J = -8.18(1)$ cm^{-1}. Interestingly, the obtained J value for **2** is rather close to the value, approx. −8.3 cm^{-1}, obtained from the Gorun and Lippard [22] empirical relationship between J in diiron(III) complexes with oxide, hydroxide and alkoxide bridges and the parameter P that corresponds to the half of the length of the shortest Fe–O–Fe-bridge in the complex. This is also supported by the value $J \approx -8.7$ cm^{-1}, which was determined by using another magnetostructural correlation originally developed for dimers that utilizes both the Fe–O distances and the Fe–O–Fe angles [23] and was later on improved and extended to polynuclear topologies [24,25]. In conclusion, all these experimental and theoretical data unambiguously prove that iron ions from the dinuclear units in compounds **1** and **2** are antiferromagnetically coupled.

Additionally, the Mössbauer spectrum in an applied external magnetic field of 5 T has been measured for **2** (Figure 4). It confirms the diamagnetic ground state for the Fe_2 units. The simulation parameters were the field at the nucleus $B_{eff} = 5.0$ T, ΔE_Q = 0.80 mm/s, δ = 0.47 mm/s, and the asymmetry parameter η = 0.95. The experimental data fit very well with $B_{eff} = B_{appl}$, i.e., there is no noticeable contribution to the magnetic hyperfine interaction other than the applied field .

Mössbauer spectroscopy senses the internal hyperfine interactions near the nucleus of the studied isotope. There are four contributions that determine the internal hyperfine field B_{int} of

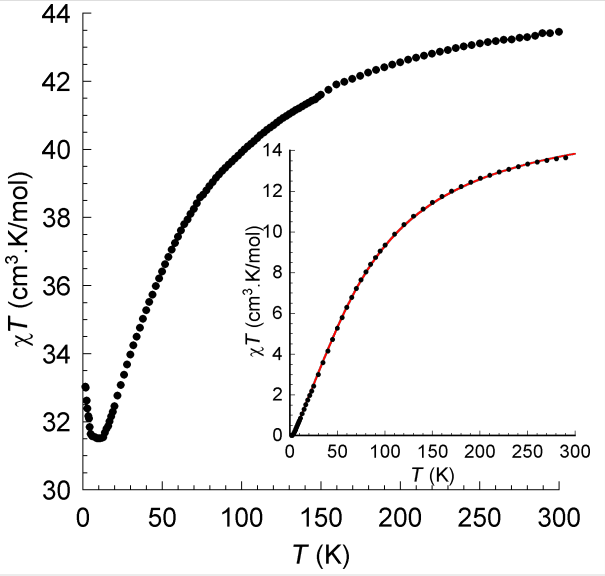

Figure 3: χT-vs-T plots at 0.1 T for **1** and **2** (inset). The solid line is the best fit to the experimental data.

an iron atom: B_{fc} (the Fermi contact interaction), B_{ls} (the orbital momentum of the 3d electrons at the nucleus), B_{dd} (the dipole field originating from the electronic shell) and B_{latt} (the lattice contribution). In both studied compounds the last three contributions can be neglected. The main contribution only results from B_{fc}. But in an applied external magnetic field this contribution can also be ignored for compound **2**. The Mössbauer spectrum of compound **2** (Figure 4) shows that even under an applied field of 5 T, there is no orientation of the zero spin of the cluster and each antiferromagnetically coupled dimer is still relaxing fast on the Mössbauer time scale. As a result, a typical MS for an iron ion with zero ground state is obtained. However, this does not mean that this contribution can be neglected for compound **1**, too. This raises the question that if the Fe_2 units in compound **1** are antiferromagnetically coupled as in compound **2**, why is the internal field felt by the iron nuclei so big to give a magnetic sextet? One contribution to the internal hyperfine field at the iron nuclei in compound **1** can result from the magnetic interaction with the anisotropic, magnetically aligned, Dy^{III} ions, which provide enough magnetic anisotropy to "block" the hyperfine field experienced by the iron nuclei. Another contribution can be a supertransferred field from Dy^{III} to Fe^{III} ions. At this time we are not confident which of the two contributions prevails.

But even without invoking a large supertransferred hyperfine field and without ignoring the contribution of the Fermi contact to the field, it is quite possible to qualitatively understand the Mössbauer spectra of both **1** and **2**. A determination of the zero-field splitting parameter for **1** would have been very useful, but it was not possible to determine. Depending on the sign of the

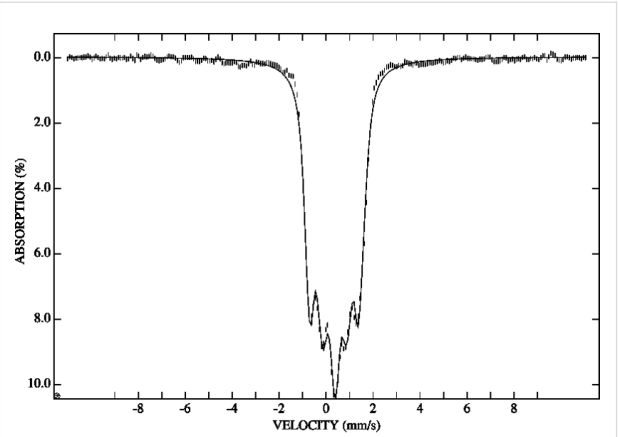

Figure 4: 3 K Mössbauer spectrum of polycrystalline **2** recorded in a perpendicularly applied field of 5.0 T. The solid line is a spectral simulation for ΔE_Q = 0.80 mm/s, δ = 0.47 mm/s, and η = 0.95, assuming an isolated ground state with S = 0 for a dinuclear Fe_2 cluster.

zero field splitting parameter, D, in **1** at 3 K the iron(III) ions will be in a ground state that could be either |±5/2> or |±1/2>. If the relaxation between the positive and negative spin states becomes slow enough, the relaxation between the different M_S states may still be rather fast. In this case the effective hyperfine field that is observed is the Boltzmann average of the fields associated with the |±5/2>, |±3/2>, and |±1/2> states, an average that may well be close to 23 T. This can explain why the internal field observed at 3 K, is 23 T and not 55 T, a value expected for S = 5/2, which will be in agreement with values obtained for oxides (≈11 T per S = 1/2) [26]. Such an unusual slowdown of the relaxation may well be the result of an interaction of local Fe moments with the total magnetisation vector on the Dy^{III} dimer. For compound **2**, it is most probable that D is larger than zero and the ground state is |±1/2>. The reversal of the spin in this state, and hence of the hyperfine field, is very fast compared to the Mössbauer time scale and no hyperfine field is observed. Why is the relaxation fast? The relaxation in the |±1/2> state is particularly fast because it involves only a change of M_S of ±1 between the |+1/2> and the |−1/2> ground states.

A further peculiarity is the different evolution of the magnetic spectra with the external magnetic field. In contrast to previously reported studies about Fe_2Dy_2 clusters [6], in which the magnetic hyperfine splitting collapses under the application of an external magnetic field, in the case of **1** this applied field results in the total effective magnetic field decreasing for one sextet and increasing for the other. This confirms that the Fe_1 and Fe_2, and Fe_3 and Fe_4 pairs are antiferromagnetically coupled. No collapse of the magnetic structure is observed. An explanation may lie in the different communication between Dy and Fe ions. Contrary to previously reported Fe_2Dy_2 compounds, in which single Dy^{III} ions are in close proximity to either side of the Fe_2 fragments, in compound **1** the Dy ions are on the same side and ferromagnetically cooperating with each other. This gives rise to a total ground spin state which cannot be affected by external applied magnetic field.

It is worth mentioning that compound **1** is a single molecule magnet. It displays an out-of-phase response to the blocking temperature 2.5 K (at 1500 Hz), which is characteristic of a slow relaxation of the magnetization (Figure 5). The characteristic measuring time for Mössbauer spectroscopy is about 10^{-7} s, whereas that for ac magnetic susceptibility measurements is typically in the range between 10^0 and 10^{-4} s (i.e., ac frequencies of 1–1500 Hz). Because of their different time windows, ^{57}Fe Mössbauer spectroscopy and ac magnetic susceptibility measurements provide an apparently different view of the relaxation dynamic: If a slow relaxation can be seen in the magnetic data at very low temperatures (1.8–3.0 K), then an intermediate relaxation can already be seen in the Mössbauer spectra at 30 K. Therefore, an accurate comparative analysis of the data obtained from these two methods cannot be done.

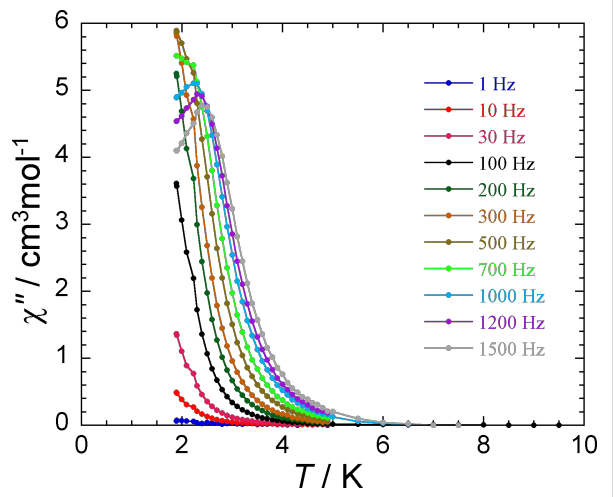

Figure 5: Plot of out-of-phase ac susceptibility signals vs temperature for **1** at the indicated oscillation frequencies.

Conclusion

This communication once more shows how additional, case-sensitive information about the unpredictable lanthanide anisotropy can be gathered by using ^{57}Fe Mössbauer spectroscopy. Due to the strong anisotropy of Dy ions, the magnetic susceptibility measurements provide only averaged information about the magnetic behaviour inside the molecules and one cannot distinguish all interactions inside the complex molecules. Mössbauer spectroscopy, on the contrary, provides us with microscopic information about the metal–metal communication and the relaxation dynamics on specific centres, in this

case Fe nuclei in the presence of very anisotropic Ln centers. Having identified the nature of the interaction in compounds **1** and **2**, it will be of interest to explore the influence of incorporating other anisotropic lanthanides to shed light on the complex magnetism of lanthanide based SMMs.

Experimental

Unless otherwise stated, all reagents were obtained from commercial sources and were used as received without further purification. All reactions were carried out under ambient conditions. Elemental analyses for C, H, and N were performed by using an Elementar Vario EL analyzer. IR spectra were measured on a PerkinElmer Spectrum One spectrometer as KBr disks.

Preparation of $[Fe_4Dy_2(OH)_2(nbdea)_4(O_2CCMe_3)_6(N_3)_2]\cdot 3MeCN$ (1): A mixture of $FeCl_2$ (0.127 g, 1.00 mmol), NaN_3 (0.130 g, 2.00 mmol) and *N*-(*n*-butyl)diethanolamine (0.48 g, 3.00 mmol) in acetonitrile (15 mL) was stirred at room temperature for 20 min before adding 10 mL of dichloromethane. The obtained cloudy solution was stirred for another 10 min at 60 °C before the addition of $Dy(NO_3)_3\cdot 6H_2O$ (0.22 g, 0.50 mmol), pivalic acid (0.41 g, 4.00 mmol) and phenol (0.05 g, 0.50 mmol),. The mixture was further stirred until it became clear. The solution was filtered and left for slow evaporation. After one week red crystals of **1** were obtained. Yield 34.7% (based on Fe); Anal. calcd for $C_{66}H_{133}Fe_4Dy_2N_{13}O_{22}$ (**1**) (dried): C, 40.17; H, 6.59; N, 8.96; found: C, 40.98; H, 6.76; N, 6.73; IR (KBr) ν: 2948 (s); 2932 (s); 2877 (m); 2057 (s); 1603 (s); 1550 (s); 1476 (s); 1463 (w); 1407 (m); 1373 (m); 1352 (m); 1330 (w) 1284 (w); 1269 (w); 1222 (m); 1164 (w); 1142 (w); 1081 (m); 1054 (m); 1049 (m); 1019 (m); 998 (w); 936 (w); 904 (w); 885 (w); 877 (w); 814 (w); 788 (w); 754 (w); 695 (w); 625 (w); 606 (w); 585 (m); 513 (w); 470 (w); 426 cm^{-1} (w).

Complex **$[Fe_4Y_2(OH)_2(mdea)_4(O_2CCMe_3)_6(N_3)_2]\cdot C_6H_5OH$** (**2**) was obtained through the same procedure by using $Y(NO_3)_3\cdot 6H_2O$ in place of $Dy(NO_3)_3\cdot 6H_2O$ and mdea in place of nbdea. Yield 32.1% (based on Fe); Anal. calcd for $C_{56}H_{106}Fe_4N_{10}O_{23}Y_2$: C, 39.83; H, 6.32; N. 8.29; found: C, 39.93; H, 6.71; N, 8.12; IR (KBr) ν: 2961 (s); 2923 (s); 2872 (m); 2061 (s); 1601 (s); 1552 (s); 1481 (s); 1461 (w); 1407 (m); 1371 (m); 1354 (m); 1332 (w) 1286 (w); 1268 (w); 1226 (m); 1165 (w); 1142 (w); 1082 (m); 1058 (m); 1051 (m); 1024 (m); 998 (w); 935 (w); 902 (w); 886 (w); 876 (w); 814 (w); 786 (w); 753 (w); 698 (w); 626 (w); 607 (w); 587 (m); 548 (w); 512 (w); 472 (w); 425 cm^{-1} (w).

Magnetic measurements: The magnetic susceptibility measurements were carried out with a Quantum Design SQUID magnetometer MPMS-XL. This magnetometer works between 1.8 and 400 K for dc applied fields ranging from −7 to 7 T. Measurements were performed on polycrystalline samples. Alternating current susceptibility measurements have been measured with an oscillating ac field of 3 Oe and ac frequencies ranging from 1 to 1500 Hz. The magnetic data were corrected for the sample holder.

Mössbauer spectroscopy: The Mössbauer spectra were acquired using a conventional spectrometer in the constant-acceleration mode equipped with a ^{57}Co source (3.7 GBq) in a rhodium matrix. Isomer shifts are given relative to α-Fe at room temperature. The sample was inserted inside an Oxford Instruments Mössbauer-Spectromag 4000 Cryostat, which has a split-pair superconducting magnet system for applied fields up to 5 T, with the field of the sample oriented perpendicular to the γ-ray direction. The sample temperature can be varied between 3.0 and 300 K.

X-Ray crystallography: Data were measured on Stoe IPDS II (**1**) or IPDS I (**2**) image plate diffractometers using graphite-monochromated Mo Kα radiation, and were corrected for polarisation and absorption. Structure solution (direct methods) and full-matrix least-squares refinement against F^2 (all data) was carried out by using the SHELXTL software package [27]. All ordered non-H atoms were refined anisotropically; disordered atoms were refined with partial occupancy and geometrical restraints, either anisotropically with rigid-bond restraints or isotropically. Organic H atoms were placed in calculated positions; the positions of H atoms bonded to O were refined with O–H restrained to 0.92(4) Å. Crystal data for **1:** $C_{68}H_{133}Dy_2Fe_4N_{13}O_{22}$, 2033.27 $g\cdot mol^{-1}$, triclinic, $P\bar{1}$, a = 13.9237(6), b = 14.5196(7), c = 25.1289(10) Å, α = 82.856(3), β = 79.710(3), γ = 65.545(3)°, Z = 2, V = 4542.9(3) $Å^3$, T = 150(2) K, ρ_{calc} = 1.486 $g\cdot cm^{-3}$, $F(000)$ = 2088, μ(Mo Kα) = 2.315 mm^{-1}; 62413 data, 21679 unique (R_{int} = 0.0342), 979 parameters, final wR_2 = 0.1201, S = 1.018 (all data), R_1 (17985 data with I > 2σ(I)) = 0.0449. **2**: $C_{56}H_{106}Fe_4N_{10}O_{23}Y_2$, 1688.72 $g\cdot mol^{-1}$, monoclinic, $P2_1/c$, a = 19.1485(18), b = 16.4725(10), c = 24.797(2) Å, β = 101.162(11)°, Z = 4, V = 7673.5(11) $Å^3$, T = 200(2) K, ρ_{calc} = 1.482 $g\cdot cm^{-3}$, $F(000)$ = 3512, μ(Mo Kα) = 2.305 mm^{-1}; 82403 data, 15075 unique (R_{int} = 0.0413), 917 parameters, final wR_2 = 0.1073, S = 0.986 (all data), R_1 (11528 data with I > 2σ(I)) = 0.0416. Crystallographic data (excluding structure factors) for the structures published in this paper have been deposited with the Cambridge Crystallographic Data Centre as supplementary publication nos. CCDC 957219 & 957220. Copies of the data can be obtained, free of charge, on application to CCDC, 12 Union Road, Cambridge CB2 1EZ, UK: e-mail: data_request@ccdc.cam.ac.uk, fax: +44 1223 336033 or http://www.ccdc.cam.ac.uk/cgi-bin/catreq.cgi.

Supporting Information

Supporting Information File 1

CIF files for the crystal structures of **1** and **2**.
[http://www.beilstein-journals.org/bjnano/content/supplementary/2190-4286-4-92-S1.zip]

Acknowledgements

This work was supported by the DFG-funded transregional collaborative research center SFB/TRR 88 “3MET”.

References

1. Ako, A. M.; Mereacre, V.; Clérac, R.; Wernsdorfer, W.; Hewitt, I. J.; Anson, C. E.; Powell, A. K. *Chem. Commun.* **2009,** 544. doi:10.1039/b814614d
2. Yamashita, A.; Watanabe, A.; Akine, S.; Nabeshima, T.; Nakano, M.; Yamamura, T.; Kajiwara, T. *Angew. Chem., Int. Ed.* **2011,** *50,* 4016. doi:10.1002/anie.201008180
3. Feltham, H. L. C.; Lan, Y.; Klöwer, F. L.; Ungur, L.; Chibotaru, F.; Powell, A. K.; Brooker, S. *Chem.–Eur. J.* **2011,** *17,* 4362. doi:10.1002/chem.201100438
4. Bernot, K.; Luzon, J.; Bogani, L.; Etienne, M.; Sangregorio, C.; Shanmugam, M.; Caneschi, A.; Sessoli, R.; Gatteschi, D. *J. Am. Chem. Soc.* **2009,** *131,* 5573. doi:10.1021/ja8100038
5. Cucinotta, G.; Perfetti, M.; Luzon, J.; Etienne, M.; Car, P.-E.; Caneschi, A.; Calvez, G.; Bernot, K.; Sessoli, R. *Angew. Chem., Int. Ed.* **2012,** *51,* 1606. doi:10.1002/anie.201107453
6. Boulon, M.-E.; Cucinotta, G.; Luzon, J.; Degl’Innocenti, C.; Perfetti, M.; Bernot, K.; Calvez, G.; Caneschi, A.; Sessoli, R. *Angew. Chem., Int. Ed.* **2013,** *52,* 350. doi:10.1002/anie.201205938
7. Chibotaru, L. F.; Ungur, L.; Soncini, A. *Angew. Chem., Int. Ed.* **2008,** *47,* 4126. doi:10.1002/anie.200800283
8. Liu, J.-L.; Guo, F.-S.; Meng, Z.-S.; Zheng, Y.-Z.; Leng, J.-D.; Tong, M.-L.; Ungur, L.; Chibotaru, L. F.; H, K. J.; Hendrickson, D. N. *Chem. Sci.* **2012,** *2,* 1268. doi:10.1039/c1sc00166c
9. Wang, Y.-X.; Shi, W.; Li, H.; Song, Y.; Fang, L.; Lan, Y.; Powell, A. K.; Wernsdorfer, W.; Ungur, L.; Chibotaru, L. F.; Shen, M.; Cheng, P. *Chem. Sci.* **2012,** *3,* 3366. doi:10.1039/c2sc21023a
10. Jiang, S.-D.; Wang, B.-W.; Su, G.; Wang, Z.-M.; Gao, S. *Angew. Chem., Int. Ed.* **2010,** *49,* 7448. doi:10.1002/anie.201004027
11. Blagg, R. J.; Muryn, C. A.; McInnes, E. J. L.; Tuna, F.; Winpenny, R. E. P. *Angew. Chem., Int. Ed.* **2011,** *50,* 6530. doi:10.1002/anie.201101932
12. Rinehart, J. D.; Fang, M.; Evans, W. J.; Long, J. R. *Nat. Chem.* **2011,** *3,* 538. doi:10.1038/nchem.1063
13. Car, P.-E.; Perfetti, M.; Mannini, M.; Favre, A.; Caneschi, A.; Sessoli, R. *Chem. Commun.* **2011,** *47,* 3751. doi:10.1039/c0cc05850e
14. Mereacre, V.; Baniodeh, A.; Anson, C. E.; Powell, A. K. *J. Am. Chem. Soc.* **2011,** *133,* 15335. doi:10.1021/ja206941e
15. Baniodeh, A.; Mereacre, V.; Magnani, N.; Lan, Y.; Wolny, J. A.; Schünemann, V.; Anson, C. E.; Powell, A. K. *Chem. Commun.* **2013,** *49,* 9666. doi:10.1039/c3cc45695a
16. Feig, A. L.; Lippard, S. J. *Chem. Rev.* **1994,** *94,* 759. doi:10.1021/cr00027a011
17. Zang, Y.; Pan, G.; Que, L., Jr.; Fox, B. G.; Münck, E. *J. Am. Chem. Soc.* **1994,** *116,* 3653. doi:10.1021/ja00087a083
18. Zang, Y.; Dong, Y.; Que, L., Jr.; Kauffmann, K.; Münck, E. *J. Am. Chem. Soc.* **1995,** *117,* 1169. doi:10.1021/ja00108a050
19. Hatert, F.; Long, G. J.; Hautot, D.; Fransolet, A.-M.; Delwiche, J.; Hubin-Franskin, M. J.; Grandjean, F. *Phys. Chem. Miner.* **2004,** *31,* 487. doi:10.1007/s00269-004-0400-4
20. Girerd, J. J.; Papaefthymiou, G. C.; Watson, A. D.; Gamp, E.; Hagen, K. S.; Edelstein, N.; Frankel, R. B.; Holm, R. H. *J. Am. Chem. Soc.* **1984,** *106,* 5941. doi:10.1021/ja00332a031
21. Bartolomé, J.; Filoti, G.; Kuncser, V.; Schinteie, G.; Mereacre, V.; Anson, C. E.; Powell, A. K.; Prodius, D.; Turta, C. *Phys. Rev. B* **2009,** *80,* 014430. doi:10.1103/PhysRevB.80.014430
22. Gorun, S. M.; Lippard, S. J. *Inorg. Chem.* **1991,** *30,* 1625. doi:10.1021/ic00007a038
23. Weihe, H.; Güdel, H. U. *J. Am. Chem. Soc.* **1997,** *119,* 6539. doi:10.1021/ja970320r
24. Canãda-Vilalta, C.; O’Brien, T. A.; Brechin, E. K.; Pink, M.; Davidson, E. R.; Christou, G. *Inorg. Chem.* **2004,** *43,* 5505. doi:10.1021/ic049413h
25. Mukherjee, S.; Bagai, R.; Abboud, K. A.; Christou, G. *Inorg. Chem.* **2011,** *50,* 3849. doi:10.1021/ic200256j
26. Greenwood, N. N.; Gibbs, T. C. *Mössbauer Spectroscopy;* Chapman and Hall: London, 1971. doi:10.1007/978-94-009-5697-1
27. Sheldrick, G. M. *Acta Crystallogr., Sect. A* **2008,** *A64,* 112. doi:10.1107/S0108767307043930

License and Terms

BEILSTEIN JOURNAL OF NANOTECHNOLOGY

Self-organization of mesoscopic silver wires by electrochemical deposition

Sheng Zhong[*1,2], Thomas Koch[1,2], Stefan Walheim[*1,2], Harald Rösner[3], Eberhard Nold[4], Aaron Kobler[2,5], Torsten Scherer[2,6], Di Wang[2,6], Christian Kübel[2,6], Mu Wang[7], Horst Hahn[2,5,8,9] and Thomas Schimmel[1,2,9]

Full Research Paper

Open Access

Address:
[1]Institute of Applied Physics and Center for Functional Nanostructures (CFN), Karlsruhe Institute of Technology (KIT), 76128 Karlsruhe, Germany, [2]Institute of Nanotechnology (INT), Karlsruhe Institute of Technology (KIT), 76021 Karlsruhe, Germany, [3]Institute of Materials Physics, University of Muenster, 48149 Muenster, Germany, [4]Institute for Materials Research I (IMF I) Karlsruhe Institute of Technology (KIT), 76021 Karlsruhe, Germany, [5]Joint Research Laboratory Nanomaterials (KIT and TUD), Technische Universität Darmstadt (TUD), Petersenstr. 32, 64287 Darmstadt, Germany, [6]Karlsruhe Nano Micro Facility (KNMF), Karlsruhe Institute of Technology (KIT), Hermann-von-Helmholtz-Platz 1, 76344 Eggenstein-Leopoldshafen, Germany, [7]National Laboratory of Solid-State Microstructures, Nanjing University, Nanjing 21009, China, [8]Helmholtz Institute Ulm Electrochemical Energy Storage, Albert-Einstein-Allee 11, 89081 Ulm, Germany and [9]Herbert Gleiter Institute of Nanoscience, NUST, Nanjing 21009, China

Email:
Sheng Zhong[*] - sheng.zhong@kit.edu; Stefan Walheim[*] - stefan.walheim@kit.edu

* Corresponding author

Keywords:
crystal growth; electrochemistry; electrodeposition; mesowires; nanoelectrochemistry; nanowires; self-organization; silver nanowires; silver nitrate; stability

Beilstein J. Nanotechnol. **2014,** *5,* 1285–1290.
doi:10.3762/bjnano.5.142

Received: 31 October 2013
Accepted: 25 June 2014
Published: 15 August 2014

This article is part of the Thematic Series "Advances in nanomaterials".

Guest Editors: H. D. Gleiter and T. Schimmel

Abstract

Long, straight mesoscale silver wires have been fabricated from $AgNO_3$ electrolyte via electrodeposition without the help of templates, additives, and surfactants. Although the wire growth speed is very fast due to growth under non-equilibrium conditions, the wire morphology is regular and uniform in diameter. Structural studies reveal that the wires are single-crystalline, with the [112] direction as the growth direction. A possible growth mechanism is suggested. Auger depth profile measurements show that the wires are stable against oxidation under ambient conditions. This unique system provides a convenient way for the study of self-organization in electrochemical environments as well as for the fabrication of highly-ordered, single-crystalline metal nanowires.

Introduction

Nanoscale and mesoscale metal wires have attracted considerable attention due to their potential application in new electronic, sensor, and optical devices [1-10]. Furthermore, metallic nanowires and -contacts play a key role as leads and contacts for contacting molecules in the field of molecular electronics (for a collection of recent work see [11-19]). Silver wires, in particular have been the focus of research due to their excellent electric and optical properties [4-6,9,10,20]. For example, itinerant electrons in silver wires can strongly interact with incident electromagnetic waves at specific frequencies and induce a collective resonant absorption on the surface known as surface plasmon resonance [21]. Because of this feature, noble metals can serve as plasmon waveguides [22,23]. Especially, single-crystalline metallic materials are preferred in order to reduce the loss in transmitting signals. Therefore, the fabrication of microscopic building blocks, such as single-crystalline silver wires, is a crucial step towards the implementation of nanodevices and represents a significant challenge in nanoscale science. There are various existing methods to fabricate mesoscale metallic wires: Electron beam lithography is a precise and well-controlled method, yet for larger numbers of wires rather expensive and time consuming. Electrochemically oxidized anodic alumina membrane (AAM) templates are also often used to fabricate metallic nanowires [24]. Yet the AAM-mediated nanowires are often inhomogeneous in morphology, poly-crystalline in structure, and fragile in their mechanical properties. This is also true for nanowires fabricated with the tip of an atomic force microscope used as a mechano-electrochemical pen [25]. As reported recently, this technique allows to fabricate predefined metallic structures on surfaces with nanoscale resolution, which, however cannot be fabricated as freestanding wires [25,26].

Here we report a unique method to long, straight, and single-crystalline mesoscopic silver wires by electrochemical deposition in the potentiostatic mode without the need to use any templates, surfactants or additives. At the same time, our method has the advantages of high deposition rate, low reaction temperature, and low cost which are traditionally associated with electrochemical deposition techniques [27].

Results and Discussion

The fabrication process of the mesoscopic silver wires is summarized in Figure 1. It is similar to that described in our previous work [28-31]. Before electrodeposition, the electrolyte in the deposition cell is carefully solidified by lowering

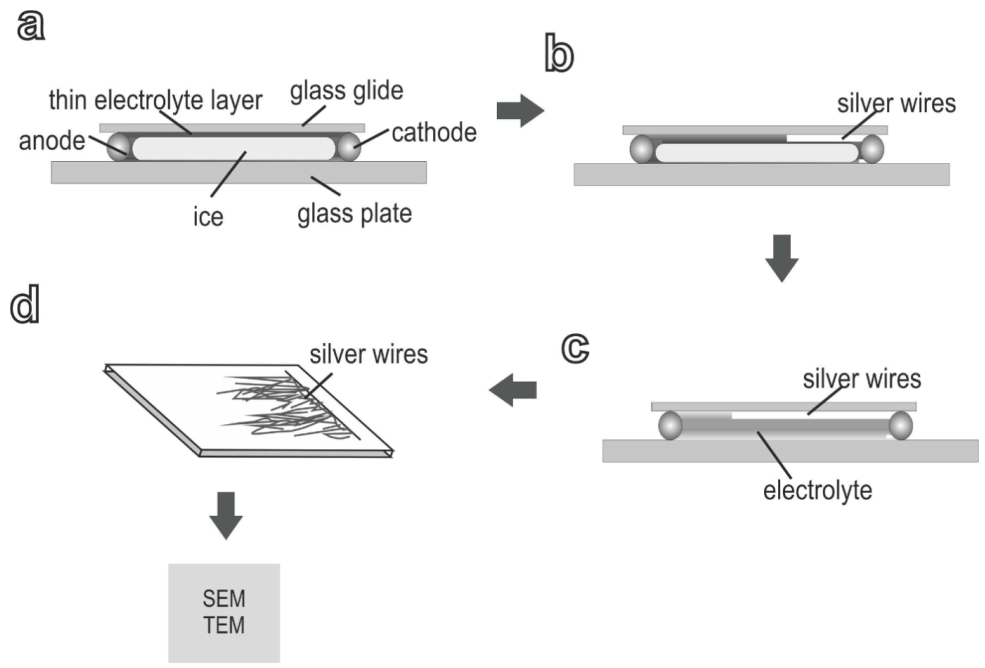

Figure 1: Schematic diagrams of the experimental procedure. (a) By slowly freezing the silver nitrate electrolyte a thin aqueous layer of electrolyte forms between the glass slide and the ice. The concentration of electrolyte is higher than the initial concentration due to the segregation effect. (b) Applying a constant voltage across the two electrodes let the silver grow from the cathode into the electrolyte. (c) Cooling is stopped and the temperature rises after deposition. After melting the ice the silver wires can be taken out of the deposition cell and rinsed with deionized water (d). After drying they are ready for further TEM- and SEM-analysis.

the temperature to a preset value, which is usually just below the freezing point of the electrolyte. Due to the segregation effect, $AgNO_3$ is partially expelled from the ice of the electrolyte during solidification [32]. As a consequence, the concentration of aqueous $AgNO_3$ electrolyte in the deposition cell increases. When equilibrium is reached, a thin layer of concentrated $AgNO_3$ electrolyte is formed between frozen electrolyte and the glass plates of the deposition cell (Figure 1a).

Thereafter, a constant voltage is applied across the two electrodes, and deposits first nucleate from the cathode, grow laterally into the aqueous electrolyte, and form aligned wires which grow towards the anode (Figure 1b). It takes several minutes before the deposit occupy an area of about 0.5 cm^2. When electrodeposition is finished, the temperature is increased to melt the ice (Figure 1c). The wire deposits stack on the glass substrate and can be easily taken out of the electrodeposition cell for further examinations (Figure 1d). The thickness of the electrolyte layer can be roughly estimated by two methods: 1. the thickness of the deposits piled on the substrate [28,31] and 2. by measuring the electric resistance across the cell [33]. Using method 2 the authors showed, that the thickness of the $CuSO_4$ electrolyte layer can be tuned from 100 nm to 1.4 µm by changing the temperature from −8 °C to −1 °C [33]. In the experiments presented here the thickness of the layer was in the range of several micrometers based on the observed thickness of the deposition.

Scanning electron microscopy (SEM) shows that the silver wires are growing parallel to the glass substrate (Figure 2). Bunches of silver wires initially nucleate on the cathode and propagate laterally on the glass substrate parallel to the local electric field. Eventually silver wires cover the glass substrate and pile up like log stacks. The overall morphology of the deposits exhibits bunch- and tree-like structures, as shown in Figure 2a. Detailed features of the silver wires are illustrated in Figure 2b and 2c, where the wires are straight uniform in diameter and exhibit a smooth surface. The diameter of the wires ranges from about 150 nm to 600 nm. Preliminary results show a strong influence of the applied voltage on the diameter of the wires.

Several long wires are shown in Figure 2d. Sometimes the length of the wires exceeds 150 µm. As illustrated in Figure 2, the deposits macroscopically consist of long and straight wires, occasionally with regular side branches. Microscopically, straight silver wires are often aligned and form ordered arrays. In our experiments, the silver wires are robust and can be taken out of the cell together with the substrates without being damaged. They can be removed from the substrate and subsequently rearranged on other substrates.

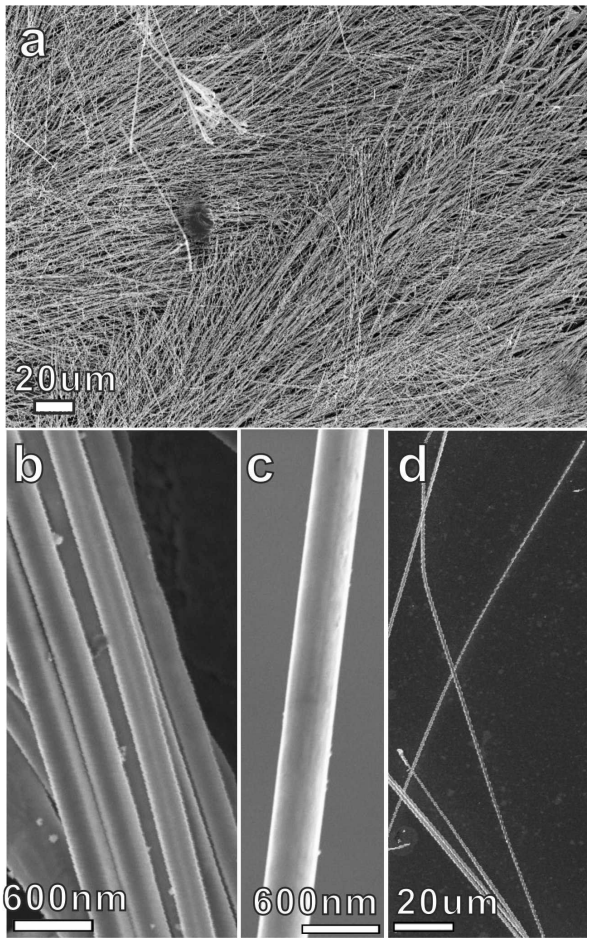

Figure 2: SEM images of silver wires: (a) Overview: low-magnification image. (b) Zoom-in of (a). (c) Image of one silver wire, illustrating the homogeneous thickness and smooth surface. (d) Image of several long silver wires.

The microstructure and chemical composition of the silver wires were analyzed by transmission electron microscopy (TEM) and energy dispersive X-ray (EDX) spectroscopy.

Figure 3a shows a typical bright-field TEM image of silver wires and the corresponding selected area electron diffraction (SAED) pattern (Figure 3b). The SAED patterns demonstrate a distinct single-crystalline feature. The data show that the growth direction of the wire is perpendicular to the [111] direction, along the [112] direction. Figure 3c is a scanning TEM (STEM) image of a silver wire. Figure 3d shows the EDX spectrum collected from the marked region in Figure 3c. Strong silver element peaks are identified, together with very weak gold, iron, carbon, and cobalt peaks. Gold and carbon signals most likely come from the carbon-covered gold TEM grid, on which the sample has been deposited. Cobalt and iron most likely come from the pole pieces of the objective lens. Oxygen and sulfur signals are not observed. Therefore, one can conclude

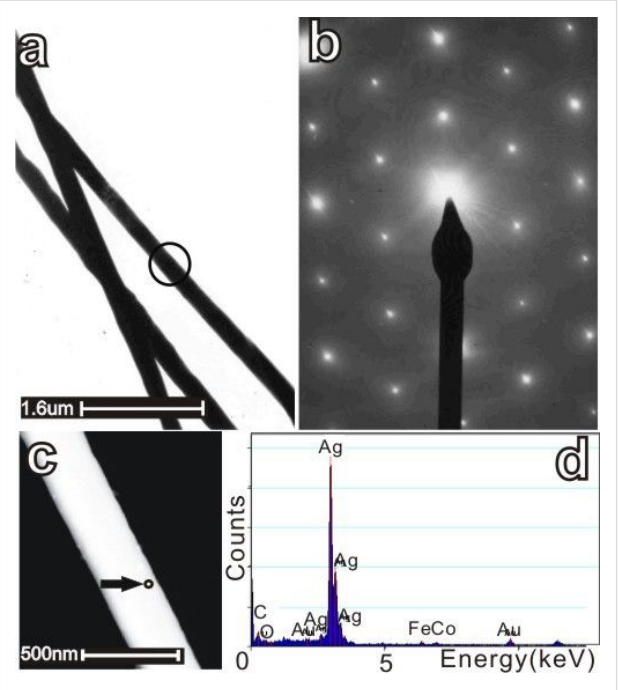

Figure 3: TEM analysis of thin silver wires and corresponding EDX information. (a) Bright-field image of typical silver wires with the axes which should be oriented in [112] direction and (b) the corresponding SAED patterns recorded from the marked region, the growth direction is mostly like [112]. The zone axis is <111>. (c) HAADF-STEM image of a silver wire and (d) the corresponding EDX spectrum taken at the labelled position on the wire of Figure 3c. Strong silver element peaks can be identified. Very weak gold, iron, carbon, and cobalt peaks were also found. Gold and carbon come from the substrate. The cobalt and iron signal comes from the pole pieces of the objective lens; no peak can be attributed to sulfur, nitrogen or oxygen, the latter demonstrating that the silver wires are not oxidized at ambient conditions in air.

that the silver wires grown in the experiments presented here are chemically pure.

The application of silver wires as building blocks for microelectronics requires good chemical stability, especially the stability against oxidation under ambient conditions. For most metallic microstructures, however, stability against oxidation is a challenge. The reason is that reducing the length scale means increasing the surface/volume ratio and thus induces more instability in comparison with bulk systems. Therefore, the aging of the silver wires was investigated by scanning Auger micro spectroscopy (SAMS).

Figure 4 shows the element depth profiles of silver wires, which were exposed to ambient conditions for different times. The profiles are determined by Auger measurements between several short sputtering steps. The left diagram shows data obtained from a freshly-prepared sample (exposed to ambient air for less than one hour) and the right one the data of an aged sample that had been exposed to ambient conditions for four months. Comparing the two depth profiles, no significant differences can be identified. As illustrated in Figure 4, in a depth of only 5 nm, the concentration of the oxide already virtually approaches zero. The thickness of the oxide layers did not change significantly during the aging process and the oxide layer is not more than approx. 5 nm thick. Therefore, Figure 4 indicates that the silver wires are stable against oxidation under ambient conditions. Silver typically corrodes under ambient conditions by silver sulfidation with hydrogen sulfide (H_2S) and/or carbonyl sulfide (OCS) in the atmosphere, with this phenomenon being amplified by water and oxygen [34]. The origin of the stability of our structures is the subject of an ongoing study.

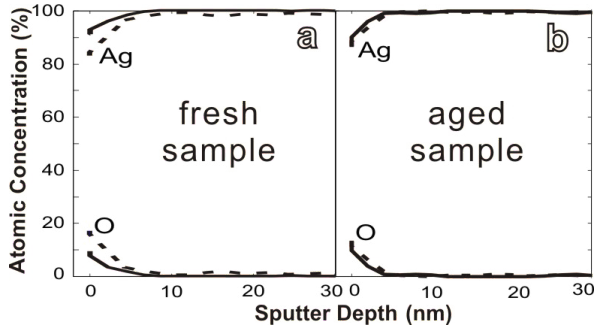

Figure 4: Auger depth profile curves of freshly prepared and aged silver wires. The full and dotted curves correspond to data obtained from two different wires. The relative atomic concentration is plotted versus the sputter depth; (a) freshly-prepared sample taken out of the electrodeposition cell and washed by deionized water and immediately investigated by SAMS. (b) Sample aged by exposure to ambient conditions for four months. Freshly-prepared and aged samples show similar depth profiles, indicating that the single-crystalline silver wires are stable under ambient conditions on this time scale.

It is interesting to consider the mechanism for electrochemical self-organization of such long, smooth silver wires, bearing in mind, that the growth rate of the wires is of the order of 10 μm/s in our experiments and that the entropy of interfacial phase transition for silver is small. The faces tend to be roughened [34] and the surfaces of the wires are rounded without obvious faces. This may indicate that the surface is rough on atomic scale. It is known, that the (112) surface energy is relatively high and that the growth speed of [112] is faster than that of other facets [35]. Hence elongated silver wires are generated due to the anisotropy in growth rate. However, anisotropy in growth rate cannot guarantee for the formation of smooth silver wires with homogeneous diameter as that shown in Figure 2b,c. The point is that the side faces of the wires are rough on the atomic scale, and should possess linear growth kinetics. Thus, any small driving force should make the side faces to grow. If this would

be the case, then we would observe conical silver wires instead of iso-diameter ones. We suggest that the formation of uniform silver wires in our system is due to the unique geometric restriction of the deposition cell and the screening effect in Laplacian field [36,37]. According to Chazalviel, the cation concentration behind the growing front decreases dramatically in a two-dimensional electrodeposition system [37]. Therefore, active deposition takes place only on the growth front, and growth in those parts behind the growth front is virtually stopped. In a thick electrodeposition cell, this condition cannot be realized easily because of convection and migration of the ions in the electric field. Our thin film electrodeposition system is closer to an ideal two-dimensional growth system, which helps to explain the low diameters of the silver wires.

The growth mechanism of the silver wires can be explained in the following model: Initial silver wires nucleate on the cathode and grow towards the anode, presumably with [112] as the preferred growth direction. Behind the growth front the wires do not increase their diameter due to the depletion effect. These two factors allow the wires, once they are initiated along the direction of local concentration gradient, to develop into homogeneous, non-branching wires, as shown in Figure 2b,c. However, if the axis of the wire deviates from the local concentration gradient, e.g., if in the initial direction of the axis of the wire is not perpendicular to the cathode (anode), sidebranches will be triggered. Since the sides of the silver wires are rough, there is no significant energy barrier to prevent the generation of sidebranches. When this sidebranching mechanism works, the sidebranches should develop on only one side of the wires, that is, from the side facing the cation supply. Indeed such comb-like structures were observed in our experiments, too. As illustrated in Figure 5, side branching takes place only on one side of the wire and forms a 60 degree angle with respect to the main stem. Electron diffraction indicates that the side branches maintain the same crystallographic direction.

These observations confirm our understanding of the silver wire growth and support the nutrient-supply-flux induced side branching mechanism in silver wire growth. This branching mechanism is valid when the wire growth has very strong anisotropy and the side faces of the wire are rough.

Conclusion

We have reported a novel technique for fabricating single-crystalline silver wires by electrochemical deposition, without introducing templates, additives and surfactants. The simple experimental setup and the wide range of control parameters make this approach a versatile and simple pathway to fabricate metal meso- and nanostructures. This unique system provides a convenient way to investigate fundamental processes of self-organization in electrochemical environments. Our results are pointing the way to a controlled fabrication of highly-ordered, single-crystalline metal nanowires, opening perspectives, e.g., for on-chip electrical connectors, sensors as well as photonic and plasmonic devices.

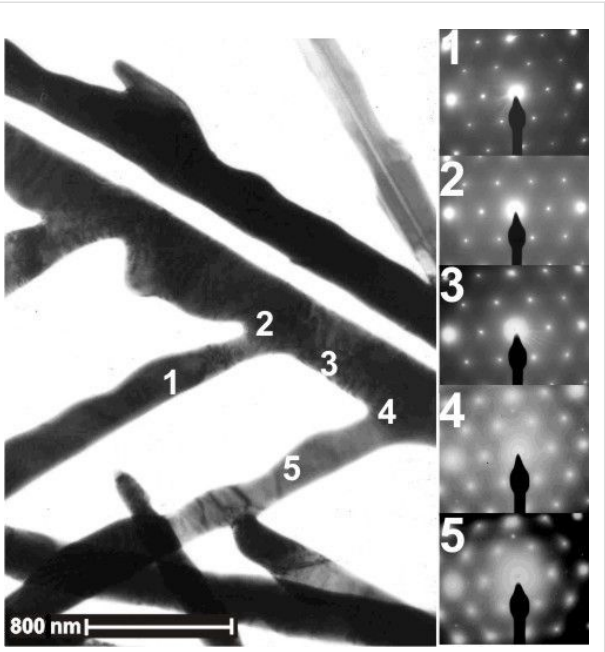

Figure 5: TEM analysis of thin comb-like silver dendrites (dark areas in the image left) and corresponding SAED patterns. Patterns (1)–(5) (right) were recorded at different spots marked by the corresponding number in the TEM image (left). The zone axis is <111>. This suggests that the comb structure is single-crystalline. All SAED patterns display the same hexagonal pattern. This suggests that the comb structure is single- crystalline. Each branch should grow along one of the <112> directions.

Experimental

Electrodeposition was carried out in a cell with two parallel electrodes made of silver wires (99.99%). The electrolyte solution was prepared with $AgNO_3$ (99.8%) and deionized water. The concentration of the solution was 0.05 M.

Scanning electron microscopy (SEM) was performed with a Gemini 2 system from Zeiss (LEO). The scanning Auger micro spectroscopy (SAMS) investigations were done with a PHI 680 AUGER NANOPROBE UHV system with 15 nm resolution and depth profile equipment. Transmission electron microscopy (TEM) investigations were performed with a Philips Tecnai F20 ST system operated at 200 kV. EDX analyses were carried out in STEM (scanning transmission electron microscopy) mode in order to measure nanometer-scale samples (1 nm spot size for the EDX measurements presented in this article). STEM micrographs were acquired using an HAADF (High-Angle Annular Dark-Field) detector.

Acknowledgements

We thank Prof. Cynthia Volkert for stimulating discussions. This work was financially supported by the DFG-Center for Functional Nanostructures (CFN) at the Karlsruhe Institute of Technology and by the Baden-Wuerttemberg Foundation within the Network of Excellence "Functional Nanostructures".

References

1. Lieber, C. M. *Sci. Am.* **2001,** *285,* 58–64. doi:10.1038/scientificamerican0901-58
2. Chen, J.; Wiley, B. J.; Xia, Y. *Langmuir* **2007,** *23,* 4120–4129. doi:10.1021/la063193y
3. Kuchibhatla, S. V. N. T.; Karakoti, A. S.; Bera, D.; Seal, S. *Prog. Mater. Sci.* **2007,** *52,* 699–913. doi:10.1016/j.pmatsci.2006.08.001
4. Rycenga, M.; Cobley, C. M.; Zeng, J.; Li, W.; Moran, C. H.; Zhang, Q.; Qin, D.; Xia, Y. *Chem. Rev.* **2011,** *111,* 3669–3712. doi:10.1021/cr100275d
5. Hartland, G. V. *Chem. Rev.* **2011,** *111,* 3858–3887. doi:10.1021/cr1002547
6. Dawson, K.; Strutwolf, J.; Rodgers, K. P.; Herzog, G.; Arrigan, D. W. M.; Quinn, A. J.; O'Riordan, A. *Anal. Chem.* **2011,** *83,* 5535–5540. doi:10.1021/ac2004086
7. Wild, B.; Cao, L.; Sun, Y.; Khanal, B. P.; Zubarev, E. R.; Gray, S. K.; Scherer, N. F.; Pelton, M. *ACS Nano* **2012,** *6,* 472–482. doi:10.1021/nn203802e
8. Mann, S. A.; Garnett, E. C. *Nano Lett.* **2013,** *13,* 3173–3178. doi:10.1021/nl401179h
9. Garnett, E. C.; Cai, W.; Cha, J. J.; Mahmood, F.; Connor, S. T.; Greyson Christoforo, M.; Cui, Y.; McGehee, M. D.; Brongersma, M. L. *Nat. Mater.* **2012,** *11,* 241–249. doi:10.1038/nmat3238
10. van de Groep, J.; Spinelli, P.; Polman, A. *Nano Lett.* **2012,** *12,* 3138–3144. doi:10.1021/nl301045a
11. May, F.; Wegewijs, M. R.; Hofstetter, W. *Beilstein J. Nanotechnol.* **2011,** *2,* 693–698. doi:10.3762/bjnano.2.75
12. Hong, W.; Valkenier, H.; Mészáros, G.; Manrique, D. Z.; Mishchenko, A.; Putz, A.; García, P. M.; Lambert, C. J.; Hummelen, J. C.; Wandlowski, T. *Beilstein J. Nanotechnol.* **2011,** *2,* 699–713. doi:10.3762/bjnano.2.76
13. Perrin, M. L.; Martin, C. A.; Prins, F.; Shaikh, A. J.; Eelkema, R.; van Esch, J. H.; van Ruitenbeek, J. M.; van der Zant, H. S. J.; Dulić, D. *Beilstein J. Nanotechnol.* **2011,** *2,* 714–719. doi:10.3762/bjnano.2.77
14. Todorov, T. N.; Dundas, D.; Paxton, A. T.; Horsfield, A. P. *Beilstein J. Nanotechnol.* **2011,** *2,* 727–733. doi:10.3762/bjnano.2.79
15. Obermair, C.; Kuhn, H.; Schimmel, T. *Beilstein J. Nanotechnol.* **2011,** *2,* 740–745. doi:10.3762/bjnano.2.81
16. Strange, M.; Thygesen, K. S. *Beilstein J. Nanotechnol.* **2011,** *2,* 746–754. doi:10.3762/bjnano.2.82
17. Nakashima, S.; Takahashi, Y.; Kiguchi, M. *Beilstein J. Nanotechnol.* **2011,** *2,* 755–759. doi:10.3762/bjnano.2.83
18. Lü, J.-T.; Gunst, T.; Hedegård, P.; Brandbyge, M. *Beilstein J. Nanotechnol.* **2011,** *2,* 814–823. doi:10.3762/bjnano.2.90
19. Solomon, G. C.; Bergfield, J. P.; Stafford, C. A.; Ratner, M. A. *Beilstein J. Nanotechnol.* **2011,** *2,* 862–871. doi:10.3762/bjnano.2.95
20. Gaynor, W.; Burkhard, G. F.; McGehee, M. D.; Peumans, P. *Adv. Mater.* **2011,** *23,* 2905–2910. doi:10.1002/adma.201100566
21. El-Sayed, M. A. *Acc. Chem. Res.* **2001,** *34,* 257–264. doi:10.1021/ar960016n
22. Barnes, W. L.; Dereux, A.; Ebbesen, T. W. *Nature* **2003,** *424,* 824–830. doi:10.1038/nature01937
23. Wang, W.; Yang, Q.; Fan, F.; Xu, H.; Wang, Z. L. *Nano Lett.* **2011,** *11,* 1603–1608. doi:10.1021/nl104514m
24. Nishizawa, M.; Menon, V. P.; Martin, C. R. *Science* **1995,** *268,* 700–702. doi:10.1126/science.268.5211.700
25. Obermair, C.; Wagner, A.; Schimmel, T. *Beilstein J. Nanotechnol.* **2011,** *2,* 659–664. doi:10.3762/bjnano.2.70
26. Obermair, C.; Kress, M.; Wagner, A.; Schimmel, T. *Beilstein J. Nanotechnol.* **2012,** *3,* 824–830. doi:10.3762/bjnano.3.92
27. Wang, Z. L. *Characterization of nanophase materials;* Wiley-VCH: Weinheim, New York, 2000.
28. Wang, M.; Zhong, S.; Yin, X.-B.; Zhu, J.-M.; Peng, R.-W.; Wang, Y.; Zhang, K.-Q.; Ming, N.-B. *Phys. Rev. Lett.* **2001,** *86,* 3827. doi:10.1103/PhysRevLett.86.3827
29. Zhong, S.; Koch, T.; Wang, M.; Scherer, T.; Walheim, S.; Hahn, H.; Schimmel, T. *Small* **2009,** *5,* 2265–2270. doi:10.1002/smll.200900746
30. Zhong, S.; Wang, D.; Koch, T.; Wang, M.; Walheim, S.; Schimmel, T. *Cryst. Growth Des.* **2010,** *10,* 1455–1459. doi:10.1021/cg9012747
31. Zhong, S.; Wang, Y.; Wang, M.; Zhang, M.-Z.; Yin, X.-B.; Peng, R.-W.; Ming, N.-B. *Phys. Rev. E* **2003,** *67,* 061601. doi:10.1103/PhysRevE.67.061601
32. Bruinsma, O. S. L.; van der Eerden, J. P. *Science and technology of crystal growth;* Kluwer: Dordrecht, 1995.
33. Weng, Y.-Y.; Si, J.-W.; Gao, W.-T.; Wu, Z.; Wang, M.; Peng, R.-W.; Ming, N.-B. *Phys. Rev. E* **2006,** *73,* 051601. doi:10.1103/PhysRevE.73.051601
34. Elechiguerra, J. L.; Larios-Lopez, L.; Liu, C.; Garcia-Gutierrez, D.; Camacho-Bragado, A.; Yacaman, M. J. *Chem. Mater.* **2005,** *17,* 6042–6052. doi:10.1021/cm051532n
35. Galanakis, I.; Bihlmayer, G.; Bellini, V.; Papanikolaou, N.; Zeller, R.; Blügel, S.; Dederichs, P. H. *EPL* **2002,** *58,* 751–757. doi:10.1209/epl/i2002-00413-7
36. Marsili, M. *J. Phys. A: Math. Gen.* **1992,** *25,* 3493. doi:10.1088/0305-4470/25/12/011
37. Chazalviel, J.-N. *Phys. Rev. A* **1990,** *42,* 7355. doi:10.1103/PhysRevA.42.7355